Atlantic Water properties and circulation north of Svalbard in a changing Arctic

Zoé Koenig

To cite this version:

Zoé Koenig. Atlantic Water properties and circulation north of Svalbard in a changing Arctic. Oceanography. Université Pierre et Marie Curie - Paris VI, 2017. English. NNT : 2017PA066306 . tel-01721467v2

HAL Id: tel-01721467

https://theses.hal.science/tel-01721467v2

Submitted on 9 Mar 2018

THÈSE DE DOCTORAT DE
L'UNIVERSITÉ PIERRE ET MARIE CURIE – PARIS 6

Spécialité : Océanographie
École Doctorale 129

réalisée au
Laboratoire d'Océanographie et du Climat
Expérimentations et Approches Numériques

en vue de l'obtention du grade de
DOCTEUR DE L'UNIVERSITÉ PIERRE ET MARIE CURIE

présentée par
ZOÉ KOENIG

Atlantic Water properties and circulation north of Svalbard in a changing Arctic

Soutenue le 20 octobre 2017
devant le jury composé de:

Mme	Christine Provost	LOCEAN UPMC, Paris	*Directrice*
M.	Gilles Garric	Mercator-Océan, Toulouse	*Directeur*
Mme	Pascale Bouruet-Aubertot	LOCEAN UPMC, Paris	*Président*
M.	Luc Rainville	Univ. of Washington, USA	*Rapporteur*
M.	Michael Karcher	AWI, Allemagne	*Rapporteur*
Mme	Camille Lique	LOPS, Brest	*Examinatrice*
Mme	Amelie Meyer	NPI, Norway	*Examinatrice*
M.	Jean-Claude Gascard	LOCEAN UPMC, Paris	*Expert Invité*

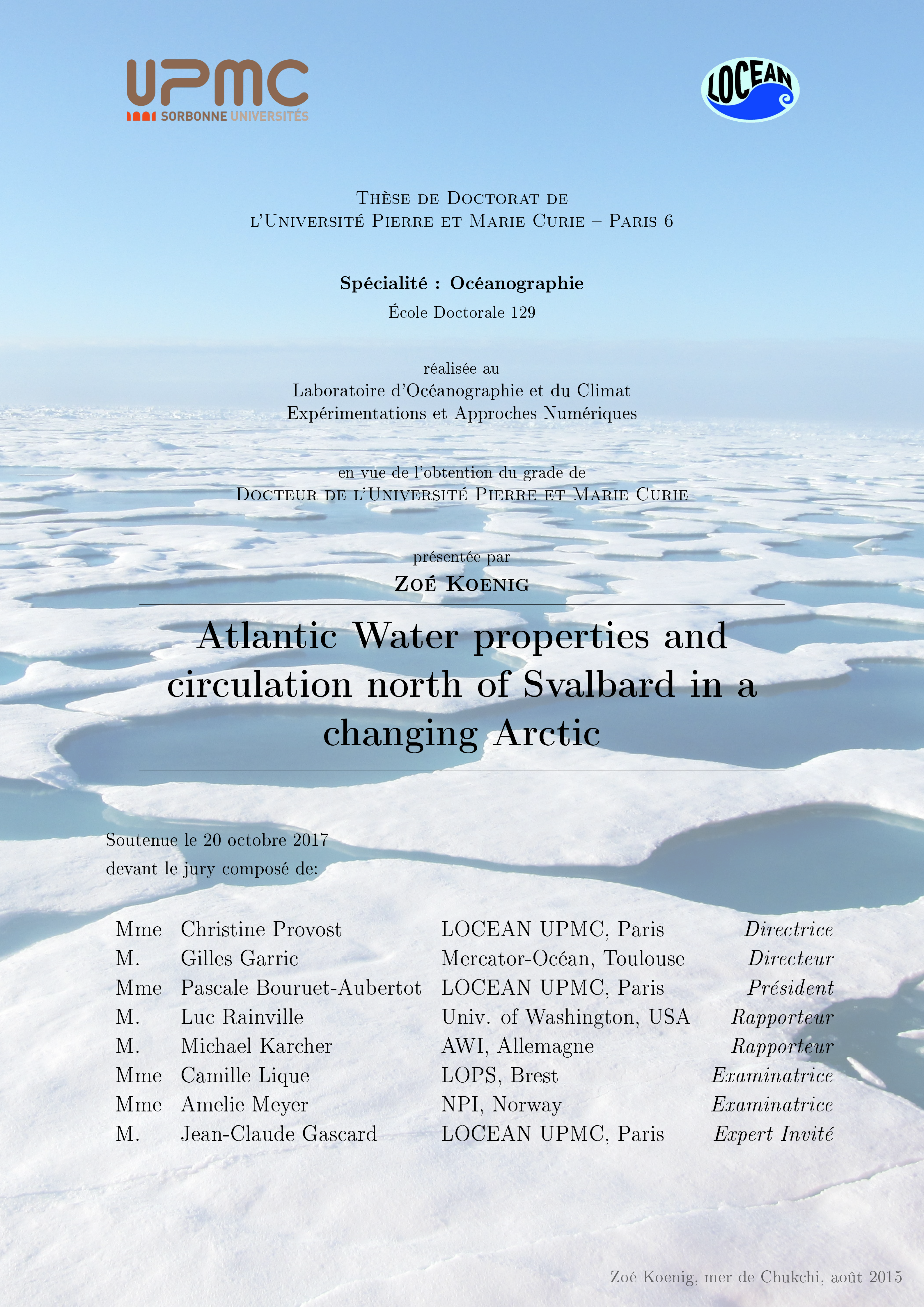
Zoé Koenig, mer de Chukchi, août 2015

Remerciements

Je tiens tout d'abord à remercier les différents membres du Jury d'avoir accepté d'évaluer cette thèse.

Je pense ensuite bien évidemment à mes encadrants, Christine, Gilles et Nathalie. Merci pour tous vos conseils et votre soutien dans les bons comme les mauvais moments. Merci Christine de m'avoir donné l'opportunité de partir aussi souvent sur le terrain et de m'avoir fait confiance sur bien des points ! Merci Gilles de m'avoir accueilli à deux reprises à Mercator Ocean. Merci Nathalie pour le partage de toutes les petites astuces Matlab et les discussions sur tout et rien à la fois ! Je remercie aussi Nicolas pour m'avoir permis d'analyser des données prétraitées et processées avec un très grand soin :)

Je souhaite également remercier Amélie Meyer pour toutes les interactions que nous avons eu pendant cette thèse qui ont été plus que profitables, et qui j'espère continueront après.

À toute la bande du labo (Emilie, Alex, Camilla, Chris, Matthieu, Damien, Clément, Camille, Aida, Anda, Victor, Audrey, Téophile, Julie etc..), c'était chouette quand même ces années de thèse ! Les bières (et girafes) du jeudi soir (et pas que), les vacances au ski, les Solidays, le weekend à Roscoff... Des bouffées d'air pendant cette dernière année dont j'avais bien besoin.

J'allais oublier, les copains de l'ENS, mention particulière pour le B6 : on l'a tous fini finalement cette thèse. On râle souvent, mais on n'a pas fait tout ça pour rien :). Et les copains de la grimpe, le moment de franche décompression de la semaine avec les blagues salaces et le petit apéro après l'effort ! Une petite pensée aussi pour la promotion TAO avec qui j'ai passé de bonnes années d'études et qui ont rendu les stages sur le terrain toujours plus sympa les uns que les autres.

Une mention très spéciale aux 3 drôles de dames Alex, Vio et Lolo : on a fait notre thèse ensemble, vous avez été un vrai pilier surtout pendant cette dernière année qui n'a pas été facile. Je ne vous l'ai sûrement pas vraiment dit mais je tiens à vous dire un grand merci pour juste avoir été présentes aux moments où j'en avais le plus besoin : c'est là qu'on reconnait les très bonnes amies. Et aussi merci pour tous les autres bons moments de franche amitié et de rigolade : les déjeuners, la piscine, les weekends/vacances. C'est sûr, ces amitiés resteront longtemps !

Mes derniers remerciements vont à ma famille et à Pierre qui ont tous été présents à leur manière. Merci d'avoir supporter mon caractère qui peut parfois être de cochon. Malgré nos petites engueulades, nous nous sommes toujours réconciliés et c'est bien ça le plus important.

Je dédie ma thèse à ma maman, sans qui je n'en serais jamais venue à bout. Tu m'as toujours soutenu dans tous mes choix et je sais que de là-haut tu es fière et que tu aurais adoré assister à cette soutenance.

Summary

The Atlantic Water (AW) inflow is crucial for the heat and salt budget of the Arctic. This PhD thesis brings new insights to the inflow of AW in the area north of Svalbard, using several tools: hydrography from autonomous drifting buoys, currents from a mooring and 1/12° spatial resolution operational model outputs.

The IAOOS (Ice Atmosphere Ocean Observing System) platforms were deployed during the N-ICE2015 expedition which collected the first January hydrographic data in the region of the Yermak Plateau north of Svalbard. They document shallow warm water over the Svalbard continental slope melts the sea ice although the air surface temperature is $\sim -30°C$ and generates ocean to ice heat fluxes reaching values up to $400W.m^{-2}$. Warm water is brought from the AW layer up to the surface through near-inertial waves generated by winter storms, large barotropic tides over steep topography and/or geostrophic adjustments.

The 1/12° Mercator Ocean operational model is used after comparison with the IAOOS platform data from N-ICE2015 expedition. Sea ice extent between winters 2015 and 2016 differs largely. Model outputs suggest that convection-induced upward heat fluxes explain the sea ice edge further north over the continental slope north of Svalbard in winter 2016 compared to winter 2015. Model outputs are also used to examine the Atlantic Water inflow pathways. Besides the Svalbard Branch and the Yermak Branch, the model shows a robust AW winter path not documented before: the Yermak Pass Branch that flows through the Yermak Pass over the Yermak Plateau and that could partly explain the hydrography data from the IAOOS platforms during winter 2015. Finally, the model suggests an important mesoscale activity (eddies) throughout the AW flow.

The Yermak Pass Branch properties are examined using one-year (2007-2008) of moored ADCP (Acoustic Doppler Curent Profiler) data in the Yermak Pass. The flow is largely dominated by tides. In winter, baroclinic eddies of AW with a periodicity of 5 to 10 days and pulses of AW monthly/bimonthly are found. These pulses carry AW eastward through the Pass. Model outputs suggest that the Yermak Pass Branch is a robust winter pattern over the last 10 years, carrying on average 31% of the volume transport of the West Spitsbergen Current (36% in winter).

Résumé en Français

L’Arctique est une des régions du globe où l'impact du changement climatique est le plus spectaculaire. L’océan Arctique aurait selon les estimations les plus pessimistes perdu jusqu’à 75% de son volume de glace (https://nsidc.org) pour se transformer progressivement en océan libre de glace en été. Les causes et les conséquences de cette diminution rapide sont encore largement inconnues du fait des rétroactions complexes entre l’atmosphère, la neige, la glace et l’océan (Vihma et al., 2014). On sait que les échanges entre ces 4 milieux sont altérés, que la circulation océanique de surface est modifiée, et que l'apport d'eau douce due à la fonte détruit les équilibres fragiles qui existaient auparavant. A toutes les échelles spatiales, de la plus petite – celle de la turbulence – à la plus grande – celle de la circulation des Eaux Atlantiques dans les couches intermédiaires de l'océan Arctique – des changements sont observés (Fer et al., 2015; Rudels et al., 2015). Les conséquences de ces changements dans l'Arctique pourraient affecter les moyennes latitudes et en particulier l'Europe. Selon de récents résultats du GIEC, la hausse des températures de l’air en Arctique pourraient atteindre 4.8°C d'ici 2100 (https://www.ipcc.ch/report/ar5/wg1/). La diminution du gradient méridien de température entre les hautes et moyennes latitudes modifierait alors la circulation atmosphérique et induirait une augmentation de la fréquence des incursions d’air polaire aux moyennes latitudes.

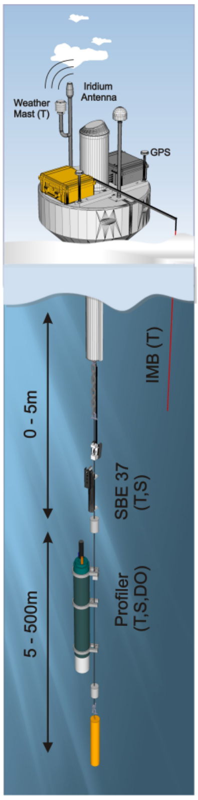

La zone au Nord du Svalbard est un des points de rencontre entre les eaux chaudes et salées venant de l'Atlantique et les eaux froides de l'Arctique. En 2015, un camp de glace s'est tenu pendant 6 mois (de Janvier à Juin, campagne N-ICE2015, http://www.npolar.no/en/projects/n-ice2015.html) dans cette région clé, et a permis de documenter cette zone à partir du bateau de recherche norvégien *R/V Lance*.

Durant cette campagne, trois plate-formes autonomes dérivantes développées dans le cadre du projet Equipex IAOOS du Grand Emprunt (http://www.iaoos-equipex.upmc.fr) ont été déployées en Janvier-Février 2015. Ces plates-formes effectuent des sondages dans l'atmosphère (jusqu'à 5 km d'altitude) grâce à un microlidar, dans l'océan jusqu'à 800m de profondeur avec un profileur (température, salinité et oxygène dissous) et à travers la neige et la glace à l'interface océan-atmosphère grâce à un IMB (Ice Mass Balance), une chaîne avec des capteurs de température tous les 2 cm (Figure 1). Lors de ma thèse j'ai acquis les compétences techniques pour déployer ces plate-formes (participation à 3 campagnes de déploiement) et analyser certaines de leur observations.

Figure 1 : *Schéma de la bouée IAOOS qui montre le mat météo et iridium, le GPS, l'IMB, une microcat SBE37 et le profileur océanique.*

La première partie de ma thèse a consisté à analyser les données océaniques des plate-formes IAOOS déployées pendant la campagne N-ICE2015, qui représentent les premières données d'hiver récoltées dans la région (Koenig et al., 2016). Trois régions ont été traversées lors de la dérive des plate-formes : le bassin de Nansen, le Sofia Deep et le talus continental du Svalbard (Figure 2). En profondeur, les eaux chaudes sont soit des Eaux Atlantiques provenant directement du détroit de Fram (via la branche du Svalbard et la branche du Yermak), soit des Eaux Atlantiques modifiées, moins chaudes, qui ont déjà circulé en Arctique.

En hiver, le bassin de Nansen est caractérisé par une couche chaude d'Eaux Atlantiques modifiées à plus de 100 m de profondeur et une glace qui s'épaissit. Le long du talus continental du Svalbard, les Eaux Atlantiques s'écoulent près de la surface (20 m de profondeur) et la glace fond malgré des températures extérieures de – 30 °C. Au sein du Sofia Deep, les eaux profondes sont d'origines variées : des Eaux Atlantiques qui proviennent de la branche du Svalbard ou de la branche du Yermak, mais aussi des Eaux Atlantiques modifiées qui proviennent du bassin de Nansen. L'épaisseur de glace est stable.

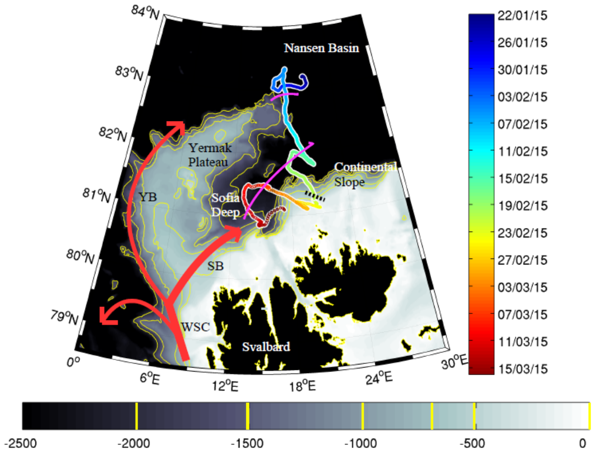

Figure 2 : *Trajectoire de la plateforme IAOOS pendant la campagne N-ICE2015. La carte de fond est la bathymétrie et l 'échelle de couleur verticale est le temps. Le courant West Spitsbergen (WSC) d'eaux atlantiques se divise en trois branches : une branche de recirculation vers le Sud dans le détroit de Fram, la branche du Yermak (YB) et la branche du Svalbard (SB).*

Une analyse des interactions océan-glace en hiver a été réalisée. Une fonte basale de la glace au milieu de l'hiver le long du talus continental du Svalbard est observée et est associée à des flux de chaleur de l'océan vers la glace pouvant atteindre plus de 400 Wm^{-2}. Les événements de fonte sont associés à des ondes quasi inertielles autour de la période 12 h visibles dans la température et la salinité de la couche de mélange. Ces ondes sont potentiellement générées par les tempêtes hivernales, les grandes marées barotropes sur une topographie abrupte et/ou des ajustements géostrophiques (Figure 3). Tous ces processus permettent à la chaleur des Eaux Atlantiques d'atteindre la surface.

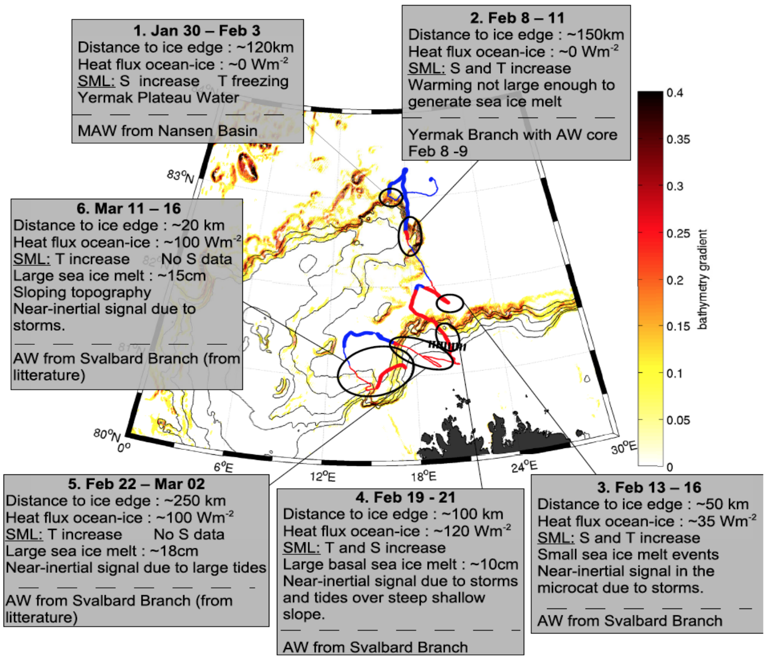

1. Jan 30 – Feb 3
Distance to ice edge : ~120km
Heat flux ocean-ice : ~0 Wm^{-2}
SML: S increase T freezing
Yermak Plateau Water
MAW from Nansen Basin

2. Feb 8 – 11
Distance to ice edge : ~150km
Heat flux ocean-ice : ~0 Wm^{-2}
SML: S and T increase
Warming not large enough to generate sea ice melt
Yermak Branch with AW core Feb 8 -9

3. Feb 13 – 16
Distance to ice edge : ~50 km
Heat flux ocean-ice : ~35 Wm^{-2}
SML: S and T increase
Small sea ice melt events
Near-inertial signal in the microcat due to storms.
AW from Svalbard Branch

4. Feb 19 - 21
Distance to ice edge : ~100 km
Heat flux ocean-ice : ~120 Wm^{-2}
SML: T and S increase
Large basal sea ice melt : ~10cm
Near-inertial signal due to storms and tides over steep shallow slope.
AW from Svalbard Branch

5. Feb 22 – Mar 02
Distance to ice edge : ~250 km
Heat flux ocean-ice : ~100 Wm^{-2}
SML: T increase No S data
Large sea ice melt : ~18cm
Near-inertial signal due to large tides
AW from Svalbard Branch (from litterature)

6. Mar 11 – 16
Distance to ice edge : ~20 km
Heat flux ocean-ice : ~100 Wm^{-2}
SML: T increase No S data
Large sea ice melt : ~15cm
Sloping topography
Near-inertial signal due to storms.
AW from Svalbard Branch (from litterature)

Figure 3 : *Résumé de la première étude. La bathymétrie (contour) et et le gradient bathymétrique sont en arrière plan. La trajectoire de la plate-forme IAOOS est bleue lorsque les eaux profondes sont des eaux Atlantiques modifiées, et rouge lorsque ce sont des eaux Atlantiques. La trajectoire est épaisse quand il y a une tempête et fine sinon. Dans les encarts gris, le trait pointillé sépare les commentaires sur la surface (en haut) et sur les eaux plus profondes (en bas) (extrait de Koenig et al., 2016b).*

Dans un second temps, l'étude des données des plateformes IAOOS a été complétée par une analyse de sorties de modèle océanique avec assimilation et haute résolution spatiale (1/12°) de Mercator Océan (Koenig et al., 2017a). Les données *in situ* des plateformes IAOOS de la campagne N-ICE215 et des données satellitales de couverture de glace ont été utilisées pour évaluer la performance du modèle dans la zone marginale de glace au nord du Svalbard. La limite de glace, les flux de chaleur océaniques, la profondeur de la couche de mélange et les caractéristiques des Eaux Atlantiques sont en bon accord avec les données *in situ* et satellitales. Le modèle est ensuite utilisé pour replacer les données dans un contexte spatio-temporel plus large.

Les sorties du modèle montrent que les chemins empruntés par les Eaux Atlantiques autour et à travers le Plateau de Yermak diffèrent en hiver et en été (Figure 4). En hiver, le transport d'Eaux Atlantiques le long du West Spitsbergen Current (WSC) est important et se divise en trois branches à l'approche du plateau de Yermak : la branche du Svalbard, la branche du Yermak et la branche du Yermak Pass à travers un passage dans le plateau de Yermak à 80.8°N. En été, le transport des Eaux Atlantiques dans le WSC est moindre (divisé par deux) et le transport à travers la Yermak Pass est quasi nul. A notre connaissance, la branche du Yermak Pass n'avait été mise en évidence qu'une seule fois dans le passé par le passage de flotteurs à travers cette passe pendant l'hiver 1988 (Gascard et al., 1995) et l'écoulement des Eaux Atlantiques à travers cette branche serait typique de la situation hivernale de la circulation autour du Plateau du Yermak.

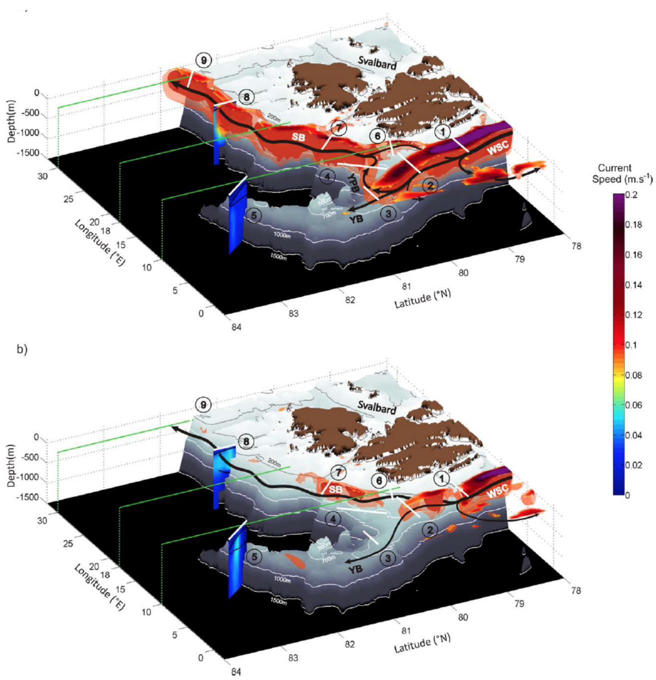

Figure 4 : *Représentation 3D des chemins de l'eau Atlantique en hiver (panel du haut) et en été (panel du bas). 2 enveloppes de vitesses sont montrées : le rouge foncé est 0.12m/s et et le rouge claire est 0.08m/s (extrait de Koenig et al., 2017).*

Le modèle suggère une activité méso-échelle importante le long des courants d'eaux Atlantiques, en accord avec les observations (Vage et al., 2016). Enfin, une comparaison entre les sorties de modèle de l'hiver 2014 à l'hiver 2016 montre de grandes différences notamment dans la couverture de glace. Cela fait suite à des conditions atmosphériques et océaniques durant les précédant été et autumne très distinctes et à de la convection hivernale qui génère de large flux de chaleur de l'océan vers la glace en hiver 2016.

Enfin, la troisième partie de la thèse a consisté à examiner les variations de vitesse dans la branche du Yermak Pass, grâce à un courantomètre Acoustic Doppler Current Profiler (ADCP) déployé en 2007 au milieu de ce passage dans le cadre du projet européen Damoclès (http://www.damocles-eu.org). Le signal est largement dominé par la marée (Koenig et al., 2017b). En automne/hiver, ce signal est mélangé à des signaux de plus basse fréquence. Des tourbillons baroclines de périodicité 5-15 jours et des entrées sporadiques d'Eaux Atlantiques avec une périodicité d'un-deux mois sont observés en hiver. Les 10 ans disponibles de sorties du modèle opérationnel avec assimilation de Mercator Océan au 1/12° (2007-2017), qui représente bien les variations basses fréquences de vitesse du West Spitsbergen Current et de la Yermak Pass, suggèrent que la Yermak Pass Branch est une structure spatiale d'hiver robuste. Dans le modèle, la Yermak Pass branch transporte en moyenne 31% du volume transport du West Spitsbergen Current (36% en hiver), mais ce résultat est à prendre avec précaution car le modèle ne représente pas la marée qui sur le plateau de Yermak génère des courants résiduels significatifs (environ 5 cm/s) et qui s'opposent à l'écoulement des Eaux Atlantiques.

Références :

Fer I., et al. (2015) *Ocean Sci.*, Doi : 10.5194/os-11-287-2015

Gascard, J.-C. Et al., (1995) vol. 49, edited by W. O. Smith, Jr. and J. M. Greibmeier, pp. 131–182, AGU, Washington, D. C.

Koenig Z., et al., (2017b) *J. Geophys. Res*. Doi : 10.1002/2017JC013271

Koenig Z., et al., (2017a) *J. Geophys. Res*. Doi : 10.1002/2016JC012424

Koenig Z., et al., (2016b) *J. Geophys. Res*. Doi : 10.1002/2016JC01219

Rudels et al., (2015) *Progress in Oceanography*, doi: 10.1016/j.pocean.2014.04.003.

Vage K., et al., (2016) *J. Geophys. Res.*, doi:10.1002/2016JC011715.

Vihma T., et al., (2014) *Atmospheric Chemistry and Physics* Doi : 10.5194/acp-14-9403-2014

Glossary

AW	Atlantic Water
IAOOS	Ice Atmosphere Ocean Observing System
ITP	Ice Tethered Profiler
MAW	Modified Atlantic Water
N-ICE2015	Norwegian Young sea ICE Cruise 2015
SB	Svalbard Branch
YB	Yermak Branch
YPB	Yermak Pass Branch
WSC	West Spitsbergen Current

Contents

Chapter 1
Introduction

Contents

1.1 Climate change in the Arctic

The climate in the Arctic is drastically changing as illustrated by the United Nations Intergovernmental Panel on Climate Change (IPCC). The atmosphere in the Arctic is warming two to three times faster than the rest of the world (*Stocker et al.*, 2013) (Figure 1.1). The fact that the Arctic is changing faster than the rest of the world is called the "Polar Amplification" of climate change.

Part of the Polar Amplification is due to the surface albedo feedback. When sea ice melts, the radiative energy from the atmosphere is not reflected anymore by the sea ice but is absorbed by the dark ocean. It warms the ocean surface and melts even more sea ice. Recent works highlight other processes that can participate in the Polar Amplification (warming of Arctic atmosphere and decline in the sea ice

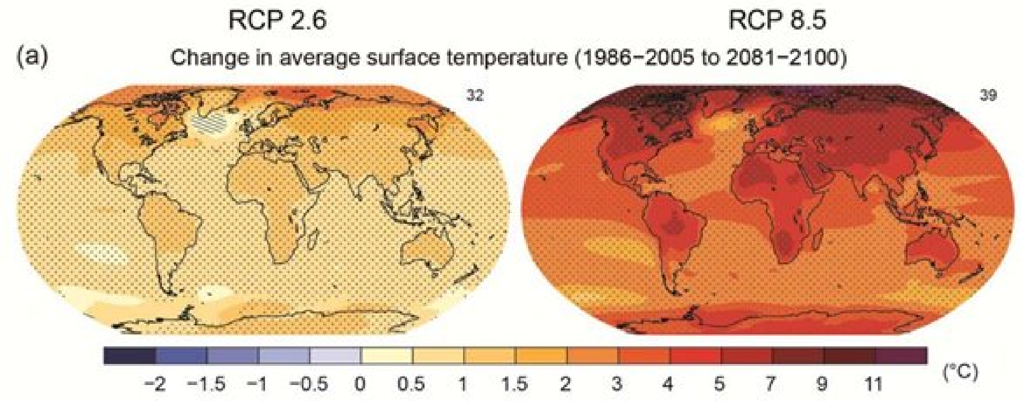

Figure 1.1: *Multimodel average of sea surface temperature difference (°C), between the period 1986-2005 and 2080-2100, for 2 climate scenarios: on the left an optimistic one (RCP 2.6) and on the right a pessimistic one (RCP 8.5). RCP 2.6 scenario infers that the global annual greenhouse gas emissions peak between 2010-2020, with emissions declining substantially after. RCP 8.5 scenario supposes that the emissions continue to rise throughout the 21st century. From (Stocker et al., 2013)*

cover), of which the importance of downward longwave radiation (*Park et al.*, 2015) that can explain the faster warming of the atmosphere near the surface: the polar amplification of the atmospheric warming is "bottom amplified" (*Screen and Simmonds*, 2010).

The Arctic has been shifting from an ice-covered ocean to a seasonally ice-covered ocean for the last decades. This new regime is called "the New Arctic" and needs to be understood to better assess the impact of the global warming on the Arctic climate and vice-versa. Climate change in the Arctic affects all media, the atmosphere, the sea ice and the ocean, and has consequences on ecosystems at all scales (phytoplancton, polar bear population...). In the following sections I briefly describe the impact of the climate change on the atmosphere and on the sea ice and then I focus on the Arctic ocean, its properties and the changes it is undergoing.

1.1.1 Atmosphere circulation and changes

The Arctic atmosphere circulation is dominated by the polar vortex, a persistent, large-scale, low-pressure zone that rotates counter-clockwise near and around the North Pole. The polar vortex lies between the middle/upper troposphere and the stratosphere. The vortex shows large interannual variations: some years the polar vortex is strong and the Arctic air is well contained; some other years the polar vortex is weaker and may break in several vortices (Figure 1.2). The polar front is the location of the interface between the cold dry air mass from the Arctic with the wam moist air mass from the midlatitudes, roughly at 60°N latitude.

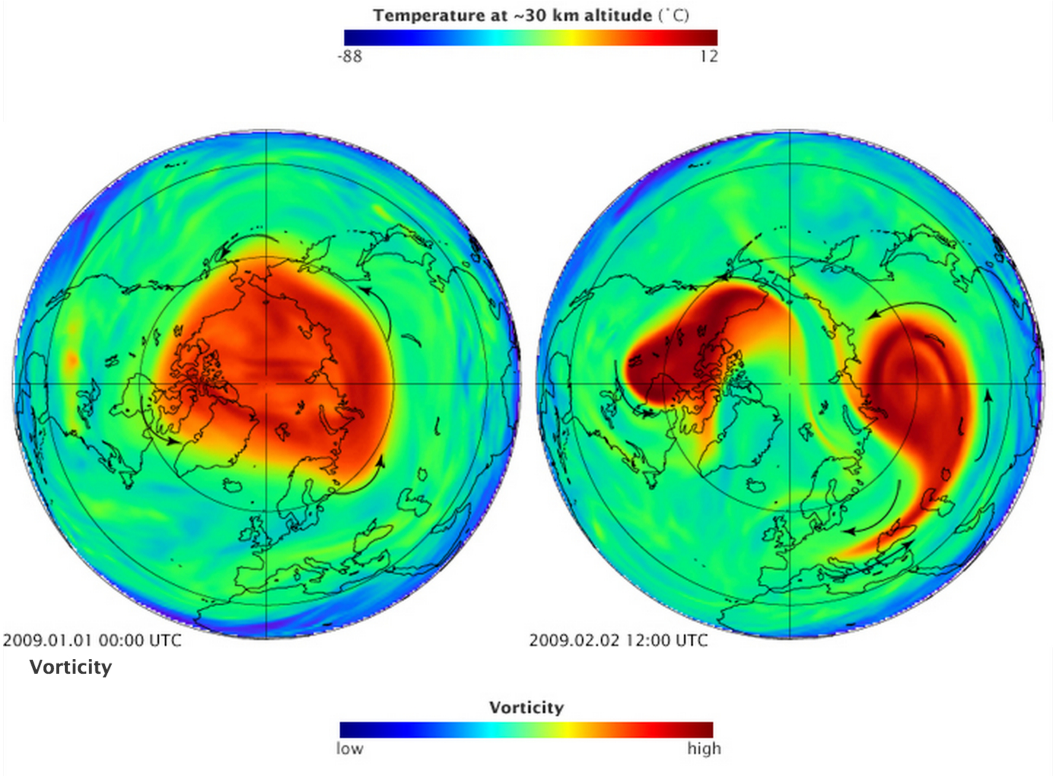

Figure 1.2: *The Polar Vortex on January 10, 2009 to the left and on February 2, 2009 to the right, at* $30km$ *altitude. From NASA Earth Observatory.*

Variations of the atmosphere in the Arctic are partly captured in the Arctic Oscillation (AO) index (www.cpc.ncep.noaa.gov/products/precip/CWlink/daily-ao-index/ao.shtml), the time series associated to the leading mode of Empirical Orthogonal Function analysis of monthly mean $1000hPa$ height during 1979-2000 period. Depending on the sign of the AO index, Arctic air can penetrate into mid latitudes. When the AO index is positive, surface pressure is low in the Arctic and mid-latitude jet stream can blow strongly, keeping the cold Arctic air locked in the Arctic. When the AO index is negative, pressure is higher in the Arctic, which causes weaker zonal winds and larger intrusions of cold Arctic air in the mid latitudes.

Combined with the polar air intrusion at mid-latitudes, warm moisture air (polar lows) can enter the Arctic Ocean and affect the sea ice decline. *Woods and Caballero* (2016) found that the passage of a moisture intrusion causes the retreat of the marginal ice zone for many days after the passage of the intrusion. The warm moisture intrusion could be responsible of 45% of the surface air temperature trend (increase) and of 30% of the sea ice concentration trend (decrease) in the Barents Sea over the last 20 years (*Woods and Caballero*, 2016).

With the decrease of temperature gradient between high and low latitudes associated with climate change, the atmospheric circulation would change and an increase in the frequency of the incursions of polar air at mid-latitudes is expected (*Gervais et al.*, 2016). The frequency of the polar lows is also expected to increase (*Woods and Caballero*, 2016), melting more and more sea ice.

Climate models project a strong increase in Arctic precipitation over the next century, due to enhanced surface evaporation associated with sea-ice retreat (*Bintanja and Selten*, 2014). As air temperature is quite cold, it has been suggested that this precipitation will principally fall as snow. However, *Bintanja and Andry* (2017) suggested using climate models that the main increase in precipitation will fall as rain, which would largely impact the Arctic. For instance, by diminishing the snow cover, it will affect the surface albedo, reinforcing surface warming and amplifying the retreat of ice and snow (*Bintanja and Andry*, 2017).

1.1.2 Sea ice state and changes

Several main parameters characterize the sea ice: extent/cover, thickness, age, morphology and many others that are all affected by climate change.

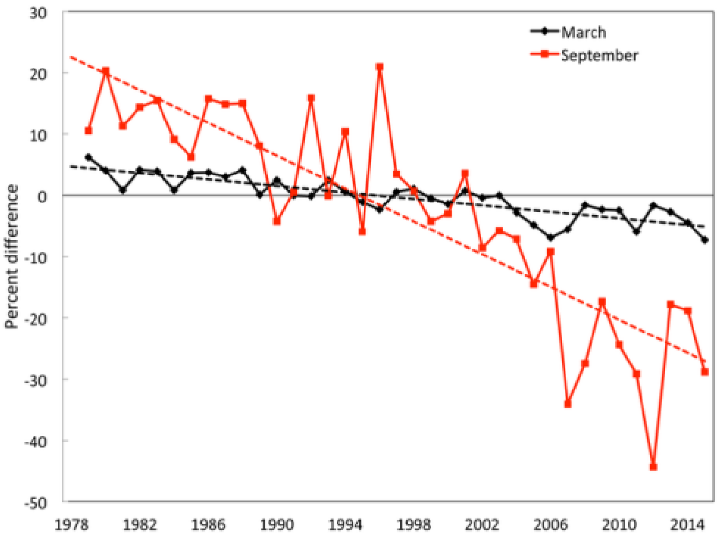

Figure 1.3: *Time series of sea ice extent anomalies in March (in black) and in September (in red). The anomalie value is referenced to the mean value of the period 1981-2010. The dashed lines are linear regression lines (−2.6%/decade in March and −13.4%/decade in September). From Perovich et al. (2015).*

Sea ice extent is getting smaller and smaller especially in summer (Figure 1.3), dropping by 13.4% per decade in September (*Vaughan et al.*, 2013) since the satellite era, but the decline is also significant in winter (Figure 1.3, black line). The sea ice thickness has decreased by at least 1.7m in the central Arctic (*Kwok and Rothrock*, 2009; *Kwok and Cunningham*, 2015). This decline is not regular and is punctuated by strong anomalies in the sea ice extent such as in summer 2007 and summer 2012 (loss of 1.5 and 2.37 millions of km^2 respectively) (Figure 1.3). The last 10 years are also the ten lowest minimum ever observed by satellites. (Figure 1.3). The multi-year sea ice progressively disappears and is replaced by young and seasonal sea ice (Figure 1.4).

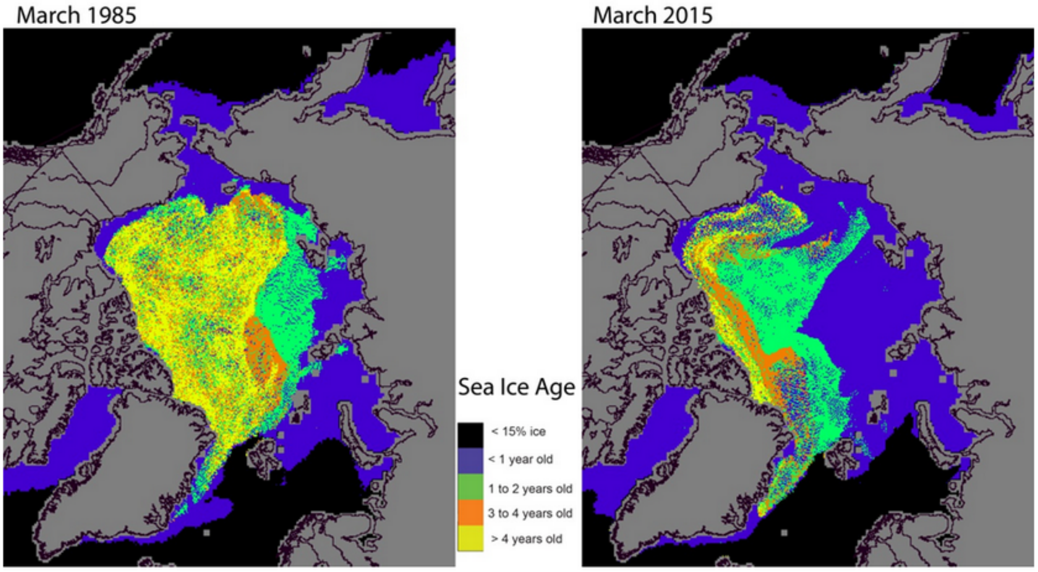

Figure 1.4: *Sea ice age in March 1985 (left) and March 2015 (right). Sea ice in blue is first year ice and sea ice in other colors is multi-year ice. From Perovich et al. (2015).*

The beginning of the sea ice melt occurs earlier and earlier in the year, and the freeze-up is more and more delayed (*Boisvert and Stroeve*, 2015), hence the length of the melting season is increasing. With more open water, the evaporation rate and the cloud cover increase in summer in the Arctic, warming up the Arctic surface atmosphere. The increased specific humidity in May induces an earlier melt onset. The increase in the water vapor content and in the cloud cover delays the sea ice freeze-up in autumn (*Boisvert and Stroeve*, 2015).

Ice-ocean-atmosphere interaction processes are essential to understand the evolution of the sea-ice. Although leads constitute only a small fraction of the sea ice cover, they could play a main role in the ice-ocean-atmosphere interface and cause

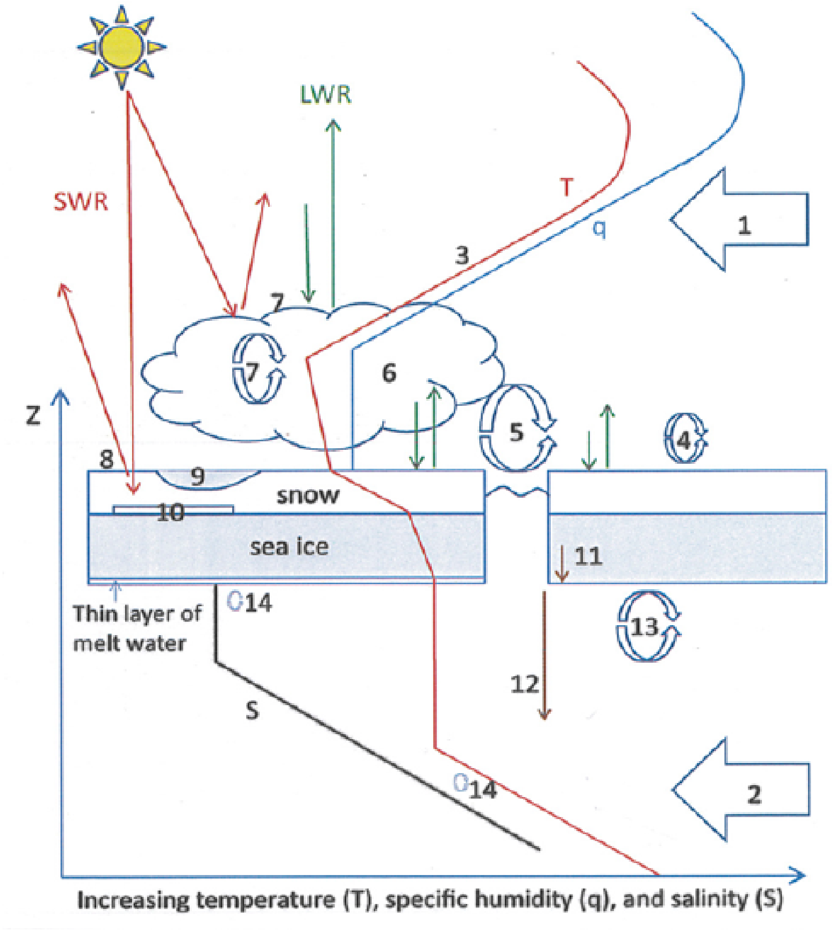

Figure 1.5: *Simplified scheme of the physical processes and vertical profiles of Temperature (T), air humidity (q) and ocean salinity(S) in the Arctic climate system. Numbers indicate the following processes. 1- Heat and moisture atmospheric advection. 2- Heat and salt oceanic advection. 3- Temperature and moisture inversion generation. 4- Turbulence in the sable boundary layer. 5- Convection over leads and polynias. 6- Cloud microphysics. 7- Cloud/radiation/turbulence interactions. 8- Reflection and penetration of the solar radiations in the snow and the ice. 9-Melt of the surface of the ice and melt pond formation. 10- Formation of superimposed ice and of snow ice. 11- Gravity drainage of the salt in the sea ice. 12- Brine formation. 13- Turbulent exchange of momentum, salt and heat during sea ice growth. 14- Double diffusive convection. From Vihma et al. (2014).*

perturbations in both the atmosphere and the ocean (*Perovich and Richter-Menge*, 2000). Leads affect the surface heat loss, the low level cloud formation and the penetration of shortwave radiation in the ocean (*Perovich et al.*, 2011). The heat released into the atmosphere results in forced convection in the atmosphere and in the upper ocean in brine rejection generated when the sea ice grows causing mixing

(*Pinto et al.*, 1995; *Morison et al.*, 1992). Ice ridges change the surface roughness at the sea-ice/atmosphere interface but also at the ocean/sea-ice interface, increasing cloud formation and low level turbulence in both atmosphere and ocean (*Martin et al.*, 2016; *Vihma et al.*, 2014). The presence of low-level clouds in the Arctic may increase longwave fluxes at the surface and modify the energy and sea ice mass budgets. *Vihma et al.* (2014) summarized the physical processes occurring in the Arctic climate system, with a focus on ice-ocean-atmosphere interactions, such as brine rejection that creates convection in the upper ocean, snow-ice formation, double diffusive convection...

In this context of large changes in the Arctic, each media (sea ice, atmosphere and ocean) need attention to identify the processes at stake. In the following sections, we focus on the Arctic Ocean: hydrography, circulation, dynamic and sea ice - ocean interface.

1.2 General ocean circulation and water masses in the Arctic

1.2.1 Bathymetry of the Arctic

The Arctic Ocean is quite a complex ocean regarding its bathymetry (Figure 1.6). It is composed of several deep basins (deeper than $2500m$): the Eurasian basin, the Makarov Basin and the Canada Basin. Two main ridges separate these basins: the Lomonosov ridge and the Mendeleev ridge. The Eurasian Basin is divided into two smaller basins by the Gakkel Ridge: the Amundsen Basin to the north and the Nansen Basin to the south. The Arctic Ocean is also characterized by large continental platforms around the deep ocean with several shallow seas that occupy one third of the total area of the Arctic Ocean: the Barents sea, the Chukchi Sea, the Laptev Sea, the Kara Sea, the East Siberian Sea and the Beaufort Sea.

The Arctic Ocean is connected to the other oceans by 4 main passages: Bering Strait, a very shallow and narrow passage ($50m$ depth and $85km$ width) that connects with the Pacific ocean; Fram Strait with a sill at $2545m$ and a width of $450km$ although the deep part without the continental shelves of Greenland and Svalbard is only 300 km wide; the shallow Barents Sea (average depth $230m$) entering the Arctic through the Santa Anna Trough; the Canadian Archipelago with its multiple passages. These last 3 passages connect with the Nordic Seas and the Atlantic Ocean.

The bathymetry of the Arctic strongly constrains the open ocean circulation and provides singularity in current and hydrography characteristics in each basin.

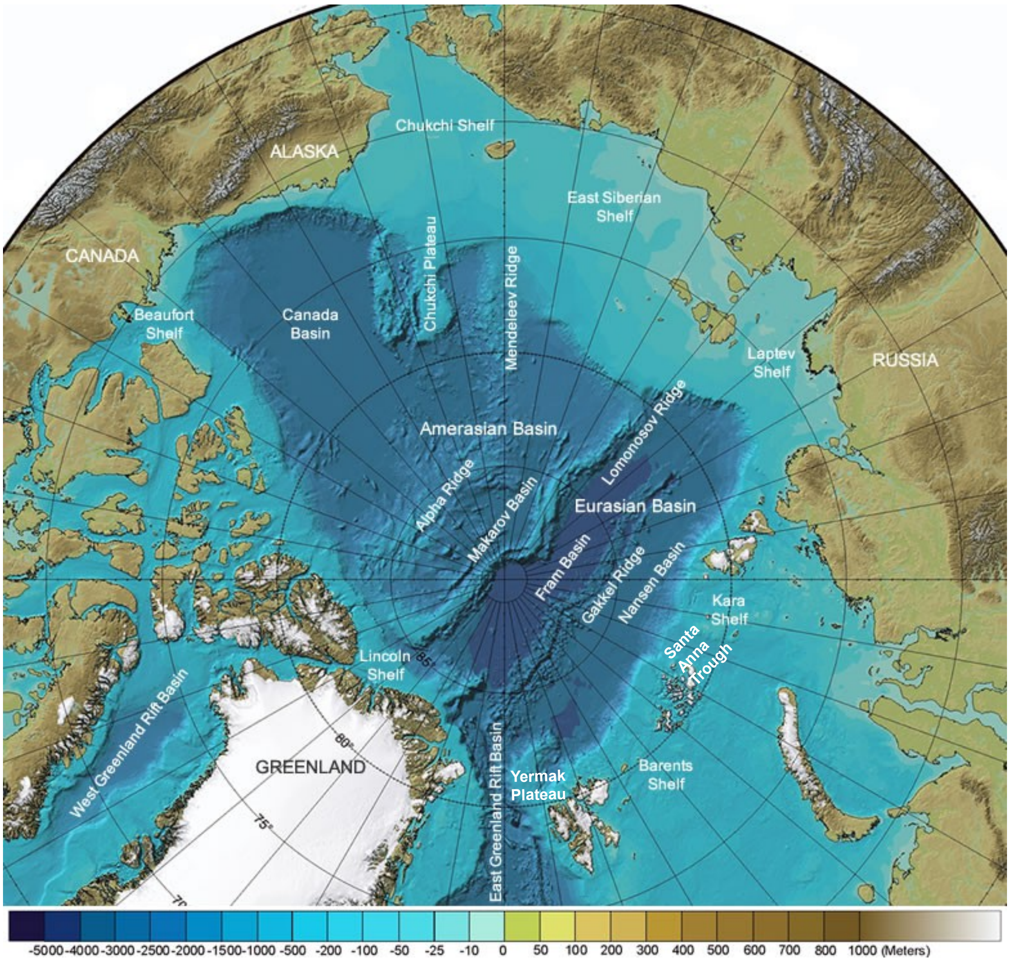

Figure 1.6: *International Bathymetric Chart of the Arctic Ocean annotated with the names of seafloor features. Adapted from http://geology.com/articles/arctic-ocean-features/*

1.2.2 Subsurface currents and water masses

The surface currents in the open Arctic Ocean are principally composed of Pacific Waters entering the Arctic through the Bering Strait and of fresh river runoff from Russia and Greenland (Figure 1.7). The flow entering through the Bering Strait has been monitored for more than 25 years now with a mooring array (*Woodgate et al.*, 2005). The Pacific waters are fresh and cold and feature a large seasonal cycle: in winter, temperature around the freezing temperature, $-1.8°C$, salinity around $33psu$ (called the winter Pacific Water); in summer, temperature around $2.3°C$ and salinity around $31.9psu$ (called the Summer Pacific Water) (*Woodgate et al.*, 2005). Both water masses (Summer and Winter Pacific water) flow between the mixed layer and the Atlantic Water layer in the Arctic ocean: between $30-40m$ for the Summer

Pacific Water and $\sim 100m$ for the Winter Pacific Water. The seasonal variability of the volume transport in Bering Strait is large, from $0.4Sv$ in winter to $1.2Sv$ in summer, with a mean volume transport of $0.8Sv$. Recent data suggest a larger flow, with a mean around $1.1Sv$ (*Woodgate et al.*, 2017), and interannual variations that are significant.

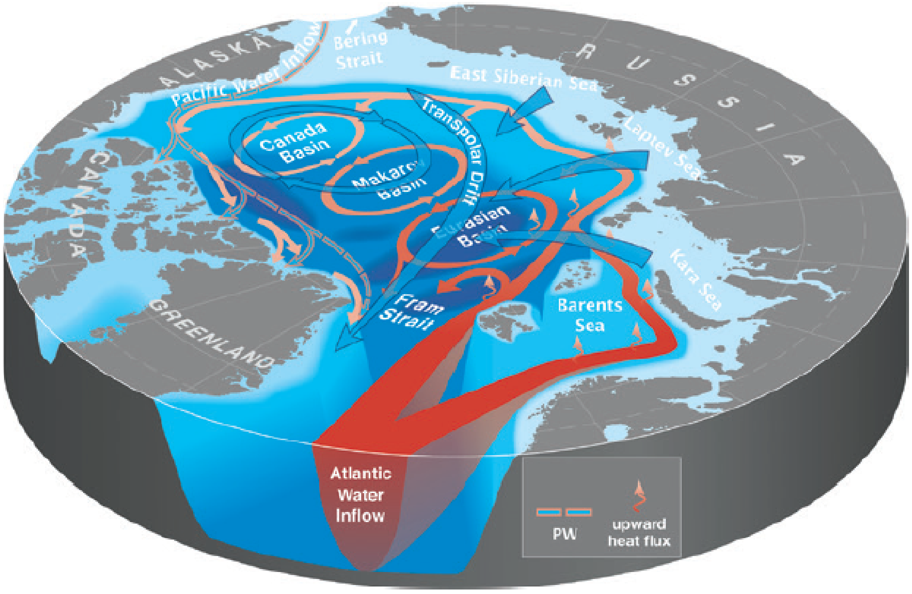

Figure 1.7: *Circulation of the surface water (blue), intermediate Pacific Water (orange/blue), and Atlantic Water (red) of the Arctic Ocean. From Carmack et al. (2015).*

In the Arctic, because of the almost year-round sea ice cover, surface current velocity is only a few cm/s and the currents are partially decoupled from the wind action, they follow at first order the sea ice drift. The forcing of the surface ocean circulation is now changing as the Arctic ocean is more and more free of ice and in direct contact with the atmosphere that transfer momentum and heat to the Arctic Ocean (*Dosser and Rainville*, 2016).

Two main surface circulations coexist (Figure 1.7) that exit the Arctic either through Fram Strait or through the Canadian Archipelago:

- The Beaufort Gyre, an anticyclonic gyre in the Canada Basin. This circulation is due to the high pressure centered on the northern part of the Beaufort Sea, south of the Canada Basin.
- The Transarctic Current, a transpolar drift mainly from north of Bering Strait to Fram Strait where it becomes the East Greenland Current. The Transarctic

Current and the East Greenland Current transport a large amount of the Eurasian river runoff, and carry with them several cubic kilometers of ice out of the Arctic at Fram Strait.

1.2.3 The Atlantic Water and its associated current

The layer centered around $300m$ in the Arctic is composed of warm (T $> 2°C$) and salty (34.8<S<35.2 psu) Atlantic Water that enters the deep basins through Fram Strait and the Santa Anna Trough at the exit of the Barents Sea (Figure 1.7). At the entrance of the Arctic, in Fram Strait and at the exit of the Barents Sea, the Atlantic water inflow is shallower and even at the surface north of Fram Strait, and then deepens as propagating cyclonically along the continental slopes between the isobaths 500 and $3000m$ depth (*Rudels*, 2012). The mean speed of the Atlantic Water Boundary Current, the current that carries the Atlantic Water along the continental slopes, is a few cm/s (about 5-$10cm/s$). The core of the current is well identified along the Siberian continental slope of the Arctic, and probably recirculates in each deep basin (*Rudels*, 2012). The circulation on the Canadian side is less documented but probably also follows the continental slope (*Aksenov et al.*, 2011).

Waters entering through Fram Strait constitute the warm and saline Fram Strait Branch Waters (FSBW). These waters quickly dive under the sea ice and stay warm as they melt sea ice and form the halocline (*Rudels et al.*, 2000, 2015). Waters from the Barents Sea, called the Barents Sea Branch Waters (BSBW) are exposed for quite a long time to the atmosphere as the Barents Sea is not covered by sea ice in summer. The BSBW cool and freshen in contact to the atmosphere in the Barents Sea before joining the FSBW along the continental slope through the Santa Anna Trough.

While recirculating along the Arctic continental slope and along deep ridges that delimitate the different basins, the Atlantic Water cools and freshens; salinity and temperature are quite different from one basin to another. *Rudels et al.* (2015) suggested that the FSBW remain in the Nansen Basin while the BSBW propagate along the continental slope and through the Amundsen Basin, the Makarov Basin and the Canadian Basin. Waters resulting from the modification of the AW during its propagation in the Arctic are called Modified Atlantic Water (MAW, $T < 2°C$ and salinity between 34.5 and $35.5psu$, from *Rudels et al.* (2000)) and recirculate in Fram Strait.

As the Atlantic Water is the main source of heat and salt in the Arctic, the monitoring of the boundary current is important to understand the New Arctic Regime. Several moorings are maintained since 1997 in Fram Strait for this purpose (collaboration between the *Alfred Wegener Institute*, Germany and the *Norwegian Polar Institute*, Norway). The monitoring of the Atlantic Water Boundary Current along the Siberian continental shelf in Kara and Laptev Sea is provided by the NABOS program (Nansen and Amundsen Basins Observational System) and along the Canadian shelf by the CABOS program (Canadian Basin Observational System) (http://nabos.iarc.uaf.edu/).

The Atlantic Water inflow in Fram Strait varies seasonally with a volume transport twice as large in winter than in summer ($4Sv$ versus $2Sv$ respectively) (*Beszczynska-Möller et al.*, 2012). The seasonal signal is still pronounced in the Nansen Basin and progressively dampens along the boundary current (*Lique and Steele*, 2012). The Atlantic Water Boundary Current carries a large amount of heat and salt in the Arctic. At Fram Strait, the heat transport varies from around $28TW$ in summer to $46TW$ in winter (*Beszczynska-Möller et al.*, 2012). Even if some heat recirculates directly into Fram Strait without entering the Arctic Ocean, the net annual heat transport into the Arctic Ocean through Fram Strait is estimated to be about $40TW$ (*Schauer and Beszczynska-Möller*, 2009).

Superimposed to the seasonal variability, over the last 20 years, time series of summer observations of temperature and salinity indicate positive trends (*Walczowski et al.*, 2012), respectively about $0.03°C/year$ and $0.0046psu/year$. Five to six year cycles are also observed. The warming of the Atlantic Water at Fram Strait has an important impact on Svalbard ecosystems and largely influence the oceanic climate and sea-ice conditions north of Svalbard (*Walczowski et al.*, 2012).

The Atlantic Water Boundary Current is the vector of transport of heat along the continental shelf and deep ridges in the Arctic, but how is the heat transferred to the central part of the basins? Indeed, Atlantic Water masses are not only found along the continental slopes but also in the interior of each basins. Lateral intrusions and eddies can partly explain the signature of Atlantic Water everywhere in the Arctic. *Våge et al.* (2016) found signature of eddies along the continental slope northeast of Svalbard at $30°E$. These eddies may be an efficient way to diffuse heat and salt in the interior of the deep basins. *Zhao et al.* (2014) looked at the eddy field in the entire Arctic from autonomous drifting ice-tethered profilers. They document numerous eddies in the Canadian Basin and less in the Eurasian Basin (Figure 1.8). The eddies are concentrated in the Beaufort Gyre region and along the transpolar drift stream. The radius of the eddies is of the same order as the Rossby radius of deformation in the Arctic: $\sim 13km$ in the Canadian Basin and $\sim 8km$ in the Eurasian Basin. The eddies are formed by instability of the boundary current and over ridge features and shelf regions (*Timmermans et al.*, 2008). Although the eddy generation is located close to fronts or continental slope, they are encountered in the center of the different basins (*Zhao et al.*, 2014). *Manucharyan and Timmermans* (2013) found that in the Arctic frontal instabilities lead to the development of eddies which can propagate far from the front if any interactions with other eddies are avoided. Eddies are found at different depths (above and below $80m$ depth), some are in the Atlantic Water layer (depth $> 80m$) or located around the thermocline

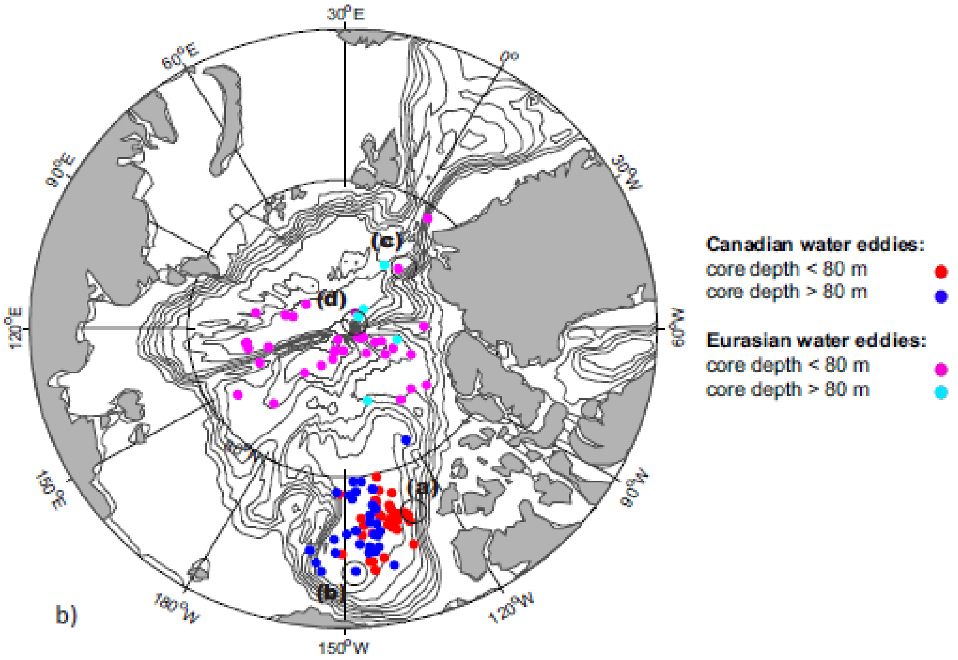

Figure 1.8: *Core depth and distribution of a total of 109 cold-core anticyclonic eddies with numbered examples of typical eddies belonging to different eddy-types (shown in Figure 10). For Canadian water eddies, red: core depth above 80 m, blue: core depth below 80 m; for Eurasian water eddies, pink: core depth above 80 m; cyan-blue: core depth below 80 m. From Zhao et al. (2014).*

and can bring heat in the interior of the different basins in the Arctic. The lifetime of the eddies is expected to be from 0.9 to 5 years (*Zhao et al.*, 2014).

1.3 Ocean stratification

1.3.1 The surface mixed layer

The mixed layer in the ocean is an homogenized layer at the surface of the ocean characterized by active turbulence. In the rest of the ocean, the turbulence in the mixed layer is mainly generated by winds, surface heat fluxes or evaporation, while in the Arctic sea ice that partially isolates the ocean from the atmosphere has to be taken into account.

The mixed layer in the Arctic Ocean is composed of cold and fresh waters, close to the freezing temperature, called the Polar Surface Water (Figure 1.9). The depth of the mixed layer differs for each basin: $\sim 20 - 30m$ in the Canadian Basin and $\sim 100m$ in the Eurasian Basin. In the Canadian Basin, two water masses are found

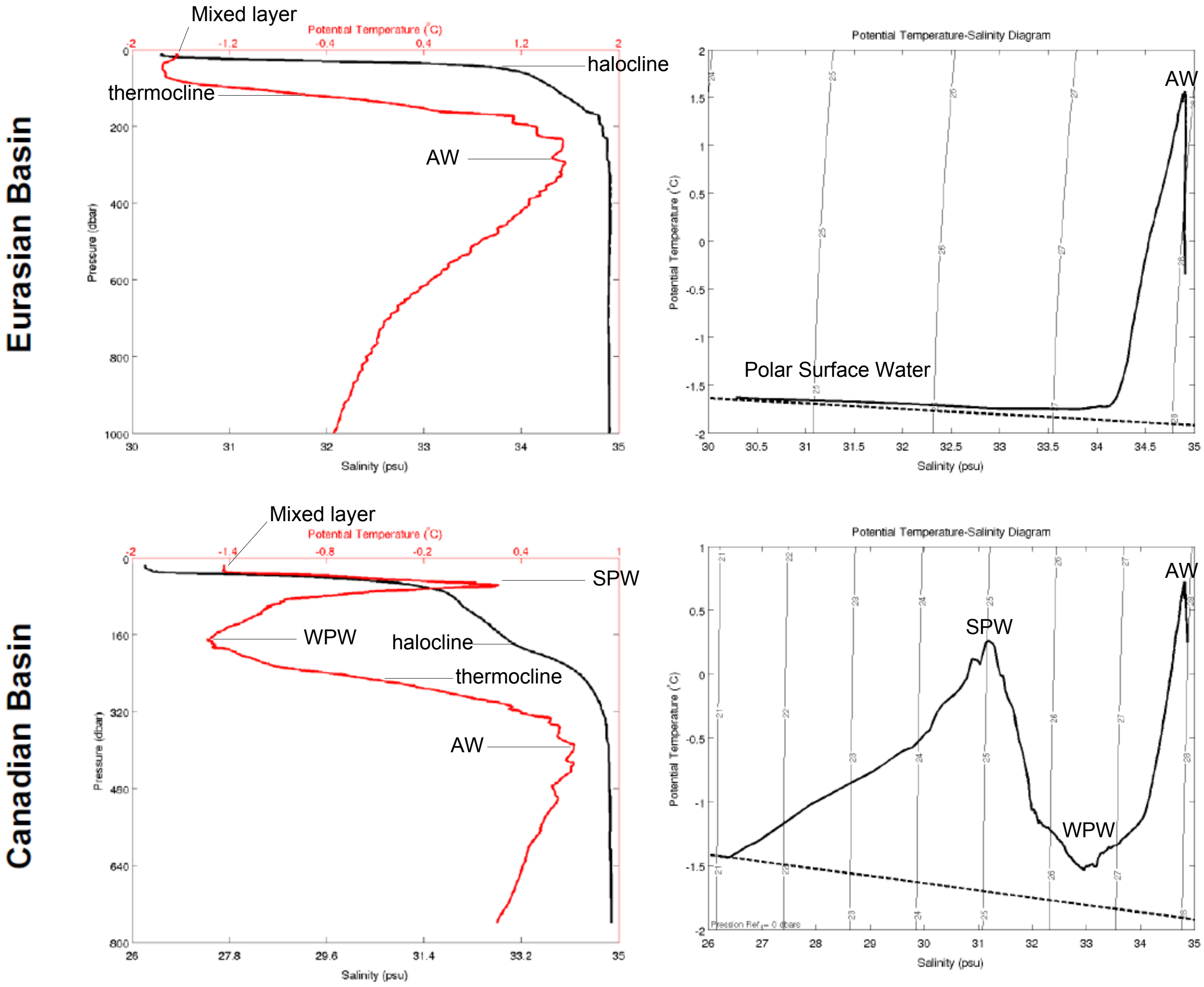

Figure 1.9: *Vertical profiles of potential temperature (θ) and salinity (S) typical of the Eurasian (upper panels) and Canadian (lower panels) Basins and their corresponding θS diagrams. Adapted from Bourgain (2012). AW: Atlantic Water. WPW: Winter Pacific Water. SPW: Summer Pacific Water.*

just below the mixed layer: the Summer Pacific Water, quite warm at 40 meters that lies above the Winter Pacific Water, relatively cold at 80-100 meters (*Woodgate et al.*, 2005). The first large stratification in salinity is the halocline. The strong stratification in temperature, the thermocline (at $\sim 180m$ in the Canadian Basin and at $\sim 100m$ in the Eurasian Basin) delimitates the upper limit of the Atlantic Water, found in the entire Arctic Ocean.

1.3.2 Halocline

The halocline is the area in the water column of strong salinity gradient between the fresh mixed layer and the salty deep waters in the Arctic Ocean. The halocline is usually located between 50 and $200m$ depth. At low temperatures typical of high latitudes, density changes are mainly driven by salinity changes. The halocline corresponds then to the area of large density stratification, the pynocline. As the halocline separates the surface mixed layer from the Atlantic Water, it is considered as a barrier that prevents any upwelling of warm Atlantic Water to the surface.

The halocline is subject to large seasonal variations (*Bourgain and Gascard*, 2012). In winter, sea ice grows, brines are released and the mixed layer cools, gets saltier and deepens by convection: the halocline is deeper and saltier. In summer, sea ice melts, releasing fresh and cold water; the surface ocean is more stratified, the halocline shallower.

The origin of the halocline and of the mixed layer is still under debate and two main hypotheses exist. Some argue that the halocline forms on the continental shelf north of Eurasia and is advected (*Aagaard and Carmack*, 1989). On the other hand, *Rudels et al.* (2004) suggested a convective origin to the halocline formation. When the Atlantic Water enters the Arctic Ocean in Fram Strait, it encounters and melts the sea ice north of Svalbard. A convection is established in winter as the surface water cools and creates the mixed layer from the transformed upper part of the entering Atlantic Water. The halocline is formed but is more or less coincident with the thermocline. The difference between thermocline and halocline is established farther east along the continental slope. First, north of the Barents Sea, winter convection reaches the thermocline and can bring warm water in the mixed layer. Then along the russian shelf, the runoff of the siberian rivers creates a stratification in the mixed layer and a salinity gradient is established between the mixed layer and the thermocline: the halocline (*Rudels et al.*, 2004). The scientific community is now more in favor of the latter hypothesis from *Rudels et al.* (2004).

In the Eurasian Basin, the halocline is composed of 2 main steps, forming the Upper Halocline layer and the convectively Cold Halocline layer. The convective cold halocline is formed in 2 steps (Figure 1.10) (*Rudels et al.*, 1996; *Kikuchi et al.*, 2004). First in winter, when sea ice grows, deep winter convection occurs, forming the cold salty water of the cold halocline. The following summer, there is a subsequent input of fresh water by either sea-ice melt or low salinity shelf water, creating the upper halocline. The double halocline is formed over an entire year and is found in the Eurasian Basin for waters that have been in the Arctic for more than 6 months.

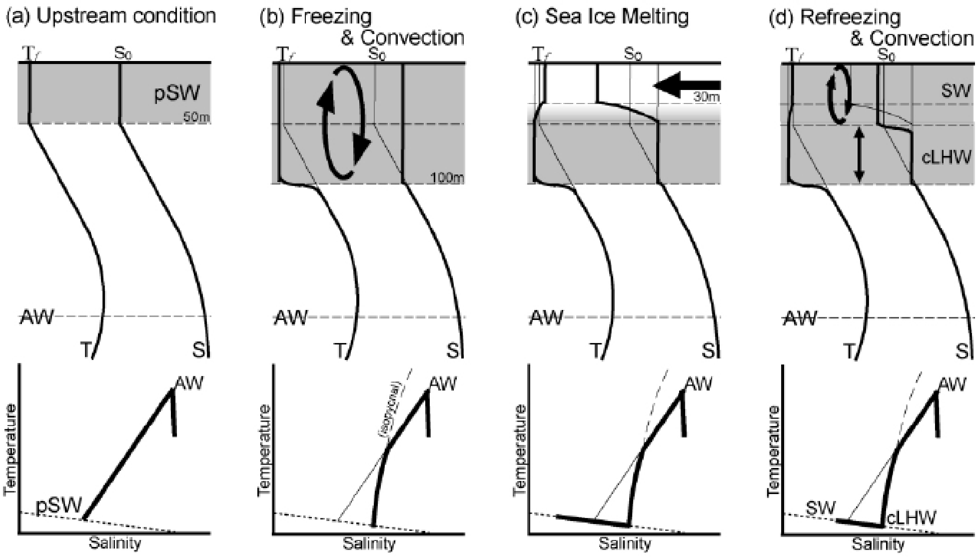

Figure 1.10: *Schematic view of the formation process of the convective cold halocline in the eastern Arctic Ocean. Dotted lines of the lower panels show the freezing point. The labels for water types are pSW for pre-existing surface water, SW for surface water, cLHW for convectively formed Lower Halocline water, and AW for Atlantic water. From Kikuchi et al. (2004).*

1.3.3 Thermocline stratification and double diffusion

The thermocline is located below the base of the halocline. Compared to other oceans, the Arctic ocean is characterized by very low turbulence especially in the deep Arctic Basin (*Rainville and Winsor*, 2008), which enables vertical mixing by molecular diffusion. Double diffusion originates from the difference in molecular diffusivities between temperature and salinity (100 times faster for temperature than for salinity), and forms when temperature and salinity gradient are in the same direction. Two types of double diffusion can emerge (*Bebieva and Timmermans*, 2017).

- The diffusive convection mode, when both temperature and salinity increase with depth.
- The salt-finger regime when both temperature and salinity decrease with depth.

Double diffusion processes in the Arctic are identified by the presence of staircases (thickness about 1-5 meters) around the thermocline (*Timmermans et al.*, 2008). These staircases are mainly observed far from the continental shelf and in areas covered by sea ice such as the Canadian basin where the turbulence is the lowest in the Arctic Ocean, even if some studies show that they are also observed in weakly turbulent area (*Padman and Dillon*, 1987).

Double diffusion is important for the Arctic ocean heat budget far from the continental shelf, and remains the main source of vertical heat diffusion there. However, heat fluxes associated with the double diffusion are still at least one order of magnitude smaller than ocean-to-ice heat fluxes ($0.2W/m^{-2}$ compared to several W/m^{-2}) (*Timmermans et al.*, 2008).

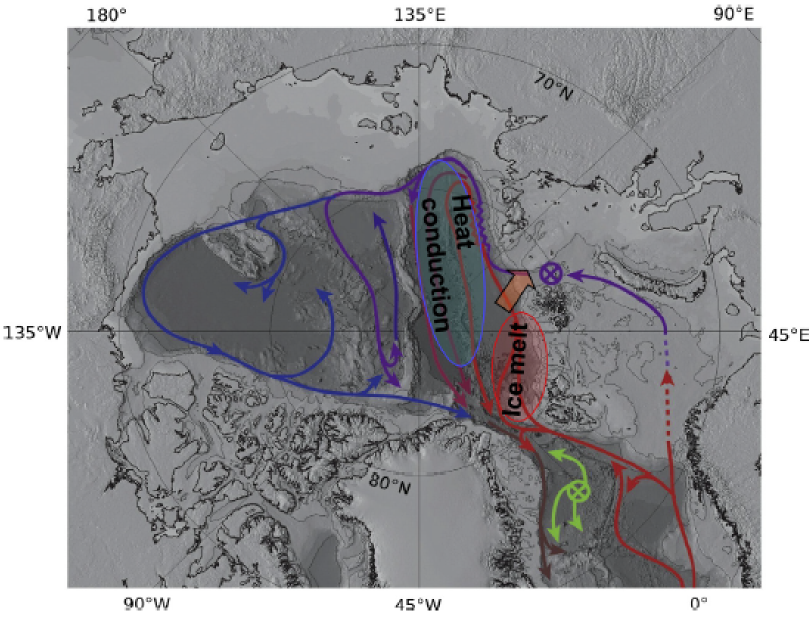

Figure 1.11: *Schematic of the circulation of the Atlantic Water and heat exchanges. The red area shows where the Atlantic Water is transformed into halocline water by melting sea ice and losing heat to the atmosphere. The orange wide arrow indicates the possible transfer of warm Atlantic Water from the Fram Strait branch to the Barents Sea Branch. The blue area is where the heat transport takes place by double-diffusive convection from the Atlantic Water layer to the mixed layer and then by haline convection from the mixed layer to the ice and atmosphere. Red color indicates Fram Strait branch water and magenta the colder Barents Sea branch water. From Rudels et al. (2015).*

Although staircases and double diffusion processes are mainly observed in the quiet Canada Basin, *Rudels et al.* (2009) argued that double diffusion processes explain the formation of the large steps in the Atlantic Water layer once FSBW and BSBW merge. The intrusive layers created during the merging of the FSBW and BSBW are probably of smaller thickness than the large steps observed in the rest of the Arctic. Double diffusive processes occur, that tend to smooth the gradients between some layers and mix the surrounding waters. After this first mixing, only large steps remain. They are quite stable and propagate following the Atlantic Water flow in the entire Arctic Ocean.

The Atlantic Water Boundary Current is largely decoupled from the surface forcings (e.g. wind, sea surface temperature) as the halocline and the thermocline prevent exchanges between the mixed layer/sea ice and the warm Atlantic Water. However, several documented dynamic processes such as winter convective mixing or upwelling can diffuse heat and salt from the Atlantic Water layer vertically. Winter convective mixing occurs along the continental shelf north-east of Svalbard near the entrance of Atlantic Water into the Arctic (*Ivanov et al.*, 2016; *Rudels et al.*, 2015), (Figure 1.11), bringing heat to the surface, and melting the sea ice (*Ivanov et al.*, 2016). Upwelling of the warm water in the Laptev Sea has been recently observed and is the result of the barotropic shoreward response from the flow near the bottom to offshore surface Ekman transport that pushes the ice and the surface current of the continental shelf (*Janout et al.*, 2013). Upwelling of Atlantic Water has also been observed in winter north of Svalbard along the continental slope, having significant impacts on the primary production (*Falk-Petersen et al.*, 2014).

1.4 Closure of the budgets in the Arctic Ocean

Large international efforts have been deployed to close the heat, volume and freshwater budgets in the Arctic ocean. Monitoring of the ocean budgets in the Arctic is needed to estimate the impact of climate change on the Arctic Ocean.

Several mooring arrays have been deployed for more than 13 years in different gateways of the Arctic: in Fram Strait and Bering Strait as explained previously, but also in Davis Strait and through the Barents Sea Opening. With these mooring array data and using an inverse method, *Tsubouchi et al.* (2012) established the heat, volume and freshwater budget during summer 2005 (Figure 1.12). More recently, they estimated transports and budgets over 2004-2010 (*Tsubouchi et al.*, 2017). They found that the volume transport through the Barents Sea Opening is large in winter, whereas the Bering Inflow is large in summer. The mean heat transport is $180 \pm 57TW$, with $\sim 250TW$ in November and $\sim 100TW$ in May. The mean freshwater transport is $156 \pm 91mSv$, with $\sim 250mSv$ in November-March and $\sim 50mSv$ in June-August. The budgets present a large inter-annual variability: year 2004-2005 and year 2007-2008 differ drastically in heat transport, $196 \pm 56TW$ and $165 \pm 71TW$ respectively, and in freshwater budget, $163 \pm 79mSv$ and $121 \pm 103mSv$ respectively. Despite all the changes occurring in the Arctic Ocean, no large trend is noticed from 2004 to 2010 in the heat, volume and freshwater budgets.

We now focus on the area North of Svalbard, with the entrance of the Atlantic Water from Fram Strait into the Arctic.

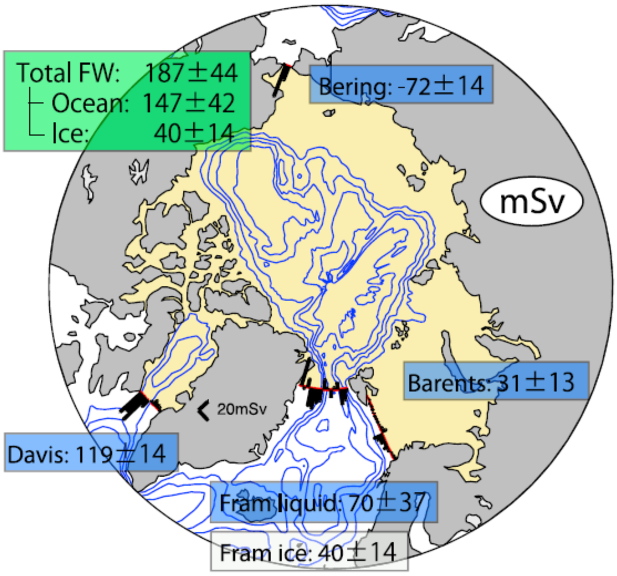

Figure 1.12: *Schematic Arctic Freshwater (FW) budget (mSv) in summer 2005. Total net FW transports of* $187 \pm 44 mSv$ *is balanced with surface FW input, which is received in the yellow hatched area. Each component of FW sources and sinks are shown: Ocean transports are in blue boxes and Fram Strait sea ice transport in white box. Black bars along the boundary section show the ocean contribution every* $40km$ *to the calculation of the surface FW input. From Tsubouchi et al. (2012).*

1.5 The area North of Svalbard

The area north of Svalbard is a region where sea ice is abundant in summer but is absent in winter. This particularity is well known among the fishermen in Svalbard that have access in winter to the area called "Whalers Bay" (Figure 1.13). This region is key to understand the effect of the global warming on the Arctic and also on the entire world. Indeed, this area is the link between the Arctic Ocean, the ocean the most affected by the climate change, and the main source of freshwater for the global ocean, and the rest of the world ocean. They are in contact through the descending branches of the global thermohaline circulation and the East Greenland Current, a surface fresh current (section 1.2.1).

Major changes have occurred north of Svalbard during the recent years. The sea ice decline in winter north of Svalbard has reached $10\%/decade$ since 1979. The Atlantic Water west of Svalbard has warmed in winter by $0.3°C$ since 1979 and air temperature in winter by $2°C/decade$ in this area (*Onarheim et al.*, 2014).

The area north of Svalbard is difficult to monitor because of the large sea ice extent in summer and the polar night in winter. Here we present a state of the art

Figure 1.13: *European whaling for bowhead whales off Spitsbergen. Place usually called Whalers bay north of Svalbard. From Abraham Stork, Rijksmuseum Amsterdam.*

of the ocean properties and circulation and ice-ocean interactions in this changing area.

1.5.1 Atlantic Water paths

The Atlantic Water from Fram Strait enters the Arctic Ocean along the western continental shelf of the Svalbard Archipelago through the West Spitsbergen Current (WSC). Then the current encounters an obstacle: the Yermak Plateau at $\sim 80°N$, a shallow topography (less than $700m$) that forms a barrier to the inflow of Atlantic Water in the Arctic.

On the southwestern tip of the Yermak Plateau, the WSC splits in 3 branches as isobaths diverge (*Sirevaag and Fer*, 2009) (Figure 1.14): one directly recirculates in Fram Strait; one follows the $400 - 500m$ isobaths along the Svalbard continental slope, the Svalbard Branch; one follows the western side of the Yermak Plateau along the isobaths $700 - 800m$, the Yermak Branch. The Yermak Branch has been identified until the northern tip of the Yermak Plateau but its path after is not sure: the main hypothesis is that it keeps flowing along the eastern shelf of the Yermak Plateau before joining the Svalbard Branch north of Svalbard.

The Atlantic Water inflow in the WSC is largely dominated by mesoscale activity (eddies). A large portion of the eddies does not propagate in the Arctic Ocean

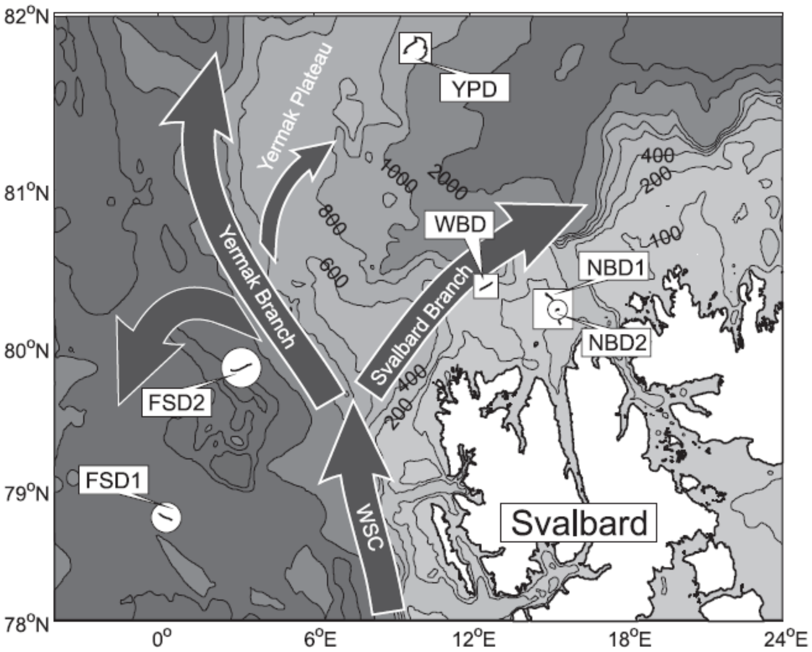

Figure 1.14: *Map of the study area showing the locations and drift trajectories of the six individual drifts using TIC instrumentation (squares) and MSS instrumentation (circles) plotted over the bathymetry around Svalbard. Bathymetry is from the General Bathymetric Chart of the Oceans (GEBCO) dataset (IOC, IHO, and BODC 2003) and isobaths are in meters. Wide arrows indicate the WSC, the Svalbard branch, the Yermak branch, and the recirculation branch. The thinner arrow indicates recirculation across the Yermak Plateau. From Sirevaag and Fer (2009)*

and rather flows in the Fram Strait recirculating branch (*Von Appen et al.*, 2016; *Hattermann et al.*, 2016). North of Svalbard, the Atlantic Water current is slow (a few cm/s), larger in the Svalbard Branch than in the Yermak Branch (*Perez-Hernandez et al.*, 2017). The dynamic of the current in this branches is still poorly documented although some studies (e.g. *Våge et al.* (2016)) suggest that north of Svalbard eddies are present along the continental slope.

1.5.2 Near inertial waves, internal waves, tides and mixing

Although the Arctic Ocean is an ocean often qualified as "quiet", near inertial waves have been detected in the Arctic. *Dosser and Rainville* (2016); *Dosser et al.* (2014) looked at the generation of near inertial waves and internal waves in the Canadian Basin with observations from ice-tethered profilers. They identified 3 main forcings:

- The wind stress forcing the ocean at the near inertial frequency,
- The motion of drifting sea ice,

- Tides and rough topography.

Near inertial and internal waves are documented along the shelf and over the Yermak Plateau north of Svalbard (periodicity around 12h north of Svalbard) where topography is rough. *Fer et al.* (2010) observed that near inertial waves over the Yermak Plateau are $0.1 - 0.3$ times the midlatitude levels and compare with the most energetic levels in the central Arctic. This near-bottom mixing over the Yermak Plateau removes $15W.m^{-2}$ of heat from the Atlantic Water layer and the diapycnal mixing occurring over the Yermak Plateau is of sufficient magnitude to influence the heat anomaly pulses entering the Arctic Ocean. *Rippeth et al.* (2015) showed that turbulent mixing rates are enhanced over rough topography, hence over the Yermak Plateau at localized hotspots. This result is independent from the sea ice cover.

Tides are large over the Yermak Plateau. *Padman and Dillon* (1991) showed that the diurnal tide is predominant in this area. Over the Yermak Plateau, trapped internal waves generated by tide forcing are one of the main energy source to generate large vertical heat fluxes. Tides can also create significant tidal currents. *Padman et al.* (1992) showed that the Yermak Branch of the western coast of the Yermak Plateau is mainly the result of residual current from tidal rectification. *Luneva et al.* (2015) found with a model study that the tide-induced internal waves generated over the Yermak Plateau influence the water mass mixing and the sea ice.

With the increase in the open ocean fraction north of Svalbard and the increased transfer of momentum from the atmosphere to the ocean, an increase in vertical mixing and mixing hotspots is expected (*Rippeth et al.*, 2015). These changes over the Yermak Plateau could have major impact for the Arctic Ocean biology, with a change in the vertical flux of nutrients and heat and on the sea ice.

1.5.3 Ice-ocean interaction

As the Atlantic Water core is still relatively close to the surface along the continental slope north of Svalbard (less than $100m$, *Fer et al.* (2010)), exchanges between the sea ice and the surface ocean in the region of the Yermak Plateau have drastic effects on the sea ice thickness and extent.

One particularity of the continental slope north of Svalbard is that sea ice melt is not only observed in summer but also in winter. *Onarheim et al.* (2014) showed that extra oceanic heat brought into the region with the warmer Atlantic Water during winter the recent years can have caused the recent sea ice loss anomaly in winter (Figure 1.15). They rule out the wind as the main factor as there is no temporal trend in the local wind. The local wind only influences the year-to-year variability of the ice concentration.

It has also been suggested recently that a lagged positive feedback exists between the sea ice cover and the ocean heat along the continental slope north of

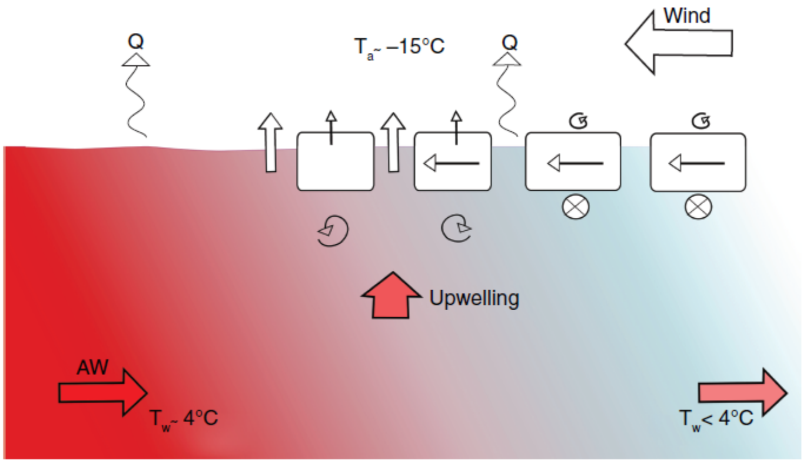

Figure 1.15: *Schematic of air-ice-sea interactions north of Svalbard. Northerly winds transport sea ice from the Arctic Ocean (slightly deflected to the right) and bring cold air masses, facilitating larger ice cover. Upwelling of warm Atlantic Water (AW, reddish) melts the approaching sea ice, and a fresh, cold layer forms below the ice (bluish). Depending on the vertical mixing below the ice, the freshwater layer reduces further ice melt. The large ocean-to-atmosphere heat flux, Q, is strongly reduced by the presence of sea ice. In winter, Q is the sum of net longwave radiation, latent heat and sensible heat. Excess heat is lost to space through longwave radiation. Ta: air temperature, and Tw: water temperature. From Onarheim et al. (2014).*

Svalbard (*Ivanov et al.*, 2016). When the sea ice cover is small in summer, the warm atmosphere transfers an excess of heat in the upper mixed layer, hence the sea ice growth during the following autumn and winter is diminished. The new ice is young, thin and more mobile which facilitates the formation of polynia and leads. The weak stratification at the base of the mixed layer supports thermohaline convection, which entrains warm and salty Atlantic Water up in the mixed layer. This **convection-induced upward heat flux** slows or even blocks sea ice formation.

1.6 Scientific objectives

The area north of Svalbard, with the entrance of Atlantic Water in the Arctic, is crucial to the heat budget of the Arctic ocean. The area North of Svalbard can be seen as a laboratory to study physical and biological changes happening in the Arctic. Although the inflow of Atlantic Water is larger in winter than in summer, winter data north of Svalbard are sparse as it is a difficult area to sample, with polar night in winter and sea ice present year around.

1.6.1 The N-ICE2015 expedition

From January to June 2015, a drifting ice camp was organized by the **Norwegian Polar Institute**, Tromsoe, Norway with the *R/V Lance* north of Svalbard (Figure 1.16), the N-ICE2015 expedition (Norwegian young sea ICE cruise). The objectives of the N-ICE2015 expedition were to: "understand how the rapid shift to a younger and thinner sea ice regime in the Arctic affects energy fluxes, sea ice dynamics and the ice-associated system, as well as global and local climate" (http://www.npolar.no/en/projects/n-ice2015.html).

Figure 1.16: *Leads in the Arctic sea ice with the R/V Lance. Photo shot from a helicopter as it was approaching the Lance. From Nick Cobbing/Norwegian Polar Institute*

A total of 6 legs were organized; 2 rotations in winter lasted 6 weeks and were made by the Coast Guard Vessel *K/V Svalbard*; in summer the 4 legs lasted 3 weeks with change of crew by helicopter. The N-ICE2015 campaign collected the first winter data in the area North of Svalbard. Four drifts (called floe) were accomplished (the ship was relocated in the sea ice at each time floes broke apart), during which the atmosphere, the sea ice, the ocean and the biology were documented (Figure 1.17). The first drift was from mid January to mid February over the Nansen Basin, the continental slope and the northern tip of the Yermak Plateau; the second drift over the Nansen Basin in March; the third drift was the longest one and lasted more than 2 months (mid April- June). During Floe 3, the ice camp drifted over the Yermak Plateau. Finally Floe 4 lasted less than a month in june, on the southern part of the Yermak Plateau.

Concerning the ocean instrumentation, salinity and temperature profiles were performed several times a week, microstructure profiles were obtained in the upper $200m$ several times a day. Turbulence under the ice was measured with a Turbulence Cluster Instrument. Current were documented from the surface down to $500m$ with ship ADCP and a downward looking 75kHz ADCP attached to the floe. The air-ice-ocean interface was monitored with a large buoy array of snow buoys and ice mass balance buoys.

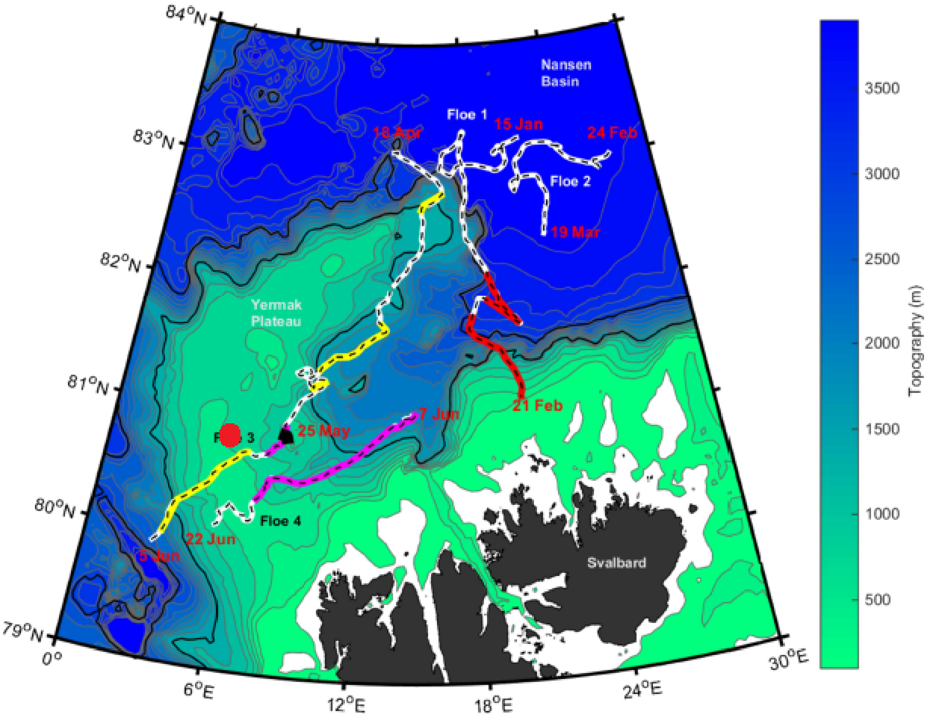

Figure 1.17: *Trajectories of the four N-ICE2015 drift between 15 January and 22 June 2015 with underlying topographic contours ranging from 100 to* $5000m$ *at* $200m$ *intervals. Presence of Atlantic Water in the water column is indicated and labeled from either the Yermak Branch (yellow drift track), from undetermined origin (magenta drift track), or from the Svalbard Branch (red drift track). The red dot is the location of the ADCP mooring deployed in 2007. Adapted from Meyer et al. (2017a)*

The atmospheric context of January-June 2015 is presented in *Cohen et al.* (2017). Winter atmospheric circulation is characterized by a succession of storms that produced an increase of surface temperature of more than $20 - 30°C$ in a few days. The storms are driven by large scale pattern that affects the entire hemisphere.

In winter 2015, the meridional component of the polar jet stream is particularly large, which steers the North Atlantic storms into the high Arctic. Several storms are also encountered in spring/summer and are the result of synoptic systems in the Barents Sea and in the Arctic Basin.

1.6.2 PhD objectives

The area north of Svalbard is key for the heat and salt budget in the Arctic with the Atlantic Water inflow from Fram Strait. With climate change that has a large impact in this area, it is important to document the region north of Svalbard and better understand its characteristics. A good knowledge of the Atlantic Water inflow will help to better constrain the global ocean model and will improve the climate predictions in the Arctic first as well as in the rest of the world. This PhD has focused on the Atlantic Water properties and circulation in the area north of Svalbard. We tried to answer or at least provide elements of response to the following questions:

- What are the characteristics of the Atlantic Water inflow (pathways, hydrogaphy) in the recent years?
- How does the Atlantic Water influence the sea ice?
- How has the inflow been varying over the last 10 years?

These questions are addressed from an experimental point of view. I performed this PhD in the laboratory LOCEAN, within the framework of the French Equipex IAOOS (Ice Atmosphere Ocean Observing System, www.iaoos.ipev.fr) and of the European FP7 project Ice-Arc (www.ice-arc.eu). The goal of the IAOOS project is to develop and maintain an observational network in the Arctic Ocean that will transmit data in real time via satellite transmission. Each platform is composed of instruments measuring atmosphere, sea ice and ocean parameters (Figure 1.18). The atmospheric part is composed of a microlidar, an optical depth sensor (ODS) and a weather mast (*Mariage et al.*, 2017), the sea ice properties are documented with an ice mass balance instrument (IMB) and the ocean with an ice-tethered profiler from $5m$ down to $800m$. A detailed description of the IAOOS platforms is presented in Chapter 2. During these 3 years, I fully participated to the project and deployed several IAOOS platforms in the Arctic Ocean: one during the N-ICE2015 expedition north of Svalbard in April 2015, two from the Korean Icebreaker *R/V Araon* in August 2015 in the Chukchi Sea (Figure 1.19) and finally two from the Russian ice camp Barneo in the central Arctic near the North Pole in April 2017. Although the analysis of the platforms I have deployed is not presented here, I participated to the entire processing of *in situ* ocean data, from deployment to analysis and data quality control. More recently, I have deployed a glider North of Svalbard in July 2017 to examine the dynamic of the Atlantic Water inflow in the West Spitsbergen Current around $79°N$.

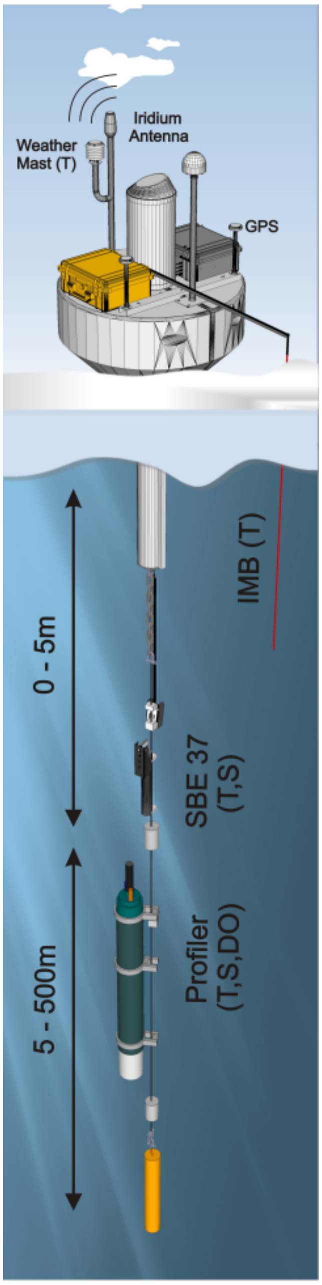

Figure 1.18: *Schematic of the IAOOS platform: ocean, ice and atmosphere part*

In addition to the *in situ* observations from IAOOS platforms during N-ICE2015 and from a moored ADCP over the Yermak Plateau in 2007-2008, I used model outputs provided by Mercator-Ocean in Toulouse to put the *in situ* data in a broader spatial and temporal context. Although I did not run the model myself, the close collaboration with Mercator-Ocean enabled me to spend several weeks there to interact with modelers and understand the parametrisations, capabilities and limitations

Figure 1.19: *Picture from the deploiement of one IAOOS platform in August 2015*

of the model outputs I used.

The thesis is organized as follows: Chapter 3 presents winter hydrographic *in situ* data North of Svalbard and ice-ocean interactions in winter in this area documented during N-ICE2015 expedition. In Chapter 4, *in situ* observations from the winter 2015 IAOOS platforms are put in a broader spatial and temporal context using the 1/12° resolution Mercator Ocean operational ocean model in the region North of Svalbard. Model output analysis highlights a winter path of the Atlantic Water over the Yermak Plateau: the Yermak Pass Branch, not well documented before. Chapter 5 presents year-round *in situ* current data collected in the Yermak Pass over the Yermak Plateau north of Svalbard in 2007-2008. Finally Chapter 6 concludes and presents some perspectives.

Chapter 2

Winter Hydrography and influence of the Atlantic Water on the sea ice North of Svalbard in winter

---

Contents

2.1 Introduction

The inflow of Atlantic Water is the main source of heat and salt for the Arctic Ocean, but observations are sparse in one of its entrance area North of Svalbard in winter (December-January-February). Moreover, the volume transport of the Atlantic Water inflow in the West Spitsbergen Current doubles in winter compared to summer (*Beszczynska-Möller et al.*, 2012). Summer observations do not catch this large flow that could have main impacts on the area north of Svalbard (sea ice, ecosystems...) and on the entire Eurasian Basin especially in areas where the seasonal cycle is still present (*Lique and Steele*, 2012).

In this first study, we focus on the winter hydrography of the area north of Svalbard using IAOOS platform data from Floe 1 (January-February 2015) of the N-ICE2015 expedition. Floe 1 drifted over the Nansen Basin, the northern tip of the Yermak Plateau and the Svalbard continental slope. Norwegian Research Vessel *R/V Lance* was used as a testbed for the IAOOS platforms, to examine the behavior of the different instruments in the polar night with air temperature $\sim -30°C$ (development of frost on the window of the microlidar, impact of insulation, iridium transmission quality in winter, batteries...). Two IAOOS platforms were deployed (Figure 2.1) during floe 1 and a testing hole with only an ice-tethered profiler was set up to examine the hydrodynamic of the profiler.

Figure 2.1: *Photo of one of the IAOOS platform deployed during N-ICE2015, in the middle of the polar night. By Nicolas Villacieros-Robineau.*

2.2 Winter ocean-ice interactions under thin sea ice observed by IAOOS platforms during N-ICE2015: Salty surface mixed layer and active basal melt

Journal of Geophysical Research: Oceans

RESEARCH ARTICLE
10.1002/2016JC012195

Special Section:
Atmosphere-ice-ocean-ecosystem Processes in a Thinner Arctic Sea Ice Regime: The Norwegian Young Sea ICE Cruise 2015 (N-ICE2015)

Key Points:
- Large sea-ice melt over the inflowing Atlantic Water on the Svalbard northern continental slope in winter
- Sea-ice bottom melt associated with near-inertial waves and tides
- Winter hydrography shows a salty mixed layer and three Atlantic Water pathways across and around the Yermak Plateau

Correspondence to:
Z. Koenig,
zklod@locean-ipsl.upmc.fr

Citation:
Koenig, Z., C. Provost, N. Villacieros-Robineau, N. Sennéchael, and A. Meyer (2016), Winter ocean-ice interactions under thin sea ice observed by IAOOS platforms during N-ICE2015: Salty surface mixed layer and active basal melt, *J. Geophys. Res. Oceans*, *121*, 7898–7916, doi:10.1002/2016JC012195.

Received 28 JUL 2016
Accepted 1 OCT 2016
Accepted article online 5 OCT 2016
Published online 28 OCT 2016

Winter ocean-ice interactions under thin sea ice observed by IAOOS platforms during N-ICE2015: Salty surface mixed layer and active basal melt

Zoé Koenig[1], Christine Provost[1], Nicolas Villacieros-Robineau[1], Nathalie Sennéchael[1], and Amelie Meyer[2]

[1]Laboratoire LOCEAN-IPSL, Sorbonne Universités, UPMC, Univ. Paris 6, CNRS-IRD-MNHN, Paris, France, [2]Norwegian Polar Institute, Fram Centre, Tromsø, Norway

Abstract IAOOS (Ice Atmosphere Arctic Ocean Observing System) platforms, measuring physical parameters at the atmosphere-snow-ice-ocean interface deployed as part of the N-ICE2015 campaign, provide new insights on winter conditions North of Svalbard. The three regions crossed during the drifts, the Nansen Basin, the Sofia Deep, and the Svalbard northern continental slope featured distinct hydrographic properties and ice-ocean exchanges. In the Nansen Basin, the quiescent warm layer was capped by a stepped halocline (60 and 110 m) and a deep thermocline (110 m). Ice was forming and the winter mixed layer salinity was larger by ~0.1 g/kg than previously observed. Over the Svalbard continental slope, the Atlantic Water (AW) was very shallow (20 m from the surface) and extended offshore from the 500 m isobath by a distance of about 70 km, sank along the slope (40 m from the surface) and probably shed eddies into the Sofia Deep. In the Sofia Deep, relatively warm waters of Atlantic origin extended from 90 m downward. Resulting from different pathways, these waters had a wide range of hydrographic characteristics. Sea-ice melt was widespread over the Svalbard continental slope and ocean-to-ice heat fluxes reached values of 400 W m^{-2} (mean of ~150 W m^{-2} over the continental slope). Sea-ice melt events were associated with near 12 h fluctuations in the mixed-layer temperature and salinity corresponding to the periodicity of tides and near-inertial waves potentially generated by winter storms, large barotropic tides over steep topography, and/or geostrophic adjustments.

1. Introduction

With the rapid sea-ice decline [*Comiso*, 2012], the Arctic is the region in the world where climate change is most evident. The Arctic Ocean carries a large amount of ocean heat that has to be taken into account in the energy balance at the ice-ocean-atmosphere interface. Atlantic Water (AW) entering the Arctic Ocean through the Fram Strait with the West Spitsbergen Current (WSC) provides the main source of heat and salt to the Arctic Basin [*Schauer et al.*, 2008; *Aagaard et al.*, 1987]. The WSC splits into three branches upstream from the Yermak Plateau (Figure 1) [*Quadfasel et al.*, 1987; *Manley et al.*, 1992]: one branch recirculates back into the Fram Strait between 78°N and 80°N [*Hattermann et al.*, 2016]; a narrow branch follows the western slope of the Yermak Plateau along the 1000 m isobath (called hereafter the Yermak Branch, YB) [*Manley et al.*, 1992; *Manley*, 1995] and a main branch follows the northern continental slope of the Svalbard Archipelago along the 400–500 m isobath (called hereafter the Svalbard Branch, SB) [*Sirevaag et al.*, 2011; *Muench et al.*, 1992; *Cokelet et al.*, 2008]. The Yermak Branch and the Svalbard Branch recombine east of the Yermak Plateau to continue as a boundary current eastward along the Eurasian continental slope [*Rudels et al.*, 2015].

A cold and fresh mixed layer lies above a strong pynocline and usually prevents the upwelling of AW up to the surface and hence sea-ice melt. This upper layer originates from low salinity shelf waters in most of the deep basins except in the Nansen Basin [*Rudels*, 2016]. In the Nansen Basin, as the warm AW inflow encounters and melts sea ice, it creates an upper, low salinity surface layer that isolates the warm water from the sea ice and the atmosphere. The mixed layer in the Nansen Basin northeast of Svalbard forms as a result of AW cooling and freshening from sea-ice melt in the upper part of the water column. The AW heat released in the process is partly consumed by ice melt and partly escapes to the atmosphere. Evidence of basal sea-ice melt has been observed northeast of Svalbard in autumn [*Steele and Morison*, 1993] and on the Yermak

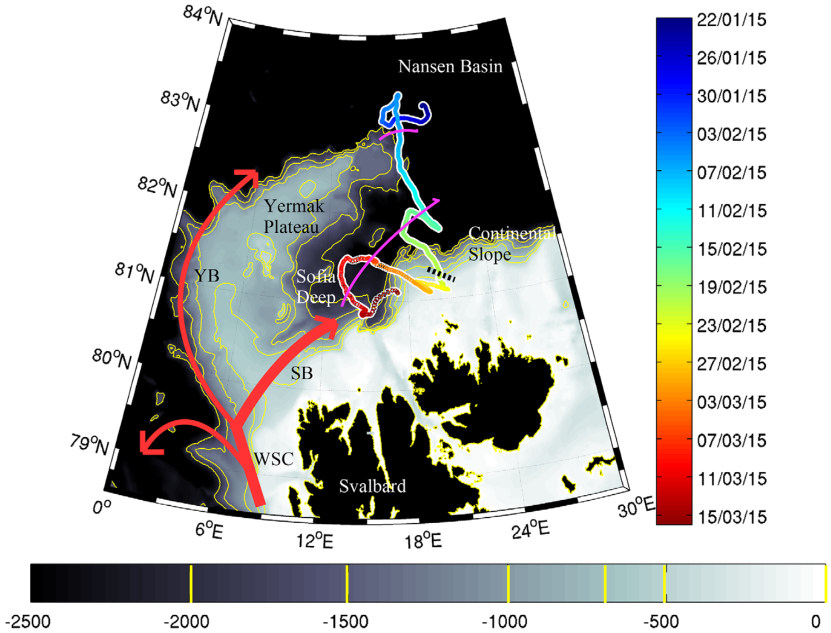

Figure 1. Drift trajectory of the IAOOS platform during Floe 1 of N-ICE2015 campaign. Vertical colorbar is time. The Atlantic Water inflow of the West Spitsbergen Current (WSC) splits into three branches, a recirculation to Fram Strait, the Yermak Branch (YB), and the Svalbard Branch (SB) [*Sirevaag et al.*, 2011]. The dashed line indicates the location of Floe 1 breakup when R/V Lance left and IAOOS7 continued drifting alone. The two magenta lines show the offshore limit of the water originating from the Svalbard Branch over the Svalbard continental slope and the boundary between the Nansen Basin hydrography and the Sofia Deep hydrography, according to the data. Background is bathymetry (m). Yellow isolines are 0, 500, 700, 1000, 1500, and 2000 m. Bathymetry is from IBCAO (http://www.ngdc.noaa.gov/mgg/bathymetry/arctic/arctic.html).

Plateau from late January to Mid-March 2003 [*Mc Phee et al.*, 2003]. Winter sea-ice melt is also documented by ice mass balance instrument during winter 2015 over the Svalbard Continental slope with ocean-to-ice heat fluxes peaking at 400 W m^{-2} (C. Provost et al., Observations of snow-ice formation in a thinner Arctic sea ice regime during the N-ICE2015 campaign: Influence of basal ice melt and storms, submitted to *Journal of Geophysical Research*, 2016). The trend in winter ice area loss North of Svalbard is close to 10% per decade and the ice edge has retreated to the northeast along the AW pathway [*Onarheim et al.*, 2014; *Ivanov et al.*, 2012]. *Ivanov et al.* [2016] suggest that the reemerging anomalies of ice free areas in midwinter Northeast of Svalbard reveal a positive feedback with a "memory" of ice depleted conditions in summer transferring to mid-winter via thinner ice more susceptible to lead formation allowing convection-induced upward heat fluxes from the AW.

The Norwegian young sea ICE (N-ICE2015) expedition from January to June 2015 took place in this region north of Svalbard to study ice-ocean-atmosphere interactions in a thinner Arctic sea-ice regime than it used to be (Figure 1). This 6 month long campaign consisted of four drifting ice camps, relocated northward each time the floes broke [*Granskog et al.*, 2016]. The general hydrography and circulation patterns observed during the 6-month drift are presented in Meyer et al. (A. Meyer et al., Winter to summer hydrographic and current observations in the Arctic north of Svalbard, submitted to *Journal of Geophysical Research*, 2016). Here we focus on mid-winter conditions as documented by IAOOS (Ice Atmosphere Arctic Ocean Observing System) platforms deployed during Floe 1 of N-ICE2015 in January–February 2015 in the middle of the polar night. These platforms carry an ice mass balance instrument monitoring temperature across the air/snow/ice/ocean interface and an ocean profiler measuring conductivity hence salinity, temperature and dissolved oxygen concentration down to 500 m or more. We use the IAOOS platform data to examine the winter hydrography in the region and the ocean processes responsible for the winter basal sea-ice melt over the Svalbard continental slope.

Section 2 presents the IAOOS platforms, the data processing and the platform drift over the western Nansen Basin, the Sofia Deep and the Svalbard northern continental slope (Figure 1). Section 3 describes the distinct hydrographic conditions sampled by the profilers in the three regions. Section 4 focuses on the ocean-ice interface with sea-ice growth and basal melt processes. Finally in section 5 results are discussed and conclusions are drawn out.

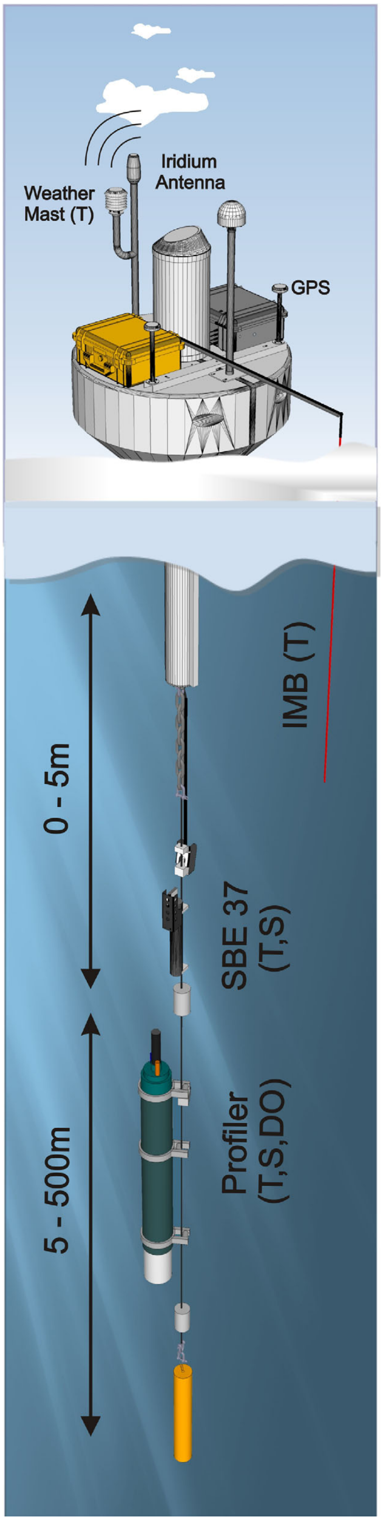

Figure 2. Schematic of the IAOOS platform showing weather mast, GPS, data transmission unit, ice mass balance unit (IMB measuring temperature through air, snow, ice, and upper ocean), SBE37 instrument (recording temperature and salinity at 4 m depth) and the ocean profiler (measuring temperature, salinity, and dissolved oxygen concentration from 5 to 500 m depth).

2. IAOOS Platform and Data

The IAOOS autonomous platforms (Figure 2) document the four media, ocean/ice/snow/atmosphere, in the Arctic while drifting with the ice [*Provost et al.*, 2015]. The atmospheric part includes a GPS, a weather mast and a microlidar [*Mariage*, 2015; *Mariage et al.*, 2016]; the ice/snow part an ice mass balance instrument [*Jackson et al.*, 2013]; and the ocean part an ice-tethered profiler [*Provost et al.*, 2015] (Figure 2). Other ice-tethered CTD profiling systems are used in the Arctic [e.g., *Krishfield et al.*, 2008; *Kikuchi et al.*, 2007]. Two platforms were deployed during Floe 1 (IAOOS7 on 22 January and IAOOS8 on 26 January, Table 1). Additional profiler tests (IAOOS 9) were carried out from 6 February to 19 February from a tent-covered testing hole on Floe 1. The three platforms were initially located close to the ship, less than 500 m from each other on a second year ice floe, Floe 1. R/V Lance drifted with Floe 1 from 15 January 15 (83.22°N, 21.26°E) until 21 February (81.22°N, 20.34°E) when the floe broke up (Figure 1). IAOOS 8 and 9 platforms were recovered during Floe 1 breakup while IAOOS 7 platform pursued its drift until its recovery by R/V Lance on March 16 (Figure 1). The profiler on IAOOS 7 was lost on 21 February as the

Table 1. Characteristics of the IAOOS Platforms

	IAOOS 7	IAOOS 8	IAOOS 9
Deployment date	22 Jan 2015	26 Jan 2015	06 Feb 2015
Profiler lost	21 Feb 2015	21 Feb 2015	
Recovery date	26 Mar 2015	23 Feb 2015	19 Feb 2015
Sampling rate (h)	12	12	12
Wire Length (m)	500	500	850
SBE37	No	Yes	No
IMB	Yes	Yes	No
Good Profiles *T*	62	50	26
Good Profiles *S*	53	47	25
Good Profiles DO	47	44	21

platforms drifted over ocean depths smaller than 500 m (Table 1). Thus, from that date on, the only ocean data available are the near-ice ocean temperature profiles from the ice mass balance instrument.

The IAOOS weather mast provides local atmospheric conditions. The ocean data collected from the IAOOS platforms document the warm water layer from the Atlantic Water inflow, the halocline, the mixed layer, the ocean-to-ice heat flux and consequent winter basal ice melt (mid-January to mid-March 2015). The snow/ice mass balance instrument data is analyzed in detail by Provost et al. (submitted manuscript) with a focus on snow-ice formation observed in February and March 2015. Here we use the ice instrument data to examine closer the ocean-ice interface.

The IAOOS weather mast recorded cold air temperatures below $-30°C$ until 1 February and signatures of the six main storms identified during N-ICE2015 by *Hudson and Cohen* [2015]: M1 (21–22 January), M2 (3–8 February), M3 (15–21 February), M4 (3–4 March), M5 (8–10 March), and M6 (15–16 March) with air temperature increase (up to 0°C on 17 February) and large decrease in sea level pressure (down to 960 hPa on 9 March) (Figure 3a). M4 and M5 are recorded after Floe 1 breakup and the ship was not close to the IAOOS platforms anymore. Hence, dates of M4 and M5 have been adjusted from *Hudson and Cohen* [2015] using the data from the IAOOS weather mast. The GPS-derived platform drift speed increased during the storms and reached 40 cm s^{-1} during M2, 60 cm s^{-1} on 16 February (M3), and even 100 cm s^{-1} during M6 (Figure 3b).

The ice mass balance instrument from the Scottish Association for Marine Sciences (SAMS), hereafter called SIMBA standing for SAMS ice mass balance for the Arctic, is composed of a thermistor chain of 5 m that provides profiles of temperature and a proxy of the thermal resistivity of the media with a 2 cm vertical resolution [*Jackson et al*., 2013]. The accuracy of each temperature sensor is 0.1°C. SIMBA data from IAOOS 7 and 8 (SIMBA_2015h and SIMBA_2015i, respectively) have a 3 h sampling frequency. The SIMBA data analysis that identifies the air/snow, snow/ice, and ice/ocean interfaces and estimates of heat flux densities is detailed in Provost et al. (submitted manuscript). Here we use temperature data from SIMBA_2015h which is the longest record with 51 days from 24 January to 16 March (Figure 3c). Snow thickness was 55 cm at deployment and increased to 90 cm during storm M3 (Figure 3c). Ice thickness was 154 cm at deployment, decreased to 125 cm on 9 March due to basal melt, and then increased to 145 cm from 9–11 March due to snow-ice formation (Provost et al. submitted manuscript). The temperature time derivative (Figure 3d) shows high-frequency variations in the atmosphere until storm M3 (there are no more sensors in the atmosphere after M3 storm snow fall) that are dampened in the snow. In the ice the major changes in temperature are the cooling due to the initial refreezing of the deployment hole (until 1 February) and the exothermal formation of snow-ice on 9 March. Changes in ocean temperature resulted in basal ice melt that starts on 16 February.

The ocean profilers, from French manufacturer NKE (PROVOR SPI), a sliding profiler with inductive transmission, carried a Seabird SBE41CP CTD (Conductivity, Temperature, Depth) with an Aanderaa 4330 dissolved oxygen (DO) optode. The profilers were set to perform two profiles a day from 500 m upward (850 m for IAOOS9) starting at 6 am and 6 pm. They gathered a total of 138 profiles (62, 50, and 26 profiles for IAOOS7, IAOOS8, and IAOOS 9, respectively; Table 1). The vertical resolution of the processed CTD data is 1 dbar in the upper 400 dbars, 5 dbars from 400 to 550 dbars, and 10 dbars from 550 to 850 dbars; the vertical resolution in DO is 2 dbars over all depths. Salinity was calibrated and quality controlled using the ship CTD salinity bottles (four dates) (Meyer et al., submitted manuscript). Following quality control, we retain all the temperature profiles and remove 1% of the salinity profiles. Finally, the accuracy is estimated to be 0.002°C in temperature, and 0.02 g/kg in salinity. Several profiles are missing or incomplete because of high drift speeds (>0.4 m s^{-1}) impeding the ascent of the profiler. There were no bottle DO measurements available during Floe 1 of N-ICE2015 to calibrate the DO data. DO accuracy is estimated comparing the deep values

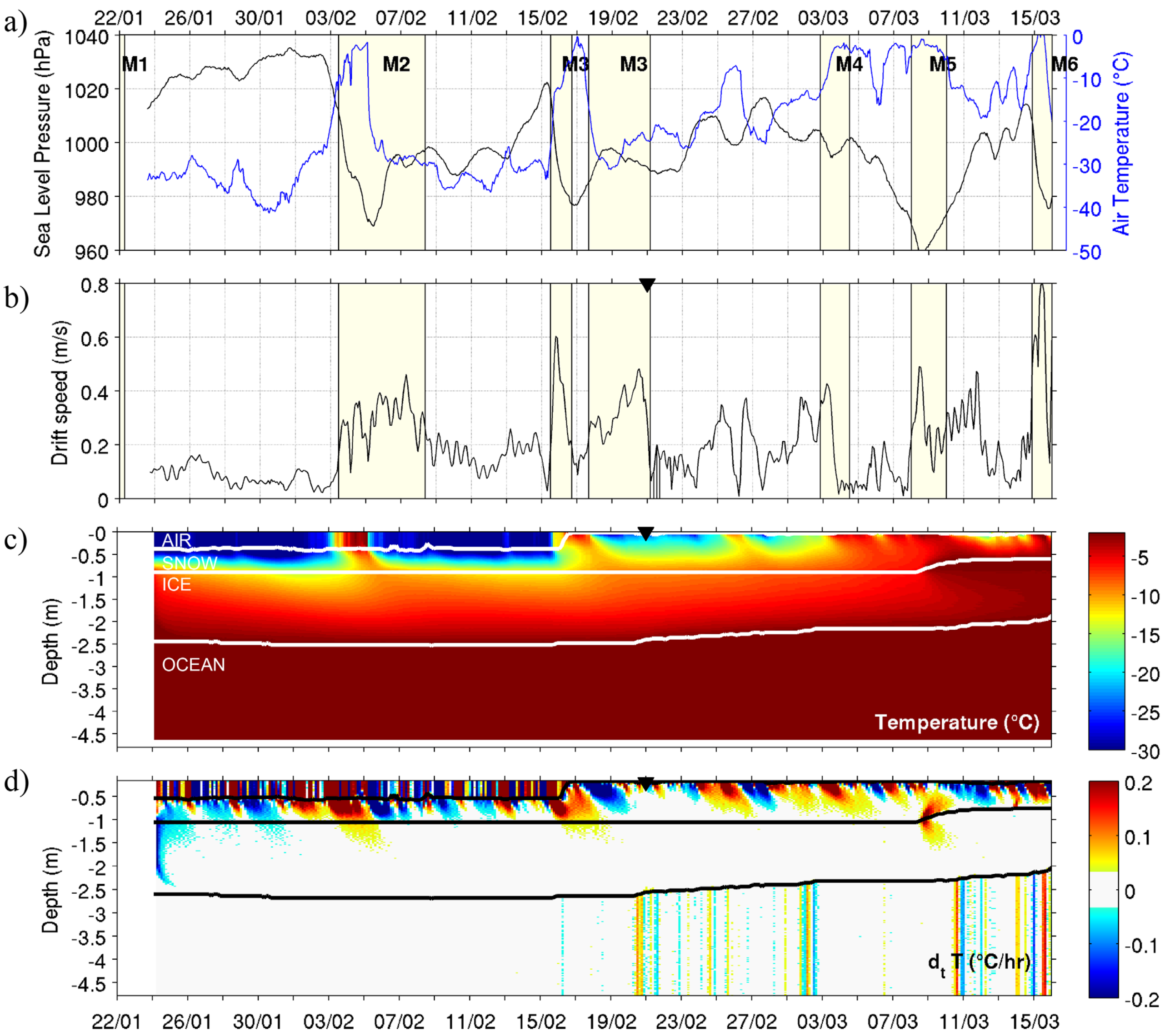

Figure 3. Atmospheric and SIMBA data from 22 January to 16 March: (a) Sea level pressure and air temperature. Major storms are shaded in light yellow (M1, M2, . . .). (b) Drift velocity estimated from GPS positions. (c) Temperature profiles from SIMBA (in °C), white lines from *Provost et al.* [2016] indicate the air/snow/ice/ocean interfaces. (d) Time derivative of the SIMBA temperatures (in °C/d). The black triangle indicates the date after which there are no profiler data.

of DO concentration (rather stable at 500m) between the three profilers. A difference of 3 μmol L^{-1} is observed between IAOOS 8 and 9, and IAOOS 7. An offset of 3 μmol L^{-1} is then applied to the oxygen data from IAOOS7 and the accuracy of the data is estimated to be at 3 μmol L^{-1}.

IAOOS 8 also featured a Seabird SBE37 CTD recorder at about 4 m depth, sampling temperature, salinity, and pressure every 5 min from 22 January to 21 February. However, freezing of the SBE37 during deployment prevents use of the temperature data before 27 January and of the salinity data before 6 February. The precision of the temperature sensor is 0.002°C and the conductivity sensor is 0.002 g/kg once converted in absolute salinity.

In summary, the ocean data consist of temperature profiles in the upper 2 m with a 3 h time resolution from SIMBA-2015h (record length 51 days), temperature and salinity at 4 m depth with a 5 min resolution from the SBE37 (record length 25 days for temperature and 15 days for salinity), and temperature, salinity, and DO concentration with a 12 h resolution from 5 to 500 m from the profiler (record length 30 days). The horizontal resolution depends upon drift velocity: for the profiler data it varies from 2 km on 2 February to 23 km on 15 February with an average of about 10 km.

3. Hydrography North of Svalbard in January–February 2015

The hydrographic sections presented in Figure 4 are composites of the three ocean profiler data. We use the International Thermodynamic Equations of Seawater (TEOS-10) framework [*McDougall et al*., 2012] with conservative temperature CT (°C) and absolute salinity S_A (g/kg). In the region, absolute salinity values exceed practical salinity values by about 0.16. We follow water mass definitions from *Rudels et al*. [2000, Figure 2] (Figure 5a) adapted to absolute salinity and conservative temperature. The warm layer comprises two main water types: Modified Atlantic Water (MAW) (temperatures between 0 and 2°C) and Atlantic Water (AW) (temperatures larger than 2°C). DO concentration varies from low values (290–310 μmol L^{-1}) in the warm layer to larger values in the upper layer (range 340–367 μmol L^{-1}) (Figure 4c). The surface layer shows absolute salinities between 34.35 and 34.55 g/kg, corresponding to practical salinities of $\sim$34.19 and 34.39 psu, respectively, slightly larger than those observed previously in the region (e.g., 34.1–34.2 psu) [*Kikuchi et al*., 2004; *Rudels et al*., 2000; *Sirevaag and Fer*, 2009]. Near-surface temperatures are often at the freezing point or close to it. The three regions crossed by Floe 1 drift, the Nansen Basin from 22 January to 6 February, the Sofia Deep and the tip of the Yermak Plateau from 6 to 12 February and on 17 February (called hereafter Sofia Deep) and the Svalbard continental slope the rest of the time, present clearly distinct characteristics in the warm water layer and in the surface layer (Figures 1 and 4).

3.1. The Warm Water Layer From the Atlantic Ocean

The warm water layer (with temperatures larger than 0°C) extends from around 100 m to deeper than 500 m (Figure 4a), the deep 0°C isotherm is at about 800 m in the 850 m deep IAOOS 9 profiles (Figures 6a and 7a).

In the Nansen Basin (depth $>$ 4000 m), the warm water, composed of MAW, shows layering with two cores (at depths of around 250 and 400 m) with the same temperatures (around $+$1.8°C), different salinities (35.08 and 35.12 g/kg), and thus densities of 27.91 and 27.95, respectively (Figure 5a). The constant depth of the two cores is highlighted in the Brunt Väisälä frequency panel (Figure 4d). DO concentration is around 305 μmol L^{-1} in the MAW (Figures 4d and 5b). Hydrographic properties of Nansen Basin profiles (in blue in Figure 6) show little scatter in the AW range below 150 m. Isopycnals remain at the same depth except for significant isopycnal displacements at depth (80 m displacement at 400 m) after 3 February coincident with storm M2.

Over the continental slope off Svalbard, roughly from 12 February onward, the warm water is AW with a single shallower core ($\sim$150 m), warmer temperature ($>$2.5°C), higher salinity ($>$35.15 g/kg), and slightly larger DO concentration ($\sim$315 μmol L^{-1}) (Figure 5). This AW appears to come directly from Fram Strait (Figure 1) [*Sirevaag and Fer*, 2009]. The last profile (21 February) on the slope over 600 m shows AW as close as 20 m from the surface (black profile in Figures 5b and 6). It is the warmest profile below 300 m (2.9°C), and among the saltiest and the lowest in DO concentration (35.19 g/kg, 312 μmol L^{-1}). The peculiar upper structure of the profile is examined more closely in section 3.2. Profiles over the Svalbard Continental Slope show an offshore deepening of the top of the AW layer (0°C isotherm) and a scatter of hydrographic properties at depth indicative of lateral mixing. On 17 February, as the platform drifted to the north, the profiler sampled MAW from the Sofia Deep at 81.8°N and 18.5°E–19°E. This provides a local offshore limit of the location of the Atlantic Water coming from the Svalbard Branch (Figure 1, magenta line and Figure 7).

Between 6 and 12 February, the profiler measured water over the northern tip of the Yermak Plateau and over the Sofia Deep (Figures 1 and 4). The warm layer shows variations in isopycnal depths with amplitudes of about 100 m at 400 m decreasing toward the surface to values of 80 m at 200 m, and 10 m at 100 m. The troughs in isopycnal depth observed on 7 February likely correspond to topographically induced upwelling of deep fresher water that mixes with AW (Figure 7) (see section 5). Apart from these upwelling events, the warm layer comprises water from the Nansen Basin (Figure 4, 10–11 February). During 8 February and 11–12, the layer contains water warmer and saltier than in the Nansen Basin associated with isopycnal ridges. The warm water on 8 February at about 82.2°N located on the slope of the Yermak Plateau (depth around 1800 m) is probably the Yermak Branch, with an AW core at 300 m, propagating southward from the tip of

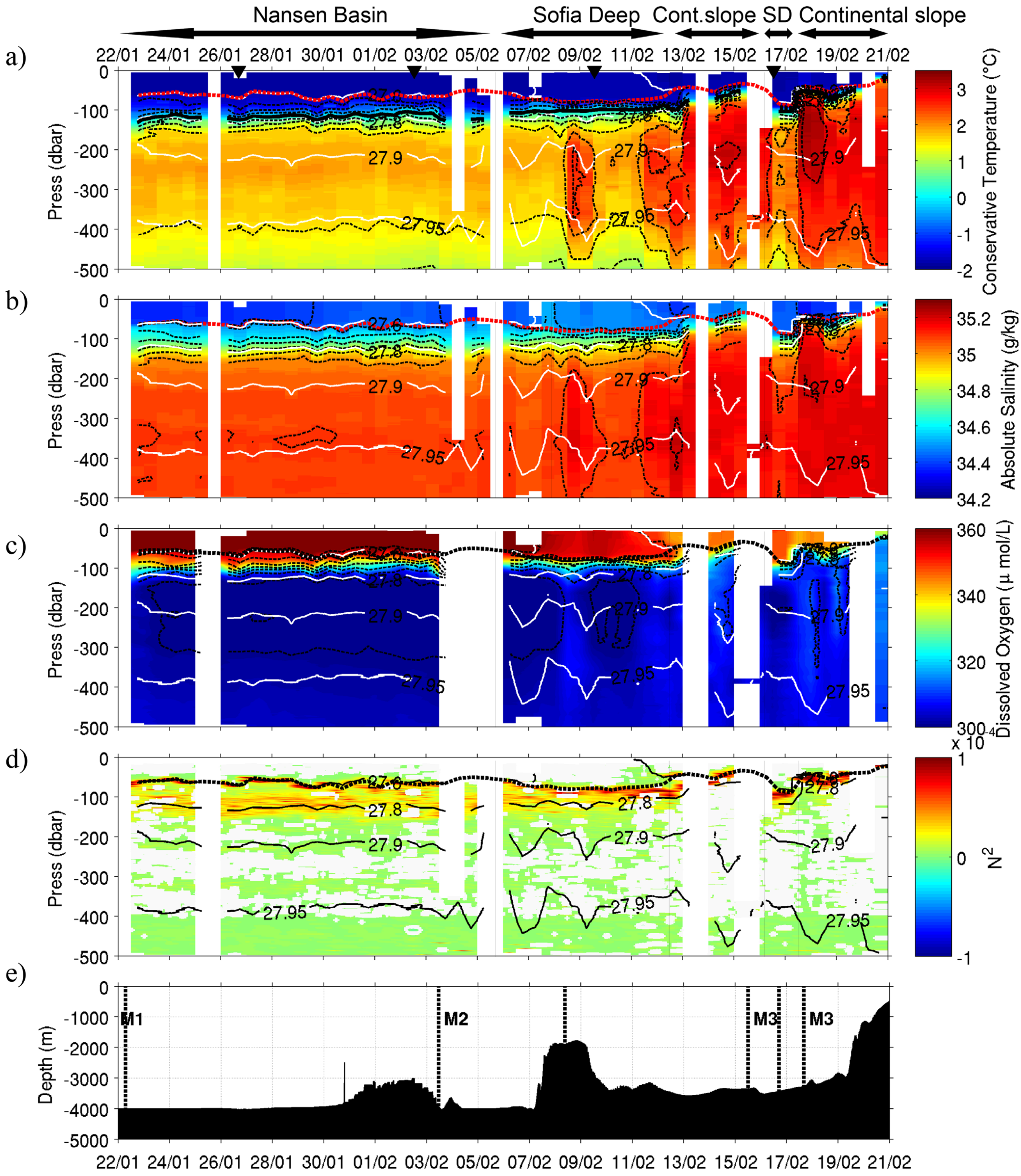

Figure 4. Composite section from the 3 profiler data (12 h averaged) of (a) conservative temperature (°C). The thick black line is the 0°C isotherm. (b) Absolute salinity (g/kg). (c) Dissolved oxygen concentration (μmol L^{-1}). Thin black dashed lines are, respectively, temperature, salinity, and dissolved oxygen concentration isolines. Thin white lines are isopycnals. (d) Brunt Väisälä frequency (N^2) along the drift (10^{-4} s^{-1}). The thin black lines are isopycnals. (e) Bathymetry along the drift trajectory. Dashed lines delimit storms. Thick dashed lines (red or black) are the mixed layer depth. Dates when the ship CTD were used to calibrate salinity data appear as black triangles. Arrows on the top indicate the "hydrographic regions" of Nansen Basin, Sofia Deep (SD), and Svalbard continental slope. Missing profiles are white.

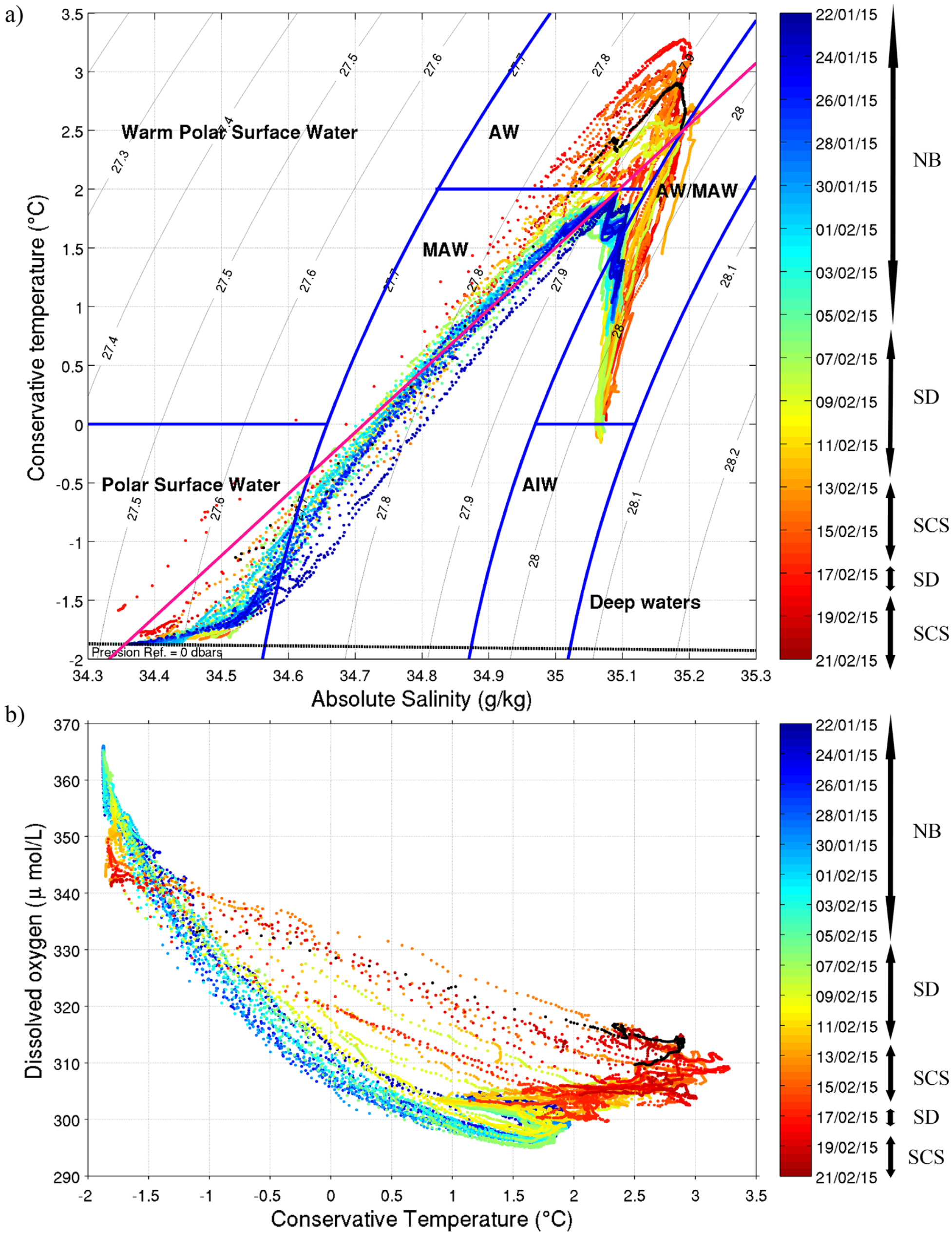

Figure 5. (a) Conservative temperature-absolute salinity diagram from the IAOOS profiler data. Water mass boundaries are from *Rudels et al.* [2000]: Atlantic Water (AW), Modified Atlantic Water (MAW), and Atlantic Intermediate Water (AIW). (b) Conservative temperature-DO concentration diagram. Colorbar is time and corresponding hydrographic provinces, Svalbard continental slope (SCS), Sofia Deep (SD), and Nansen Basin (NB), crossed during the drift are indicated. The black profile in both diagrams corresponds to the last one (20 February afternoon) over very shallow waters. The magenta line is the mixing line in the Nansen Basin between Polar Surface Water and Modified Atlantic Water. The blue dots under the magenta line in Figure 5a draw the shape of the convective halocline.

the Yermak Plateau (82.8°N, 16°E) following the 1000–2000 m isobath (Figures 1, 4, and 7). The warm water on 11–12 February (82.2°N, 19°E) with a core at 300 m may originate from a branch flowing through the Yermak Pass (a 700 m deep passage through the Yermak Plateau at 81°N) [*Gascard et al.*, 1995, Figure 34] or could be a deep eddy that detached from the Svalbard Branch and sank (Figure 7). There is not enough data to draw further conclusions. As a result of these different processes or paths, the range of hydrographic characteristics in the warm water layer is larger in the Sofia Deep profiles (red in Figure 6) than in the

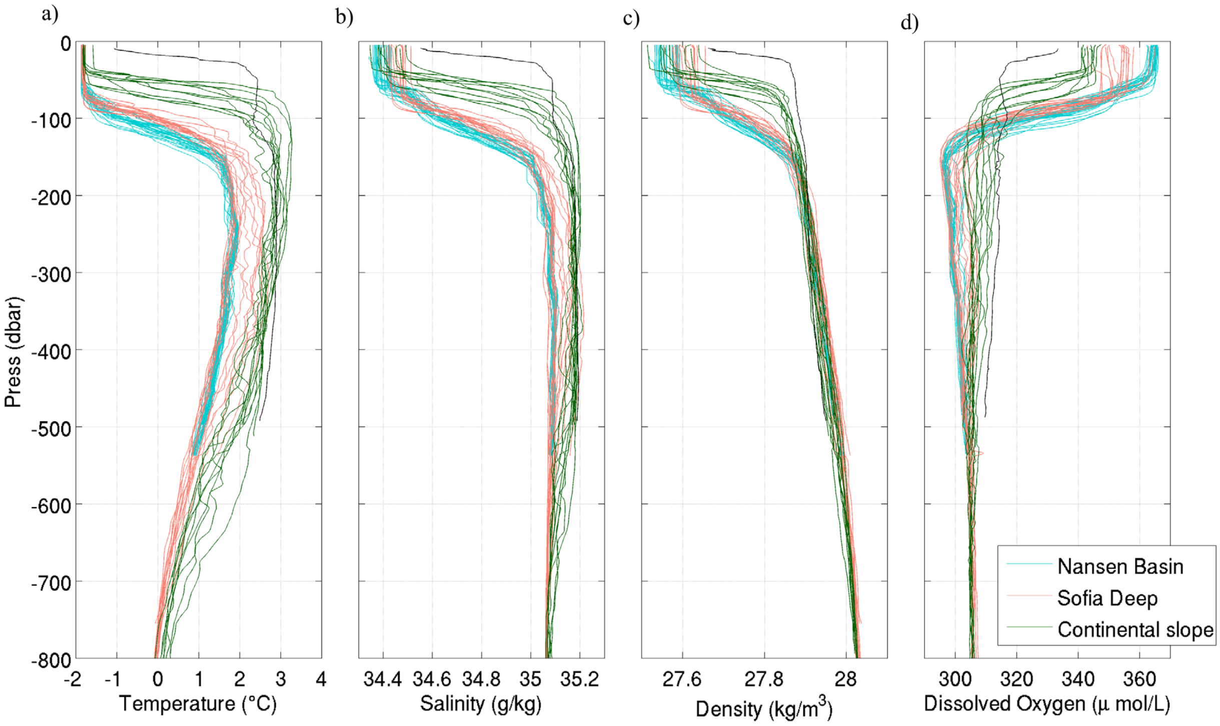

Figure 6. Vertical profiles from the profilers of (a) conservative temperature (°C), (b) absolute salinity (g/kg), (c) density (kg m^{-3}), and (d) dissolved oxygen concentration (μmol L^{-1}). Blue profiles are from the Nansen Basin, red profiles from the Sofia Deep and green profiles from the Svalbard continental slope. Black profiles correspond to the last profile of the drift (20 February afternoon) over very shallow waters.

Nansen Basin (blue in Figure 6) or the Svalbard continental slope profiles (green in Figure 6). In particular, the lowest salinity observed on 7 February where 35.05 g/kg at 300 m depth (Figure 6b), and the largest salinity at 370 m were 35.21 g/kg on 12 February (Figures 5a and 6b).

The AW is DO-enriched (from 300 to 315 μmol L^{-1}) compared to the MAW (295–305 μmol L^{-1}) indicating that warm waters from the Svalbard Branch have been in contact with the atmosphere more recently than waters from the Nansen Basin (Figures 4c and 5b). The Nansen Basin (MAW) profiles show a DO-minimum ($\sim$ 300 μmol L^{-1}) at about 140–150 m at the base of the lower halocline (blue in Figure 6d) whereas the shallowest Svalbard Branch (AW) profile (black in Figure 6d) is homogeneous below 20 m with DO values of 310 μmol L^{-1}. The spread in DO concentration in the other profiles is indicative of vertical mixing (Figure 6d).

3.2. The Upper Layer Characteristics

Over the Svalbard continental slope and the Sofia Deep, the depths of the thermocline, the halocline, and the pycnocline coincide. Gradients are steeper and shallower (40 m) above the Svalbard Branch, while weaker and deeper (90 m) over the Sofia Deep (Figure 6). Over the Nansen Basin, the thermocline is centered at 110 m whereas the halocline (pycnocline) comprises an upper halocline (upper pycnocline) centered at 60 m and a lower halocline (lower pycnocline) centered at 110 m (Figure 6). The processes responsible for this double pycnocline structure potentially involve formation of a convective cold halocline as ice is formed and/or the advection of cold salty water from shelves [e.g., *Rudels et al.*, 1996; *Kikuchi et al.*, 2004]. The observed T-S curves from the Nansen Basin fall below the mixing line joining T-S values at 220 and 140 m (magenta line in Figure 5) and form a bend separating low salinity freezing surface layers from the thermocline waters. Indeed, the lower halocline water and the top of the thermocline water have salinity larger (temperature lower) than the mixing line between the AW and the Polar Surface Water. This feature in the T-S diagram in the Nansen Basin indicates a convective mechanism leading to a stepped halocline after summer melt and refreezing [*Kikuchi et al.*, 2004, Figure 4].

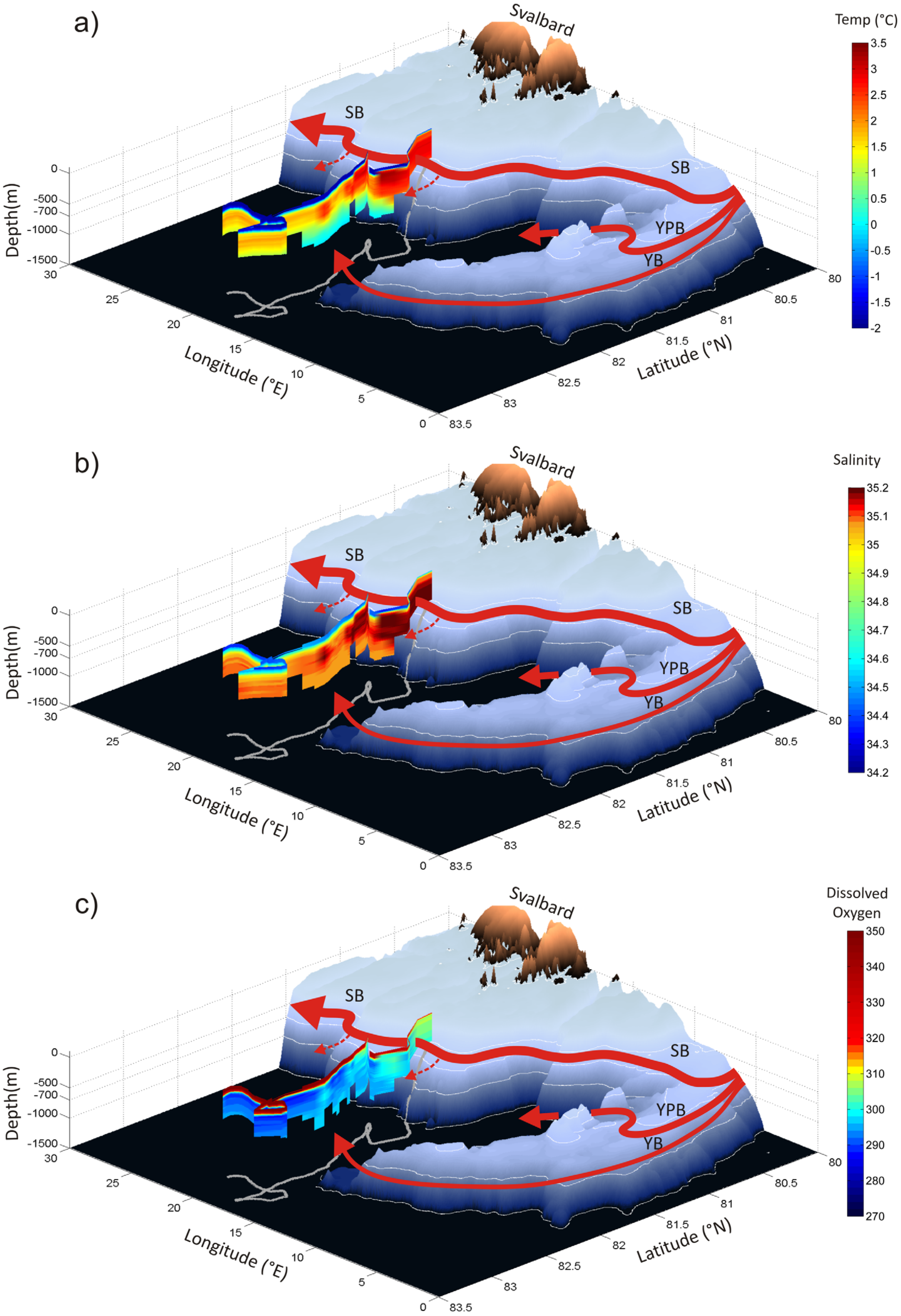

Figure 7. Three-dimensional plot of (a) conservative temperature (°C), (b) absolute salinity (g/kg), and (c) dissolved-oxygen concentration (μmol L^{-1}). Isolines are 500, 700, 1000, and 1500 m. Red full arrows describe paths for the warm Water Inflow: the Yermak Branch (YB), the Svalbard Branch (SB), and the Yermak Pass branch (YPB) [*Sirevaag et al.*, 2011; *Rudels et al.*, 2000]. Dashed red lines are indication of downwelling of the Atlantic Water down the continental slope into the Sofia Deep.

The last profile on the slope with near-surface Atlantic Water at 20 m measures the warmest and among the saltiest waters below 300 m and shows a stepped structure in both temperature and salinity, with a gradient at 130 m, compensated in density (black profile in Figures 5 and 6). Below 30 m depth, stratification is very weak (Figures 4d and 6c) and temperature and salinity profiles are well mixed on each side of the step (Figures 6a and 6b). This structure suggests the loss of heat in the upper 120 m laterally and vertically along the Svalbard Branch, followed by the advection of a layer of fresher melt water on top of it or active ice melt creating a sharp near-surface thermocline and halocline [*Rudels*, 2016].

Apart from this peculiar profile, on the slope, the mixed layer depth (MLD) (here defined as the depth where density is larger than the density at 10 m by 0.03 kg m^{-3}) is on average 40 m in the Svalbard Branch, 90 m in the Sofia deep, and 60 m in the Nansen Basin. Note that the MLD is quite insensitive to the precise criterion as the pycnocline is sharp [e.g., *Timmermans et al.*, 2012; *Toole et al.*, 2010]. The surface mixed layer is cold (~ -1.8°C, the freezing temperature), with low salinity ($\sim$34.35–34.50 g/kg) and DO-enriched compared to the MAW/AW ($\sim$340–370 μmol L^{-1}). The DO-enriched mixed layer corresponds to Polar Surface Water (Figure 5). The salinity range is quite large from 34.35 to 34.51 g/kg and even reaching 34.55 g/kg for the last profile (Figure 6b). These salinity values are high compared to MIMOC climatological values, +0.25 g/kg (Meyer et al., submitted manuscript).

The Brunt-Väisälä frequency [*Gill*, 1982] is larger above the Svalbard continental slope as the warm waters are denser in the AW than in the MAW (Figure 4d). The main pynocline reaches Brunt-Väisälä frequency values larger than 2×10^{-4} s^{-1} (Figure 4d), of the same order as in *Fer* [2009]. The deeper thermocline and lower halocline in the Nansen Basin show large Brunt-Väisälä frequency (5×10^{-5} s^{-1}) under the main pycnocline.

The mixed layer DO concentration is larger in the Nansen Basin than over the Svalbard Branch (360 μmol L^{-1} and 345 μmol L^{-1}, respectively, Figures 4c and 5b). This may be an indication of oxygen consumption and hence of biomass remineralization over the AW that does not occur in the mixed layer over the MAW. It may also be due to upwelling of low DO concentration AW through the pynocline over the Svalbard Branch that does not occur in the Nansen Basin.

4. Upper Ocean, Sea-Ice Formation and Basal Melt

We now focus on the ice-ocean interface in two steps, first analyzing and comparing the SIMBA, SBE37, and profiler data until 21 February, and then second by analyzing the only data available after 21 February which is the SIMBA temperature data.

4.1. Upper Ocean Until the Loss of the Profilers (21 February)

4.1.1. Consistency Between the Instruments in the Vertical

Temperature time series from the upper 2 m of the ocean from SIMBA (3 h resolution shown with an adapted colorbar to focus on the ice-ocean interface, Figure 8a) are consistent with the temperature time series at 4 m from the SBE37 (5 min sampling) (Figure 8e) and the temperature time series in the upper 30 m from the profiler (12 h sampling) (Figure 8b). Several events with under-ice temperatures above freezing temperature are identified.

The temperature increase observed from 7 to 11 February in the SIMBA, SBE37, and upper-ocean profiler data ($T \sim -1.75$°C; Figures 8a and 8b, Figure 8e) coincides with an increase in salinity measured by the SBE37 ($S \sim$ 34.35–34.5 g/kg) and the ocean profiler ($S \sim 34.48$ g/kg; Figures 8e and 8c).

On 16, 18, and 20 February (Figure 8a), the under-ice temperature is above freezing (about 0.15°C, 0.2°C, and 1.8°C, respectively). The 18 and 20 February events are associated with warmer water down to the halocline (profiler data; $T \sim -1.55$°C and $T \sim -1$°C, respectively) (Figure 8b). There is no profiler data on 16 February. These three warm events occur over the Svalbard Branch, where the 0°C isotherm is shallow (between 60 and 18 m, Figure 8c).

From 30 January to 3 February, profiler data (below 8 m) indicate a salinity increase in the mixed layer ($\sim$34.45 g/kg instead of $\sim$34.4 g/kg, Figure 8c), while temperature remains stable (around -1.85°C, Figure 8b). There is no signal in temperature in the upper 4 m of the ocean (SIMBA or SBE37) (Figures 8a and 8e). This salinity-only event happens before M2, when the platform is located on the edge of the slope of the

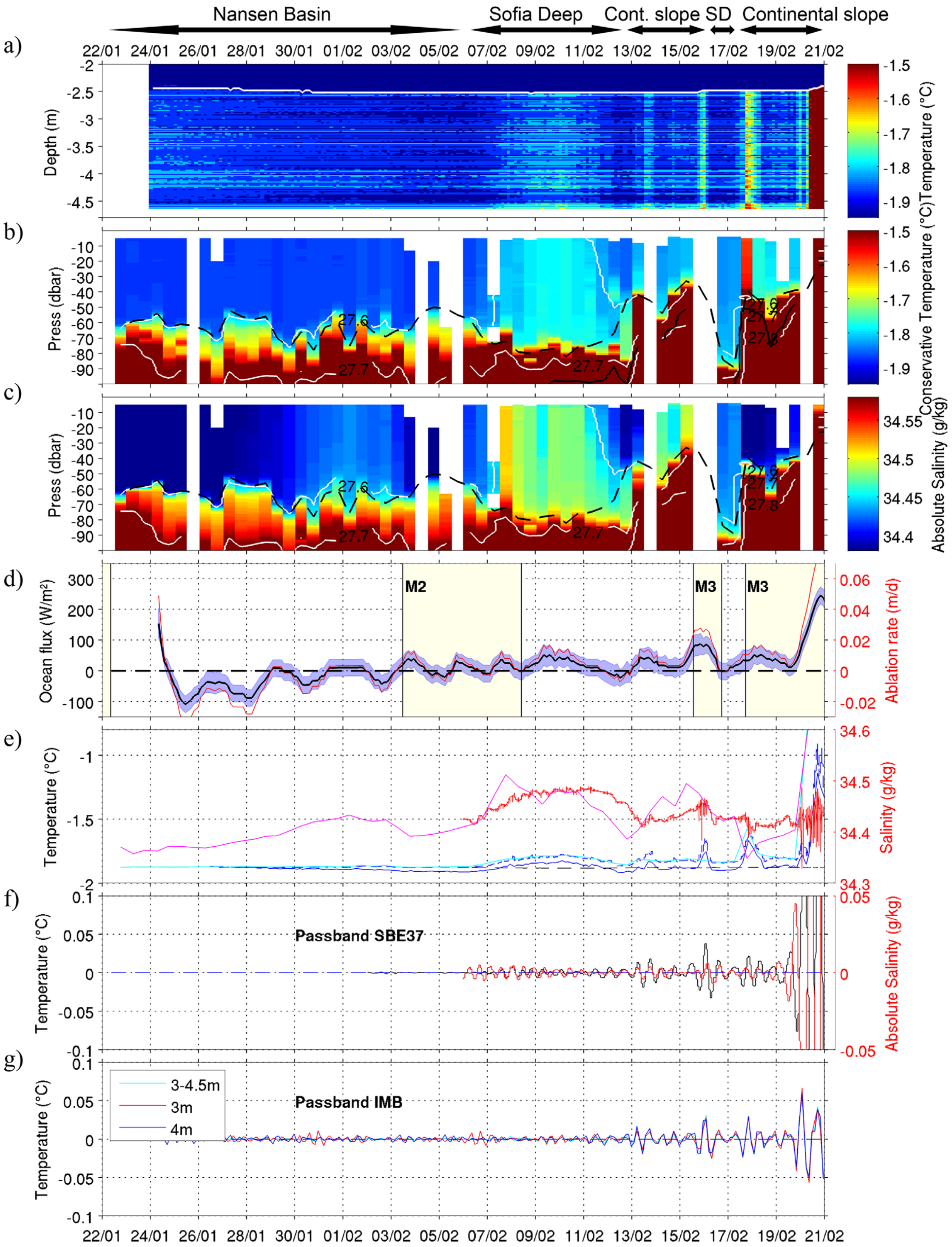

Figure 8. (a) SIMBA temperature zoomed on the ocean (scale −2°C; −1.5°C). (b) Conservative temperature (°C) in the upper 100 m from the profilers. The full black line is the 0°C isotherm. (c) Absolute salinity (g/kg) in the upper 100 m from the profilers. White lines are isopycnals. The thick dashed line is the mixed layer depth. Missing data points are white. (d) Ocean Flux (left axis, W m^{-2}) and ablation rate (right axis, m/d), at the ice/ocean interface deduced from SIMBA data [*Provost et al.*, 2016]. Blue shaded area is the ocean heat flux uncertainty [*Provost et al.*, 2016]. Storm periods are shaded in light yellow. (e) Left axis: temperature from SIMBA (mean of the upper 2 m, 3 h sampling, blue), from SBE37 (4 m, 5 min sampling, dashed blue) and from profilers at 20 m (12 h sampling, cyan). The dotted line is the freezing temperature. Right axis: Salinity from SBE37 (red) and from profilers at 20 m (magenta). (f) Data from SBE37 filtered between 8 and 16 h: temperature (left axis, black), salinity (right axis, red). (g) Band-pass filter between 8 and 16 h of SIMBA temperatures at 3 m (red), 4 m (blue), and averaged between 3 and 4.5 m (black).

Yermak Plateau (seafloor depth about 3000 m). A salty mixed layer is characteristic of the Yermak Plateau (Meyer et al., submitted manuscript).

The ocean (SIMBA, profilers and SBE37) data, therefore, provide a consistent picture of the upper-ocean vertical structure despite the difference in time resolution (3 h for the SIMBA, 12 h for the profiler and 5 min for the SBE37). For the following, it is important to recall that in the Nansen Basin the thermocline located at about 90 m depth is deeper than the pycnocline/halocline (around 60 m), while in the Sofia Deep and Svalbard Branch the three gradients coincide and are shallower than 60 m, around 40 m. The ocean heat flux (Figure 8d) was estimated as the sum of the latent heat flux (calculated from the time evolution of the ice-ocean interface depth) and the conductive flux in the ice next to the ocean interface (calculated from the vertical derivative of temperature) (Provost et al., submitted manuscript). The negative fluxes at the beginning of the time series until 26 January (Figure 3d) correspond to lateral fluxes associated with the refreezing of the deployment hole of the SIMBA. From 26 January to 1 February, sea-ice formation (growth) most likely caused the negative fluxes in accordance with the formation of the stepped halocline in the Nansen Basin. The ocean flux is significantly positive on several occasions, 9–11 February (50 W m^{-2}), 16 February (100 W m^{-2}), and 20 February (250 W m^{-2}), when the near-ice ocean temperature is above freezing and coincide with sea-ice basal melt.

We now focus on the high frequencies observed in the under-ice ocean data (SIMBA and SBE37). The daily resolution of the profiler data is not sufficient to examine the around 12 h period typical of tides and near-inertial internal gravity waves in the area.

4.1.2. High-Frequency Variations in Temperature and Salinity

The melting events, associated with ocean temperature peaks, also correspond to large high-frequency fluctuations detected in the 5 min sampling SBE37 data (Figure 8e). These high frequencies in salinity and temperature, retrieved when subtracting a 15 min running mean, have amplitudes up to 0.05 g/kg and 0.03°C and are largely anticorrelated ($r = -0.88$). These melt-associated high-frequency signatures could result from vertical mixing and overturning induced by salt releases from warming sea ice [*Widell et al.*, 2006].

Variations with a close to 12 h period are conspicuous in certain parts of the SBE37 salinity time series (Figure 8f). They are less clear in the temperature time series because of the large temperature scale adapted to the large temperature range in Figure 8e. The close to 12 h period corresponds to the period of both semidiurnal tides and near-inertial internal waves generated in the upper ocean around 82°N, by passing storms or by geostrophic adjustment of strong mesoscale structures [*Dosser et al.*, 2014]. Temperature and salinity variations in the 8–16 h bandwidth were extracted from the SBE37 data (Figure 8f). Salinity fluctuation amplitudes are below 0.006 g/kg most of the time except during the large melt events after 19 February where amplitudes larger than 0.05 g/kg are observed. Temperature fluctuations in this period range exceed 0.01°C for each melt event and even 0.35°C for the last event. This amplitude of 0.35°C corresponds approximately to an isotherm displacement of 15 m according to the last temperature profile (20 February 18:00: −1.15°C at 6 m and −0.70°C at 14 m).

In conclusion, the basal melt events until 21 February are associated with warming of the entire mixed layer when heat comes from the AW of the Svalbard Branch to the surface. Possible processes for the heat transfer from AW to the surface are discussed in section 4.2.

As observed in Fig. 3, basal melt is very active after February 21, when the only available data are that from SIMBA. SIMBA sensors do not have the accuracy of a SBE37 sensor and the sampling frequency was 3 h instead of 5 min. We cannot examine very high frequencies with the SIMBA data, however, we now show that we can get reliable information about the close to 12 h fluctuations. We produced three temperature time series out of the SIMBA profiles: two time series of the temperature averaged over 10 sensors around 3 and 4 m depth, and one time series of the temperature averaged over 75 sensors between 3 and 4.5 m. We applied an 8–16 h band-pass filter to the three temperature time series (Figure 8g). The three times series provide near 12 h fluctuations that are consistent with those extracted from the SBE37 data although with somewhat reduced amplitudes: variations near the 12 h period are observed during the melting events on 13, 16, and 20 February with similar amplitudes to those derived from the SBE37 during the first two small events and smaller amplitude on 20 February (Figure 8g). We now examine the full SIMBA time series.

4.2. Basal Ice-Melt Documented by SIMBA Data Until 15 March

Sea-ice melt is observed from 15 February to 2 March over the warm mixed layer of the Svalbard continental slope and estimated ocean to ice flux has a mean value of 100 W m^{-2} over those 2 weeks (Figures 9a

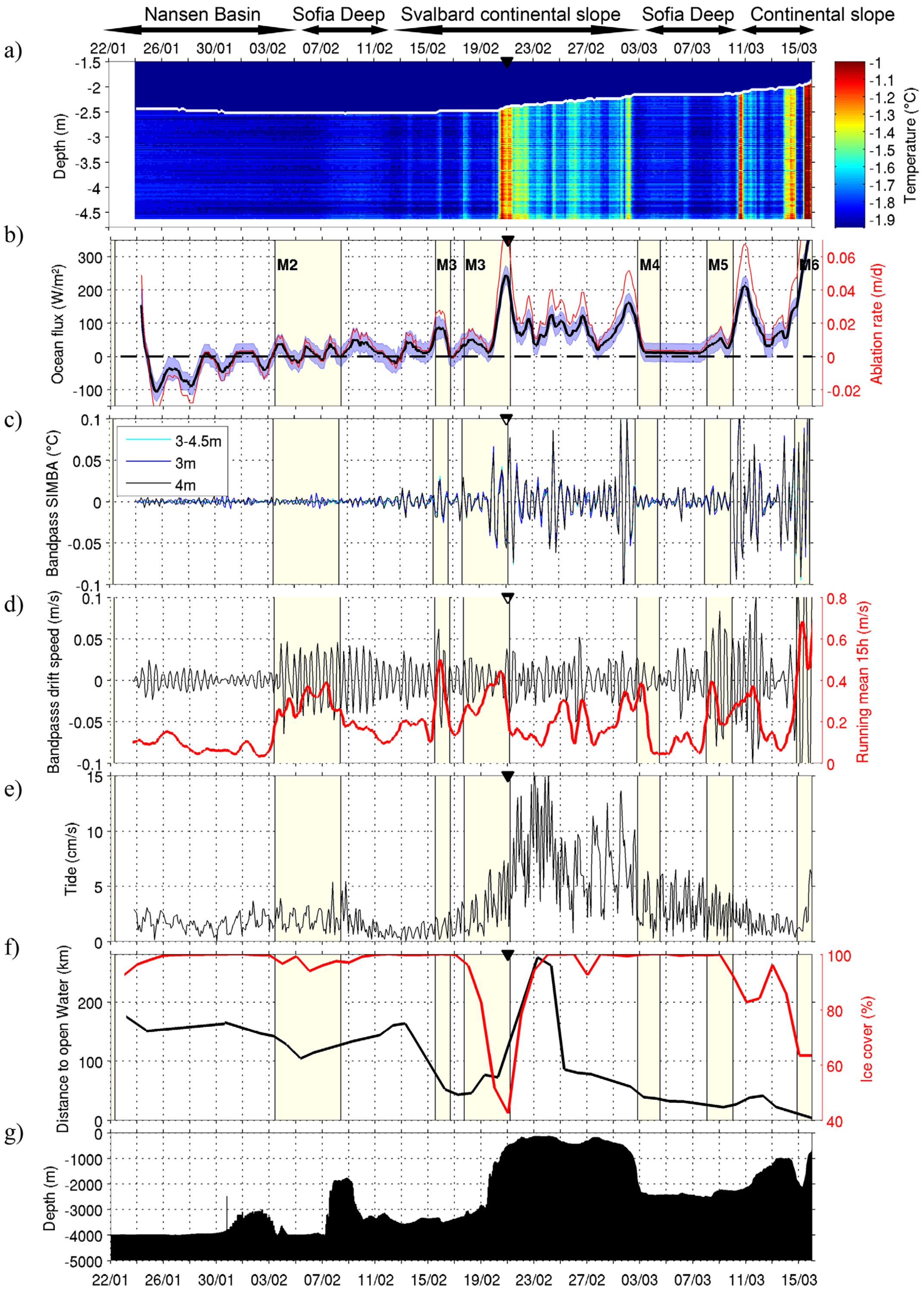

Figure 9. (a) SIMBA temperature zoomed on ocean from 22 January to 16 March. (b) Ocean flux (left axis, W m^{-2}) and ablation rate (right axis, m/d), at the ice/ocean interface deduced from the SIMBA data. Blue shaded area is the ocean heat flux uncertainty [*Provost et al.*, 2016]. The black triangle is the date after which there are no profiler data. (c) SIMBA temperature band-pass filtered between 8 and 16 h at 3 m (red), 4 m (blue) and averaged between 3 and 4.5 m (black). (d) Drift speed of IAOOS7 platform band-pass filtered between 8 and 16 h (left axis) and filtered using a 15 h running mean (right axis). (e) Tide velocity (m/s) from the AOTIM5 model [*Padman and Erofeeva*, 2004] colocated with the IAOOS7 platform drift. (f) Distance of SIMBA-2015h to open water (left axis) from *Itkin et al.* [2016] and colocated ice cover (%) from AMSR-2 (right axis). (g) Bathymetry along the track. Storm periods are shaded in light yellow.

and 9b). On 3 March, SIMBA drifts away from the continental slope (Figures 1 and 9d) and sea-ice melt stops as the under-ice water is at freezing temperature (−1.8°C, Figure 9a). Sea-ice melt resumes on 11 March, as the platforms drifts back over the continental slope and the shallow Svalbard Branch. A maximum sea-ice melt is observed at the end of the time series (15 March) as the platforms drifts southward over warm waters (around −1°C). The estimated heat flux then exceeds 350 W m^{-2} (Figure 9b). In 1 month, the SIMBA witnessed 71 cm of sea-ice basal melt.

In the SIMBA under-ice temperatures, large fluctuations with periodicities around 12 h and amplitudes reaching 0.1°C are observed and coincide with basal sea-ice melt (19 February to 2 March and 10–16 March) (Figures 9c and 9a). These large 12 h period fluctuations occur over rough topography (Figure 9g) and/or after large storms M5 and M6 (Figure 9c).

A variety of energy sources can generate near-inertial internal gravity waves with fluctuations close to 12 h, including atmospheric forcing [*Fer*, 2014], tides interacting over topography and geostrophic adjustment of mesoscale features [*Alford et al.*, 2016]. Amplitudes of near-surface temperature variations at the near-inertial wave frequency estimated from the SIMBA observations (Figure 9c) were compared to ice drift speeds (Figure 9d), barotropic tide velocity amplitudes (estimated using AOTIM-5 model outputs, *Padman and Erofeeva* [2004] as in Meyer et al., (submitted manuscript)) (Figure 9e), sea-ice concentration from AMSR2 (https://earthdata.nasa.gov), distance to ice edge (P. Itkin et al., Sea ice deformation from the buoy array: Identification of deformation events and comparison to other datasets (SEDNA, FRAMZY, atmosphere), submitted to *Journal of Geophysical Research*, 2016, Figure 9f), and seafloor roughness (Figure 9g) to get some insight into the mechanisms responsible for those 12 h near-surface temperature variations. Ice drift speed was decomposed into inertial ice speed using the same 8-16 h band pass filter and subinertial low frequency ice speed (Figure 9d). Large amplitudes in inertial ice drift velocities are observed during and just after M3, and the ice pack concentration falls to 40% (Figures 9d and 9f). The presence of leads and open water (lower ice concentration) and the proximity to the ice edge (Figure 9f) allow more direct transfer of energy from the atmosphere to the ocean, as observed during the second part of M3 and during M5 and M6 (Figure 9c). The fluctuations in temperature with amplitude larger than 0.1°C could be storm-induced inertial waves. They are generated over ice-free ocean and detected when the platform is near open waters (ice edge or leads). The 12 h fluctuation signature in under-ice temperature is modulated by the depth of the thermocline: when the thermocline is below the pycnocline as in the Nansen Basin there is no signature of inertial waves in under-ice temperature.

The large episodic 12 h temperature fluctuations from 21 February to 3 March are concomitant with large tides over shallow topography at a time when the ice edge is distant by over 200 km and sea-ice concentration is close to 100%. The barotropic tide interacting with the shallow bottom topography could induce near-inertial waves with the observed under-ice temperature signal. As described in *Rippeth et al.* [2015], large bathymetry gradients associated with large barotropic tides can cause enhanced vertical heat flux from the AW across the pynocline through near-inertial waves development.

Geostrophic adjustment of mesoscale features can also generate near-inertial waves [*Alford et al.*, 2016]. The largest 12 h under-ice temperature signal is observed over the maximum of gradient of the continental shelf (21 February, 3, 11, and 15 March, Figures 9g and 10), which corresponds with the offshore boundary of the Svalbard Branch (Figure 1).

The precise mechanisms that could have generated the near-inertial waves in the area are difficult to assess as tides, rough topography, and fronts are often concomitant when near-inertial wave signatures are recorded in the SIMBA and SBE37 data. Furthermore an internal wavefield is composed of both locally and remotely generated waves. The data do not permit to distinguish between locally generated downward propagating waves and remotely generated upward propagating waves. However, it seems that the wind has a major influence at the end of the time series when the platforms are in less compact ice, near leads or the ice edge, and that the tidal effects dominate from 10 February to 3 March.

5. Summary and Discussion

The deployment of IAOOS platforms during the N-ICE2015 campaign [*Granskog et al.*, 2016] provided new insights on winter conditions in an area historically poorly sampled during that season (Meyer et al., submitted manuscript).

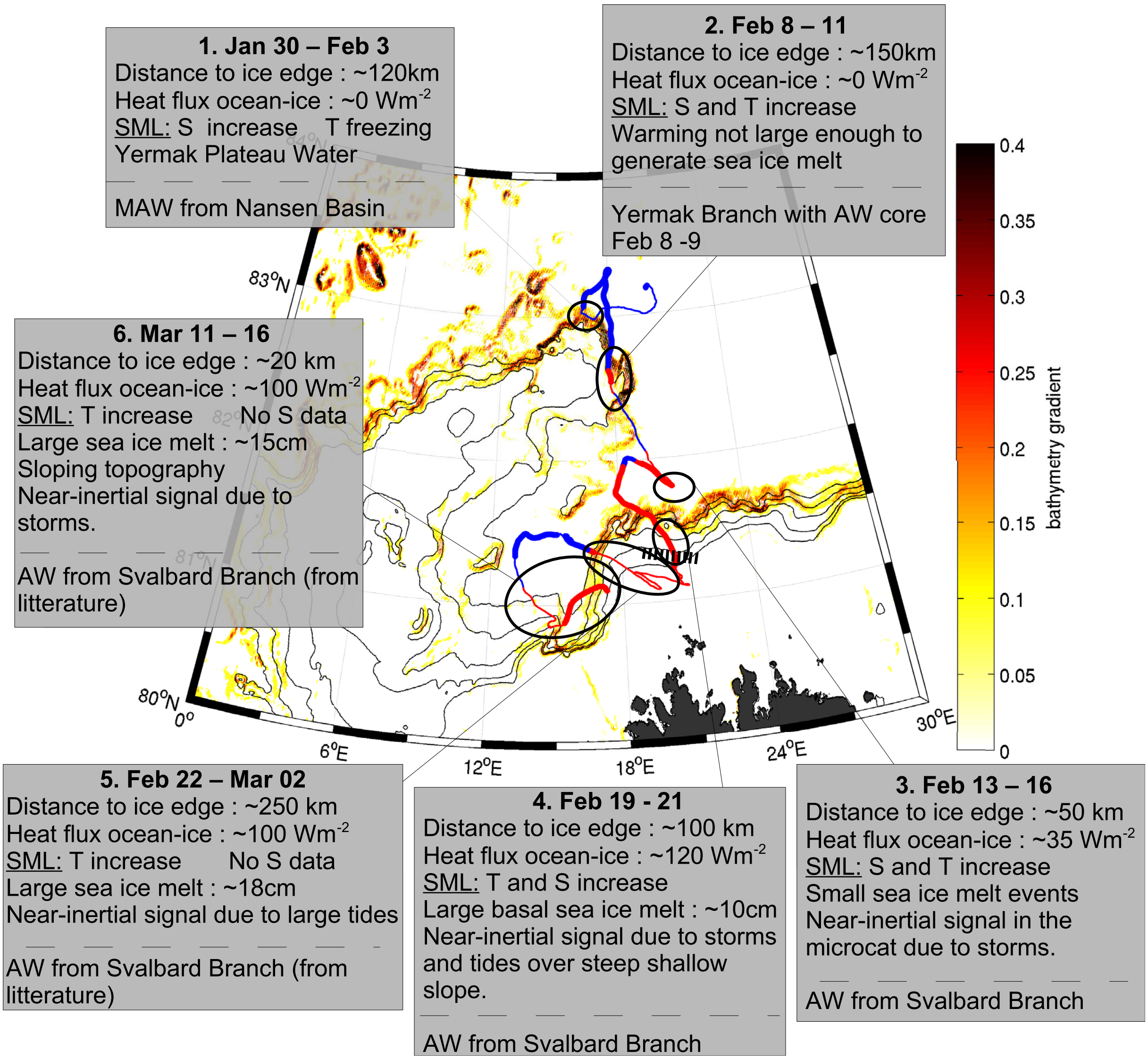

1. Jan 30 – Feb 3
Distance to ice edge : ~120km
Heat flux ocean-ice : ~0 Wm^{-2}
SML: S increase T freezing
Yermak Plateau Water

MAW from Nansen Basin

2. Feb 8 – 11
Distance to ice edge : ~150km
Heat flux ocean-ice : ~0 Wm^{-2}
SML: S and T increase
Warming not large enough to generate sea ice melt

Yermak Branch with AW core Feb 8 -9

3. Feb 13 – 16
Distance to ice edge : ~50 km
Heat flux ocean-ice : ~35 Wm^{-2}
SML: S and T increase
Small sea ice melt events
Near-inertial signal in the microcat due to storms.

AW from Svalbard Branch

4. Feb 19 - 21
Distance to ice edge : ~100 km
Heat flux ocean-ice : ~120 Wm^{-2}
SML: T and S increase
Large basal sea ice melt : ~10cm
Near-inertial signal due to storms and tides over steep shallow slope.

AW from Svalbard Branch

5. Feb 22 – Mar 02
Distance to ice edge : ~250 km
Heat flux ocean-ice : ~100 Wm^{-2}
SML: T increase No S data
Large sea ice melt : ~18cm
Near-inertial signal due to large tides

AW from Svalbard Branch (from litterature)

6. Mar 11 – 16
Distance to ice edge : ~20 km
Heat flux ocean-ice : ~100 Wm^{-2}
SML: T increase No S data
Large sea ice melt : ~15cm
Sloping topography
Near-inertial signal due to storms.

AW from Svalbard Branch (from litterature)

Figure 10. Summary of the study. Background is the bathymetry gradient amplitude (without units). Black contours are 0, 500, 700, 1000, 1500, and 2000 m depths. The drift trajectory is red when Floe 1 drifted over Atlantic Waters, and blue when Floe 1 drifted over the Modified Atlantic Waters. The trajectory is thick during storms and thin otherwise. The black dashed line (around 81.2°N, 20°E) in the map indicates the location of Floe 1 breakup when R/V Lance left and IAOOS7 continued drifting alone. The gray plots describe the ice-ocean interface and the warm water layer at several key locations. The dashed line in the panel separate comments on the surface (top part) and on the deep warm waters (bottom part).

The three regions crossed by Floe 1, the Nansen Basin, the Sofia Deep, and the Svalbard continental slope (Figures 7 and 10) presented distinct hydrographic conditions and ice-ocean interactions.

1. In the Nansen Basin the warm layer was deep, quiescent with layering in agreement with a description by *Rudels et al*. [2000] and capped by a stepped halocline due to local ice formation after summer melt as described in *Kikuchi et al*. [2004]. Ice was forming in the Nansen Basin as SIMBA-derived ocean-to-ice fluxes were negative and the upper layer salinity was larger than previously observed by 0.1 g/kg. A possible explanation for this larger salinity is that, in an Arctic region with thinner ice and leads, new-ice would grow faster in winter and salt release would be more important [*Ivanov et al*., 2016].
2. Over the Svalbard continental slope, the warm AW from the Svalbard Branch was only 20–40 m from the sea surface. Profiler observations documented an ~70 km AW extension offshore the 500 m isobath and an offshore deepening of the AW over the continental slope. They were supportive of offshore AW eddy

shedding as recently documented further east (30°E) with velocity observations by *Våge et al*. [2016]. The lateral extension and mesoscale activity may be only winter features as the Atlantic Water inflow is seasonally variable with a larger transport in winter [*Hattermann et al*., 2016] (Z. Koenig et al., Atlantic Waters inflow north of Svalbard: insights from IAOOS observations and Mercator Ocean global operational system during N-ICE2015, submitted to *Journal of Geophysical Research*, 2016). SIMBA documented very large ocean surface temperature on the shelf and large sea-ice basal melt. Mixed layer temperatures were large because of enhanced local vertical heat fluxes from AW possibly due to: tides, mesoscale features, vertical convection during overturning events, steep bathymetry, or wind forcing near the ice edge and over leads.

3. In the Sofia Deep, the range of warm water characteristics was large and suggested different processes and water paths (Figures 7 and 10): upwelling of deep fresher water into the AW layer as possibly linked to tidal activity over rough topography [*Luneva et al*., 2015], mesoscale structures with AW cores from the Yermak Branch, the Svalbard Branch, or coming from the Yermak Pass (a passage through the Yermak Plateau deeper than 700 m at 81°N) [*Gascard et al*., 1995; *Rudels et al*., 2000] (Figure 7). High-resolution operational model outputs analyzed in a companion paper (Koenig et al., submitted manuscript) support these interpretations in terms of warm water paths and eddy activity.

The mixed layer was at the freezing temperature except above the Yermak Plateau slope and above the Svalbard Branch (Figure 10). The salty surface mixed layer located on the deep edge of the Yermak Plateau probably originates from the Yermak Plateau (Meyer et al., submitted manuscript). Operational model outputs confirm the difference in salinity between the salty Yermak Plateau and the fresh Nansen Basin mixed layers in winter (Koenig et al., submitted manuscript). The under-ice temperature, slightly above freezing over the deep slope of the Yermak Plateau, did not generate significant melt. In contrast, the thin and warm mixed layer above the Svalbard continental slope resulted in significant sea-ice melt in the middle of winter (Figure 10). The warming of the under-ice ocean is clearly visible in the SIMBA data. Near-inertial fluctuations in the under-ice temperature records suggest that near-inertial gravity waves bring heat from the shallow AW inflow up to the surface. However, the deep expression of the near-inertial signal could not be examined with the 12 h sampling of the IAOOS profiler during N-ICE2015. A higher sampling rate should be used in the future to enable studies like those by *Dosser et al*. [2014] or *Dosser and Rainville* [2016]. Near-inertial waves in the upper ocean formed over the Svalbard Branch could be caused by several mechanisms: tides interacting with topography, storms and mesoscale features. The largest near-inertial signal was observed close to the ice edge (Figure 10), in less packed ice, as the wind could directly force the ocean. In the changing Arctic, with more ice-free area and leads [*Willmes and Heinemann*, 2016], an increase in near-inertial waves is expected [*Dosser and Rainville*, 2016] potentially bringing heat up to the surface and promoting sea-ice melt.

In situ observations of large sea-ice basal melt (more than 71 cm in less than 2 months) over the Svalbard continental slope caused by heat coming from the Atlantic Water confirmed previous influences from theoretical considerations and indirect data [e.g., *Rudels et al*., 1996; *Ivanov et al*., 2016]. Large ocean-to-ice heat flux is a main process responsible for the sea-ice melt in winter north of Svalbard.

We showed that the easy-to-deploy SIMBA instrument can capture some near-inertial signals in the under-ice ocean temperatures. The deployment of a SIMBA network in the Arctic with a high-frequency sampling combined with current data would improve the monitoring of the near-inertial wavefield at a time when the Arctic is rapidly changing.

Acknowledgments
We thank Michel Calzas, Christine Drezen, Magali Garracio, Antoine Guillot, Jean-Luc Maria, Vincent Mariage, Jacques Pelon, and Jean-Philippe Savy for their contribution to the IAOOS platform preparation and tests. We also thank Ilker Fer, Mats Granskog, and Arild Sundfjord for their most valuable comments on the manuscript. This work was supported by the Equipex IAOOS (Ice Atmosphere Ocean Observing System) (ANR-10-EQPX-32-01), and by funding from the ICE-ARC program from the European Union 7th Framework Progamme grant number 603887. Z. Koenig acknowledges a PhD scholarship from Université Pierre et Marie Curie (UPMC). This work has been supported by the Norwegian Polar Institute's Centre for Ice, Climate and Ecosystems (ICE) through the N-ICE project. N-ICE acknowledges the in-kind contributions provided by other national and international projects and participating institutions, through personnel, equipment, and other support. The IAOOS platforms data are available at LOCEAN (Christine Provost, cp@locean-ipsl.upmc.fr).

References

Aagaard, K., A. Foldvik, and S. R. Hillman (1987), The West Spitsbergen Current: Disposition and water mass transformation. *J. Geophys. Res.*, *92*(C4), 3778–3784.

Alford, M. H., J. A. MacKinnon, H. L. Simmons, and J. D. Nash (2016), Near-inertial internal gravity waves in the ocean, *Ann. Rev. Mar. Sci.*, *8*, 95–123, doi:10.1146/annurev-marine 010814-015746.

Cokelet, E. D., N. Tervalon, and J. G. Bellingham (2008), Hydrography of the West Spitsbergen Current, Svalbard Branch: Autumn 2001, *J. Geophys. Res.*, *113*, C01006, doi:10.1029/2007JC004150.

Comiso, J. C. (2012), Large decadal decline of the Arctic multiyear ice cover, *J. Clim.*, *25*(4), 1176–1193, doi:10.1175/JCLI-D-11-00113.1

Dosser, H. V., and L. Rainville (2016), Dynamics of the changing near-inertial internal wave field in the Arctic Ocean, *J. Phys. Oceanogr.*, *46*, 395–415, doi:10.1175/JPO-D-15-0056.1.

Dosser, H. V., L. Rainville, and J. M. Toole (2014), Near inertial internal wave field in the Canada Basin from ice-tethered profilers, *J. Phys. Oceanogr.*, *44*, 413–426, doi:10.1175/JPO-D-13-0117.1.

Fer, I. (2009), Weak vertical diffusion allows maintenance of cold halocline in the central Arctic, *Atmos. Oceanic Sci. Lett.*, *2*(3), 148–152.

Fer, I. (2014), Near-inertial mixing in the central Arctic Ocean. *J. Phys. Oceanogr.*, *44*(8), 2031–2049, doi:10.1175/JPO-D-13-0133.1.

Gascard, J.-C., C. Richez, and C. Rouault (1995), New insights on large-scale oceanography in Fram Strait: The West Spitsbergen Current, in *Arctic Oceanography, Marginal Ice Zones and Continental Shelves*, vol. 49, edited by W. O. Smith, Jr. and J. M. Greibmeier, pp. 131–182, AGU, Washington, D. C.

Gill, A. E. (1982), *Atmosphere-Ocean Dynamics*, vol. 30, Academic, N. Y.

Granskog, M. A., P. Assmy, S. Gerland, G. Spreen, H. Steen, and L. H. Smedsrud (2016), Arctic research on thin ice: Consequences of Arctic sea ice loss, *Eos*, *97*, 22–26, doi:10.1029/2016EO044097.9.

Hattermann, T., P. E. Isachsen, W.-J. von Appen, J. Albretsen, and A. Sundfjord (2016), Eddy-driven recirculation of Atlantic Water in Fram Strait, *Geophys. Res. Lett.*, *43*, 3406–3414, doi:10.1002/2016GL068323.

Hudson, S., and L. Cohen (2015), *N-ICE2015 Surface Meteorology v1*. Norwegian Pol. Inst., Tromsø, Norway. [Available at https://data.npolar.no/dataset/056a61d1-d089-483a-a256-081de4f3308d.]

Ivanov, V. V., V. A. Alexeev, I. A. Repina, N. V. Koldunov, and A. V. Smirnov (2012), Tracing Atlantic Water signature in the Arctic sea ice cover east of Svalbard, *Adv. Meteorol.*, *2012*, 201818, doi:10.1155/2012/201818.

Ivanov, V., V. Alexeev, N. Koldunov, I. Repina, A. Sandø, L. Smedsrud, and A. Smirnov (2016), Arctic Ocean heat impact on regional ice decay—A suggested positive feedback, *J. Phys. Oceanogr.*, *46*, 1437–1456, doi:10.1175/JPO-D-15-0144.1.

Jackson, K., J. Wilkinson, T. Maksym, D. Meldrum, J. Beckers, C. Haas, and D. Mackenzie (2013), A novel and low-coast sea ice mass balance buoy, *J. Atmos. Oceanic Technol.*, *30*, 2676–2688, doi:10.1175/JTECH-D-13-00058.1.

Kikuchi, T., K. Hatakeyama, and J. H. Morison (2004), Distribution of convective Lower Halocline Water in the eastern Arctic Ocean, *J. Geophys. Res.*, *109*, C12030, doi:10.1029/2003JC002223.

Kikuchi, T., J. Inoue, and D. Langevin (2007), Argo-type profiling float observations under the Arctic multiyear ice, *Deep Sea Res., Part I*, *54*(9), 1675–1686.

Krishfield, R., J. Toole, A. Proshutinsky, and M. L. Timmermans (2008), Automated ice-tethered profilers for seawater observations under pack ice in all seasons, *J. Atmos. Oceanic Technol.*, *25*(11), 2091–2105, doi:10.1175/2008JTECHO587.1.

Luneva, M. V., Y. Aksenov, J.D. Harle, and J. T. Holt (2015), The effects of tides on the water mass mixing and sea ice in the Arctic Ocean, *J. Geophys. Res.*, *120*, 6669–6699, doi:10.1002/2014JC01310.

Manley, T. O. (1995), Branching of Atlantic Water within the Greenland-Spitsbergen passage: An estimate of recirculation, *J. Geophys. Res.*, *100*(C10), 20,627–20,634.

Manley, T. O., R. H. Bourke, and K. L. Hunkins (1992), Near-surface circulation over the Yermak Plateau in northern Fram Strait, *J. Mar. Syst.*, *3*(1), 107–125.

Mariage, V. (2015), *Développement et mise en œuvre de LiDAR embarqués sur bouées dérivantes pour l'étude des propriétés des aérosols et des nuages en Arctique et des forçages radiatifs induits*, UPMC, Villeurbanne, France. [Available at https://hal-insu.archives-ouvertes.fr/tel-01264610.]

Mariage, V., et al. (2016), IAOOS microlidar-on-buoy development and first atmospheric observations obtained during 2014 and 2015 arctic drifts, *Opt. Express.*, *119*, 4 pp.

McDougall, T. J., D. R. Jackett, F. J. Millero, R. Pawlowicz, and P. M. Barker (2012), A global algorithm for estimating Absolute Salinity, *Ocean Sci.*, *8*, 1123–1134.

Mc Phee, M. G., T. Kikuchi, J. H. Morison, and T. P. Stanton (2003), Ocean-to-ice flux at the North Pole environmental Observatory, *Geophys. Res. Lett.*, *30*(24), 2274, doi:10.1029/2003GL018580.

Muench, R. D., M. G. McPhee, C. A. Paulson, and J. H. Morison (1992), Winter oceanographic conditions in the Fram Strait-Yermak Plateau region, *J. Geophys. Res.*, *97*(C3), 3469–3483.

Onarheim, I. H., L. H. Smedsrud, R. B. Ingvaldsen, and F. Nilsen (2014), Loss of sea ice during winter north of Svalbard, *Tellus, Ser. A*, *66*, 23933, doi:10.3402/tellusa.v66.23933.

Padman, L., and S. Erofeeva (2004), A barotropic inverse tidal model for the Arctic Ocean, *Geophys. Res. Lett.*, *31*, L02303, doi:10.1029/2003GL019003.

Provost, C., et al. (2015), IAOOS (Ice-Atmosphere-Arctic Ocean Observing System, 2011–2019), *Mercator Ocean Quart. Newsl.*, *51*, 13–15. [Available at http://www.mercator-ocean.fr/eng/actualitesagenda/newsletter/newsletter-Newsletter-51-Special-Issue-with-ICE-ARC.]

Quadfasel, D., J. C. Gascard, and K. P. Koltermann (1987), Large scale oceanography in Fram Strait during the 1984 Marginal Ice-Zone Experiment. *J. Geophys. Res.*, *92*(C7), 6719–6728.

Rippeth, T. P., B. J. Lincoln, Y. D. Lenn, J. M. Green, A. Sundfjord, and S. Bacon (2015), Tide-mediated warming of Arctic halocline by Atlantic heat fluxes over rough topography, *Nat. Geosci.*, *8*(3), 191–194, doi:10.1038/ngeo2350.

Rudels, B. (2016), Arctic Ocean Stability: The effects of local cooling, oceanic heat transport, freshwater input and sea ice melt with special emphasis on the Nansen Basin, *J. Geophys. Res.Oceans*, *121*, 4450–4473, doi:10.1002/2015JC011045.

Rudels, B., L. G. Anderson, and E. P. Jones (1996), Formation and evolution of the surface mixed layer and the halocline of the Arctic Ocean, *J. Geophys. Res.*, *101*(C4), 8807–8821.

Rudels, B., R. Meyer, E. Fahrbach, V. V. Ivanov, S. Østerhus, D. Quadfasel, U. Schauer, V. Tverberg, and R. A. Woodgate (2000), Water mass distribution in Fram Strait and over the Yermak Plateau in summer 1997, *Ann. Geophys.*, *18*(6), 687–705.

Rudels, B., M. Korhonen, U. Schauer, S. Pisarev, B. Rabe, and A. Wisotzki (2015), Circulation and transformation of Atlantic water in the Eurasian Basin and the contribution of Fram Strait inflow branch to the Arctic Ocean heat budget, *Prog. Oceanogr.*, *132*, 128–152, doi:10.1016/j.pocean.2014.04.003.

Schauer, U., A. Beszczynska-Möller, W. Walczowski, E. Fahrbach, J. Piechura, and E. Hansen (2008), Variations of measured heat flow through the Fram Strait between 1997 and 2006, in *Arctic- Subarctic Ocean Fluxes: Defining the Role of the Northern Seas in Climate*, edited by R. R. Dickson, J. Meincke, and P. Rhines, pp. 65–85, Springer Sci, Amsterdam, Netherlands.

Sirevaag, A., and I. Fer (2009), Early spring oceanic heat fluxes and mixing observed from drift stations north of Svalbard, *J. Phys. Oceanogr.*, *39*(12), 3049–3069, doi:10.1175/2009JPO4172.1.

Sirevaag, A., S. D. L. Rosa, I. Fer, M. Nicolaus, M. Tjernström, and M. G. McPhee (2011), Mixing, heat fluxes and heat content evolution of the Arctic Ocean mixed layer, *Ocean Sci.*, *7*(3), 335–349, doi:10.5194/os-7-335-2011.

Steele, M., and J. Morison (1993), Hydrography and vertical fluxes of heat and salt northeast of Svalbard in Autumn, *J. Geophys. Res.*, *98*(C6), 10,013–10,024.

Timmermans, M. L., S. Cole. and J. Toole (2012), Horizontal density structure and restratification of the Arctic Ocean surface layer, *J. Phys. Oceanogr.*, *42*(4), 659–668.

Toole, J. M., M.-L. Timmermans, D. K. Perovich, R. A. Krishfield, A. Proshutinsky, and J. A. Richter-Menge (2010), Influences of the ocean surface mixed layer and thermohaline stratification on Arctic Sea ice in the central Canada Basin, *J. Geophys. Res.*, *115*, C10018, doi: 10.1029/2009JC005660.

Våge, K., R. S. Pickart, V. Pavlov, P. Lin, D. J. Torres, R. Ingvaldsen, A. Sundfjord, and A. Proshutinsky (2016), The Atlantic Water boundary current in the Nansen Basin: Transport and mechanisms of lateral exchange, *J. Geophys. Res. Oceans*, *121*, doi:10.1002/2016JC011715.

Widell, K., I. Fer, and P. M. Haugan (2006), Salt release from warming sea ice, *Geophys. Res. Lett.*, *33*, L12501, doi:10.1029/2006GL026262.

Willmes, S., and G. Heinemann, G. (2016), Sea-ice wintertime lead frequencies and regional characteristics in the Arctic, 2003–2015, *Remote Sens.*, *8*(1), 4, doi:10.3390/rs8010004.

2.3 The N-ICE2015 special issue

Profiler and IMB data from the IAOOS platforms presented in the previous study have been used in several studies published in the N-ICE2015 special issue in *Journal of Geophysical Research Ocean*. I am co-authoring two of them: *Provost et al.* (2017) and *Meyer et al.* (2017a), their full text is in the Appendix. In these studies, the IAOOS team I am part of provided the IAOOS profiler data and I participated in the scientific discussions, writing and corrections of each manuscript. I will present here some perspectives on how this unique dataset was used in other studies, and some complementary process studies to *Koenig et al.* (2016).

2.3.1 Hydrography and currents North of Svalbard from January to June

Duing Floe 1, only one deep CTD cast per week was performed, and the MSS (microstructure sensor) only sampled the upper 150 m. The IAOOS profiler observations, with 2 profiles per day down to 500-800m, were used to complement the CTD and MSS data in winter, especially at depth in the Atlantic Water core. *Meyer et al.* (2017a) presented the general hydrography during N-ICE2015 compiling all the available datasets from January to June 2015, one of which the IAOOS profiler data in winter. I will present here some salient results of this study.

Meyer et al. (2017a) compared the hydrographic data from N-ICE2015 with the climatology MIMOC (global Monthly Isopycnal Mixed-layer Ocean Climatology, Figure 2.2), which nicely complements *Koenig et al.* (2016) where comparison with climatology is only mentioned. In January, the MIMOC climatology in the area north of Svalbard is based on less than 10 profiles, while it is based on more than 40 profiles in March and 70 in May. Compared to the climatology, the Atlantic water layer is warmer, more saline and shallower in the N-ICE2015 dataset. This is particularly true over the Nansen Basin and the northern tip of the Yermak Plateau, area sampled in winter during the N-ICE2015 expedition. The surface mixed layer is more saline in winter and early spring, which could be caused by the larger sea ice formation during winter 2015 releasing brines in the upper water column. In late spring, the sea ice melts over the Yermak Plateau, creating a fresh surface layer in the N-ICE2015 data which is not captured in the climatology. The climatology does not represent accurately the hydrography north of Svalbard in winter. Hydrographic data recorded by the IAOOS platforms complement the sparse winter Arctic ocean dataset and can be used to improve climatologies that are used in model initialization.

Meyer et al. (2017a) also examined the current data provided by the ship-based ADCP, which are a good complement to the IAOOS platforms that measure temperature, salinity and dissolved oxygen (Figure 2.3). The structure of the current is mainly barotropic, except during storms. In the Nansen Basin, mean current

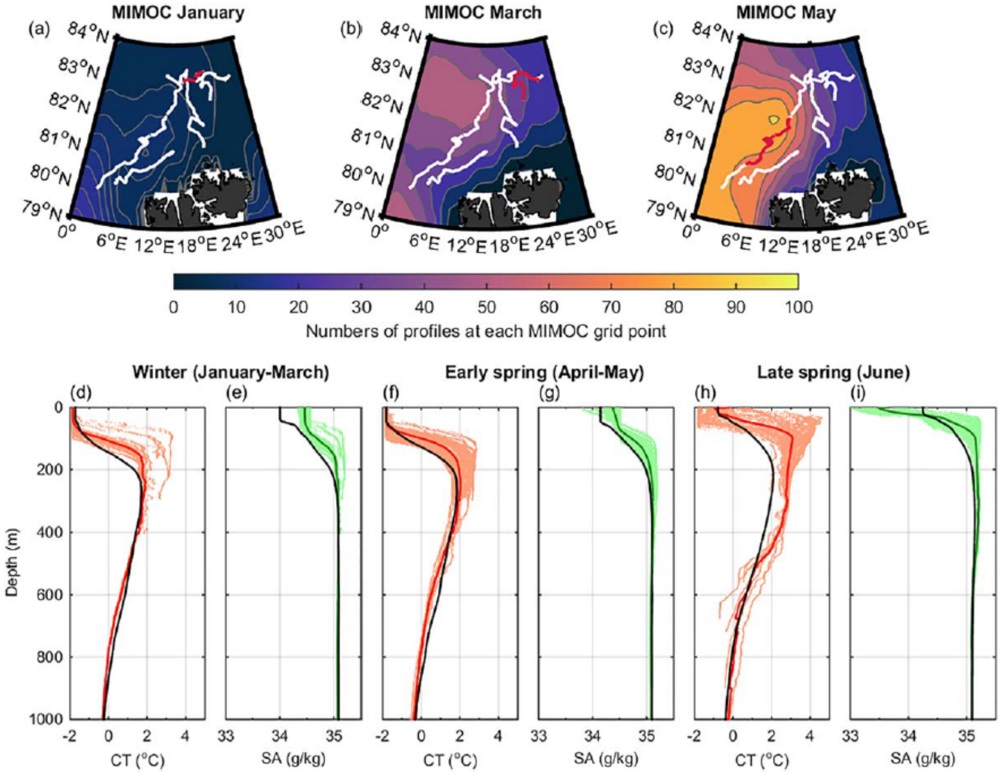

Figure 2.2: *Maps with the number of profiles at each grid point of the MIMOC climatology for the month of January with contour intervals every two profiles (a), March with contour intervals every ten profiles (b), and May with contour intervals every ten profiles (c). Overlay in white are the drift tracks of the N-ICE2015 expedition and in pink the respective drift sections for the shown month. Mean vertical profiles of conservative temperature (CT) and absolute salinity (SA) from the N-ICE2015 expedition observations (color) and from MIMOC climatology (black), for winter (d-e), early spring (f-g) and late spring (h-i). Data above* 300m *include microstructure profilers and ship-board CTD. Data below* 300m *is from the ship-boad CTD only. From Meyer et al. (2017a).*

is very weak, 0.02m/s with no preferential direction, and reaches 0.20m/s flowing northeast on the Svalbard continental shelf during Floe 1. On the southwest part of the Yermak Plateau, current is orientated west and north-west, mean of 0.11m/s during Floe 3 and 0.17m/s during Floe 4 (summer floes). It corresponds to the Svalbard Branch. The mean current curls around the northern tip of the Yermak Plateau, which is the signature of the Yermak Branch. These observations confirm that warm Atlantic Water found at depth in *Koenig et al.* (2016) over the continental slope is part of the Svalbard Branch and that the patch of warm Atlantic Water over the Yermak Plateau is probably linked to the Yermak Branch. Unfortunately, ship ADCP did not record current on the last part of the drift of the IAOOS platform in March along the continental slope north of Svalbard where much of the sea ice melt occurs once *R/V Lance* had to relocate. It would have been interesting to examine if during the melting events the Atlantic Water inflow was weak or strong compared to the average, and if there is a correlation between the Atlantic Water current speed and the sea ice melt intensity.

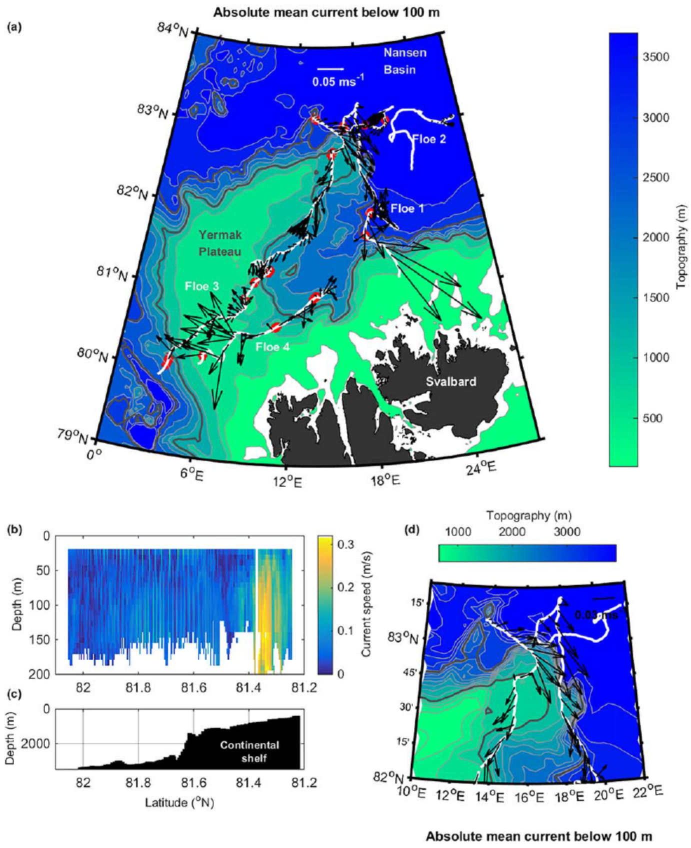

Figure 2.3: *(a) Mean absolute ocean currents below 100m depth from available Vessel-Mounted ADCP data overlaying topographic contours ranging from 100 to* 4000*m at* 400*m intervals (color). Red sections along drift tracks correspond to areas where estimated tidal speed dominates observed absolute current speed. (b) Section plot of residual current speed while drifting onto the continental shelf at the end of Floe 1 (Vessel-Mounted ADCP data). (c) Corresponding underlying topography. (d) Mean absolute currents at the northern tip of the Yermak Plateau below 100m depth from available Vessel-Mounted ADCP data overlaying topographic contours at* 200*m intervals (color). In both (a) and (d) the* 3000*m and* 1500*m isobaths are shown as thick grey lines while the trajectories of Floe 1 and 3 are indicated with white lines. From Meyer et al. (2017a).*

2.3.2 Heat fluxes at the sea ice-ocean interface

The Ice Mass Balance (IMB) from IAOOS platforms provided estimates of heat fluxes at the sea ice-ocean interface (*Provost et al.*, 2017). The Ice Mass Balance under-ice ocean temperature time series suggest the existence of near inertial gravity waves that melted the sea ice in winter (*Koenig et al.*, 2016). However the temperature sensor of the IMB is not very accurate and its time resolution is only 3h. It would be interesting to examine other datasets with larger temporal resolution and see if they provide similar results as those deduced from the IAOOS platforms.

Mixing across the thermocline and at the sea ice - ocean interface has been quantified during the N-ICE2015 experiment. *Meyer et al.* (2017b) observed large heat fluxes exceeding $300 W.m^{-2}$ in the late spring close to the surface over the Yermak Plateau. Mixing is enhanced over the steep topography of the Yermak Plateau. They concluded that it is the combination of storms and shallow Atlantic Water that leads to the highest heat flux rates found all along the 4 drifts of N-ICE2015 experiment (Figure 2.4).

Peterson et al. (2017) documented the under-ice ocean from January to June 2015 during the four floes of the N-ICE2015 expedition with a Turbulence Cluster Instrument (TIC). They observed weak ocean heat fluxes at the ice-ocean interface in winter over the Nansen Basin that increased during storms. Heat fluxes in winter are small compared to *Koenig et al.* (2016) (no more than $100 W.m^{-2}$ compare to $350 W.m^{-2}$) because they did not sample the continental slope north of Svalbard. Indeed, Floe 1 broke before reaching the continental slope (end of February) and the *R/V Lance* had to relocated, while the IAOOS platform kept drifting over the Svalbard continental slope for another month. Over the Yermak Plateau in summer, mean heat fluxes are around $100 W.m^{-2}$, and reach $350 W.m^{-2}$ during storms and over the continental slope where the Atlantic Water is close to the surface. These large heat fluxes are concomitant with rapid sea ice melting. This is in agreement with the ice - ocean heat fluxes deduced from the IMB during the large melting events over the Svalbard continental slope in winter (*Koenig et al.*, 2016; *Provost et al.*, 2017).

All the datasets from the N-ICE2015 expedition highlight the crucial role of the Atlantic Water in the sea ice melt in the Arctic, in summer as well as in winter. The basal melt of the sea ice has important implications on the sea ice state, with for instance the formation of snow ice as explained in the next subsection.

2.3.3 Snow ice formation

IAOOS platforms are equipped with an Ice Mass Balance (IMB) which enables computing sensible heat fluxes, latent heat fluxes and the heat fluxes at the ice-ocean interface, presented in *Koenig et al.* (2016) (*Provost et al.*, 2017). During

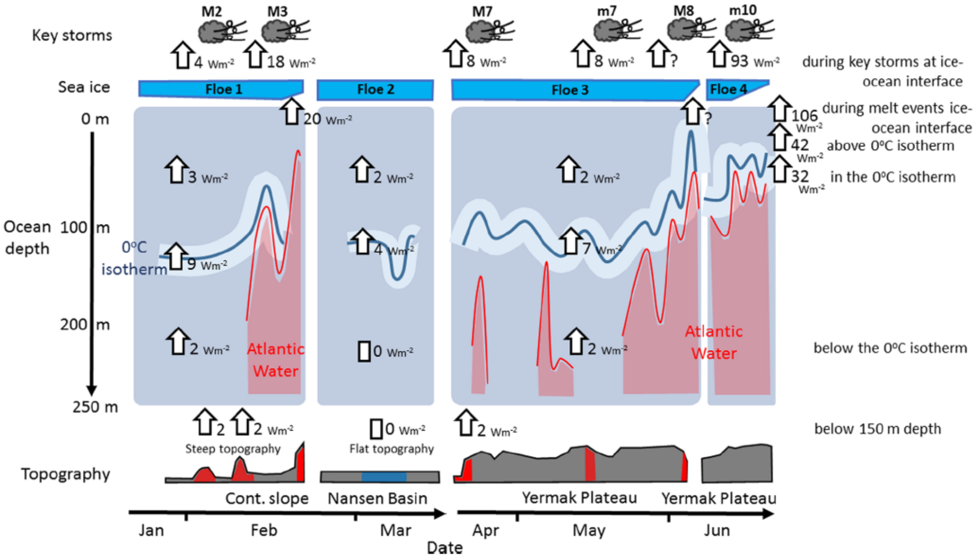

Figure 2.4: *Schematic of ocean heat flux estimates on various time and spatial scales during the N-ICE2015 campaign. Clouds indicate key storms and associated mean heat flux at the ice-ocean interface (1m depth from TIC data). The thinning of blue blocks indicate large basal ice melt events and associated mean heat flux in the ice-ocean interface are shown. In the ocean, the blue line shows the 0°C isotherm depth and associated mean heat flux within a 50m window centered on it. Mean heat flux (from MSS data) above and below the 0°C isotherm layer are indicated for each floe. Vertical distribution of Atlantic Water is indicated by red shading. Topography is shown in gray with steep regions highlighted in red and flat regions in blue; associated mean heat flux below 150m depth for steep and flat sections are indicated. Question marks indicate events during which heat flux estimates are not available. From Meyer et al. (2017b).*

Floe 1, a total of 7 IMBs were deployed in a 20km radius around the ice camp. The N-ICE2015 floes were characterized by a large amount of snow which is not typical of the area. Large amount of snow and negative freeboard in winter 2015 made flooding and snow ice formation possible and these processes were documented by 4 of the 7 IMBs (Figure 2.5), (*Provost et al.*, 2017).

Two processes were suggested to form snow ice in *Provost et al.* (2017). First, flooding happens just after a break-up of snow loaded floes. The ice is cold and not permeable, the flooding is quick and probably due to lateral intrusion of seawater which leads to slush and snow-ice layers at freezing temperature (Figure 2.5, SIMBA 2015f and SIMBA 2015i). Other floodings happen after loss of buoyancy due to basal sea ice melt in winter. Along the continental slope north of Svalbard, heat fluxes from the warm Atlantic Water to the sea ice peak at more than $400 W.m^{-2}$, warming

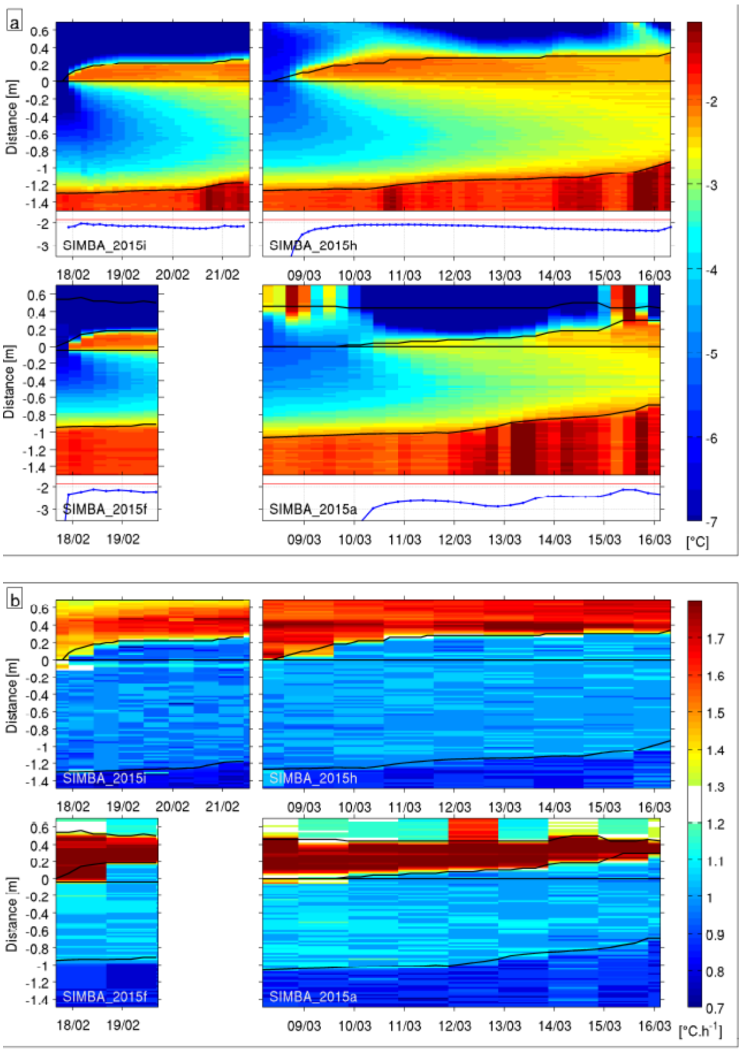

Figure 2.5: a) Close-up of temperature profiles (°C) during periods of flooding and snow-ice formation. Temperature scale is non-linear. The blue curve below corresponds to the averaged temperature values between real-time and initial snow/ice interface. Red line is ocean-freezing temperature. b) Close-up of diffusivity proxy profiles (°C) during periods of slush/snow-ice formation. The black curve below corresponds to the flooded snow thickness, the blue (red) curve to the part that solidified into snow-ice due to conductive fluxes through the ice (ice and snow). Y-axis is vertical distance (in m) referenced to the initial ice-snow interface. Vertical resolution is 2 cm. Black isolines from top to bottom represent air/snow interface, initial snow/ice interface and ice/ocean interface. Green isolines represent snow/ice interface evolution. From Provost et al. (2017).

the sea ice. This warm ice is permeable, flooding is slow with vertical intrusions of brines, and creates a colder slush and snow ice ($-3°C$) (Figure 2.5, SIMBA 2015f and SIMBA 2015h and SIMBA 2015a). A summary of the processes is presented in Figure 2.6.

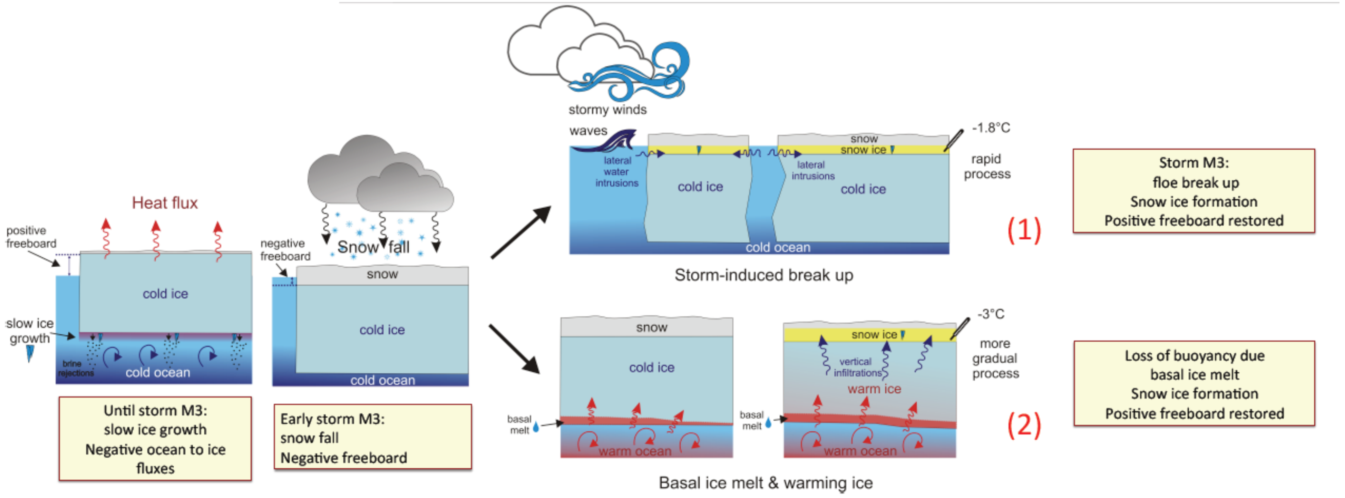

Figure 2.6: *Schematic of the two processes that forms snow ice during Floe 1 of N-ICE2017. From Provost et al. (2016).*

This study is the first documentation of significant flooding and snow ice formation in the high Arctic. It may become more frequent in a thinner Arctic with an increase in snow precipitation. The Arctic sea ice could become similar to Antarctic sea ice, with a large amount of snow ice (*Provost et al.*, 2017).

CHAPTER 3

Atlantic Water in an operational model north of Svalbard: pathways and properties

Contents

3.1 Introduction

Since the Arctic Ocean is difficult to monitor, ocean models are a very useful tool to study this ocean. The atmosphere - sea ice - ocean coupled models can be divided in 2 main categories:

- Models without data assimilation (*Aksenov et al.*, 2010a,b)
- Models with assimilation of *in situ* data (e.g. Mercator Ocean in France) (*Lellouche et al.*, 2012). However most of these models do not assimilate ocean observations under the ice and hence assimilate very few observations in the Arctic.

Ilıcak et al. (2016) compared the Atlantic Water layer in the Arctic Ocean in 15 different models without assimilation. Large discrepancies are observed in the Atlantic Water inflow and the models generally show large differences compared to the observed temperature at intermediate depths. The assimilation of *in situ* observations (very few in the Arctic) improves the Artic Ocean properties and circulation by improving the Atlantic and Pacific Water inflows in the Arctic Ocean; the vertical and horizontal structure in the Atlantic Water boundary current and in the Beaufort Gyre and the freshwater content (*Zuo et al.*, 2011).

All models, with and without observation assimilation, need *in situ* data to evaluate parameterisation and boundary limit conditions, but they are sparse in the Arctic compared to other oceans. Moreover, in the Arctic, the Rossby radius of deformation varies between 10 and 6 km (*Zhao et al.*, 2014). High resolution models (1/12°) are eddy-resolving in most oceans but not on the Arctic continental slope where they are only eddy-permitting (*Dupont et al.*, 2015). Very high resolution models have been recently developed to reproduce small-scale processes in the Arctic. For instance, *Wekerle et al.* (2017) compared the performances of a $4.5km$ spatial resolution (high resolution eddy-resolving) and of a $24km$ spatial resolution (low resolution, eddy-permitting only) in the Nordic Seas. The simulated ocean temperature is improved in the Barents Sea Opening and the Atlantic Water volume is closer to the observations in terms of magnitude and variability in the increased mesh resolution model. The higher resolution model improves the circulation pattern and reduces the temperature bias in the eastern Nordic Seas. Eddy-resolving models are required to improve the representation of dynamical processes in Fram Strait.

We used model experiments to put the *in situ* data of the IAOOS platforms deployed during Floe 1 of N-ICE2015 (*Koenig et al.*, 2016) in a broader and continuous temporal and spatial context. We chose the 1/12° Mercator operational model with assimilation (*Lellouche et al.*, 2012) for several reasons. First of all, we selected a coupled ice-ocean model that could reproduce reasonably well the observations as opposed to an idealized model that could have large biases. Moreover, models with 1/12° resolution are eddy-permitting in the Arctic and enable the study of the mesoscale dynamic of the Atlantic Water inflow North of Svalbard. We also looked at model outputs without data assimilation from Mercator Ocean (Orca12) and the comparison with the *in situ* observations was not as satifactory as for the model with data assimilation. The better perfomance of the model with assimilation is shown in *Zuo et al.* (2011).

3.2 Atlantic waters inflow north of Svalbard: Insights from IAOOS observations and Mercator Ocean global operational system during N-ICE2015

AGU PUBLICATIONS

Journal of Geophysical Research: Oceans

RESEARCH ARTICLE

10.1002/2016JC012424

Special Section:

Atmosphere-ice-ocean-ecosystem Processes in a Thinner Arctic Sea Ice Regime: The Norwegian Young Sea ICE Cruise 2015 (N-ICE2015)

Key Points:

- Operational 1/12° global ocean model remarkably reproduces observations in the complex region north of Svalbard
- Evidence of an important winter feature of AW inflow in the Arctic: the Yermak Pass Branch through the Yermak Plateau
- Modeled upwelling and convection contribute to realistic year-to-year variations in winter sea-ice edge location over the AW inflow

Correspondence to:

Z. Koenig,
zklod@locean-ipsl.upmc.fr

Citation:

Koenig, Z., C. Provost, N. Villacieros-Robineau, N. Sennéchael, A. Meyer, J.-M. Lellouche, and G. Garric (2017), Atlantic waters inflow north of Svalbard: Insights from IAOOS observations and Mercator Ocean global operational system during N-ICE2015, *J. Geophys. Res. Oceans*, *122*, doi:10.1002/2016JC012424.

Received 4 OCT 2016
Accepted 15 JAN 2017
Accepted article online 21 JAN 2017

Atlantic waters inflow north of Svalbard: Insights from IAOOS observations and Mercator Ocean global operational system during N-ICE2015

Zoé Koenig[1], Christine Provost[1], Nicolas Villacieros-Robineau[1], Nathalie Sennéchael[1], Amelie Meyer[2], Jean-Michel Lellouche[3], and Gilles Garric[3]

[1]Laboratoire LOCEAN-IPSL, Sorbonne Universités (UPMC, Univ. Paris 6)-CNRS-IRD-MNHN, Paris, France, [2]Norwegian Polar Institute, Fram Centre, Tromsø, Norway, [3]Mercator Ocean, Research and Development, Ramonville Saint-Agne, France

Abstract As part of the N-ICE2015 campaign, IAOOS (Ice Atmosphere Ocean Observing System) platforms gathered intensive winter data at the entrance of Atlantic Water (AW) inflow to the Arctic Ocean north of Svalbard. These data are used to examine the performance of the 1/12° resolution Mercator Ocean global operational ice/ocean model in the marginal ice zone north of Svalbard. Modeled sea-ice extent, ocean heat fluxes, mixed layer depths and AW mass characteristics are in good agreement with observations. Model outputs are then used to put the observations in a larger spatial and temporal context. Model outputs show that AW pathways over and around the Yermak Plateau differ in winter from summer. In winter, the large AW volume transport of the West Spitsbergen Current (WSC) (~4 Sv) proceeds to the North East through 3 branches: the Svalbard Branch (~0.5 Sv) along the northern shelf break of Svalbard, the Yermak Branch (~1.1 Sv) along the western slope of the Yermak Plateau and the Yermak Pass Branch (~2.0 Sv) through a pass in the Yermak Plateau at 80.8°N. In summer, the AW transport in the WSC is smaller (~2 Sv) and there is no transport through the Yermak Pass. Although only eddy-permitting in the area, the model suggests an important mesoscale activity throughout the AW flow. The large differences in ice extent between winters 2015 and 2016 follow very distinct atmospheric and oceanic conditions in the preceding summer and autumn seasons. Convection-induced upward heat fluxes maintained the area free of ice in winter 2016.

1. Introduction

The circulation and modification of the Atlantic Water (AW) inflow is a fundamental aspect of the Arctic Ocean. The AW inflow supplies heat and salt to the Arctic Ocean impacting the thermohaline structure of the water column and influencing the distribution of sea ice [e.g., *Rudels*, 2012]. The Atlantic Water enters the Arctic Ocean via two routes: through Fram Strait to the north of Svalbard and through the St. Anna Trough via the Barents Sea [e.g., *Dmitrenko et al.*, 2015]. Despite its importance to the Arctic system, the AW inflow (pathways and volume transports) north of Svalbard is still poorly known. The Arctic Ocean is a region where data are particularly sparse and model outputs are thus very useful to complement the analysis of in situ data. For instance, model outputs and in situ data have been combined to study the Arctic Circumpolar Boundary Current [*Aksenov et al.*, 2011] and to examine the seasonal cycle of AW temperature in the Arctic [*Lique and Steele*, 2012].

The area north of Svalbard is key to the Arctic Ocean heat budget as it is the major inflow point of AW (Figure 1). Two AW pathways have been identified: the shallow Svalbard Branch along the continental slope of Svalbard, and the deeper Yermak Branch on the western side of the Yermak Plateau [*Cokelet et al.*, 2008]. The shallow Svalbard Branch generates large sea ice melt along the continental slope, and leaves this area called the Whalers Bay free of ice in winter [e.g., *Ivanov et al.*, 2012; *Onarheim et al.*, 2014].

The Norwegian young sea ICE (N-ICE2015) campaign [*Granskog et al*, 2016; *Meyer et al.*, 2017] took place from January until June 2015 north of Svalbard to study the Arctic atmosphere, ice, ocean, and biology. IAOOS (Ice Atmosphere Ocean Observing System) platforms carrying ice mass balance instruments and ice-tethered ocean profilers provided new insights on oceanic conditions in winter north of Svalbard (C. Provost et al., Observations of snow-ice formation in a thinner Arctic sea ice regime during the N-ICE2015 campaign:

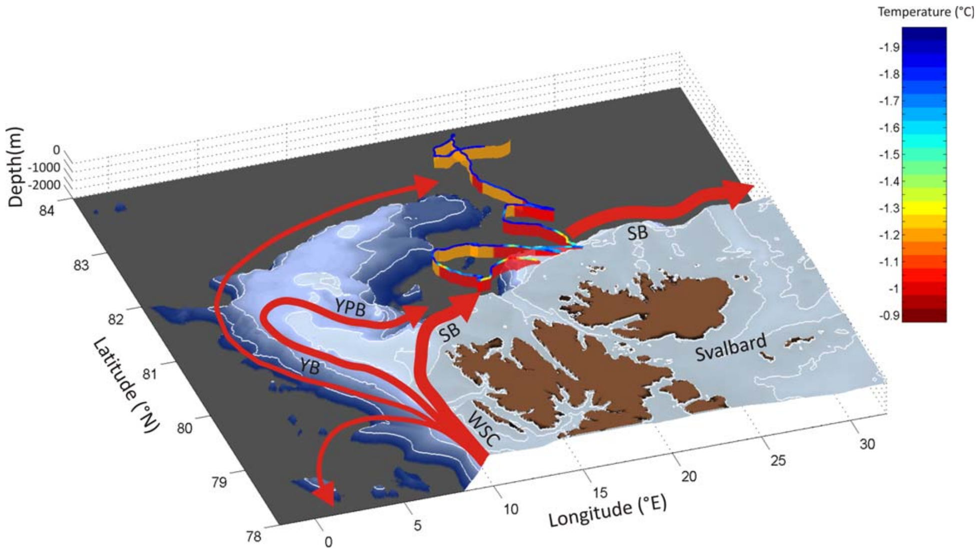

Figure 1. Summary of the in situ data results from *Koenig et al.* [2016] and *Provost et al.* [submitted]. The background of the 3-D plot is the bathymetry from IBCAO (http://www.ngdc.noaa.gov/mgg/bathymetry/arctic/arctic.html). The red lines are the warm water paths. YB: Svalbard Branch. WSC: West Spitsbergen Current. YPB: Yermak Pass Branch. SB: Svalbard Branch. Summary of the warm water layer is the orange/red ruban: orange corresponds to Modified Atlantic Water and red to Atlantic Water. The overlaying data are the surface temperature obtained from the SIMBA instrument (colorbar on the side).

Influence of basal ice melt and storms, submitted to *Journal of Geophysical Research Oceans*, 2017) [*Koenig et al.*, 2016] (Figure 1). The parts of the Nansen Basin and of the Svalbard northern continental slope crossed during the platform drift featured distinct hydrographic properties and ice-ocean exchanges. In the Nansen Basin, the quiescent warm layer was capped by a stepped halocline (60 and 110 m) and a deep thermocline (110 m). Ice was forming and the winter mixed layer salinity was larger by $\sim$0.1 g.kg^{-1} than previously observed [*Koenig et al.*, 2016]. Over the Svalbard continental slope, AW was very shallow (20 m from the surface) and extended offshore from the 500 m isobath by a distance of about 70 km. Considerable basal sea-ice melt was observed with ocean-to-ice heat fluxes inferred from ice mass balance instruments peaking to values of 400 Wm^{-2} (C. Provost et al., submitted manuscript, 2017).

Operational models, such as the one from Mercator Ocean, use a global network of satellite and ocean-based measuring systems to monitor and forecast the world's oceans [*Lellouche et al.*, 2013]. Operational models assimilate ocean measurements and use them to produce estimates of the full depth ocean state including sea-ice. Then, forced at the surface by weather prediction systems, these models forecast ocean currents, temperature, salinity, sea-ice and biogeochemistry. Quality control of operational ocean forecast system is a core activity in operational centers and independent data, not assimilated in the operational model, are used to evaluate model performances [e.g., *Hernandez et al.*, 2015; *Ryan et al.*, 2015]. AW inflow is well represented in operational model outputs as the models assimilate, among other observations, data in Fram Strait [*Lien et al.*, 2016]. In contrast, free-running models do not reproduce well the AW inflow and show large differences in the AW propagation through the Arctic Ocean [*Ilicak et al.*, 2016]. The low horizontal resolution of these free-running models (larger or equal to 0.25°) can partially explain the difficulties in representing the AW inflow and propagation. Indeed, the deformation radius in the Arctic Ocean is small, less than 10 km [*Zhao et al.*, 2014; *Nurser and Bacon*, 2013].

We took advantage of the observations gathered by IAOOS platforms during the N-ICE2015 campaign to evaluate 1/12° Mercator Ocean operational model north of Svalbard in winter (Figure 1). The IAOOS platform provided the first hydrographic data in the region in winter. Numerous processes at play in the Marginal Ice Zone (MIZ) north of Svalbard make comparisons between model outputs and observations a stringent test for the model performance, especially as the Mercator Ocean model does not explicitly represent some processes such as tides and inertial waves. Note that the model 1/12° horizontal resolution grid, 4–5 km resolution north of Svalbard, is only an eddy-permitting grid in the area as the Rossby deformation radius is about 6–8 km [*Zhao et al.*, 2014; *Nurser and Bacon*, 2013].

The main goal of the present study is to provide answers to the two following questions: (1) How does Mercator Ocean global operational model perform in the winter north of Svalbard? (2) What can we learn about the spatial and temporal context of N-ICE2015 IAOOS data from model outputs? We used outputs from the Mercator Ocean model from January 2014 to March 2016 to put in situ Lagrangian observations of midwinter 2015 in a larger spatial and temporal context. In particular, we focus on AW circulation (pathways, volume transports, heat contents) and surface conditions (ice edge location and upper ocean temperatures).

Mercator Ocean global operational model outputs and IAOOS data are introduced in section 2. Model outputs are compared to the extensive winter observational data set in section 3. Once the model outputs are evaluated, they are used to discuss AW inflow and seasonal and year-to-year variations in section 4, and upper ocean temperature and ice edge location in section 5. Finally, section 6 summarizes the results and puts forward perspectives.

2. Description of Operational System and In Situ Data

2.1. Mercator Ocean Operational System and First Assessment

Hindcasts from the global 1/12° real-time operational system developed at Mercator Ocean for the Copernicus Marine Environment Monitoring Service (CMEMS; http://marine.copernicus.eu/) are used. The system is based on the NEMO (Nucleus for European Modelling of the Ocean) [*Madec*, 2008] platform and uses a multidata and multivariate reduced order Kalman filter based on the Singular Extended Evolutive Kalman (SEEK) filter formulation introduced by *Pham et al*. [1998]. The model has 50 vertical levels with typically 1 m resolution at the surface decreasing to 450 m at the bottom and 22 levels within the upper 100 m. The model uses the LIM2 thermodynamic-dynamic sea ice model and is driven at the surface by atmospheric analysis and forecasts from the IFS (Integrated Forecasting System) operational system at ECMWF (European Centre for Medium-Range Weather Forecasts). The assimilated observations are along-track satellite altimetry, sea surface temperature (SST), and in situ vertical profiles of temperature and salinity. The data assimilation scheme is fully operational for SST warmer than -1°C and is switched off for SST colder than the freezing point (in ice covered areas). Sea ice is not assimilated in this version of the model. Full description of the system components is available in *Lellouche et al*. [2013]. The model outputs have a daily resolution and are used from 8 January 2014 to 15 March 2016 over a region extending from -5 to 35°E in longitude and from 78 to 84°N in latitude.

A preliminary comparison of model outputs with data from the mooring transect monitoring the flow at Fram Strait (79°N across the West Spitzbergen Current) since 1997 [*Beszczynska-Moller et al*., 2012] shows that the model produces reasonable seasonal cycles in volume transports and temperatures at that location. Indeed, the model provides a northward AW (with $T>2$°C) volume transport of 3.7 ± 1.4 Sv in winter and 1.7 ± 1.5 Sv in summer in 2015, in agreement with the 13 year statistics (1997–2010) from in situ data [*Beszczynska-Moller et al*., 2012]. The monitoring array showed that the northward volume transport of AW ($T > 2$°C) at 79°N undergoes a marked seasonal cycle with a maximum in winter (4 ± 1 Sv) and a minimum in summer (2 ± 1 Sv) [*Beszczynska-Moller et al*., 2012]. Model temperature in Fram Strait are also in agreement with the mooring transect at 79°N (4.5°C at the surface and 3°C at 500 m, to be compared with Figure 2 in *Beszczynska-Moller et al*. [2012]).

Further East, at 30°E and 81.8°N, the model temperature outputs can be compared with mooring data [*Ivanov et al*., 2009] and to temperature from the A-TWAIN campaign [*Våge et al*., 2016]. Seasonal variations in the model temperature outputs are in good agreement with NABOS (Nansen and Amundsen Basins Observational System, http://nabos.iarc.uaf.edu/) data ($\sim 2.7 \pm 0.3$°C in summer and $\sim 3.5 \pm 0.4$°C in winter). The large temperatures observed recently at 30°E are in the variability range of the modeled temperature at that location [*Våge et al*., 2016].

Comparisons to contemporaneous data can be made with satellite data. Sea-ice concentration maps from the model compare rather well with maps derived from AMSR-2 (Advanced Microwave Scanning Radiometer) brightness temperature data with a 6 km × 6 km spatial resolution (retrieved from https://www.zmaw.de/)

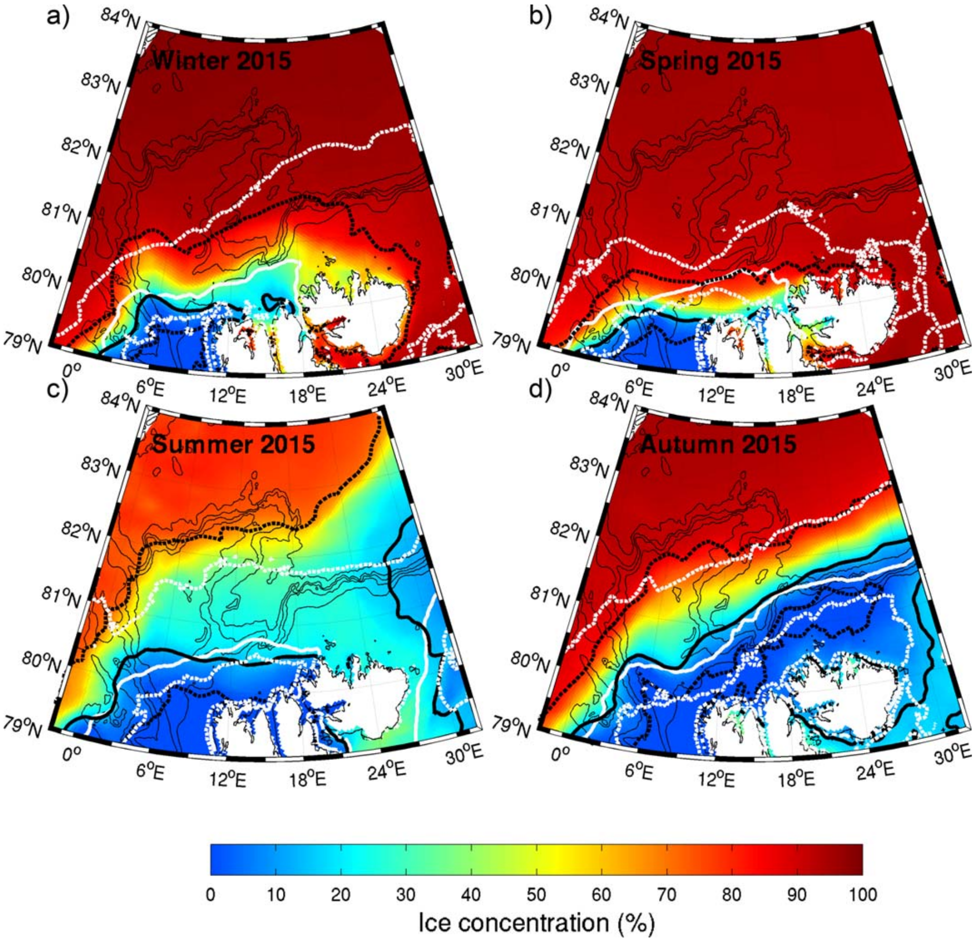

Figure 2. Seasonal comparisons of model output sea ice cover (in %) with AMSR-2 data. (a) Mean for January–February–March (Winter), (b) Mean for April–May–June (Spring), (c) Mean for July–August–September (Summer), and (d) Mean for October–November–December (Autumn). The colored background is the ice cover from the model outputs. The thick white (black) solid line is the mean ice edge from AMSR-2 data (model outputs), 15% ice cover averaged over the same periods. The dashed white (black) lines are the northern/southern location of the ice edge from AMSR-2 data (model outputs) over the same period. Thin black lines are bathymetric contours.

(Figure 2). The 15% contour line is considered as the ice edge. Winter, spring, summer, and autumn 2015 sea-ice edges from model outputs are in good agreement with the satellite-derived ice edge with zonal differences of less than 0.5° (Figure 2).

These preliminary comparisons are rather encouraging and we proceed to more detailed comparisons with the winter ocean and sea-ice IAOOS data presented below.

2.2. Data: IAOOS Ocean and Ice Data Acquired During N-ICE2015

Two IAOOS platforms were deployed in January 2015 during N-ICE2015 experiment less than 500 m apart. They were equipped with a SIMBA instrument (SAMS Ice Mass Balance for the Arctic) [*Jackson et al*., 2013; *Provost et al*., 2015] and an ice-tethered ocean profiler [*Koenig et al*., 2016]. A tent-covered testing-hole with an ice-tethered profiler was also deployed less than 500 m apart from the two IAOOS platforms. Five other SIMBAs were deployed in a 20 km radius from the IAOOS platforms (C. Provost et al., submitted manuscript, 2017).

SIMBA repeatedly observed temperature and thermal resistivity proxy profiles with 2 cm vertical resolution in air, snow, ice, and ocean below. The 7 SIMBAs located in a 20 km radius from the IAOOS platform are averaged. Drift speed, snow depth, ice thickness, near surface ocean temperature and ocean heat flux were derived from the SIMBA observations (Figure 3) (C. Provost et al., submitted manuscript, 2017). We first

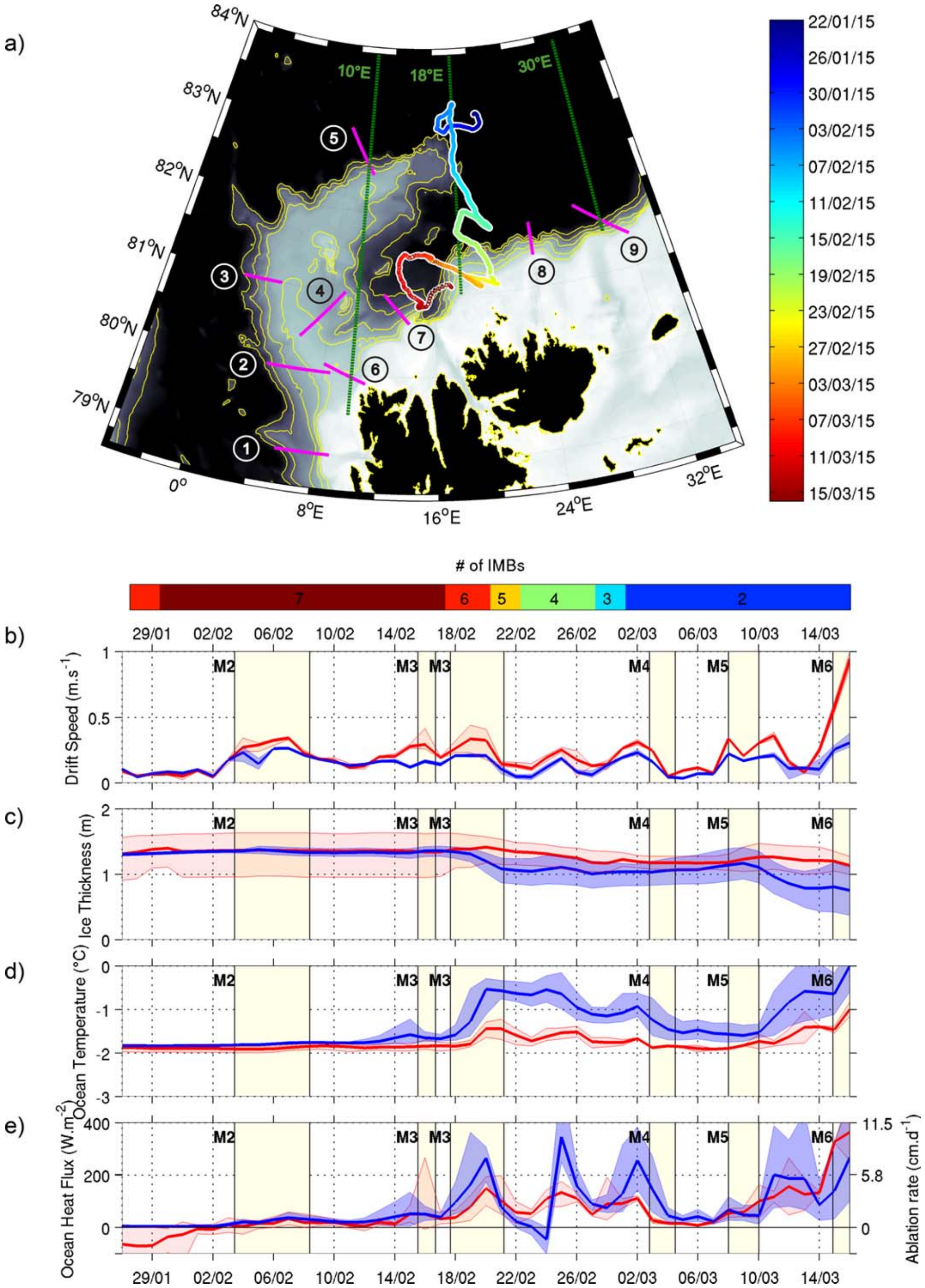

Figure 3. (a) IAOOS platform drift trajectory. The color of the drift is the date. Background is bathymetry (m). The yellow isolines are bathymetry contours (500, 700, 1000, 1500, and 2000m). The purple segments 1–9 indicate the sections through which the volume transports are calculated (Table 1). The green lines show the sections at 10,18 and 30°E used in Figures 7b–7e: Comparisons of model outputs (in blue) (mean and range in a 20 km radius around the IAOOS platform) to observations from SIMBAs (in red, mean and range of the SIMBA observations): (b) Drift speed (ms^{-1}). (c) Ice thickness (m). (d) Ocean temperature (°C). (e) Ocean heat flux density (Wm^{-2}) and corresponding ablation rate (m d^{-1}) (Ocean heat flux being considered as latent heat flux). M1–M6 indicate the storms described in *Hudson and Cohen* [submitted]. The top colorbar indicates the number of SIMBAs available along the time series.

extracted and collocated model outputs in a 20 km radius around the IAOOS platform location along the drift (corresponding to 4–5 grid cells) to examine model reproduction of the variables listed above. Since model variable outputs are daily means, observations were daily averaged (Figure 3).

The ice-tethered ocean profilers measured temperature, salinity, and dissolved oxygen in the upper 500 m twice a day. The data gathered by the three profilers were averaged to produce a composite section of upper ocean temperature and salinity with the same vertical resolution as the model outputs and a daily resolution (the model time resolution) along the platform drift (Figures 4a and 4c). As in *Koenig et al*. [2016], we used the International Thermodynamic Equations Seawater framework [*McDougall et al*., 2012] with conservative temperature CT (°C) and absolute salinity SA (g kg^{-1}). We then produced model-derived sections of conservative temperature and absolute salinity, over the upper 500 m collocated with the profiler observations (Figures 4b and 4d).

3. Comparison Between Mercator Ocean and N-ICE2015 IAOOS Observations

3.1. Comparison With SIMBA Data

Six main storms (M1, . . ., M6) were identified with wind speeds in excess of 8 ms^{-1} [*Hudson and Cohen*, 2015] (L. Cohen et al., Meteorological conditions in a thinner Arctic sea ice regime from winter through spring during the Norwegian young sea ICE expedition (N-ICE2015), submitted to *Journal of Geophysical Research Oceans*, 2017) (Figure 3). Daily means of modeled ice drift speed (in blue) are of the same order of magnitude as daily means of SIMBA drift velocities (in red) with most values between 10 and 20 cms^{-1} and larger values up to 40 cms^{-1} during storms and over the continental slope off Svalbard (after March 10) (Figure 3b). However, model ice drift during storms is smaller than observations by about 10 cms^{-1}. Model ice thickness agrees with the mean of the observed values (1.30–1.40m) until 17 February, and then decreases faster than in the observations (Figure 3c). Ice thickness is more spatially homogeneous in the model (range less than 10 cm) than in the observations (range about 70 cm) until 18 February; the range in ice thickness then increases in the model after the strong melt centered on 20 February indicative of an inhomogeneous melt. Indeed, model ocean surface temperatures (precisely 50 cm below sea surface) span quite a large range about 1°C between 18 and 26 February, whereas they are homogeneous until 10 February. Model surface ocean temperatures are always warmer than those observed, the difference being larger after 10 February with model temperature peaks at -0.5°C, instead of -1°C in the in situ data (Figure 3d). Model surface ocean temperatures are above the model freezing temperature (-1.88°C) after 2 February. Consequently modeled ocean fluxes, positive after 2 February, are large and often larger than ocean-to-ice fluxes estimated from the SIMBA (Figure 3e). Peaks in modeled ocean fluxes are consistent with those observed in magnitude and time. Modeled ocean fluxes correspond to basal melt rates that can reach up to 12 cm per day (Figure 3e).

3.2. Ocean Water Masses: Comparison With Profiler Data

Temperature and salinity in the model outputs, collocated in space and time with the winter IAOOS profiler data, show patterns similar to those observed (Figure 4). The water masses encountered in the model outputs are in good agreement with the in situ observations in winter 2015 (Figure 4): at depth, Modified Atlantic Water (MAW, $T<2$°C and the density $27.7<\sigma<27.95$) and Atlantic water (AW, $T>2$°C and $27.7<\sigma<27.95$), and near the surface, Polar Surface Water (density $\sigma<27.7$) (definition of water masses from *Rudels et al*. [2000] used by *Koenig et al*. [2016] and *Meyer et al*. [2017].

MAW is found in the Nansen Basin with a core depth at 300 m, that is 50 m deeper than in the observations. AW is observed over the continental slope of Svalbard (from 13 February to 21 February) in the boundary current with characteristics similar to those in the observations (core depth around 250 m, T$\sim$3°C, S$\sim$35.25 g.kg^{-1}), and along the northern and eastern tip of the Yermak Plateau (from 27 January to 3 February and from 6 February to 11 February, core depth around 300 m, T$\sim$2.5°C, S$\sim$35.2 g.kg^{-1}). The offshore limit of the AW originating from the Svalbard Branch in the model outputs is in good agreement with the in situ data (Figure 1 at 82.3°N and 19°E).

The warm water (AW) from the Yermak Branch observed on 8–9 February in the IAOOS data (Figure 1 at 83°N and 19°E and Figure 4a) is seen twice in the model, first between 27 January and 3 February and a second time between 7 and 13 February (Figure 4b). In the model outputs, the flow is coming from the Yermak

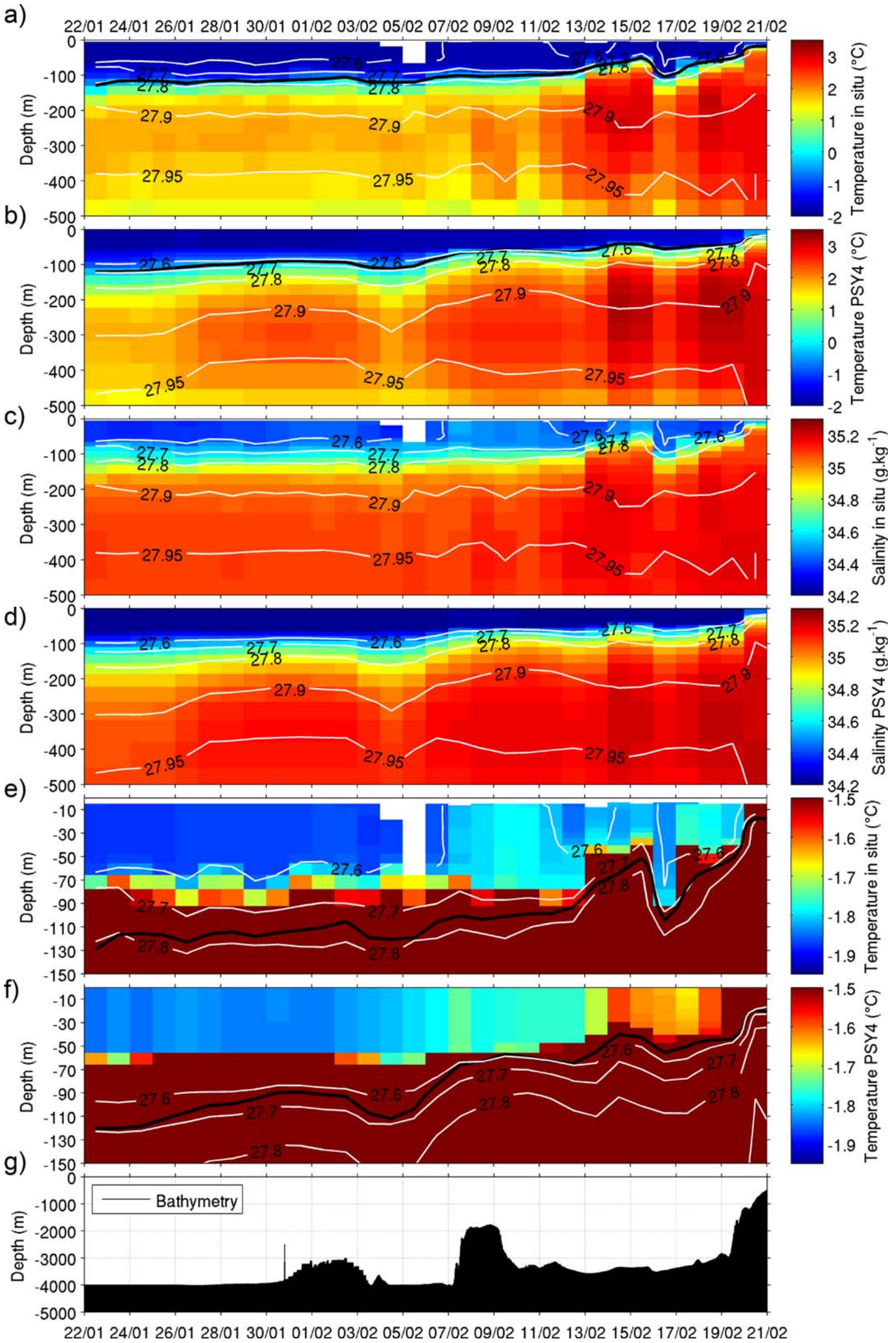

Figure 4. Hydrography from data and model. Data along the drift are daily averaged. Daily model outputs are collocated with IAOOS platform data. (a) Conservative Temperature from IAOOS ocean profilers in the upper 500 m (in °C). (b) Conservative Temperature from model (called PSY4 in the figure) (in °C). (c) Absolute Salinity from IAOOS ocean profilers over the upper 500 m (g.kg^{-1}). (d) Absolute Salinity from model (g.kg^{-1}). (e) Close-up of Conservative Temperature over the upper 100 m from IAOOS profilers (°C). (f) Close-up of Conservative Temperature over the upper 100 m from model (°C). In all plots, white lines are isopycnals. The black line in Figures 4a, 4b, 4e, and 4f is the 0°C isotherm. (g) Bathymetry along the drift in meter.

Branch in the form of pulsing eddies and is highly variable (section 4.2). Model temperatures in the core of the warm layer at 82.5°N and 18°E vary between 2 and 2.8°C while the observed temperature on 8 February at that location are ~2.1°C within the model range.

The modeled mixed layer temperature is in good agreement with the in situ data with above freezing temperature over the Yermak Plateau (−1.75°C) and values of −1.55°C over the Svalbard continental slope (Figures 4e and 4f). The modeled mixed layer salinity is smaller by about 0.25 g.kg^{-1}, its variations from one location to another are comparable to the in situ salinity. Fresher mixed layer in the model outputs results in a stronger pycnocline in the model than in the observations (Figure 4). The modeled depths of the 0°C isotherm and of the pycnocline, at ~105 m depth at the beginning and up to ~20 m depth at the end, are comparable with the in situ data.

In summary, in spite of a mixed layer that is too fresh, the hydrography of the model is in good agreement with the winter IAOOS data. Model outputs were also compared (not shown) with the CTD data from a free-

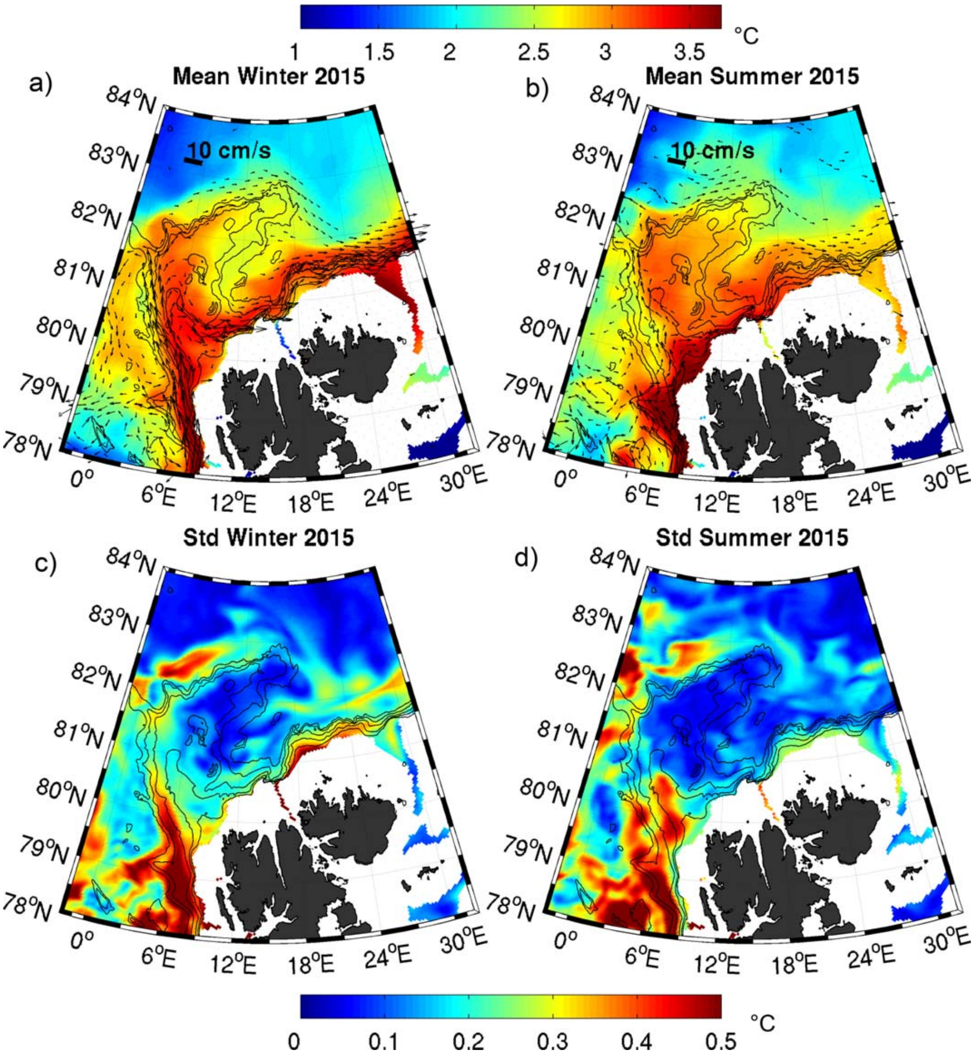

Figure 5. (top) Mean circulation (arrows in cms^{-1}) and Conservative Temperature (°C) from the model outputs for the layer centered at 266 m (50 m thick) over (a) January–February–March 2015 and (b) July–August–September 2015. The corresponding colorbar (in °C) is at the top of the figure. (bottom) Standard deviation of the Conservative Temperature (°C) for the layer centered at 266 m (50 m thick) over (c) January–February–March 2015 and (d) July–August–September 2015. White areas are shallower than 266 m. The corresponding colorbar (in °C) is at the bottom of the figure.

falling microstructure profiler (0–300 m) deployed during N-ICE2015 until 18 June 2015 [*Meyer et al.*, 2017]. Again the hydrography of the model was in remarkable agreement with the data, the only differences being a too fresh mixed layer in general (by 0.25 g.kg^{-1}) and a too shallow mixed layer over the Yermak Plateau (by 20 m). As the model ice-edge follows satellite observations, we believe that the model performances can be trusted in summer and autumn although there are no hydrographic data available in the region in summer or autumn 2015 for a precise comparison.

4. Warm Water Layer: Inferences From Model Outputs

4.1. Warm Water Pathways, Volume Transports, and Heat Contents in 2015

Warm water paths are examined using winter (January–March) and summer (July–September) mean temperature maps with mean velocity vectors in the core of the AW layer (266 m) (Figures 5a and 5b) and using time series of volume transport and heat content in the AW layer (T>2°C) through nine sections across the AW pathways (purple lines in Figure 3a and Table 1). Heat content of the warm water layer (T>2°C) in each transect was computed as in *Lique and Steele* [2013]: $\int_{z0}^{zl} \rho_0 C_p (T(t,x,y,z) - T_{ref}) dz$ with ρ_0 the density of ocean water, C_p the ocean specific heat (4000 J.kg^{-1}.K^{-1}), and T_{ref} a reference temperature (here −1.8°C).

In 2015, AW pathways differ in winter and summer (Figures 5a and 5b). In winter, the large AW volume transport of the West Spitsbergen Current (WSC) (section 1, ~ 4 Sv) proceeds to the north-east through three branches: the Svalbard Branch (section 6, 0.5 Sv) along the northern continental slope of Svalbard, the Yermak Branch (section 5, 0.3 Sv) along the western slope of the Yermak Plateau, and the Yermak Pass Branch (section 4, 1.8 Sv) over a pass in the Yermak Plateau at 80.8°N. This passage was observed by floats [*Gascard et al.*, 1995] and recalled by *Rudels et al.* [2000]. The flow in that pass follows the 600–700 m isobaths and joins the Svalbard continental slope around 10°E (Figure 5a). The Yermak Branch, well defined on the western slope of the Yermak Plateau, is weaker on the northern and eastern slope of the Yermak Plateau. The Yermak Branch can be followed all along the slope of the Yermak Plateau, and joins the Svalbard continental slope at around 20°E.

In summer 2015, the AW transport in the WSC is smaller (section 1, ~2 Sv) and there is no transport through the Yermak Pass (section 4) (Figures 5b and Table 1). The connection from the AW inflow at 78°N to the Svalbard Branch follows the northern continental slope of the Svalbard Archipelago above 400–500 m, as described in *Sirevaag et al.*, [2011] and *Muench et al.*, [1992]. A large part of the Yermak Branch bifurcates to the north-northwest at the tip of the Yermak Plateau and the flow joining the Svalbard continental slope is weaker than in winter.

Several bifurcations to the west back into Fram Strait are observed along the AW path: a first one both in summer and winter at about 79°N [e.g., *Von Appen et al.*, 2016], a second one larger in winter than summer at about 81.5°N [*Hattermann et al*, 2016], and a third one at 82.5°N (12°E) on the northern side of the Yermak Plateau larger in summer than in winter (Figure 5b).

Table 1. Volume Transport Statistics (in Sv) Across Several Sections Over the Yermak Plateau and the Svalbard Continental Slope for the Water Warmer Than 2°C (AW Pathways)[a]

2014	79°N	80°N	81°N	YPB	YB	SB	12°E	24°E	30°E
2015	1	2	3	4	5	6	7	8	9
Mean	**2.8**	**1.7**	**0.9**	**1.1**	**0.4**	**0.4**	**1.5**	**1.8**	**2.1**
	2.8	*1.9*	*1.0*	*0.7*	*0.4*	*0.7*	*1.6*	*1.8*	*1.9*
Summer mean	**2.1**	**1.2**	**0.2**	**0.6**	**0.6**	**0.5**	**1.1**	**1.2**	**1.6**
	1.3	*1.1*	*0.8*	*−0.4*	*0.5*	*0.8*	*0.9*	*0.9*	*1.0*
Winter mean	**3.9**	**2.1**	**1.1**	**1.5**	**0.2**	**0.5**	**1.8**	**2.5**	**2.6**
	4.0	*2.8*	*1.7*	*2.1*	*0.4*	*0.4*	*2.3*	*2.9*	*3.1*
Std	**1.4**	**0.9**	**0.7**	**0.7**	**0.3**	**0.5**	**0.6**	**0.8**	**0.88**
	1.8	*1.0*	*0.7*	*1.1*	*0.2*	*0.6*	*0.8*	*1.2*	*1.2*
Summer std	**1.5**	**0.7**	**0.7**	**0.4**	**0.2**	**0.3**	**0.2**	**0.5**	**0.5**
	1.3	*0.6*	*0.3*	*0.3*	*0.1*	*0.3*	*0.4*	*0.4*	*0.5*
Winter Std	**1.2**	**1.0**	**0.4**	**1.0**	**0.1**	**0.7**	**0.7**	**1.0**	**1.0**
	1.5	*0.8*	*0.7*	*0.9*	*0.3*	*0.7*	*0.7*	*0.9*	*0.8*

[a] In bold: statistics for year 2014, In italic: statistics for year 2015. Winter: January–February–March. Summer: July–August–September.

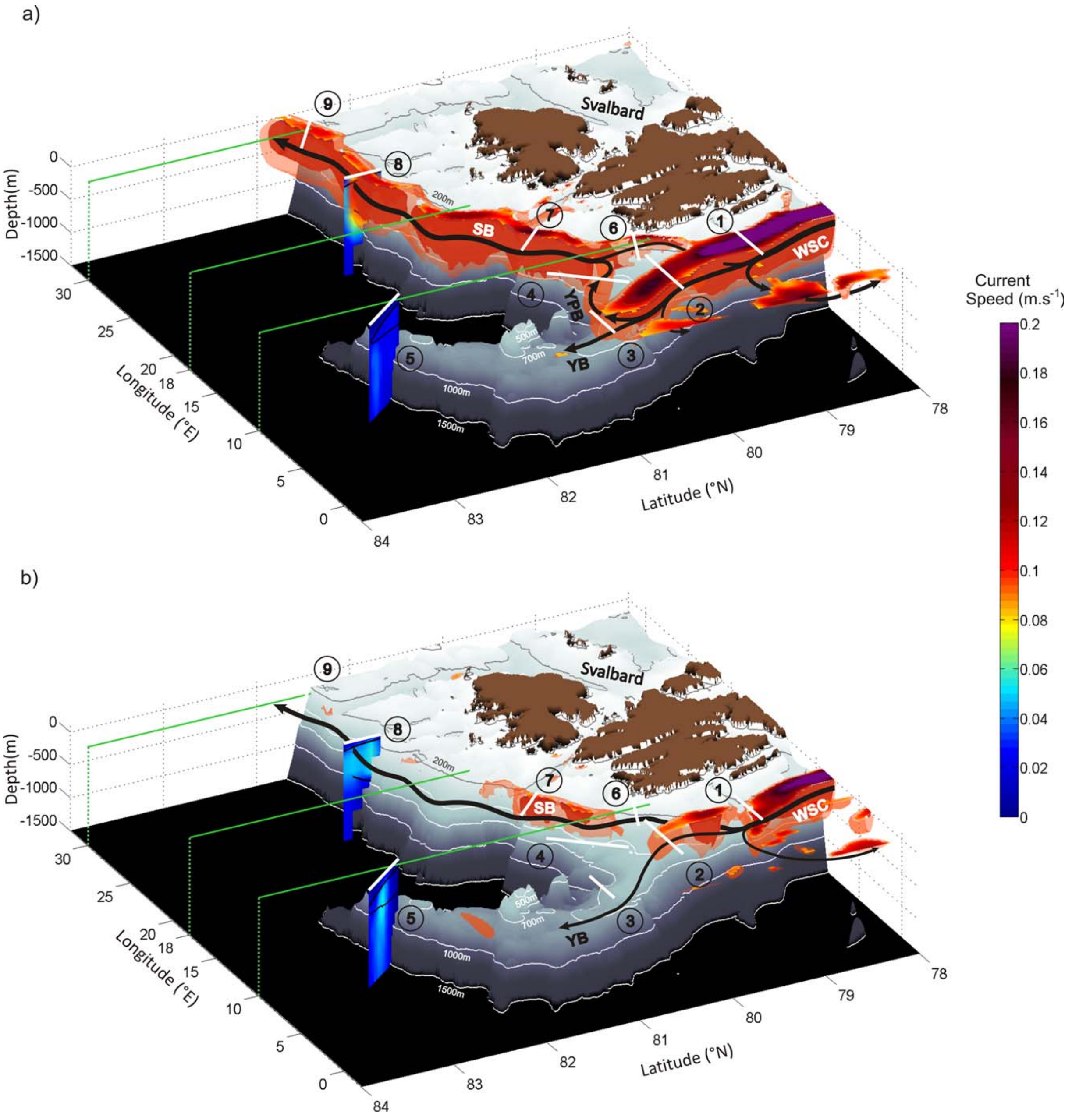

Figure 6. 3-D representation of AW winter and summer current pathways (color bar in ms^{-1}). Two speed cores are plotted: dark red inner core is 0.12 ms^{-1} and pale red outer core 0.08 ms^{-1}. (a) Winter mean (January–February–March) and (b) summer mean (July–August–September). The transects 1–9 (white lines at the surface) correspond to the sections through which the volume transport and heat content are calculated (Table 1 and Figure 7). Cross-track velocity is shown for sections 5 and 8 (the black isoline is the 0°C isotherm). The background is the bathymetry. Transects at 10, 18 and 30°E used in Figure 8 are indicated in green. SB: Svalbard Branch. YB: Yermak Branch. YPB: Yermak Pass Branch. WSC: West Spitsbergen Current.

The large seasonal variations in AW described above for year 2015 are also found in 2014 (Table 1) and are illustrated in a composite 3-D plot (three winters: 2014, 2015, and 2016 and two summers: 2014 and 2015) (Figure 6) with a strong winter circulation featuring an overflow in the Yermak Pass and a weaker summer circulation. In yearly and seasonal means, the transport at 12°E (section 7) is roughly the sum of the transports through the Yermak Pass Branch (section 4) and Svalbard Branch (section 6) while the transport at 24°E (section 8) corresponds to the sum of the transport at 12°E (section 7) and the transport through the Yermak Branch (section 5) (Table 1). Differences between the volume transports at 79°N (section 1) and

80°N (section 2) are due to the recirculation to the west which is larger in winter (1.5 Sv) than in summer (0.5 Sv) (Table 1). Year to year differences are large in the Yermak Pass Branch (section 4) especially in summer with even a reverse flow (-0.4 Sv) in 2015 (Table 1 and Figure 5b).

Heat content of the warm layer decreases away from Fram Strait (Figures 7a–7c). In the WSC, the heat content is larger in summer (33×10^{13} Jm^{-2}) than in winter (18×10^{13} Jm^{-2}). Around the Yermak Plateau, the heat content is larger in the Yermak Pass Branch and the Svalbard Branch (15×10^{13} Jm^{-2} in winter and 20×10^{13} Jm^{-2} in summer) than in the Yermak Branch (less than 8×10^{13} Jm^{-2}) (Figure 7b). Seasonal variations dominate the heat content evolution of the warm layer along the Svalbard continental slope (Figures 8a, 8c, and 8e). Lags between two time series of the warm water heat content (defined as the lag of the maximum correlation between the two time series) can be considered as an advection time scale between the two sections. The lag is 38 days between heat content time series at 79°N and 80°N ($r = 0.5$) (sections 1 and 2) and 50 days between 79°N and 81°N ($r = 0.35$) (sections 1 and 3) (Figure 7a). Along the Svalbard continental slope, the lag between heat content times series at 24°E and 30°E is 27 days ($r = 0.7$) (sections 8 and 9) and 38 days ($r = 0.7$) between 12°E and 24°E (sections 7 and 8) (Figure 7c). These time scales correspond to reasonable mean advection velocities in the warm layer of about 5 cms^{-1}. Correlations between heat content time series at 79°N and the sections across the northern continental slope of Svalbard are not significant (Figures 7a and 7c). Two years and three months of model outputs are not a long-enough time series to examine in detail the links between variations in heat content in the WSC and in the Svalbard Branch at 30°E.

4.2. Subseasonal Activity in the Warm Layer

>Summer and winter standard deviations in temperature at 266 m (the approximate depth of the core of the warm water layer, Figures 5c and 5d) provide some spatial and temporal information about the subseasonal activity in the warm water layer. Large temperature standard deviation (std) (std > 0.5°C, Figures 5c and 5d) corresponding to large intraseasonal variations in volume transport are found along the WSC and on the western side of the Yermak Plateau in agreement with the literature [e.g., *Hattermann et al*., 2016; *Kawasaki and Hasumi*, 2016]. Intraseasonal variations are also found on the northern and eastern side of the Yermak Plateau (std$\sim$0.2°C), and along the Svalbard Branch (std$\sim$0.35°C in winter and 0.25°C in summer). Volume transports of the warm ($>$2°C) water layer in most sections exhibit large variations at intraseasonal time scales with large standard deviations in winter and summer (Table 1).

The time-latitude plots of velocity and temperature at 10, 18, and 30°E document the high-frequency variations superimposed over the seasonal variations (Figure 8). At the northern tip of the Yermak Plateau, the Yermak Branch flows in pulses in eddy-like structures observed around 82.5°N in the two sections 10°E and 18°E both in temperature and velocity (Figures 8a–8d). The 18°E section is close to the IAOOS platform drift and shows large temperature variations at 82.5°N in February 2015. The modeled temperature range over a month at that location encompasses the IAOOS observations. Although the comparison of values collocated in time and space may suggest that the model is slightly too warm (Figures 4a and 4b), mesoscale pulses of the Yermak Branch provide temperature variations explaining differences between model and observations.

At 30°E, in the Svalbard Branch, pulsing temperature and velocity structures extend as north as 82.5°N (April 2014, Figure 8). They correspond to warm eddies offshore the continental slope in agreement with *Våge et al*. [2016]. These eddies do not undergo large seasonality and have a short-time scale along these sections (less than a month, Figure 8). A model with a higher spatial resolution is needed to precisely study the eddy field north of Svalbard.

5. Evolution of Ice Edge Location and Near Surface Ocean Temperature From January 2014 to April 2016

Although ice concentration data is not assimilated, the model reproduces satellite-derived ice edge variations (Figure 9). To first order, ice edge displacement are governed by wind direction [e.g., *Thorndike and Colony*, 1982; *Kwok et al*., 2013]. The strong winter winds (January–March) (mean of 7.2 ms^{-1}) turning counterclockwise around 8°E push the ice edge away from the northern Svalbard coast while the southward

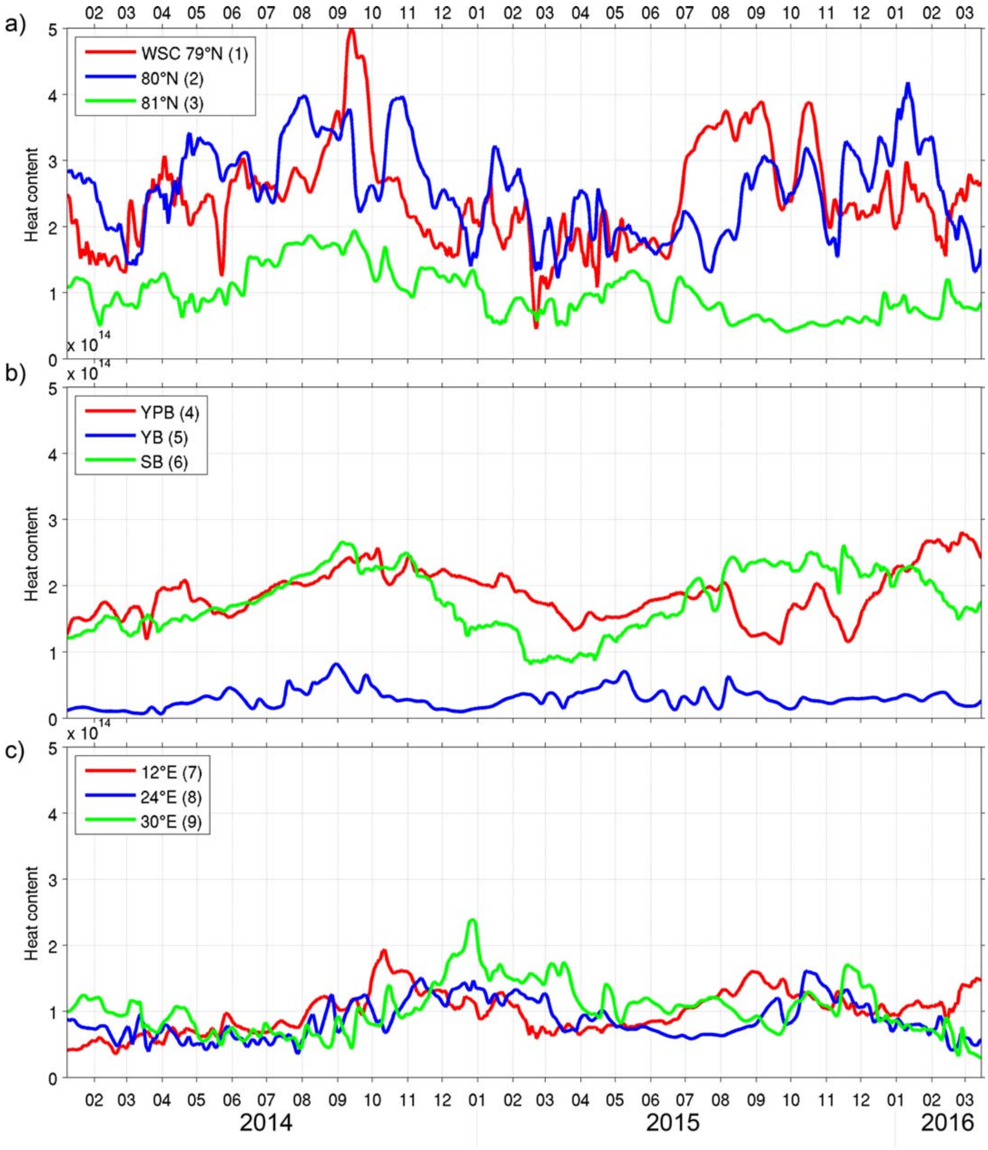

Figure 7. Time series of heat content (in Jm^{-2}) in the different sections numbered in Figures 1 and 6. (a) Sections 1, 2, 3 at 79°N, 80°N and 81°N. (b) Sections 4, 5, 6 across the Yermak Pass Branch (YPB), the Yermak Branch (YB), and the Svalbard Branch (SB). (c) Sections 7, 8, 9 across the continental slope at 12°E, 24°E and 30°E.

spring winds (southeastward in 2014 and southwestward in 2015) (mean speed of 5.2 ms^{-1}) bring the ice edge back close to Svalbard. Warm near surface ocean temperatures ($T > 0°C$) extend to the northeast in autumn and winter (Figure 9) when the strong positive wind stress curl above continental slope could induce an intense upwelling (order of 30 cmd^{-1}) (Figure 10). This upwelling occurs as the warm water volume transport over Svalbard Branch reaches its seasonal maximum as documented in section 4 (e.g., Table 1 and Figure 8). The large temperature values along the slope in winter can be caused by the upwelling of warm water.

Beyond these broad seasonal variations, year-to-year variations are observed with a much reduced ice cover in summer 2015 (24%) compared to summer 2014 (45%) and in particular less open water in winter 2015 during N-ICE2015 (mean ice cover over the plotted area: 76%) than in winter 2014 and 2016 (mean ice cover over the plotted area: 68% and 57%, respectively) (Figure 9). We focus on the differences that led to very contrasted synoptic situations in winters 2015 and 2016.

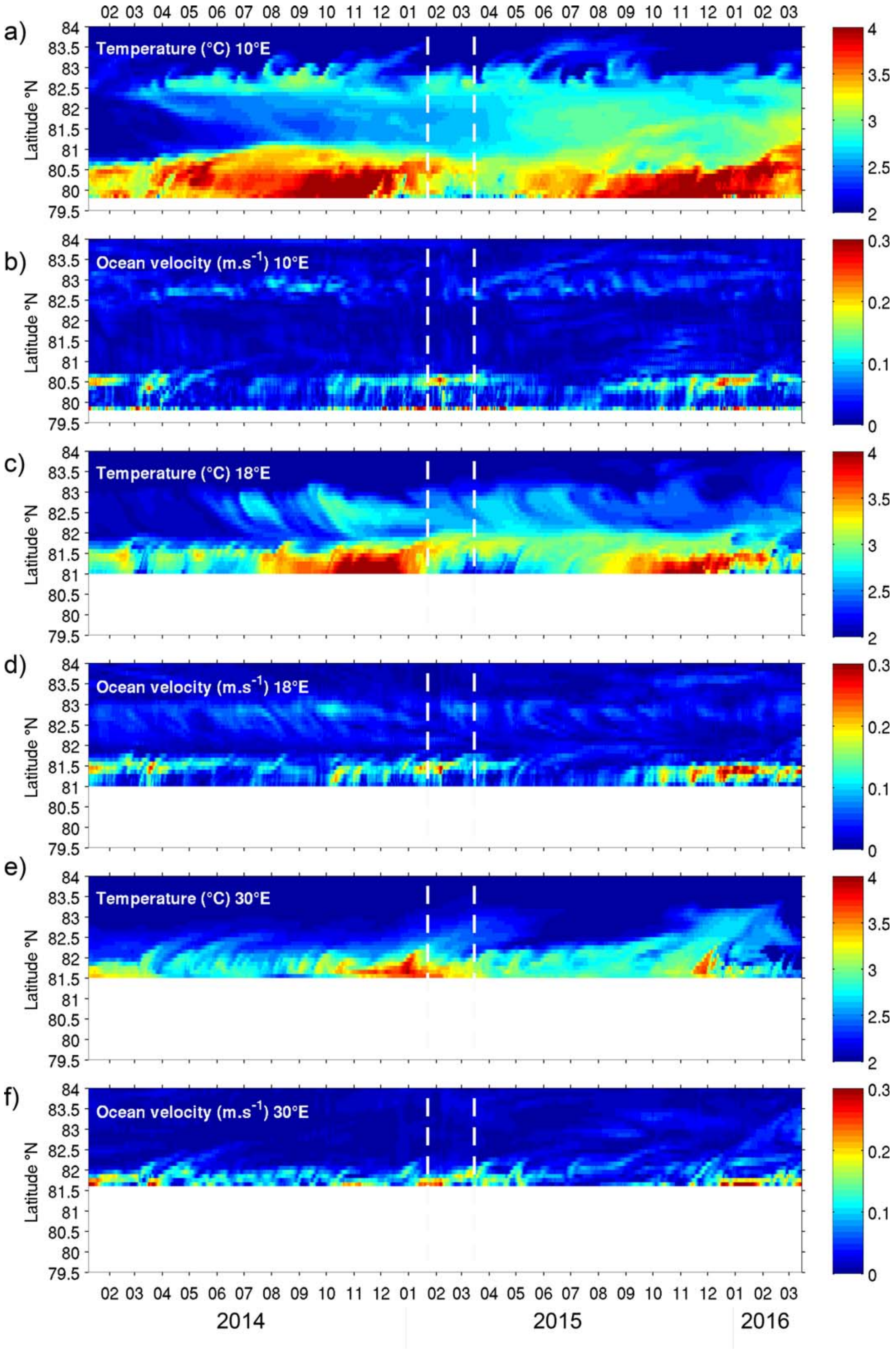

Figure 8. Evolution of (b, d, and f) ocean velocity (ms^{-1}) and (a c and e) temperature (°C) for the layer centered at 266 m (40 m thick) from January 2014 to April 2016 along meridional sections at (a and b) 10°E, (c and d) 18°E, and (e and f) 30°E. The vertical-dashed lines mark the beginning and the end of the in situ measurement from floe 1 of N-ICE 2015 campaign.

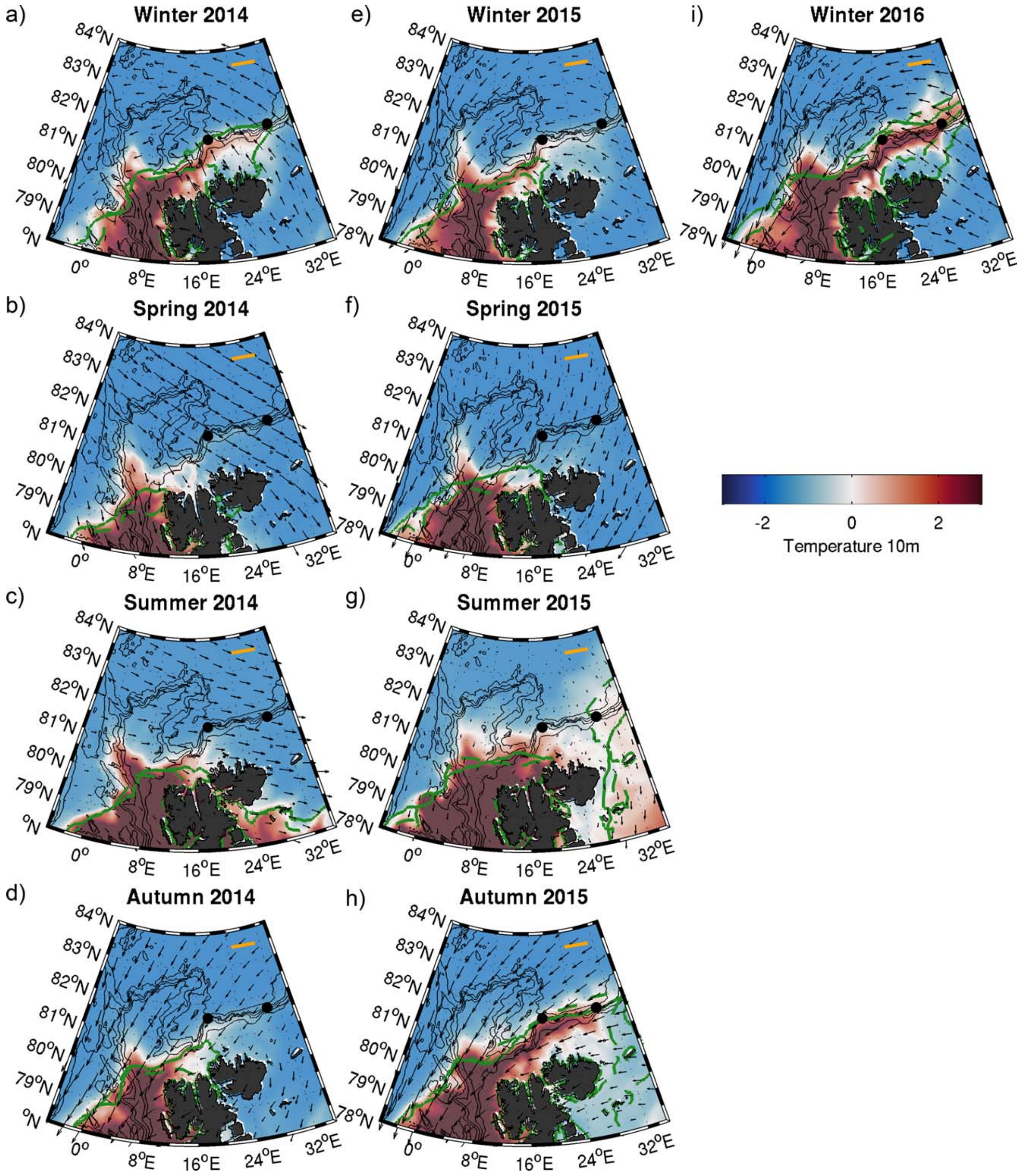

Figure 9. Wind speed at 10 m (arrows) averaged every 3 months from January 2014 to March 2016. (top right) The orange scale corresponds to 5 ms^{-1}.The green solid line (green-dashed line) is the 15% mean sea ice cover contour from AMSR-2 (model outputs) over the period and is taken as the location of the ice edge. The background color is the mean modeled ocean temperature at 10 m over the designated period. The thin black lines are the bathymetry contours. The black dots on the continental slope at 18°E and 30°E indicate the location of the shown profiles in Figure 12.

In summer 2014, westerlies (mean speed about 2 ms^{-1}) are pushing the ice toward Svalbard whereas in 2015 summer winds are extremely weak (Figures 9c and 9g). Furthermore summer 2015 air temperatures on the continental slope east of Svalbard are 0.5°C warmer than the year before (1°C instead of 0.5°C, not shown).

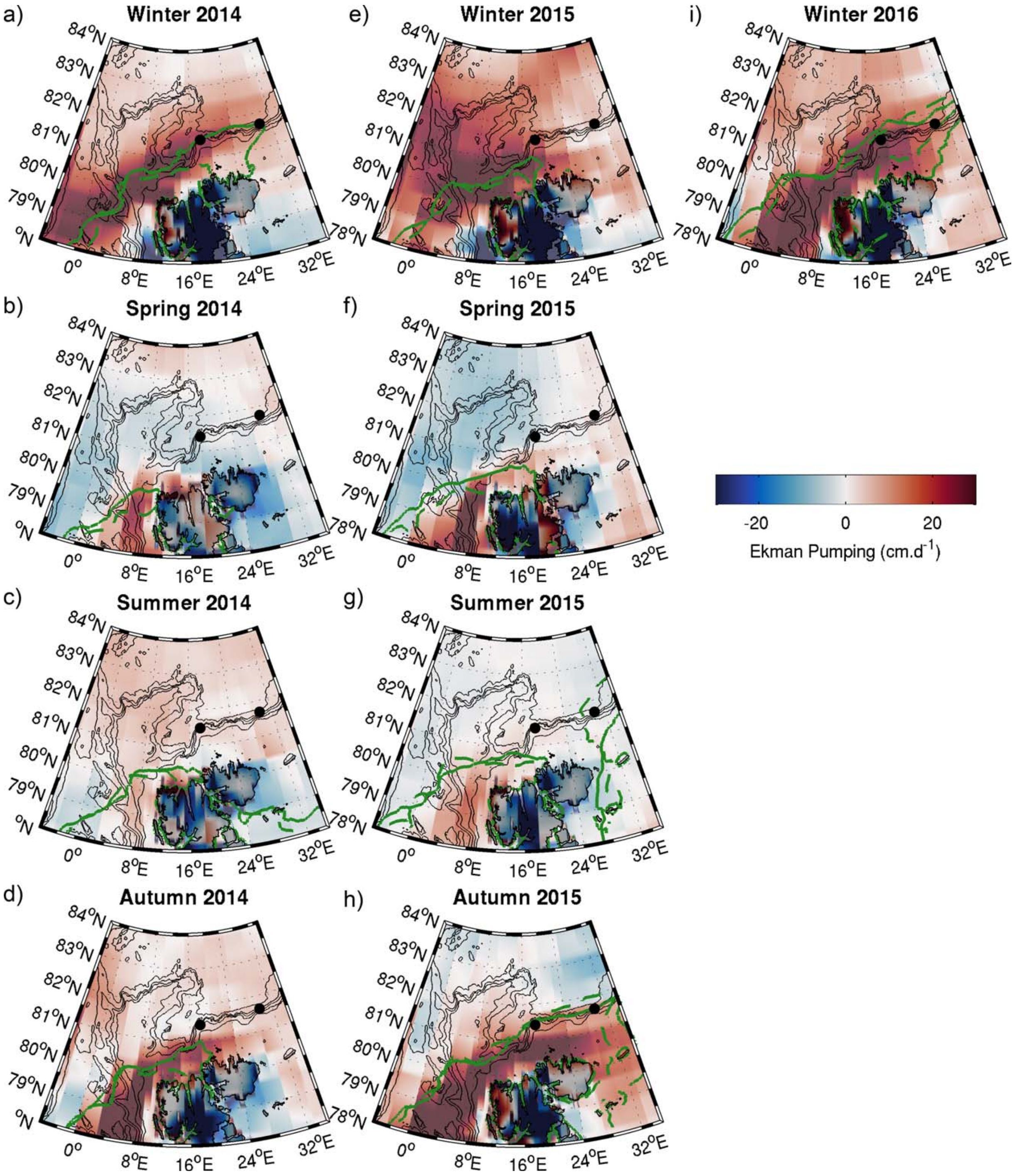

Figure 10. Ekman pumping (cm.d^{-1}) averaged every 3 months from January 2014 to March 2016. The Ekman pumping is computed from the wind stress from ECMWF (http://apps.ecmwf.int/datasets/data/interim-full-daily). The green solid line (green-dashed line) is the 15% mean sea ice cover contour from AMSR-2 (model outputs) over the period and is taken as the location of the ice edge. The thin black lines are the bathymetry contours. The black dots on the continental slope at 18°E and 30°E indicate the location of the shown profiles in Figure 12.

Time-latitude plots of wind intensity, air temperature, Ekman pumping, ocean velocity, and temperatures at 10 m provide some insight into the year-to-year variations at 18°E around the location of the N-ICE2015 drift in winter and at 30°E around the A-Twain mooring site [*Våge et al.*, 2016] (Figure 11). Wind speed and air

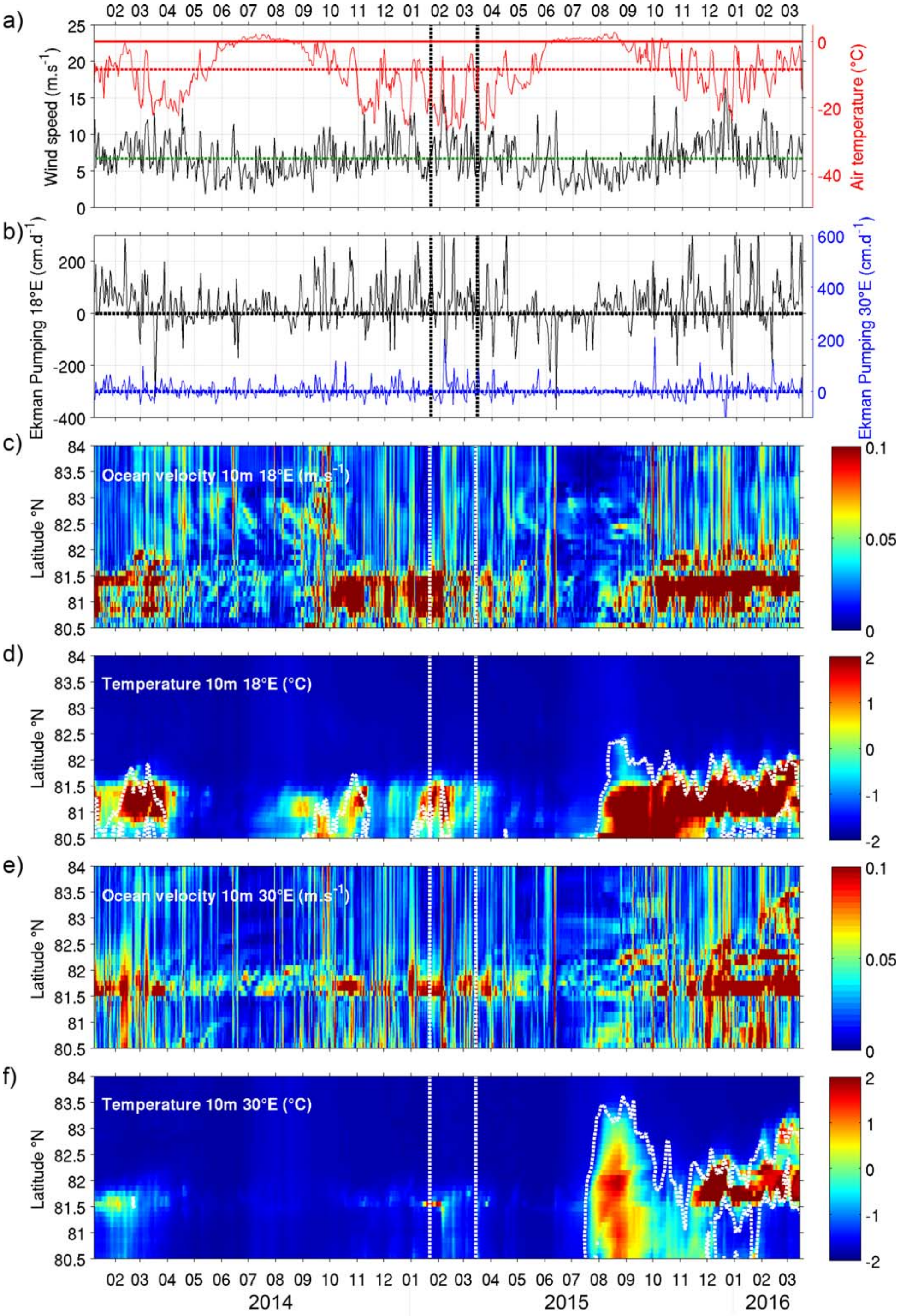

Figure 11. Evolution of model variables along 18°E and 30°E from January 2014 to April 2016. (a) Integrated wind speed over the latitudes at 18°E (ms^{-1}) (right axis). The dashed green line is the mean wind speed. (left axis) Integrated air temperature over the latitudes at 18°E. The dashed red line is the mean air temperature. (b) Ekman pumping (cmd^{-1}) averaged over the latitudes at 18°E (left axis) and 30°E (right axis). The black (blue) dashed line is the mean Ekman pumping at 18°E (30°E). (c) and (e) Ocean velocity of the layer centered at 10 m (ms^{-1}) at 18°E (30°E). (d) and (f) Model temperature of the layer centered at 10 m (°C) at 180°E (30°E). The dashed black line is the ice edge (the 15% isoline) from the model. The vertical dashed lines mark the beginning and the end of the in situ measurement from Floe 1 during N-ICE 2015 campaign.

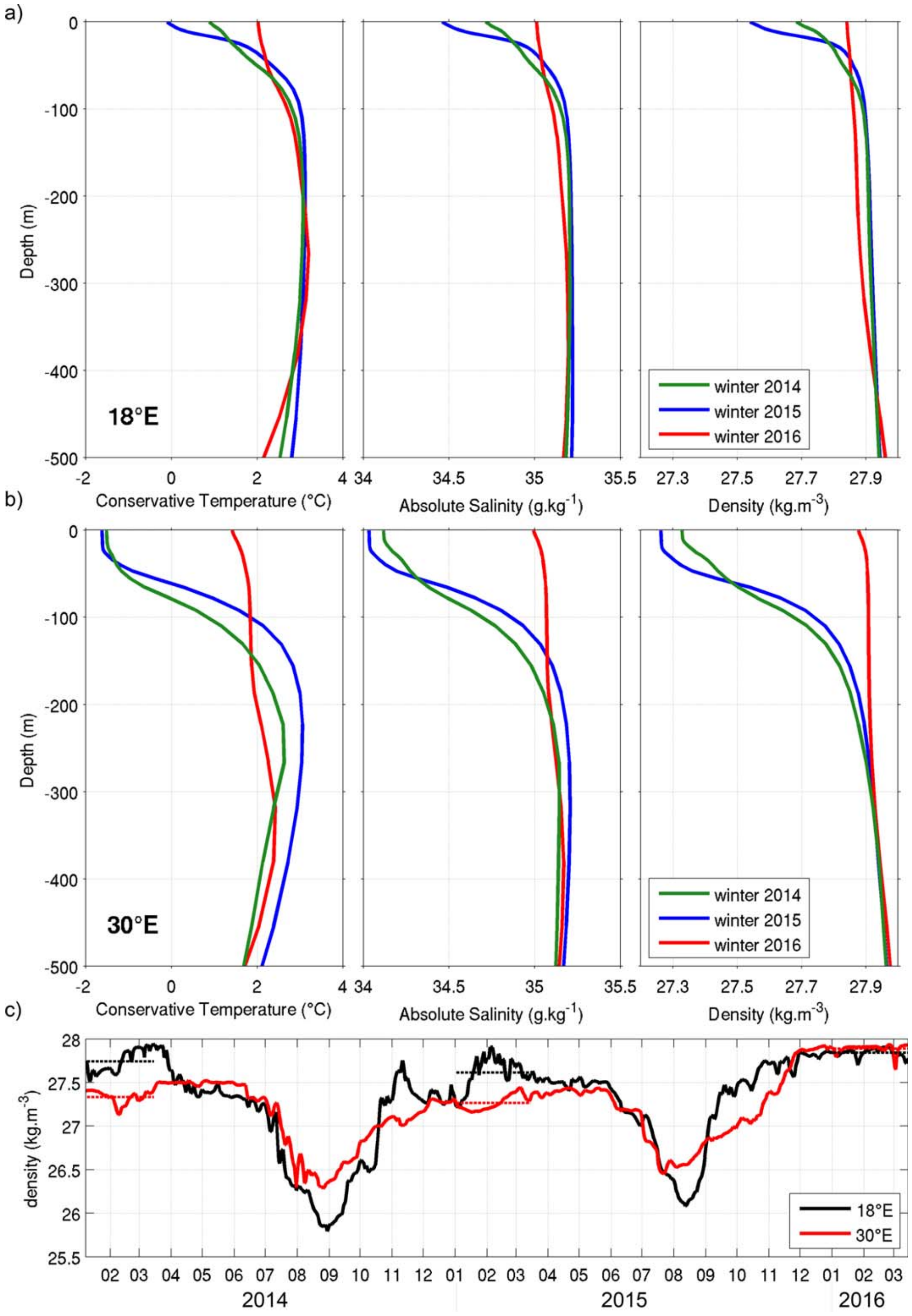

Figure 12. (a) Mean profiles of conservative temperature (°C), absolute salinity (g.kg^{-1}) and potential density (kg.m^{-3}) at 18°E, 81.4°N. (b) at 30°E, 81.85°N (black dots in Figures 9 and 10). The green profiles are averaged over winter 2014, the blue ones over winter 2015, and the red ones over winter 2016. (c) Time series of potential density (kg.m^{-3}) at 10m at 18°E, 81.4°N (in black), and at 30°E, 81.85°N (in red).

temperature time series are shown for only one site (18°E) as they do not differ much from one site to the other (Figure 11a). In contrast, Ekman pumping time series are strikingly different with values at 18°E almost one order of magnitude larger than those at 30°E (Figure 11b). At both locations, variations in ice cover are particularly striking and well correlated with ocean temperatures at 10 m with the open water in autumn

2015 and winter 2016 associated with temperatures larger than 2°C (Figures 11d and 11f). Ocean velocities at 10 m are dominated by the seasonal cycle with large values in autumn and winter and high-frequency variations reflecting wind forcing even under the ice (ice cover $>$ 15%) (Figures 11a, 11c, and 11e). The temperature and velocity time series in the AW layer do not show any significant year-to-year variation that could be directly related to the surface year-to-year variations (Figures 8c–8f, and temperature at 10 m in Figure 11).

Mean winter vertical profiles of ocean temperature, salinity and density at 18°E and 30°E over the continental slope differ from one winter to the other, with winter 2016 profiles (in red) being much less stratified, the difference being particularly striking at 30°E (Figures 12a and 12b). The time series of surface density show values larger than 27.55 kgm^{-3} each winter at 18°E (in black), whereas at 30°E winter 2016 stands out with values in excess of 27.8 kgm^{-3}, 0.5 kgm^{-3} above the winter 2014 or 2015 values (in red) (Figure 12c).

In winter 2014 and 2015, the slope at 30°E was covered with sea ice and near surface ocean water was much colder and fresher than in winter 2016 (Figures 9–12). In winter 2016, the slope at 30°E was ice-free and the very high ocean surface density values, the homogeneous vertical profiles over the water column and the rather small Ekman pumping suggest deep winter convective mixing in agreement with *Ivanov et al*. [2016]. The winter 2016 situation followed a rather warm and ice-free summer and autumn (Figures 9, 11a and 11f), favoring subsequent winter convective mixing [*Ivanov et al*., 2016]. In turn, the convection-induced upward heat flux maintained the area free of ice in winter 2016.

The slope at 18°E is at least partially ice-free during the three winters under consideration. Each winter wind-stress curl induced upwelling is large and probably plays an important role in upwelling warm water from the deep [*Falk-Petersen et al*., 2015]. The rather homogeneous vertical profiles over the water column in winter 2016 suggest however a contribution of convective mixing following the warm ice free summer and autumn as at the 30°E location.

6. Conclusions

Mercator ocean global operational system has been evaluated in the region of the Atlantic Water (AW) inflow, using historical data sets (e.g., the Fram Strait monitoring data) and contemporaneous data (satellite ice cover and IAOOS data collected during N-ICE2015 in winter). The model provides a realistic Atlantic Water inflow in Fram Strait that corresponds in intensity, temperature, and seasonal variations to historical observations in the West Spitsbergen Current (WSC) [*Beszczynska-Moller et al*., 2012]. The model also remarkably reproduces the hydrographical features observed by the IAOOS profilers in the Atlantic Water north of Svalbard in winter. Although the model is only eddy permitting and not fully eddy resolving in the Arctic, it produces mesoscale features that are consistent with those observed during the winter IAOOS drift. It helps interpretation of the in situ data in terms of warm water paths and eddy activity [*Koenig et al*., 2016].

Model outputs were used to examine the circulation of Atlantic Water at the entrance to the Arctic Ocean. Apart from recirculation branches to the West back into Fram Strait, the WSC splits into three warm water paths over and around the Yermak Plateau: the Svalbard Branch following the northern continental slope of the Svalbard Archipelago along the 400–500 m isobath [*Muench et al*., 1992], the Yermak Branch flowing along the western slope of the Yermak Plateau along the 1000 m isobath [*Manley et al*., 1992], and a third branch going through a narrow 700 m-deep depression in the Yermak Plateau, the Yermak Pass Branch, that was previously observed in deep float trajectories [*Gascard et al*., 1995].

The volume transports of the three branches ($T>2$°C) exhibit large seasonal variations in phase with the WSC volume transport that almost doubles in winter compared to summer [*Beszczynska-Moller et al*., 2012] (Table 1). The Yermak Pass Branch is mostly a winter feature associated with an overflow of the strong winter WSC. During the three winters of the model outputs (2014, 2015, and 2016), more than 70% of the WSC volume transport at 80°N goes through the Yermak Pass in winter, with a particularly large value (75%) in winter 2015 at the time of the IAOOS observations [*Koenig et al*., 2016]. The Yermak Pass Branch shows up as a warm feature in the AW layer crossed between the 6 and 13 February in both the observations and model outputs (Figure 4). Beyond the dominant seasonal variations, intraseasonal and year-to-year variations in the AW volume transport of the three branches above and around the Yermak Plateau can be almost as large as the mean amplitude (Table 1).

The three branches recombine further east along the Svalbard northern continental slope (Figure 1) and the volume transports in the AW layer along the slope at 12°E, 24°E, and 30°E show again a coherent seasonal cycle in phase with the WSC with large winter values. The heat content in the AW layer (T>2°C) decreases away from Fram Strait as expected and varies seasonally. Lags in the seasonal variations of the heat content time series provide rough estimates of advection time scales that are coherent with mean velocities (5 cms^{-1}) along the western (79 and 80°N) and northern (12, 24, and 30°E) continental slopes of Svalbard considered separately (Figure 7). However, correlations in heat content between 79°N and the sections further east (12, 24 and 30°E) cannot be established in a 2.25 year long-time series.

Although the eddy-permitting model (4–5 km grid) does not fully explicitly resolve the Rossby radius of deformation in this area (6–8 km) [*Zhao et al.*, 2014; *Nurser and Bacon*, 2013], outputs point out to a large mesoscale activity and a flow in form of pulses in the branches over and around the Yermak Plateau, and in the flow along the continental slope (Figure 8 and std values in Table 1). Mesoscale activity in the WSC and on the western side of the Yermak Plateau is in agreement with the literature [e.g., *Hattermann et al.*, 2016; *Kawasaki and Hasumi*, 2016]. Model also shows the detachment of eddies from the boundary current on the slope in agreement with the N-ICE2015 IAOOS observations [*Koenig et al.*, 2016] and observations at 30°E [e.g., *Våge et al.*, 2016].

Compared to 2016, winter 2015 stands out with colder air temperatures (mean −19°C versus −9°C), larger sea ice cover (mean ice cover around the Svalbard 76% versus 57%) and colder ocean temperatures at 10 m on the continental slope to the northeast of Svalbard (Figure 10). A qualitative consideration of the wind, ice extent, and temperature (surface atmosphere and 10 m depth ocean) sequence from January 2014 to April 2016 (Figure 9–12) tends to support the *Ivanov et al.* [2016] concepts that (i) the ice cover (wind forced ice drift) and water temperature in summer and autumn appear to “precondition” the situation for the coming winter and (ii) wind stress curl-induced ocean upwelling and convective mixing are key drivers for supplying ocean heat to the surface and maintaining an ocean ice free area in winter along the continental slope (section 5). The relative importance of Ekman pumping and convective mixing along the Svalbard continental slope in maintaining ice-free conditions in winter 2016 requires further analysis. The balance of ocean-atmosphere heat fluxes, not examined here, needs to be carefully examined as well.

The short-time span of the model outputs analyzed here (2.25 years) precludes any significant statistical analysis in a system with large year-to-year variations and expected long-term trends [*Lind and Ingvaldsen*, 2012; *Onarheim et al.*, 2014; *Ivanov et al*, 2012, 2016]. Such longer time scales trends and variability are the subject of future investigation since 10 years (2007–present) of date from the Mercator Ocean global operational model are now available.

Acknowledgements
This work was supported by the Equipex IAOOS (Ice Atmosphere Ocean Observing System) (ANR-10-EQPX-32-01), and by funding from the ICE-ARC program from the European Union 7th Framework Programme grant number 603887. Z. Koenig acknowledges a PhD scholarship from Université Pierre et Marie Curie (UPMC). This work has been supported by the Norwegian Polar Institute’s Centre for Ice, Climate and Ecosystems (ICE) through the N-ICE project. N-ICE acknowledges the in-kind contributions provided by other national and international projects and participating institutions, through personnel, equipment, and other support. The Mercator Ocean global operational system is part of the Copernicus Marine Environment Monitoring Service CMEMS (http://marine.copernicus.eu/). The IAOOS platform data are available at LOCEAN (Christine Provost, cp@locean-ipsl.upmc.fr).

References

Aksenov, Y., V. V. Ivanov, A. J. Nurser, S. Bacon, I. V. Polyakov, A. C. Coward, A. C. Naveira-Garabato, *and* A. Beszczynska-Moeller (2011), The Arctic circumpolar boundary current, *J. Geophys. Res.*, *116*, C09017, doi:10.1029/2010JC006637.

Beszczynska-Moller, A., E. Fahrbach, U. Schauer, and E. Hansen (2012), Variability in Atlantic water temperature and transport at the entrance to the Arctic Ocean, 1997–2010, *ICES J. Mar. Sci.*, *69*, 852–863.

Cokelet, E. D., N. Tervalon, and J. G. Bellingham (2008), Hydrography of the West Spitsbergen Current, Svalbard Branch: Autumn 2001, *J. Geophys. Res.*, *113*, C01006, doi:10.1029/2007JC004150.

Dmitrenko, I. A., B. Rudels, S. A. Kirillov, Y. O. Aksenov, V. S. Lien, V. V. Ivanov, U. Schauer, I. V. Polyakov, A. Coward, and D. G. Barber (2015), Atlantic water flow into the Arctic Ocean through the St. Anna Trough in the northern Kara Sea, *J. Geophys. Res. Oceans*, *120*, 5158–5178, doi:10.1002/2015JC010804.

Falk-Petersen, S., V. Pavlov, J. Berge, F. Cottier, K.M. Kovacs, and C. Lydersen (2015), At the rainbow’s end: High productivity fueled by winter upwelling along an Arctic shelf, *Polar Biol.*, *38*, 5–11, doi:10.1007/s00300-014-1482-1.

Gascard, J.-C., C. Richez, and C. Rouault (1995), New insights on large-scale oceanography in Fram Strait: The West Spitsbergen Current, in *Arctic Oceanography, Marginal Ice Zones and Continental Shelves*, vol. 49, edited by W. O. Smith and J. M. Greibmeier, pp. 131–182, AGU, Washington, D. C.

Granskog, M. A., P. Assmy, S. Gerland, G. Spreen, H. Steen, and L. H. Smedsrud (2016), Arctic research on thin ice: Consequences of Arctic sea ice loss, *Eos*, *97*, 22–26, doi:10.1029/2016EO044097.

Hattermann, T., P.E. Isachsen, W-J. von Appen, J. Albretsen, and A. Sundfjord (2016), Eddy-driven recirculation of Atlantic Water in Fram Strait, *Geophys. Res. Lett.*, *43*, 3406–3414, doi:10.1002/2016GL068323.

Hernandez, F., et al. (2015). Recent progress in performance evaluations and near real-time assessment of operational ocean products, *J. Oper. Oceanogr.*, *8*, suppl 2, s221–s238, doi:10.1080/1755876X.2015.1050282.

Hudson, S. R., and L. Cohen (2015), N-ICE2015 surface meteorology v1, Norwegian Polar Inst., Tromsø, Norway. [Available at https://data.npolar.no/dataset/056a61d1-d089-483a-a256-081de4f3308d.]

Ilıcak, M. et al. (2016), An assessment of the Arctic Ocean in a suite of interannual CORE-II simulations. Part III: Hydrography and fluxes, *Ocean Modell.*, *100*, 141–161, doi:10.1016/j.ocemod.2016.02.004.

Ivanov, V., I. Polyakov, I. Dmitrenko, E. Hansen, I. Repina, S. Kirillov, C. Mauritzen, H. Simmons, and L. Timokhov (2009), Seasonal variability in Atlantic Water off Spitzbergen, *Deep Sea Res., Part I*, *56*, 1–14.

Ivanov, V. V., V. A. Alexeev, I. A. Repina, N. V. Koldunov, and A. V. Smirnov (2012), Tracing Atlantic Water signature in the Arctic sea ice cover east of Svalbard, *Adv. Meteorol.*, *2012*, 11, doi:10.1155/2012/201818.

Ivanov, V., V. Alexeev, N. Koldunov, I. Repina, A. Sandø, L. Smedsrud, and A. Smirnov (2016), Arctic Ocean heat impact on regional ice decay: A suggested positive feedback, *J. Phys. Oceanogr.*, *46*, 1437–1456, doi:10.1175/JPO-D-15-0144.1

Jackson, K., J. Wilkinson, T. Maksym, D. Meldrum, J. Beckers, C. Haas, and D. Mackenzie (2013), A novel and low-coast sea ice mass balance buoy, *J. Atmos. Oceanic Technol.*, *30*, 2676–2688, doi:10.1175/JTECH-D-13-00058.1.

Kawasaki, T., and H. Hasumi (2016), The inflow of Atlantic water at the Fram Strait and its interannual variability, *J. Geophys. Res. Oceans*, *121*, 502–519, doi:10.1002/2015JC011375.

Koenig, Z., C. Provost, N. Villacieros-Robineau, N. Sennéchael, and A. Meyer (2016), Winter ocean-ice interactions under thin sea ice observed by IAOOS platforms during N-ICE 2015: Salty surface mixed layer and active basal melt, *J. Geophys. Res. Oceans*, *121*, 7898–7916, doi:10.1002/2016JC012195.

Kwok, R., G. Spreen, and S. Pang (2013), Arctic sea ice circulation and drift speed: Decadal trends and ocean currents, *J. Geophys. Res. Oceans*, *118*, 2408–2425, doi:10.1002/jgrc.20191.

Lellouche, J. M., et al. (2013), Evaluation of real time and future global monitoring and forecasting systems at Mercator Ocean, *Ocean Sci. Discuss.*, *9*, 1123–1185.

Lien, V. S., S. S. Hjøllo, M. D. Skogen, E. Svendsen, H. Wehde, L. Bertino, F. Counillon, M. Chevallier, and G. Garric (2016), An assessment of the added value from data assimilation on modeled Nordic Seas hydrography and ocean transports. *Ocean Modell.*, *99*, 43–59, doi: 10.1016/j.ocemod.2015.12.010.

Lind, S., and R. B. Ingvaldsen (2012). Variability and impacts of Atlantic Water entering the Barents Sea from the north, *Deep Sea Res., Part I*, *62*, 70–88.

Lique, C., and M. Steele (2012), Where can we find a seasonal cycle of the Atlantic water temperature within the Arctic Basin?, *J. Geophys. Res.*, *117*, C03026, doi:10.1029/2011JC007612.

Lique, C., and M. Steele (2013), Seasonal to decadal variability of Arctic Ocean heat content: A model-based analysis and implications for autonomous observing systems, *J. Geophys. Res. Oceans*, *118*, 1673–1695, doi:10.1002/jgrc.20127.

Madec, G. (2008), NEMO ocean engine. Note du pôle de modélisation, vol. 27, Inst. Pierre-Simon Laplace (IPSL), France.

Manley, T. O., R. H. Bourke, and K. L. Hunkins (1992), Near-surface circulation over the Yermak Plateau in northern Fram Strait, *J. Mar. Syst.*, *3*(1), 107–125.

McDougall, T. J., D. R. Jackett, F. J. Millero, R. Pawlowicz, and P. M. Barker (2012), A global algorithm for estimating Absolute Salinity, *Ocean Sci.*, *8*, 1123–1134.

Meyer A., et al., (2017), Winter to summer oceanographic observations in the Arctic Ocean north of Svalbard, *J.Geophys. Res.*, doi: 10.1002/2016JC012391.

Muench, R. D., M. G. McPhee, C. A. Paulson, and J. H. Morison (1992), Winter oceanographic conditions in the Fram Strait-Yermak Plateau region. *J. Geophys. Res.*, *97*(C3), 3469–3483.

Nurser, A. J. G., and S. Bacon (2013), Eddy length scales and the Rossby radius in the Arctic Ocean, *Ocean Sci. Discuss.*, *10*(5), 1807–1831.

Onarheim, I. H., L. H. Smedsrud, R. B. Ingvaldsen, and F. Nilsen (2014), Loss of sea ice during winter north of Svalbard, *Tellus Ser. A*, *66*, 1600-0870, doi:10.3402/tellusa.v66.23933.

Pham, D. T., J. Verron, and M. C. Roubaud (1998), A singular evaluative extended Kalman filter for data assimilation in oceanography, *J. Mar. Syst.*, *16*, 323–340.

Provost, C., et al. (2015), Ice-atmosphere-Arctic ocean observing system, 2011–2019, *Mercator Ocean Quart. Newsl., Mercator Ocean*, *51*, 13–15. [Available at http://www.mercator-ocean.fr/eng/actualitesagenda/newsletter/newsletter-Newsletter-51-Special-Issue-with-ICE-ARC.]

Rudels, B. (2012), Arctic Ocean circulation and variability–advection and external forcing encounter constraints and local processes. *Ocean Sci.*, *8*(2), 261–286, doi:10.5194/os-8-261-2012.

Rudels, B., R. Meyer, E. Fahrbach, V. V. Ivanov, S. Østerhus, D. Quadfasel, U. Schauer, V. Tverberg, and R. A. Woodgate (2000), Water mass distribution in Fram Strait and over the Yermak Plateau in summer 1997. *Ann. Geophys.* *18*(6), 687–705.

Ryan, A. G., et al. (2015). GODAE Ocean View Class 4 forecast verification framework: Global ocean inter-comparison, *J. Oper. Oceanogr.*, *8*(S1), s98–s111.

Sirevaag, A., S. D. L. Rosa, I. Fer, M. Nicolaus, M. Tjernström, and M. G. McPhee (2011), Mixing, heat fluxes and heat content evolution of the Arctic Ocean mixed layer, *Ocean Sci.*, *7*(3), 335–349, doi:10.5194/os-7-335-2011.

Thorndike, A. S., and R. Colony (1982), Sea ice motion in response to geostrophic winds, *J. Geophys. Res.*, *87*(C8), 5845–5852.

Våge, K., R. S. Pickart, V. Pavlov, P. Lin, D. J. Torres, R. Ingvaldsen, A. Sundfjord, and A. Proshutinsky (2016), The Atlantic Water boundary current in the Nansen Basin: Transport and mechanisms of lateral exchange, *J. Geophys. Res. Oceans*, *121*, 6946–6960, doi:10.1002/2016JC011715.

Von Appen, W.-J., U. Schauer, T. Hattermann, and A. Beszczynska-Möller (2016), Seasonal cycle of mesoscale instability of the West Spitsbergen Current, *J. Phys. Oceanogr.*, *46*, 1231–1254, doi:10.1175/JPO-D-15-0184.1.

Zhao, M., M.-L. Timmermans, S. Cole, R. Krishfield, A. Proshutinsky, and J. Toole (2014), Characterizing the eddy field in the Arctic Ocean halocline, *J. Geophys. Res. Oceans*, *119*, 8800–8817, doi:10.1002/2014JC010488.

3.3 Perspectives

3.3.1 Influence of the Atlantic Water layer on biology over the Yermak Plateau

Atlantic Water brings nutrient in the Arctic and is key to the development of phytoplantkon blooms in the Arctic (*Randelhoff et al.*, 2015). During the N-ICE2015 expedition, a phytoplankton bloom was documented under sea-ice heavily loaded with snow, and the biology samples suggested that the bloom developed under sea ice (*Assmy et al.*, 2017), a case never observed before.

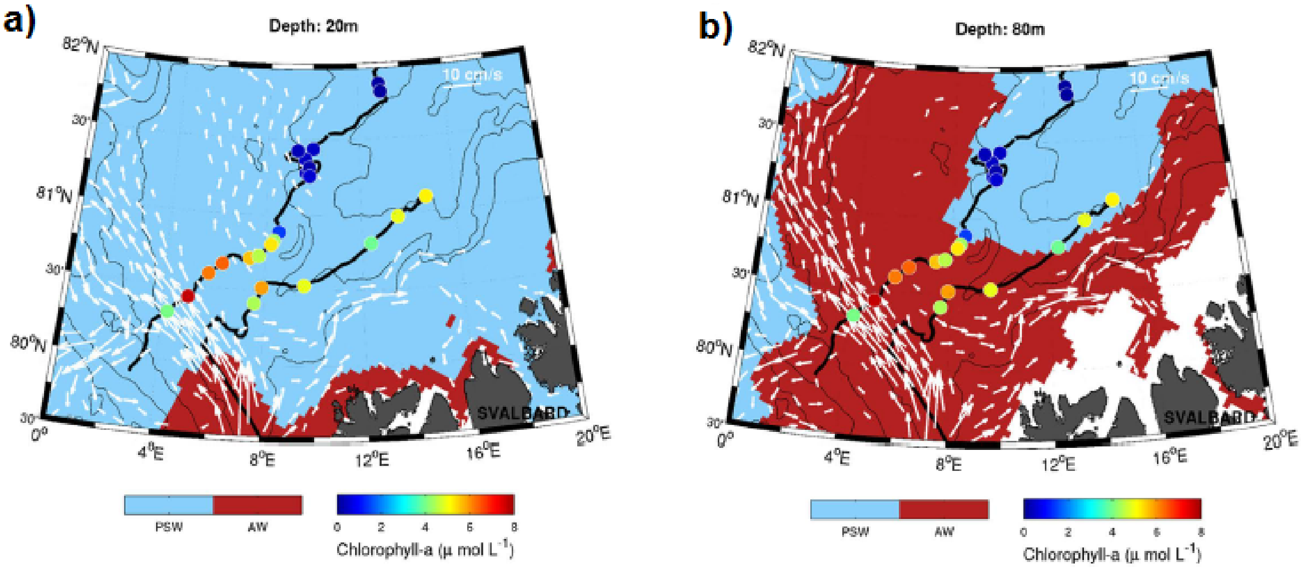

Figure 3.1: *Map of (a), surface (20 m) and (b), subsurface (80 m) simulated currents from model outputs with currents > 2cm/s. Current velocity is indicated by the size of the vectors (scale on figure). Black lines show drift trajectories. Colour dots show surface Chl a concentrations as measured along track indicating the bloom locations. Background colours show surface and subsurface water masses where blue is Polar Surface Water (PSW) and red is Atlantic Water (AW). Areas shallower than* 20m *(c) and* 80m *(d) are white. Topography of the Yermak Plateau is shown as thin black lines (500, 1000, 2000 and 3000 m). From Assmy et al. (2017).*

I contributed to this study by bringing physical evidence to sustain the hypothesis of the development of a phytoplankton bloom under the sea ice. I used the Mercator Ocean 1/12° model outputs, that represents reasonably well the hydrography and ocean circulation in the region north of Svalbard (*Koenig et al.*, 2017a). The surface ocean circulation deduced from the model outputs current data comforts this assumption (Figure 3.1). Indeed, surface waters over the Yermak Plateau are waters recirculating over the Plateau and they do not come from a foreign area.

Currents bringing water on the Yermak Plateau are weak and do not advect substantial waters from the ice edge in less than 6 weeks, age of the phytoplankton bloom when observed during the N-ICE2015 expedition.

Over the Yermak Plateau, Atlantic Water is quite shallow and the mixing documented during N-ICE2015 is large enough to advect nutrients to the surface and feed the phytoplankton bloom (*Meyer et al.*, 2017b). Finally, leads provide enough sunlight to initiate and sustain the bloom. The development of phytoplankton blooms under the sea ice could be one evidenceof the climate change-induced modification of the Arctic productivity. The full text of *Assmy et al.* (2017) is in the Appendix.

3.3.2 The Atlantification of the Eurasian Basin

Winter 2016 differs significantly from the previous winter in the area North of Svalbard, with large ice-free area extending far east along the Svalbard Continental slope (*Koenig et al.*, 2017a). It has recently been shown that over the continental slope winter convection occurs and carries heat from the Atlantic Water layer up to the surface and melts sea ice (*Koenig et al.*, 2017a; *Ivanov et al.*, 2016). This dynamic and the large sea ice melt associated with it in winter along the continental slope over Atlantic Water is now not only observed north of Svalbard but also in the entire Eurasian Basin.

The loss of sea ice in the Eurasian Basin during the last few years suggests that the eastern Eurasian Basin, usually year-round covered by sea ice, is becoming similar to the western Nansen Basin, seasonally covered by sea ice. This phenomenon is called the "Atlantification" of the Arctic (*Polyakov et al.*, 2017), (Figure 3.2). The shoaling of the Atlantic Water observed north of Svalbard is now observed farther east along the continental slope (*Polyakov et al.*, 2017). Furthermore, the strong seasonal cycle in the Atlantic Water core temperature is now observed in the center of the Laptev Sea (*Polyakov et al.*, 2017).

Changes associated with the "Atlantification" of the Eurasian Basin, e.g. weakened stratification, increased vertical mixing and sea ice decline, will have important consequences on the biogeochemisty and physic of the Arctic Ocean system. Indeed, these changes could alter the atmosphere-ocean interactions, the freshwater storage and export, increase the primary production and change the Arctic ocean response to acidification (*Polyakov et al.*, 2017). The source of changes associated to the Atlantification of the eastern Eurasian basin is still under debate. The local increase of the Ekman pumping is not large enough to substantially contribute to the warming of the Eurasian Basin. Instead, it seems that the source of changes relies on processes beginning upstream of the eastern Eurasian basin, probably between Fram Strait and North of Svalbard (*Polyakov et al.*, 2017).

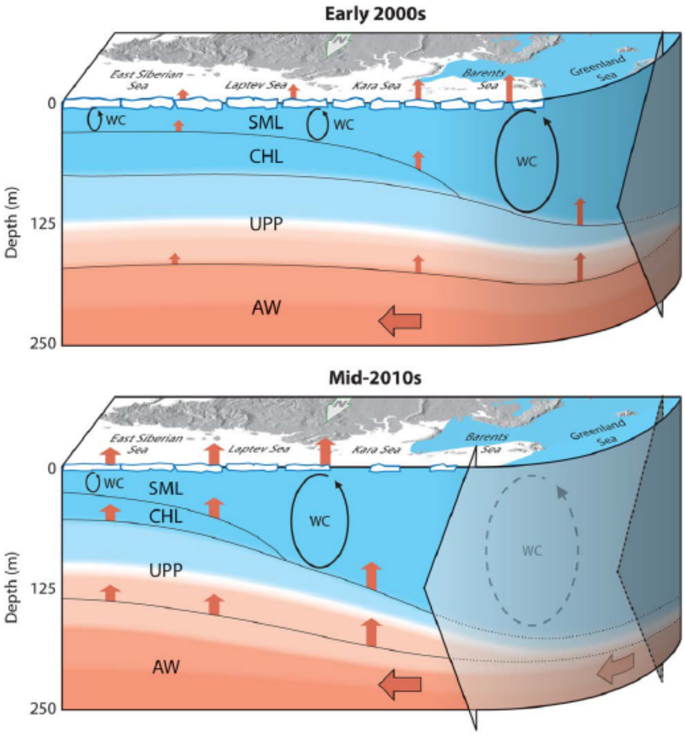

Figure 3.2: *Model of "Atlantification" of the eastern Eurasian Basin continental margin in recent years. The broad arrows show the encroachment of a series of processes associated with the Atlantification; these are 1- increased penetration of surface signature of AW (increased flow, heat content or both) into the eastern eurasian basin. 2- reduction in sea ice cover resulting in 3- greater surface heat and moisture flux and 4- increased depth of winter penetrative convection, bringing additional heat and nutrients from AW into the Arctic Surface water and transformation of the permanent cold halocline layer (CHL) to a seasonal halocline. SML and UPP indicate the surface mixed layer and upper permanent pynocline. WC shows winter convection; red arrows indicate upward heat fluxes. Horizontal red arrows show inflows. From Polyakov et al. (2017).*

Chapter 4

The Atlantic Water inflow through the Yermak Pass Branch

Contents

4.1 Introduction

We suggested in the previous chapter (*Koenig et al.*, 2017a) that the Yermak Pass Branch is a winter pathway of the Atlantic Water inflow through the Yermak Plateau. The evidence is mainly based on model outputs analysis, and needs to be confirmed by *in situ* observations. At our knowledge, the only other published evidence is the drift of 3 neutral-buoyant floats at 350m through the pass in winter 1988 (*Gascard et al.*, 1995). The existence of the Yermak Pass Branch is also suggested in *Saloranta and Haugan* (2001). After the passage of the floats in the Yermak Pass, Jean-Claude Gascard in the framework of the Damocles European project deployed an upward-looking Acoustic Doppler Current Profiler (ADCP) for more than a year (July 2007 - September 2008) in the Yermak Pass. We took advantage of these data to analyze in more detail the current in the Yermak Pass.

The next section is composed of the paper that has just been accepted in *Journal of Geophysical Research:Ocean*. I reformatted the draft here for sake of readability.

4.2 The Yermak Pass Branch, a major pathway for the Atlantic Water north of Svalbard?

The Yermak Pass Branch, a major pathway for the Atlantic Water north of Svalbard?

ZOE KOENIG, CHRISTINE PROVOST, NATHALIE SENNECHAEL, GILLES GARRIC AND JEAN-CLAUDE GASCARD

July 2017

Abstract

An upward-looking Acoustic Doppler Current Profiler deployed from July 2007 to September 2008 in the Yermak Pass, north of Svalbard, gathered velocity data from $570m$ up to $90m$ at a location covered by sea-ice 10 months out of 12. Barotropic diurnal and semi-diurnal tides are the dominant signals in the velocity (more than 70% of the velocity variance). In winter, baroclinic eddies at periods between 5 and 15 days and pulses of one-to-two month periodicity are observed in the Atlantic Water layer and are associated with a shoaling of the pycnocline. Mercator-Ocean global operational model outputs with 1/12 degree and daily resolution is shown to have skills in representing low frequency velocity variations (>1 month) in the West Spitsbergen Current and in the Yermak Pass. Model outputs suggest that the Yermak Pass Branch has had a robust winter pattern over the last 10 years, carrying on average 31% of the Atlantic Water volume transport of the West Spitsbergen Current (36% in autumn/winter). However those figures have to be considered with caution as the model neither simulates tides nor fully resolves eddies and ignores residual mean currents that could be significant.

Introduction

The Atlantic Water (AW) supplies heat and salt to the Arctic Ocean impacting the thermohaline structure of the water column and influencing the distribution of sea ice (*Rudels*, 2012). Despite the importance of AW to the Arctic system, the AW inflow (pathways and volume transports) north of Svalbard is still poorly documented in part because of the large sea ice cover at all seasons.

In Fram Strait, the Atlantic Water flows along the west coast of Svalbard through the West Spitsbergen Current (WSC) (Figure 1a). The WSC has been monitored since 1997 with a mooring array deployed at $78.5°N$ in collaboration between the Norwegian Polar Institute (NPI, Norway) and the Alfred-Wegener Institute (AWI, Germany). The seasonal variability of the Atlantic Water inflow is important, with a stronger and warmer flow in winter than in summer in the WSC (*Beszczynska-Möller et al.*, 2012). The WSC is unstable (*Teigen et al.*, 2010a,b) thereby generating eddies in the Fram Strait. The Yermak Plateau located to the northwest of Svalbard is a main obstacle to the warm AW inflow into the Arctic and the WSC splits into branches as isobaths diverge (Figure 1a). One branch, the shallow Svalbard Branch, follows the 400-500m isobaths of the continental slope inshore of the Yermak Plateau (*Sirevaag et al.*, 2011; *Muench et al.*, 1992; *Cokelet et al.*, 2008). Other branches recirculate cyclonically following the topographic fracture zones (FZ) (Molloy FZ at $79°N$ and Spitzbergen FZ at $80.5°N$)

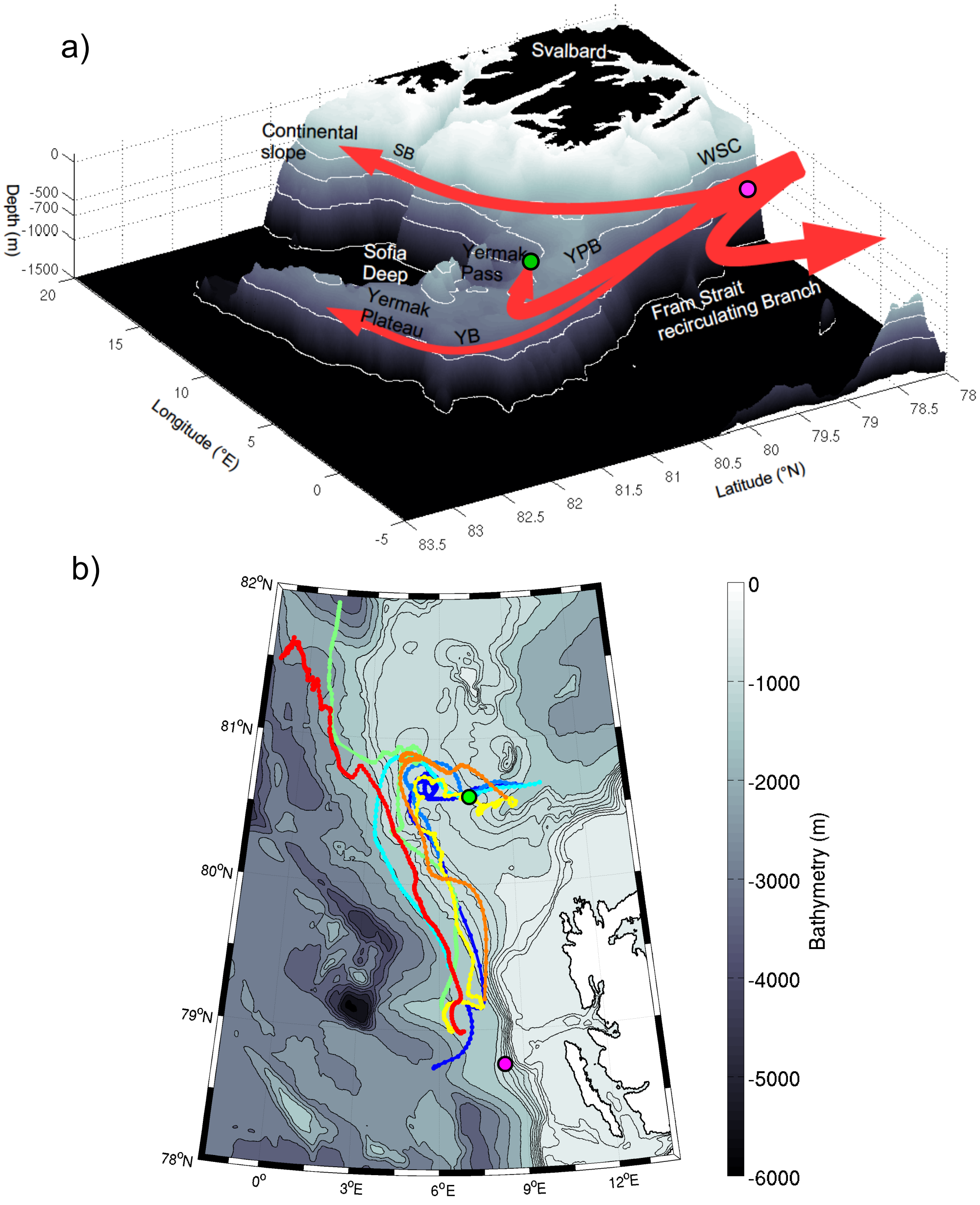

Figure 1: *a) 3D schematic of the Atlantic water inflow north of Svalbard. The red arrows represent the pathways of the Atlantic Water across and around the Yermak Plateau. WSC : West Spitsbergen Current; SB : Svalbard Branch; YB : Yermak Branch ; YPB : Yermak Pass Branch. The white lines are the 500, 700, 1000 and 1500m isobaths. b) Trajectory of the 310-340 m floats that were deployed in fall 1988 north of Svalbard and drifted through the Yermak Pass (Gascard et al., 1995). The magenta dot indicates the location of mooring F2 from the Fram Strait mooring array and the green dot the location of the mooring in the Yermak Pass. Background is the bathymetry from IBCAO (http://www.ngdc.noaa.gov/mgg/bathymetry/arctic/arctic.html). Isobaths are plotted every 200m until 1000m*

directly through Fram Strait (*Teigen et al.*, 2010b). The Fram Strait recirculating branches are largely dominated by eddies (*Gascard et al.*, 1995; *Von Appen et al.*, 2016; *Hattermann et al.*, 2016). Another branch, the deeper Yermak branch flows along the western shelf of the Yermak Plateau above the 1500 m isobath (*Manley et al.*, 1992; *Manley*, 1995). Yet, another path, the

Yermak Pass Branch, was discovered using acoustically-tracked neutrally buoyant floats during the ARCTEMIZ88 experiment (*Gascard et al.*, 1995). Five floats, stabilized around 310-350 m, made a spectacular U turn at about $80.8°N$ following the 700-800 m isobaths and crossed the Yermak Plateau through the Yermak Pass in the fall 1988 (Figure 1b). The lack of year-round observations over the ice-covered Yermak Plateau may explain why the Yermak Pass Branch has not been documented since the unique float drifts of fall 1988.

Twenty-eight months (January 2014 - April 2016) of outputs from Mercator-Ocean global operational system have been used, after a careful evaluation, to examine the circulation of Atlantic Water at the entrance to the Arctic ocean (*Koenig et al.*, 2017). The model outputs present a branching of the WSC as sketched in Figure 1a. The volume transports of the AW inflow ($T > 2°C$) in the three branches, Svalbard Branch, Yermak Branch and Yermak Pass Branch, exhibit large seasonal variations in phase with the WSC volume transport that almost doubles in winter compared to summer (*Beszczynska-Möller et al.*, 2012). The Yermak Pass Branch is mostly a winter feature associated with an overflow of the strong winter WSC (*Koenig et al.*, 2017). Although the eddy-permitting model (4–5 km grid) does not fully resolve the Rossby radius of deformation in this area (6–8 km) (*Zhao et al.*, 2014; *Nurser and Bacon*, 2013), outputs point out to a large mesoscale activity and a flow in form of pulses in the branches over and around the Yermak Plateau, and along the continental slope in agreement with observations (*Gascard et al.*, 1995; *Hattermann et al.*, 2016; *Kawasaki*, 2016; *Koenig et al.*, 2016; *Våge et al.*, 2016).

The objective of the work presented here is to re-examine the flow through the Yermak Pass taking advantage of (1) the yet unpublished year-long current time series from a mooring deployed in the middle of the Yermak Pass from July 2007 to September 2008 (Figure 1) and (2) the 10 year (2007-present) outputs from the Mercator-Ocean global operational model. The northern location of the mooring, almost covered by sea ice during the entire year, makes this dataset unique and the realistic operational model outputs help putting the year-long point measurements in a larger spatial and temporal context.

The paper is organized as follows. Section 2 presents the mooring data, environmental context, and the model outputs used. Section 3 describes the statistics and spectral content of the velocity time series. Tides appear as a major contributor to velocity variations. We removed the dominating high frequency signals with periods less than 2 days and focused on lower frequency variations. In section 4, the model outputs are shown to have skills in representing low frequency velocity variations in Fram Strait and in the Yermak Pass. The model outputs are then used to examine the variations in the AW inflow in the WSC and in the different branches downstream. Section 5 summarizes and discusses the results.

1 Data and environmental context

1.1 Yermak Pass mooring data

The mooring was deployed on 25 July 2007 from the *R/V Haakon Mosby* at $80.601°N$, $7.119°E$ (depth of $745m$) (green dot in Figure 1). It comprised an upward-looking RDI 75kHz Long Ranger Acoustic Doppler Current Profiler (ADCP) at $585m$ with $16m$ vertical resolution and a 1 hour sampling time, and an ocean profiler on a taut cable between 130 and $530m$ (*Gascard et al.*, 2017). The mooring was recovered on 23 September 2008 by the K/V Svalbard. The profiler did not record any data and the ADCP provided velocity data over more than a year.

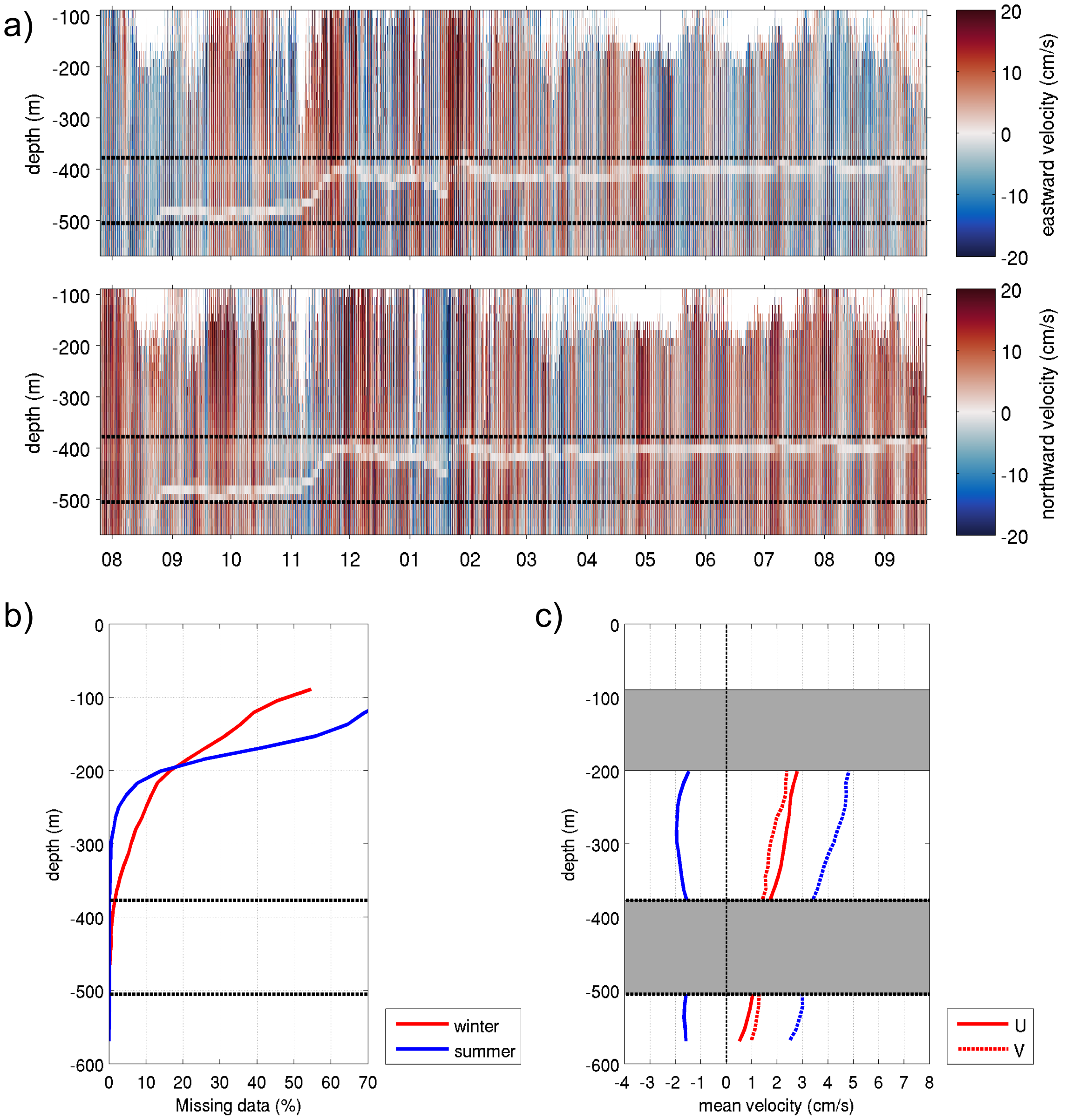

Figure 2: *a) Raw velocity time series from the ADCP in the Yermak Pass from 25 July 2007 to 23 September 2008. a) : eastward velocity (upper panel) and northward velocity (lower panel) (hourly resolution). X-axis is time in month. The shadow of the profiler shows up as a white feature between* 505 *and* 377m*. The black dashed lines delimitate the bins affected by the acoustic shadow of the profiler. b) Percentage of missing ADCP data as a function of depth, during winter in red and summer in blue. c) Mean velocity profiles (in* cm/s*). In red : winter. In blue : summer. Thick lines : eastward component. Dashed lines : northward component. The grey area is the depth not analyzed in the study because of the shadow of the profiler or of the lack of data.*

There are no simultaneous temperature data except for those presented in *Fer et al.* (2010) that were obtained during the deployment cruise. The mooring is located between stations 2 and 3 describd in *Fer et al.* (2010). These stations indicate the presence of Atlantic waters up to 25m (*Fer et al.*, 2010) (their Figure 4).

Figure 2 displays the raw data from the ADCP, after declination correction. A white shaded zone is visible in the data between 380 and 500m depth throughout the time series. It corresponds to the reflection of the acoustic bins on the profiler stuck on the cable. We ignored the data between 377m and 505m which are polluted by the profiler reflection. The upper 90m are not sampled and data are often missing above 200m especially during summer. The vertical extent of the data is probably limited by the steep pycnocline between the Atlantic and Polar Surface Waters. The scarce hydrological observations around this location document variable depths for the steep pycnocline (e. g. 25m in *Fer et al.* (2010); 150 m in *Meyer et al.* (2017a)). In particular, at the beginning of the time series, in July 2007, the ADCP provides data up to 90m in concordance with the shallow pycnocline observed during the deployment cruise (*Fer et al.*, 2010). The velocity time series at 570m is complete. The percentage of available data decreases upwards and varies with season (Figure 2b). In summer (April-September) more than 50% of data missing are in the upper 150m while time series below 300m are complete. In winter (October-March), only 35% of the data are missing at 150m, while data gaps propagate quite deep with still 5% of missing data at 300m. Mean velocity component profiles (Figure 2c) differ from summer to winter. In summer, current is orientated northwest, while in winter it is northeast. Means and standard deviations of velocity components and amplitude at different depths and with several length low-pass filtering are gathered in Table 1.

cm/s		**Total**			**Summer**			**Winter**		
		U	**V**	**Amplitude**	**U**	**V**	**Amplitude**	**U**	**V**	**Amplitude**
570m (100%)	**Full**	-0.7	1.8	10.5	-1.4	2.4	10.0	0.5	1.0	11.3
		(8.5)	(8.2)	(5.6)	(7.6)	(7.5)	(4.9)	(9.4)	(8.9)	(6.3)
	50d	-0.67	1.8	4.6	-1.4	2.4	3.6	0.5	1.0	5.5
		(3.7)	(3.3)	(2.7)	(2.1)	(2.0)	(1.7)	(4.7)	(4.1)	(3.2)
	20d	-0.68	1.9	3.0	-1.4	2.3	2.9	0.5	1.0	2.7
		(2.1)	(1.9)	(1.8)	(1.2)	(0.9)	(1.0)	(2.3)	(1.8)	(1.6)
300m (97%)	**Full**	-0.2	3.2	12.3	-1.9	3.9	11.4	2.3	1.8	13.6
		(9.5)	(9.5)	(6.3)	(8.0)	(8.6)	(5.3)	(10.8)	(10.5)	(7.2)
	50d	-0.15	3.1	7.0	-1.9	4.0	6.2	2.2	1.7	8.0
		(5.5)	(4.8)	(3.7)	(3.4)	(3.9)	(2.9)	(6.6)	(5.6)	(4.4)
	20d	-0.13	3.2	5.2	-1.9	3.9	5.1	2.2	1.7	5.2
		(4.1)	(2.9)	(2.7)	(2.3)	(2.4)	(2.1)	(4.7)	(2.8)	(3.4)
250m (94%)	**Full**	-0.05	3.7	12.9	-2.0	4.3	6.5	2.5	2.2	14.5
		(9.9)	(10.0)	(6.7)	(8.2)	(8.8)	(5.5)	(11.5)	(11.2)	(7.8)
	50d	-0.05	3.5	7.6	-2.0	4.3	6.5	2.5	1.9	8.7
		(6.0)	(5.2)	(4.1)	(3.6)	(4.2)	(3.2)	(7.2)	(6.1)	(4.9)
	20d	-0.06	3.5	5.7	-2.0	4.3	5.4	2.7	2.0	5.7
		(4.5)	(3.0)	(3.0)	(2.5)	(2.6)	(2.3)	(5.2)	(3.0)	(3.7)

Table 1: *Mean and standard deviation (in parenthesis) (cm/s) of velocity time series at different depths (570, 300 and 250m) and different seasons from the ADCP. The percentage is the percentage of available data at each depth over the time series. U : eastward velocity. V : northward velocity. Total : July 2007-September 2008. Winter : October 2007-March 2008. Summer : April 2008- September 2008. Full : full time resolution time series. 50h : time series filtered with a 50-hour low-pass butterworth filter. 20d : time series filtered with a 20-day low-pass butterorth filter.*

1.2 Ice cover and atmospheric surface conditions at the mooring location

The mooring was deployed a few kilometers from the ice edge and was recovered in the middle of ice floes. Sea-ice concentration from AMSR-E data (daily, $12.5km$ spatial resolution, https://nsidc.org/data/amsre) indicates that the mooring was under sea ice ten months out of twelve (Figure 3b). The mooring was located north of the mean position of the ice edge (Figure 4). Note that in this region, the ice edge is shifted further south in summer than in winter (Figure 4).

Era-Interim reanalysis outputs (*Dee et al.*, 2011) were used to document atmospheric surface conditions at the mooring location. Wind intensity (Figure 3c) and surface temperature (not shown) feature a large seasonal cycle with distinct signature of strong synoptic events in winter. The wind speed shows larger mean and standard deviation from October to March (winter) (mean $8.7m/s$, standard deviation (std) $3.7m/s$) than from April to September (summer) ($5.5m/s$ and $2.7m/s$). Surface temperatures are positive from June to September and reach values below $-20°C$ from December to April (not shown). A succession of storms is observed from October to March with velocities in excess of $15m/s$ associated with temperature peaks and sea level pressure drops (below $980hPa$ on several occasions, not shown).

1.3 Tidal model and ocean operational model

We used the Arctic Ocean Tidal Inverse Model (AOTIM-5) (*Padman and Erofeeva*, 2004) to estimate the tidal current velocities associated with the eight most energetic tidal components (M_2, S_2, N_2, K_2, O_1, K_1, P_1, Q_1) at the mooring location (Figure 3d). The model provides barotropic tidal velocities on a $5km$ horizontal resolution grid. The model current speeds are large with values exceeding $20cm/s$ and exhibit a striking fortnightly modulation corresponding to the beat period between O_1 and K_1. The fortnightly oscillations constitute the upper and lower envelope of the diurnal variations (Figure 3d). A visual comparison with the current speeds observed at the deepest bin of the ADCP ($570m$) (Figure 3e) suggests that AOTIM-5 model performs rather well and that tides dominate the velocity signal.

We also examined operational ocean model daily outputs to put the mooring data in a continuous and larger spatial and temporal 2007-2016 context. The model is the global ocean operational model system developed at Mercator-Ocean for the Copernicus Marine Environment Monitoring Service (CMEMS; http://marine.copernicus.eu/), with a 1/12° horizontal resolution and z-50 vertical levels. The system is based on the NEMO (Nucleus for European Modelling of the Ocean; *Madec and Team* (2008)) platform and uses a multi-data and multivariate reduced order Kalman filter based on the Singular Extended Evolutive Kalman (SEEK) filter formulation introduced by *Pham et al.* (1998). The model uses the LIM2 thermodynamic-dynamic sea ice model and is driven at the surface by atmospheric analysis and forecasts from the IFS (Integrated Forecasting System) operational system at ECMWF (European Centre for Medium-Range Weather Forecasts). The assimilated observations are along-track satellite altimetry, sea surface temperature (SST), and in situ vertical profiles of temperature and salinity. The data assimilation scheme is fully operational for SST warmer than $-1°C$ and is switched off for SST colder than the freezing point (in ice covered areas). Sea ice concentration derived from IFREMER/CERSAT satellite data (*Ezraty et al.*, 2007) is assimilated in this version of the model. Full description of the system components is available in (*Lellouche et al.*, 2013). The system starts in October 2006 from a "cold" start (initial currents are null) and from World Ocean Atlas 2013 global temperature and salinity climatology. The model outputs are compared to the mooring F2 of the Fram Strait mooring array in the core of the WSC at 78.4°N (magenta dot in Figure 1) (*Beszczynska-Möller et al.*, 2015). Comparisons, presented in section 4, are rather satisfactory

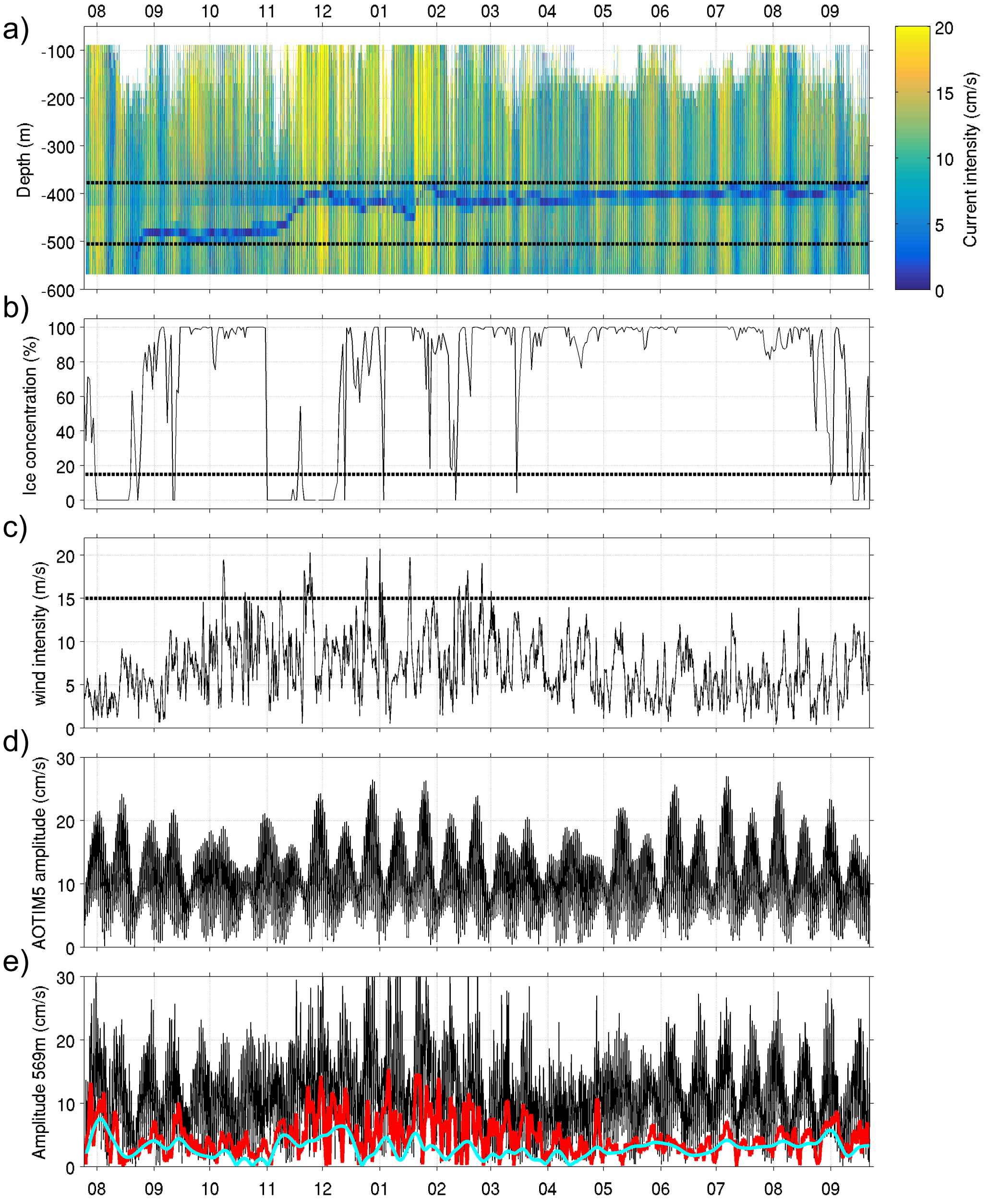

Figure 3: *Time series of several variables at the mooring location. a) Velocity intensity from* 580 *to* 90*m (in cm/s) deduced from the ADCP (hourly resolution). X-axis is time in month. The black dashed lines delimitate the bins affected by the acoustic shadow of the profiler. b) Ice concentration (%) from AMSR-E satellite data, one day time resolution and* 12.5*km spatial resolution. The dashed line highlights* 15% *concentration, usually considered as the ice edge. c) wind intensity (m/s) from Era Interim Reanalysis. The dashed line (*15*cm/s) can be considered as a criterion for storms e) Barotropic tide velocity amplitude (in cm/s) deduced from AOTIM-5 model (Padman and Erofeeva, 2004) . f) ADCP velocity amplitude at* 570*m (in cm/s), in black : full time resolution (hourly), in red : filtered with a 50-hour low pass Butterworth filter, in blue : filtered with a 20-day low pass Butterworth filter.*

(the mooring data are not assimilated).

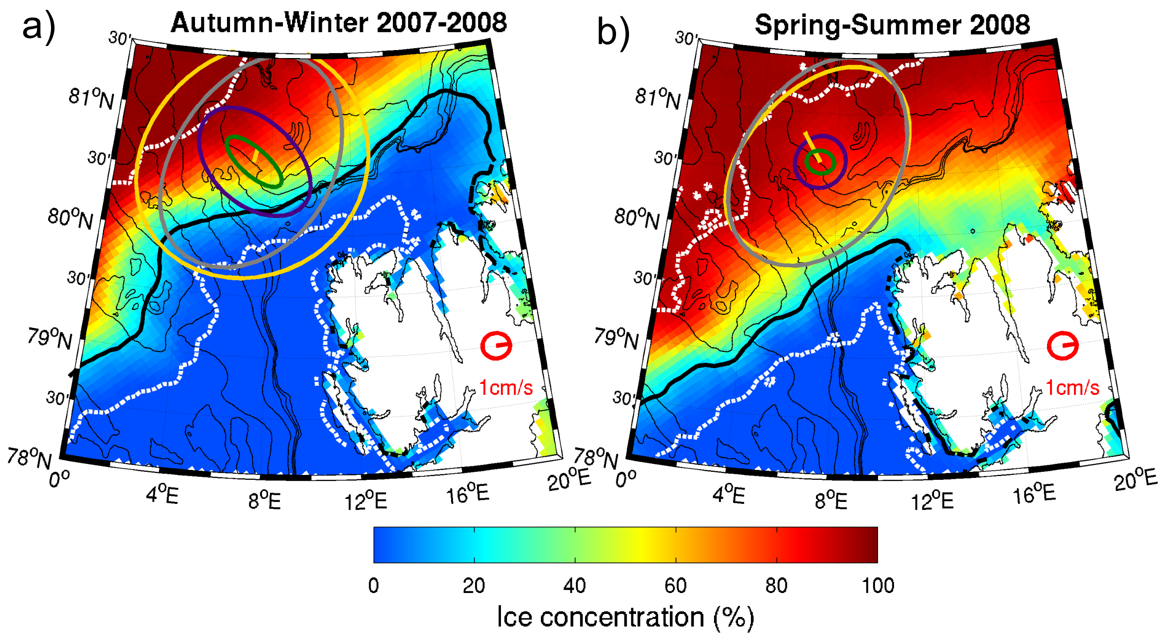

Figure 4: *Background is sea ice cconcentration (in %) from AMSR-E averaged over a) October 2007 to March 2008 (Autumn/winter) b) April to September 2008 (Spring/summer). The thick black line is the mean sea ice edge (defined as the* 15% *sea ice contour) over the corresponding period. The thick dashed white lines are respectively the southernmost sea ice edge and the northernmost sea ice edge at each longitude. On each map, means and ellipses of variances of the 570m-depth in situ velocity data and of the AOTIM-5 velocity at the corresponding season are plotted: the AOTIM-5 velocity outputs in grey, the velocity observations full time resolution in yellow, 50-hour low-pass filtered in purple, and 20-day low pass filtered in green. The red arrow and ellipse of variance show the scale. The thin black lines are bathymetry contours (500, 600, 700, 1000, 2000 and 3000m).*

2 Statistics and spectral content of the in situ velocities

2.1 Full time resolution time series: high frequencies at $570m$ depth

The ADCP current speed time series shows large high frequency variations with a conspicuous semi-monthly periodicity and higher frequencies (Figure 3a). Barotropic tides are a major contributor to velocity fluctuations and current speeds at $570m$, the deepest observed level (mean $10.5cm/s$, std $5.65cm/s$), compares rather well with the AOTIM-5 tide prediction (mean $10cm/s$, std $4.75cm/s$) (Figure 3d and e). The barotropic tide from AOTIM-5 model represents 73% of the variance of the northward component, and 97% of the eastward component. Overall correlation between the $570m$ velocity and the model tide-induced current speed time series is 0.63. Correlation is modulated over the year with larger correlation in spring/summer ($r = 0.78$ in summer 2008) than in autumn/winter ($r = 0.57$).

The ellipses of variance of the full-time resolution ADCP velocity at $570m$ are compared with the ellipses of variances of the AOTIM-5 current (Figure 4). In spring/summer, the ellipses of variance of the current data and of the AOTIM-5 model agree remarkably well in intensity and direction (std along the main axis orientated across-bathymetry $9.1cm/s$, Figure 4b). The main

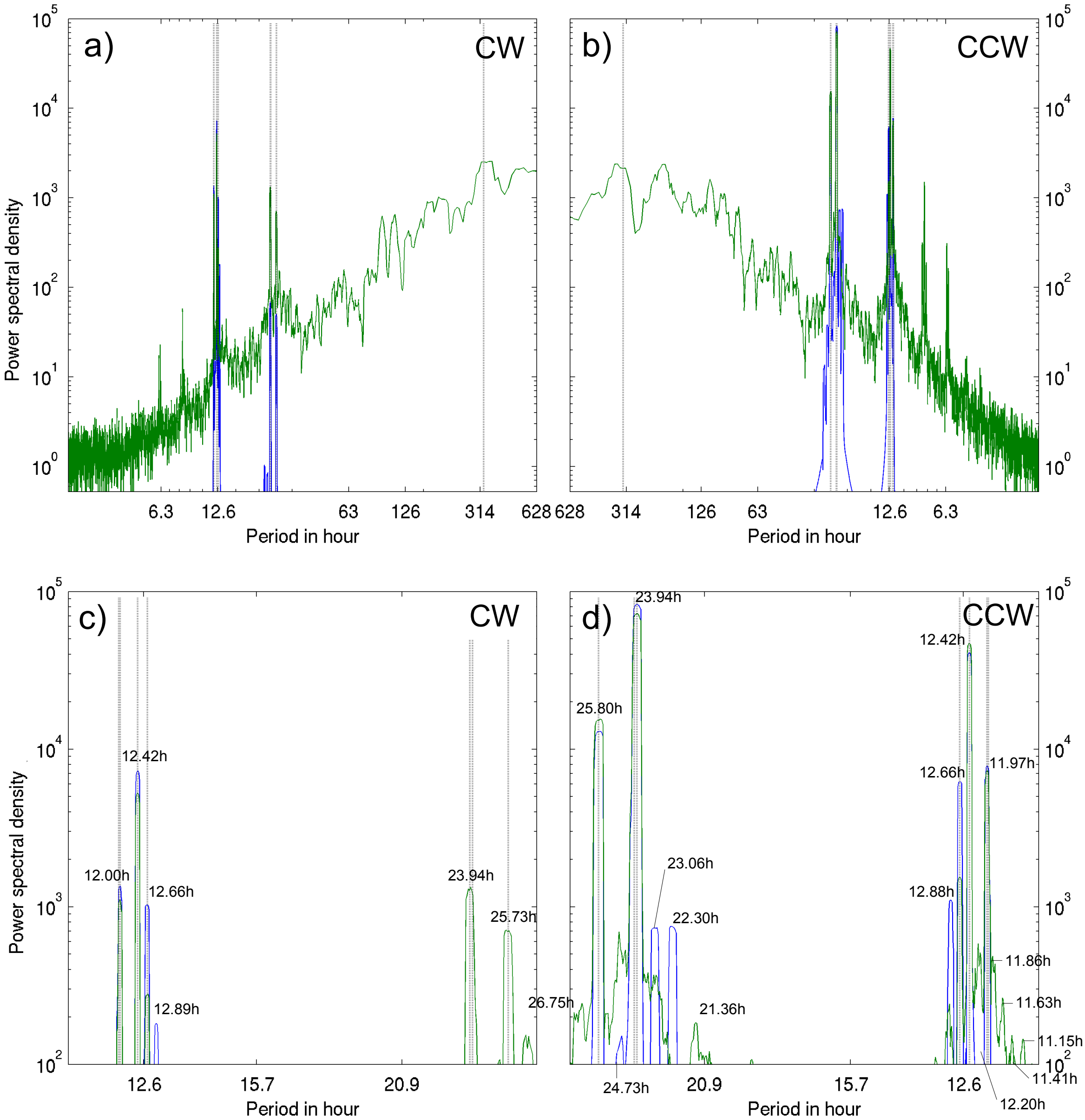

__Figure 5:__ a and b) Rotary spectra of the velocity time series at 570*m (in green) and of the AOTIM5 model time series (in blue). We use a 7-lowest order Slepian tapers with a time-bandwidth product of 4. a (b) column : negative/clockwise (positive/counterclockwise) rotary spectrum. The x axis is period in hour, the y axis is energy (in* cm/s^2*). The black vertical dashed lines correspond to the dominant periods in tide signal : 4 peaks around 12h (11.96h, 12h, 12.4h and 12.6h), 3 around 24h (23.93h, 24.06 and 25.8h) and one at 328h (13.6 days). The near inertial period (12.12h) at the mooring location cannot be distinguished from the tidal period. c and d) close-up of the rotary spectra over the semi-diurnal and diurnal periodicity. CW : clockwise. CCW : counterclockwise. Same color code and axis as in a.*

current forcing in summer is the tide. The mean current in summer (2.8cm/s to the northwest along the bathymetry Figure 4b) can be interpreted as a residual current due to the tide rectification, a superposition of Coriolis and frictional processes over steep topography (*Padman et al.*, 1992; *Polton*, 2015). In autumn/winter, the ellipse of variance of the current data is larger than the ellipse of variance from AOTIM-5 (std along the main axis $9.7 cm/s$ in the current data versus $9.1 cm/s$ in the AOTIM-5 model; along the secondary axis: $8.4 cm/s$ versus $6.4 cm/s$ respectively, Figure 4a). In autumn/winter, other processes than the tide affect the current at $570m$ and the mean current is small ($1.1 cm/s$) across bathymetry to the northeast (Figure 4a). For the sake of estimating an order of magnitude, if we suppose that the residual tidal current is the same in winter as in summer, the other processes are responsible for a mean current to the southeast of about $2.4 cm/s$ at $570m$.

Rotary spectra (clockwise (CW) panels on the left and counterclockwise (CCW) panels on the right, Figure 5) of the in situ velocity at $570m$ confirm the dominance of diurnal and semi-diurnal periods (Figure 5a). The dashed lines on the rotary spectra indicate tide component periods, with 4 periods composing the semi-diurnal signal (K_2 at $11.97h$, S_2 at $12.00h$, M_2 at $12.42h$ and N_2 at $12.66h$), 4 periods for the diurnal signal (K_1 at $23.93h$, P_1 at $24.07h$, O_1 at $25.82h$, Q_1 at $26.87h$), and a period at 13.66 days (325 hours), the fortnightly tide period, corresponding to the beat between O_1 and K_1 (*Kowalik and Luick*) (Figure 5). The near-inertial period at the mooring location is $12.13h$, very close to the semi-diurnal tide periods.

The most energetic peaks in the rotary spectra of the data and of the AOTIM-5 model are M_2 ($12.42h$) for the semi-diurnal signal and K_1/P_1 ($23.94h$ and $24.07h$, not distinguishable in the rotary spectra of the ADCP deep velocity time series) for the diurnal signal. Energy peaks of AOTIM-5 at the main diurnal and semi-diurnal tide components in both CW and CCW panels compare well with the in situ current (difference of less than a factor 2). There are differences in the amplitude of the secondary peaks between in situ an AOTIM-5 velocity spectra, especially in the CCW panel. Several causes can be at the origin of those differences: first bathymetry in the AOTIM-5 model may not be accurate. Then, other signals are probably present in the in situ data, such as internal waves and near-inertial waves.

The main signal in the CCW panel is the diurnal signal, in agreement with *Padman and Dillon* (1991). In the CW panel, the semi-diurnal signal dominates in both in situ data and in the AOTIM-5 model, probably the result of reflections of the barotropic tide on the bathymetry. The ratio of CW/CCW energy in the diurnal and semi-diurnal band (one order of magnitude, not shown) indicates that the tide has mainly an upward propagation signature. Less energetics peaks in both the CCW and CW spectra of the velocity are observed at higher frequencies (periods around 8.2 and 6.2 hours) are harmonics of the diurnal and semi-diurnal signals. The fortnightly period (13.66 days), the striking signal in the current data and in the AOTIM-5 current speed (Figure 3d and e) does not appear in the AOTIM-5 rotary spectra as it is a beat. Further analysis of the tide (e.g. baroclinic tides) and other high frequency signals (e.g. internal waves) is beyond the scope of this paper.

2.2 Mesoscale features: period less than 20 days

The large tidal signal was removed from the velocity component time series with a 50-hour low-pass Butterworth filter. The amplitude of variations is then much reduced (e.g. red curve in Figure 3e, Figure 4 and Table 1). Means and ellipses of variance vary with season and depth (Table 1, Figure 6). In figure 6, the data gaps at 300 m and 250 m, respectively 3% and 6% of the time series, are filled with the value of the upper available observation in the water column. In winter, the mean current rotates cyclonically with increasing depth, while the main axis of the ellipses rotates anticyclonically. In summer, ellipses are smaller and the mean velocities and the main axes of the ellipses have the same direction towards the northwest parallel to isobaths and decrease in amplitude with increasing depth. The velocity structure is barotropic equivalent in summer while it shows baroclinicity in autumn/winter.

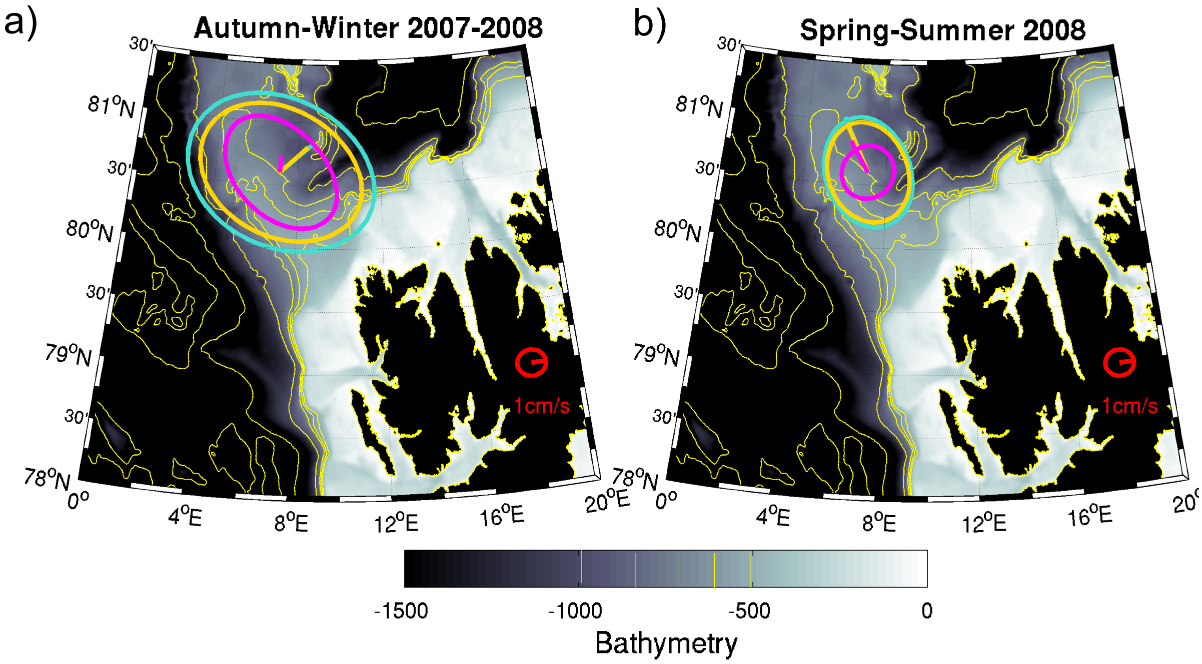

Figure 6: *Means and variance ellipses of the in situ velocity data filtered with a 50-hour low-pass Butterworth filter at several depths. magenta : at* $570m$*, yellow : at* $300m$*, blue : at* $250m$*. The red arrow and ellipse of variance are the scale. Background is bathymetry, the thin yellow lines are bathymetry contours.*

Spectra of the along-bathymetry component of the 50-hour low-pass filtered velocity time series at $570m$ and $300m$ show several salient peaks above the 95% confidence level in the range of periods from 3.4 to 50 days (Figure 7). Energy levels are twice smaller at $570m$ than at $300m$. Prominent peaks at 4.6, 9.2 and 13 days in the core of the Atlantic Water ($300m$) can be signature of mesoscale activity. Indeed, the ARCTEMIZ88 drifting floats that proceeded through the Yermak Pass (Figure 1b) documented vortices with rotating timescale from 5 to 15 days, curvature radius of about $4km$ and tangential speeds of $10cm/s$ (*Gascard et al.*, 1995; *Richez*, 1998).

2.3 Seasonal variations

We applied a 20-day low-pass Butterworth filter to the ADCP velocity components (Table 1). At $570m$, mean current and variance ellipse are small (Table 1, Figure 4 in green). At $300m$ depth, in the core depth of the Atlantic Water inflow (Fer et al., 2010), means remain small and ellipses are larger (Figure 8, yellow). In summer (April-September), the mean current at $300m$ is about $4.3cm/s$ to the northeast along the $700m$ isobath and the ellipse is circular with an std around $2.4cm/s$ (Figure 8a). In winter (October-March) the mean current at $300m$ is orientated across-bathymetry to the northeast ($2.6cm/s$), the ellipse has a main axis (std $4.9cm/s$) along bathymetry. Note that the winter mean and ellipse at $300m$ are comparable to those deduced

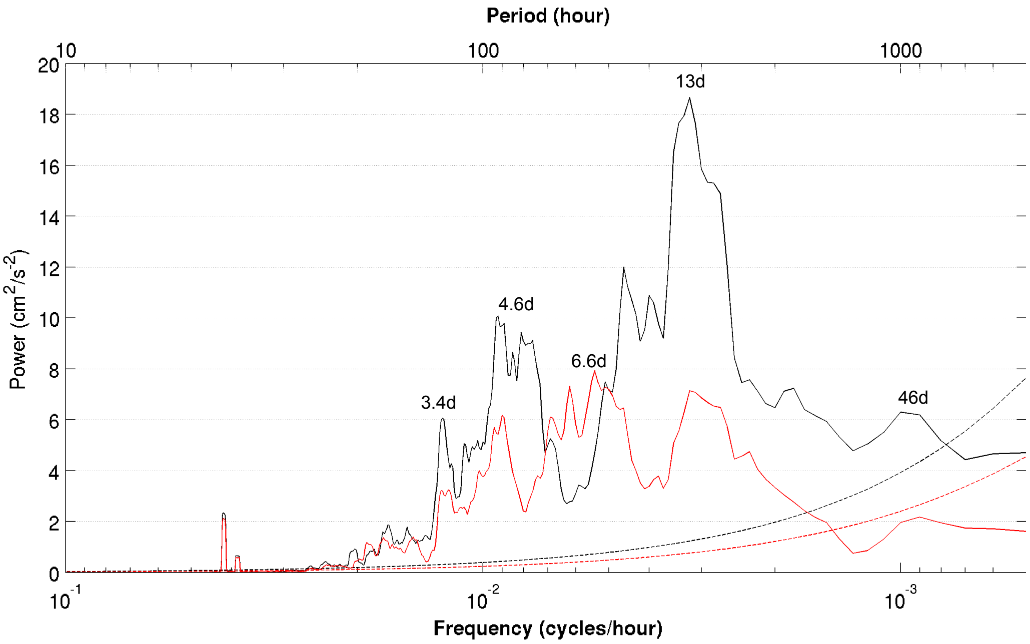

Figure 7: *Variance-preserving spectra of the along isobath velocity component velocity at* $570m$ *(red) and* $300m$ *(black) from the ADCP filtered with a 50-hour low-pass Butterworth filter along the main axis of variance (by averaging over groups of 10 adjacent frequencies). The dotted lines show the* 95% *confidence level against the red noise background from a first order autoregressive (AR1) process. The y axis is the power in* cm^2/s^{-2}*. The x-axis is frequency (bottom) labelled in period (top). The period of the most energetic peaks is indicated in days.*

from the ARCTEMIZ88 floats (*Richez*, 1998). If we suppose that the summer mean velocity at $300m$ ($4.3cm/s$ to the northwest along the slope, figure 8b yellow arrow) is essentially due to tide or eddy rectification and that the residual current is the same in winter as in summer, then a mean flow of $4.7cm/s$ to the southeast is necessary to produce the winter mean of $2.6cm/s$ to the northeast (Figure 8a; yellow vectors). This is just an order of magnitude because of the questionable hypothesis of a same residual current in winter and summer. The mean value of $4.7cm/s$ in the AW core in winter is larger than the $2.4cm/s$ estimated at $570m$ (section 3.1) (dashed yellow arrow in Figure 8a to the southeast).

The spectrum of the velocity component parallel to the main axis of the ellipse of variance shows two peaks, at 32 days and 70 days (Figure 9, black curve). These peaks could correspond to monthly/bi-monthly velocity pulses of current in the Yermak Pass Branch. The mean velocity during velocity pulses, defined as 20-day low pass filtered current with a speed larger than $10cm/s$ is eastward along the downstream bathymetry, almost parallel to the north coast of Svalbard (Figure 8a, green arrow). During the velocity pulses, ADCP data reach up to $90m$ suggesting that the pycnocline shallows to less than $90m$ from the surface (Figures 2a and 3a) and that the warm AW flows through the Pass and extends closer to the surface with potential impact on the ice cover. Indeed, the mooring is ice-free during several months in autumn-winter while it is ice-covered in summer (Figure 3b).

The ADCP current data confirm the strong seasonality of the Yermak Pass Branch, which is mostly a winter pattern as Mercator-Ocean operational model outputs suggested (*Koenig et al.*,

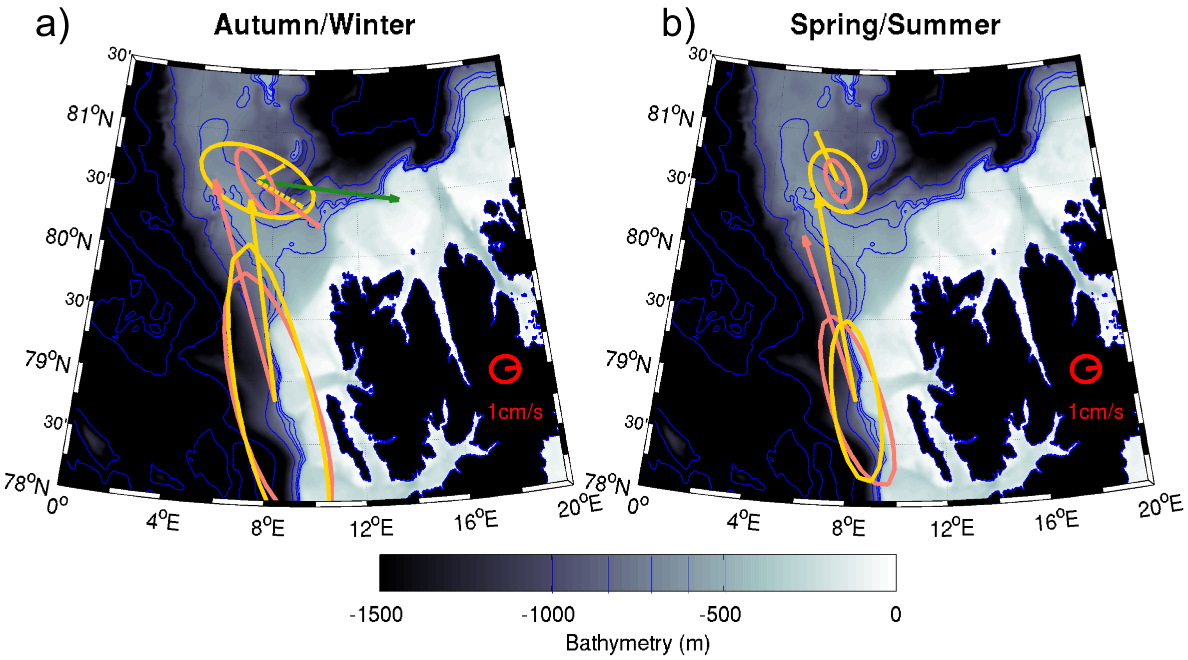

Figure 8: *Velocity means and variance ellipses of model outputs (full salmon lines) and in situ data (full yellow lines) at the location of the ADCP mooring at* $300m$ *and mooring F2 in Fram Strait at* $250m$ *a) in summer (April-September) b) in winter (October-March). The ADCP mooring data are 20-day low-pass filtered with a Butterworth filter, the currentmeter data in Fram Strait are 10-day low-pass filtered with a Butterworth filter. In winter, the green arrows in the Yermak Pass feature the composite for in situ 20-day low-pass filtered current speeds larger than* $10cm/s$*. The yellow dashed line vector is the mean velocity once the estimated tidal residual current is removed. The red arrow and ellipse is the scale. Background is bathymetry (in m). The blue isolines are 3000, 2000, 1000, 800, 700, 600 and 500m.*

2017). The eastward flow of Atlantic Water through the Yermak Pass in winter seems to occur in episodes of intense flow (velocity larger than $10cm/s$) of one-to-two month periodicity. In the nxt section we use 10 years of outputs from the operational Mercator-Ocean model to examine the Yermak Pass Branch variations.

3 AW inflow north of Svalbard in Mercator Ocean operational moodel outputs

3.1 Model performances in Fram Strait and in the Yermak Pass

Koenig et al. (2017) showed that the 1/12 degree resolution Mercator-Ocean global operational model reproduces reasonably well seasonal cycles in volume transports and temperatures of the AW inflow at Fram Strait (comparison with the 13 years statistics ,1997 - 2010, from *Beszczynska-Möller et al.* (2012) and at $30°E$ and $81.8°N$ (comparison with mooring statistics from *Ivanov et al.* (2009), and temperatures from NABOS data http://nabos.iarc.uaf.edu). Comparisons with contemporary winter hydrographic data from the IAOOS platform drift north of Svalbard during N-ICE2015 experiment also showed a remarkable agreement (*Koenig et al.*, 2017). Here,

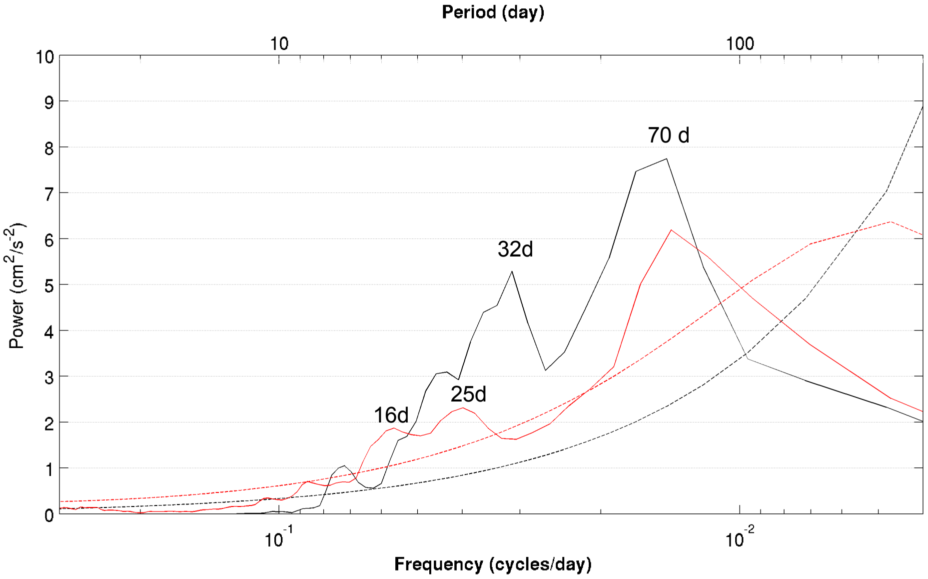

Figure 9: *Variance-preserving spectra. In black : the velocity component along isobath* $300m$ *from the ADCP filtered with a 20-day low-pass Butterworth filter (by averaging over groups of 4 adjacent frequencies). In red : the velocity at* $266m$ *from the model outputs at the mooring locations (by averaging over groups of 12 adjacent frequencies). The dotted lines (red/black) show the* 95% *confidence level against the red noise background from a first order autoregressive (AR1) process (from the ADCP data/the model outputs respectively). The y axis is the power in* cm^2/s^{-2}. *The x-axis is frequency (bottom) labelled in period (top).*

we proceed to a more detailed comparison with the currentmeter data at $250m$ from mooring F2 (magenta dot Figure 1) located in the core of the WSC in Fram Strait ($78.84°N$, $8.33°E$) for the period 2007-2009 (*Beszczynska-Möller et al.*, 2012).

Mean and standard deviation are in very good agreement between the 10-day low-pass filtered in situ data at F2 and the collocated daily model outputs. The mean current, around $12cm/s$ in summer and $16cm/s$ in winter, flows along the bathymetry. The ellipses are elongated in the northward direction in summer and winter, and are of the same order of magnitude ($7cm/s$ in summer, $10cm/s$ in winter, Figure 8). Time variations of the northward velocity of the in situ data (F2) and the model outputs are significantly correlated ($r = 0.34$) in spite of the large eddy activity of the WSC (*Von Appen et al.*, 2016; *Hattermann et al.*, 2016). Temperature variations in the model outputs and at F2 are highly correlated ($r = 0.75$), with a modeled negative bias of $0.04°C$ and root mean square error of $0.38°C$). Temperature time series (not shown) feature a large seasonal cycle with a maximum at the end of summer/beginning of fall ($4.5 - 5°C$ in October 2008) and a minimum at the end of winter/beginning of spring ($2-2.5°C$ in April 2008). The inflow of the Atlantic Water in the Arctic is well represented in the model.

At the mooring location over the Yermak Plateau (green dot in Figure 1), mean currents from the model outputs differ from the 20-day low-pass filtered in situ data in several ways. In summer, the modeled mean current is weak ($0.5cm/s$ and orientated southeast ($4.3cm/s$ to the northwest for the *in situ* data) (Figure 8b). In winter, the modeled mean current in the model outputs is orientated southeast (mean $6.3cm/s$) along bathymetry whereas it is orientated across-bathymetry in the *in situ* data (Figure 8a). Differences are probably due to the fact that the model does not represent tides. Indeed, the in situ mean velocity comprises a non-linear residual tide component. The model mean of $6.3 cm/s$ to the southeast is comparable with the mean value ($4.7 cm/s$ to the southeast) obtained by removing the tide-induced residual velocity estimate from the mean observed velocity (see section 3.3) (Figure 8 a, dashed yellow and salmon vectors).

The model does show skills in representing the annual variations of the Yermak Pass Branch with a smaller variance ellipse in summer than in winter. Eddies documented by ARCTEMIZ88 floats are small scale, about $4km$ curvature radius (Richez, 1998). This scale is not fully-resolved by the $1/12°$ resolution model outputs, the model variance ellipses are smaller than those deduced from the ADCP (Figure 8a and b). The spectrum of the along-bathymetry velocity component from the daily model outputs (in red) bears similarity in intensity and energized frequencies to the spectral content of 20-day low-pass filtered in situ data (in black) with a significant peak at about 70 days and another one about 25 days. Those periods correspond to the time scales of episodes of intense flow documented in section 3.3. The daily model velocity outputs do not have energy at periods smaller than 10 days.

3.2 Model outputs in 2007-2008: local circulation and links between the YPB and the WSC

Figure 10 shows the mean currents around the mooring location (Yermak Pass, black dot) from the model outputs at $266m$ depth in autumn/winter 2007-2008 (Figure 10a and c) and spring/summer 2008 (Figure 10b and d), in a regional map (upper panels) and in a close-up over the Yermak Pass (lower panels). The seasonality of the current in the AW core is striking: larger flow in winter in the WSC, the Yermak Pass branch and in the eastward current along the continental slope north of Svalbard. In winter, the AW Yermak Pass Branch merge with the Svalbard Branch to the east of $10°E$ along the Svalbard continental slope. The Fram Strait recirculating branches are intense in both seasons. The close-up over the Yermak Pass (lower panels c and d) highlights interesting features. In winter, the mean velocity exceeds $5cm/s$ and the current flows between the isobaths $600 - 800m$. In summer, the flow is narrower, between isobaths 600 and 700 m and a small recirculation is formed around the $600m$ isobath contour (centered at $6.5°E$, $80.5°N$). The standard deviation of the intensity (not shown) does not show large variations of the current in summer, while it is large in winter along the main flow, confirming that the Yermak Pass Branch flows in pulses in winter.

The in situ northward velocity at F2 at $250m$ and the in situ current speed of the ADCP in the Yermak Pass at $300m$ are barely correlated ($r = 0.16$) with a lag of 15 days. In the modeled velocities, the correlation is larger ($r = 0.33$) with a smaller lag of 6 days. Such short lags are due to the propagation of coastal trapped waves that are much faster than the mean current. The distance between the ADCP in Yermak Pass and F2 in Fram Strait along isobaths is about $300km$, which implies an order of magnitude of $60cm/s$ for the propagation velocity in model outputs. The larger correlation and smaller lags between modeled velocities in Fram Strait and in the Yermak Pass compared to observations are probably due to the fact that the model misses the energetic tides in the Yermak Pass Branch and their interactions with the flow which reduce correlations with the Fram Strait inflow. Modeled temperatures at F2 and in the Yermak Pass at $266m$ show a maximum correlation ($r = 0.73$) at a lag of 33 days. This lag corresponds to the time of temperature anomaly propagation of the Atlantic Water inflow with a background current velocity of $10cm/s$. (Note that there is no in situ temperature time series in the Yermak Pass).

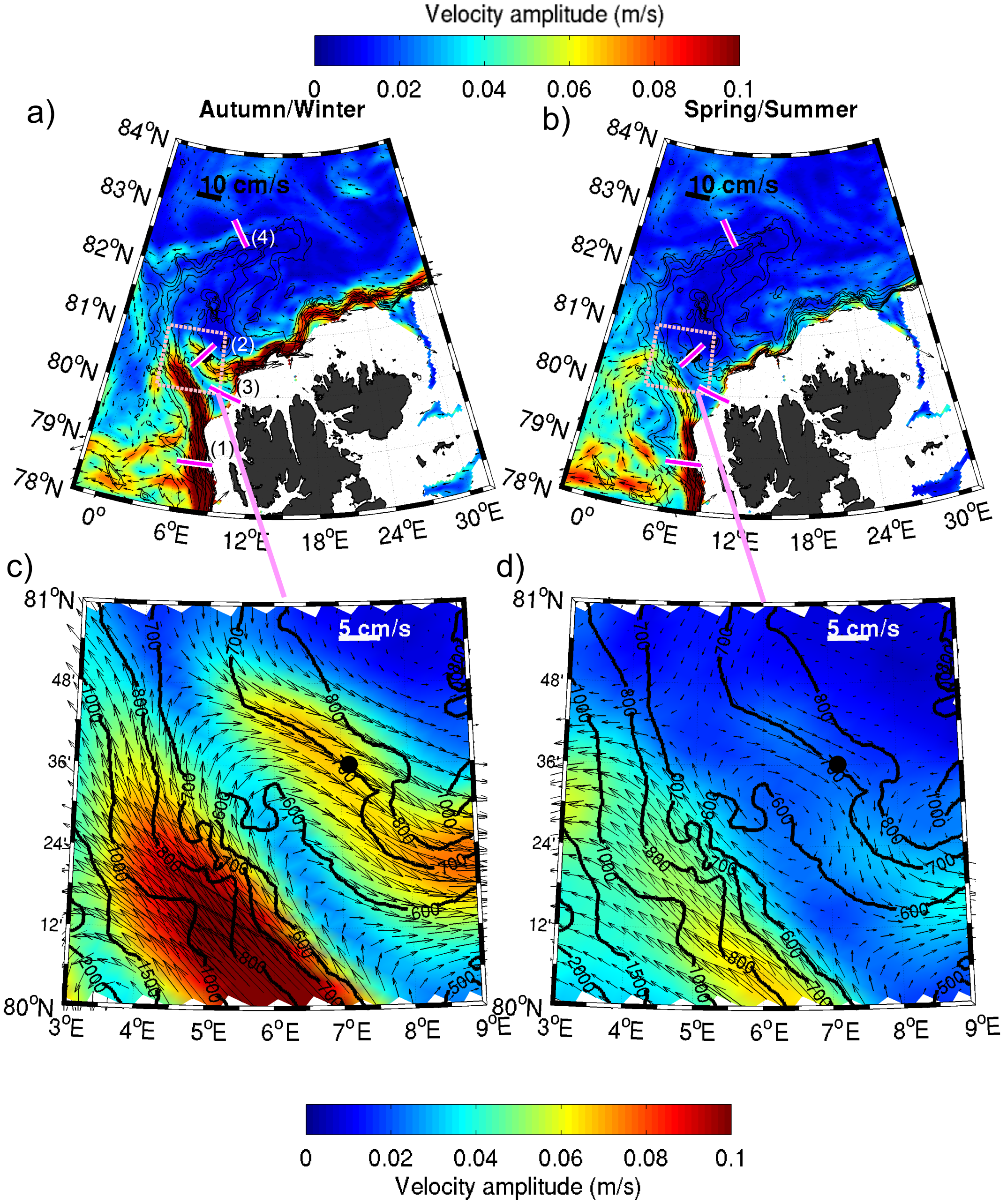

Figure 10: *Mean circulation (arrows in cms-1) from the model outputs in the AW layer (50m-thick layer centered at 266m) over a) Winter : October 2007-March 2008 b) Summer : July 2007-September 2007 and April 2008- September 2008. The current speeds smaller than 1cm/s are not plotted. Lower panels: Close up on the mean circulation in the pink box indicated in the upper panels. The black dot indicates the mooring location. The bathymetry contours are 500, 600, 700, 800, 1500 and 1500m. The magenta line are the sections used to compute the volume transport presented in Figure 9. (1) : West Spitsbergen Current (WSC) section. (2) : Yermak Pass Branch (YPB) section. (3) : Svalbard Branch (SB) section. (4) Yermak Branch (YB) section*

We now examine the evolution of the WSC and its partition downstream in the 10 years of model outputs.

3.3 Variations in the AW inflow in the WSC and its partition downstream over 2007-2016

Volume transports of waters warmer than 1.5°C (Atlantic Water) were computed from model outputs through the 4 sections drawn in Figure 10a: (1) the West Spitsbergen Current (WSC in red), (2) the Yermak Pass Branch (YPB in blue), (3) the Svalbard Branch (SB in green) and (4) the Yermak Branch (YB in magenta) (Figure 11, Table 2).

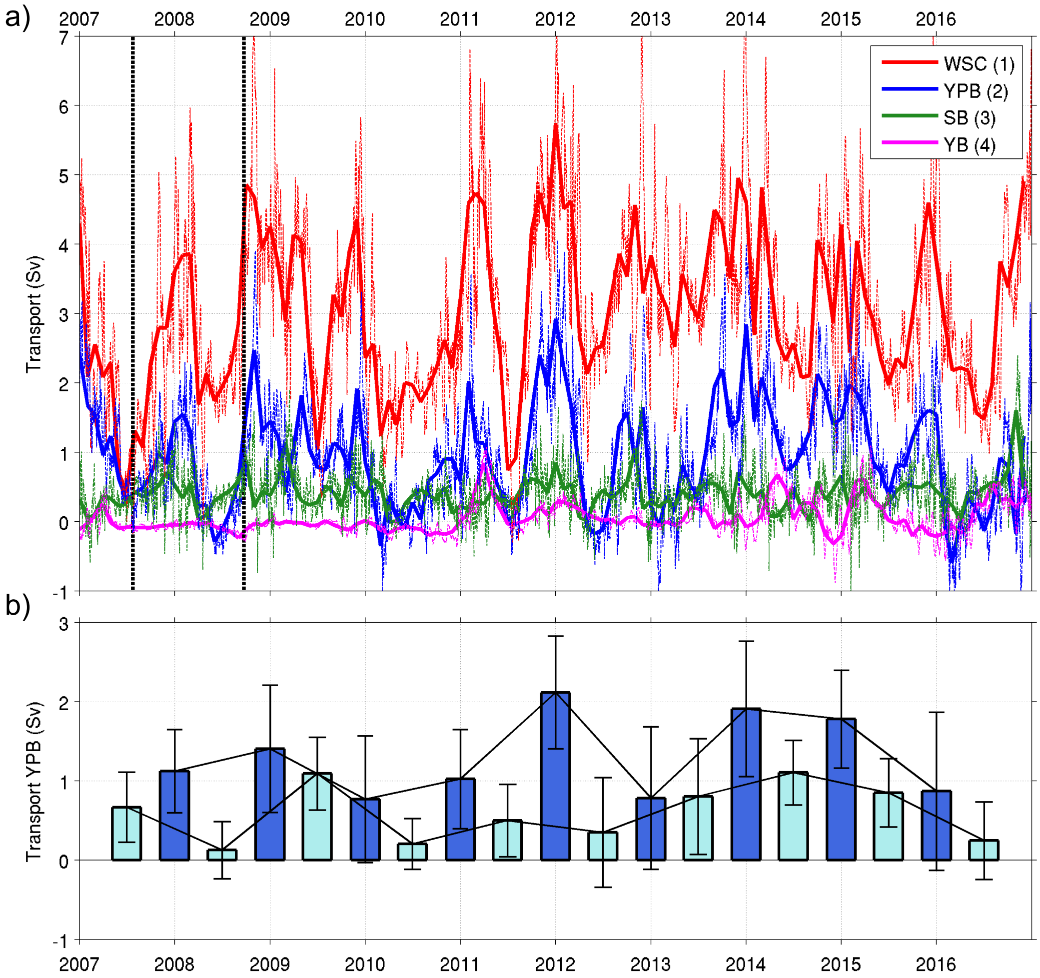

Figure 11: *a) Time series of volume transport (in Sv) of water with temperature larger than* 1.5°C *from model outputs through several sections presented in Figure 10. x-axis is time in years. Dashed lines are the full time resolution time series, thick lines are the monthly means. WSC : West Spitsbergen Current. SB : Svalbard Branch. YPB : Yermak Pass Branch, YB : Yermak Branch. The black dashed lines delimitate the period of the mooring data in the Yermak Pass. b) Seasonal mean of the volume transport of the Yermak Pass Branch (in Sv). In dark blue: over October-March (Winter). In light blue: over April-September (Summer). Vertical bars are the standard deviation of daily volume transport for each season.*

We chose this temperature criterion as the Yermak Branch is mainly composed of water colder than 2°C at the beginning of the time series. The WSC shows large (the largest among the 4 sections) annual variations (Table 2) in agreement with those in *Beszczynska-Möller et al.* (2012) (Figure 11a). The AW volume transport in the YPB (in blue) is largely correlated ($r = 0.65$)

with the AW transport in the WSC (in red) and the YPB carries 31% (36% in winter) of the AW inflow from the WSC (Figure 11a). The volume transport of the YPB is sometime negative in summer, indicating of a northwestward flow, as observed in the ADCP current data (Figure 8b). The model outputs suggest that the main pathway of the AW in winter over the Yermak Plateau is the YPB. The small SB transport (in green, mean of $0.4Sv$) is significantly correlated with the WSC transport ($r = 0.45$) (Figure 11a). In summer, the volume transport is larger in the SB than in the YPB, in agreement with observations (*Sirevaag and Fer*, 2009). The YB volume transport is very small (mean $0.04Sv$), carries quite cold waters (between 1.5 and $2°C$) and does not show any significant seasonal variations. The sum of the volume transport from the YPB, the SB and the YPB, the three branches that bring warm water from the WSC in the Arctic Ocean is largely correlated with the WSC volume transport ($r = 0.75$) and represents 46% of the volume transport of the WSC. Hence, in the model, more than 50% of the WSC volume transport does not enter the Arctic Ocean and directly turns back with the Fram Strait recirculating branches, in agreement with *Manley* (1995); *Hattermann et al.* (2016).

The model outputs suggest that the period sampled by the 2007-2008 mooring corresponded to a weak summer and an average winter YPB volume transport compared to volume transport values in the period 2007-2016 (Figure 11b, $1.1Sv$ in winter 2007-2008 compared to $1.3Sv$ on average over 2007-2017 and $0.13Sv$ in summer 2008 compared to $0.6Sv$ on average over 2007-2017). During some winters as winter 2011-2012, volume transport of AW through the Yermak Pass is twice as large as in 2008. The model suggests that the importance of the Yermak Pass Branch as a pathway of AW is modulated from one year to the other.

Sv	**WSC**	**YPB**	**SB**	**YB**
Mean	3	0.9	0.4	0.04
Summer	2.4	0.6	0.3	0.08
Winter	3.7	1.3	0.4	0.01
Std	1.3	0.8	0.3	0.2
Summer	1.0	0.6	0.2	0.2
Winter	1.3	0.9	0.4	0.2
Min	-0.3	-1.1	-1.2	-0.9
Max	7.9	4.0	2.4	1.1

Table 2: *Volume Transport statistics (in Sv) across several sections over the Yermak Plateau and the Svalbard continental slope for the water warmer than* $1.5°C$*. WSC : West Spitsbergen Current. YPB : Yermak Pass Branch. SB : Svalbard Branch. YB : Yermak Branch. In each case, the first line is the total, the second line is summer (April-September) and the third line is winter (October-March).*

4 Summary and discussion

We analyzed fourteen months (July 2007 - September 2008) of ADCP data in the Yermak Pass at $80.601°N$, $7.119°E$ on the $745m$ isobath, a location covered by sea ice 10 months out of 12. The data set documents the unique intense high frequency velocity variations (80% of the total variance at periods less than 2 days) that mask a significant eddy activity and a large seasonal variation. We focused on the low-frequency variations and used 10 years of outputs from the Mercator-Ocean global ocean operational model to put the observations into a longer perspective. The model does not represent tides and does not explicitly resolves the Rossby radius with its 1/12 degree grid. Yet we showed (section 4.1) that the model has some skills in representing the AW inflow west and north of Svalbard. The three major results can be summarized as follows: 1) barotropic tides dominate the velocity signal in the Yermak Pass, 2) the winter AW flow composed of eddies and pulses is superimposed to tides and 3) Model outputs suggest that YPB carries 31% of the AW inflow from the WSC to the Arctic Ocean (36% in autumn/winter). The results are discussed below.

Ocean velocities in the Yermak Pass are dominated by high frequencies with strong diurnal and semi-diurnal tide signals as observed in other locations of the Yermak Plateau (*Hunkins*, 1986; *D'Asaro and Morison*, 1992). Barotropic tides, well predicted in the AOTIM-5 model, represent 73% and 97% of the northward and eastward variance respectively. It has been shown that the strong tidal currents over the Yermak Plateau lead to increased internal wave activity and turbulent mixing (*Padman and Dillon*, 1991; *Padman et al.*, 1992; *Plueddemann*, 1992; *Wijesekera et al.*, 1993; *Fer et al.*, 2010, 2015). The diapycnal mixing is large enough over the Yermak Plateau to influence the heat content of the Atlantic Water inflow entering in the Arctic and varies locally depending on topography and hydrography (*Fer et al.*, 2015). Ocean to ice heat fluxes over the Yermak Plateau are large enough to melt the sea ice in summer (*Fer et al.*, 2010; *Meyer et al.*, 2017b; *Peterson et al.*, 2017). They are expected to be even larger in late autumn/winter when the AW inflow is intense and warm and storms frequent and strong (*Rainville and Woodgate*, 2009; *Koenig et al.*, 2016; *Provost et al.*, 2017). As the profiler did not work, we lack temperature data to examine internal waves and diapycnal mixing. The tidal signal is essentially the only current component in summer and leads to a residual current of $4.3cm/s$ to the northwest along bathymetry at $300m$ in the AW core. In winter the mean current is small ($2.6cm/s$) and orientated to the northeast perpendicular to isobaths, suggesting that other processes induce a mean current of $4.7cm/s$ to the southeast in the AW core to counterbalance the residual tidal current.

Once tidal variability is removed, mesoscale activity with a baroclinic component dominates the flow through the Yermak Pass in winter. The largest energy peaks were found in the core of the AW ($300m$) at period between 5 and 14 days (Figure 7). The time scales are consistent with the eddies that ARCTEMIZ88 drifting floats documented in the Yermak Pass at $300m$ in the fall 1988 (Figure 1b) (*Gascard et al.*, 1995; *Richez*, 1998). Eddies are a dominant feature of the AW inflow in the Arctic (*Padman and Dillon*, 1991; *Zhao et al.*, 2014; *Våge et al.*, 2016). In the core of the AW, another conspicuous energy band is found at the monthly and bi-monthly period (Figure 9). This is interpreted as episodes of intense AW. These pulses, occurring mainly in autumn-winter, correspond to strong eastward flow carrying AW across the Yermak Plateau (Figure 8). The four ARCTEMIZ88 floats that made a U turn at $80.7°N$ and proceeded through the Yermak Pass were probably taken in an AW pulse and documented similar velocities. The ADCP data suggest that the pulses are accompanied with a shallowing of the pycnocline potentially allowing heat from the AW to reach the sea ice (Figure 3). The monthly-scale variations in the WSC volume transport are determined by short-term variations in the offshore part of the WSC and of the westward recirculations at 78.5 and $79°N$ (*Beszczynska-Möller et al.*, 2012). Similarly, the monthly pulses in the YPB could be attributed to variations in the westward recirculating branch at $80.5°N$ (Figure 10 a and b).

After evaluation, Mercator Ocean operational model outputs were used to tentatively examine the evolution and the partition of the AW inflow downstream of the WSC. The model outputs confirm that the flow of the Atlantic Water through the Yermak Pass is a winter pattern associated with an overflow of the strong winter WSC. On average over 10 years, the volume transport of the Yermak Pass Branch ($0.9Sv \pm 0.8$) is equal to 31% of the volume transport of the West Spitsbergen Current ($3.0Sv \pm 1.3$) and, in winter, YPB is the main entrance of the Atlantic Water from Fram Strait to the Arctic Ocean. In agreement with *Hattermann et al.* (2016), the model outputs indicate that more than 50% of the AW inflow in the WSC recirculates back in Fram Strait and does not enter the Arctic Ocean. The Svalbard Branch ($0.4Sv \pm 0.3$) has a smaller volume transport than the Yermak Pass Branch in general and less seasonality. In the model, the Yermak Branch ($0.04Sv \pm 0.2$) is negligible. However those numbers have to be considered with caution. Indeed Mercator-ocean operational model does not simulate tides and does not take tides into account at all. Tides are a major player above and on the slopes of the Yermak Plateau and undoubtedly contribute to significantly altering the above figures. Indeed, *Padman et al.* (1992) argued that tidal rectification is probably responsible for the mean current of the YB. This could explain why the AW flow through the YB is so small in the model outputs. *Luneva et al.* (2015) compared two 30-year simulations of a 1/4 degree sea-ice ocean coupled model, one with explicitly resolved tides and the other without any tidal dynamics. They showed the important role of tides on the water mass mixing and sea ice in the Arctic Ocean. To properly resolve AW pathways and transport distribution north of Svalbard an eddy-resolving model (1/36 degree) with explicitly simulated tides is needed.

Acknowledgements

The mooring work was supported by the European project Damocles. The efforts of the captain and crew on board the R/V Haakon Mosby for the deployment and K/V Svalbard for the recovery are appreciated. Z. Koenig acknowledges a PhD scholarship from Université Pierre et Marie Curie (UPMC). The Mercator Ocean global operational system is part of the Copernicus Marine Environment Monitoring Service CMEMS (http://marine.copernicus.eu/). The ADCP mooring data in the Yermak Pass are available at LOCEAN (Christine Provost, cp@locean-ipsl.upmc.fr). The ADCP mooring data in the YermaK Pass are publiclt available in the SEANOE database: http://doi.org/10.17882/51023.

References

Beszczynska-Möller, A., E. Fahrbach, U. Schauer, and E. Hansen (2012), Variability in atlantic water temperature and transport at the entrance to the arctic ocean, 1997–2010, *ICES Journal of Marine Science: Journal du Conseil*, p. fss056, doi:https://doi.org/10.1093/icesjms/fss056.

Beszczynska-Möller, A., W.-J. Von Appen, and E. Fahrbach (2015), Physical oceanography and current meter data moorings f1-f14 and f15/f16 in the fram strait, 1997-2012, *PANGAEA*, doi:10.1594/PANGAEA.150016.

Cokelet, E. D., N. Tervalon, and J. Bellingham (2008), Hydrography of the west spitsbergen current, svalbard branch: Autumn 2001, *J. Geophys. Res.*, *113*(C01006), doi: 10.1029/2007JC004150.

D'Asaro, E., and J. Morison (1992), Internal waves and mixing in the arctic ocean, *Deep Sea Res, Part A*, *39*(supple 2), S459–S484.

Dee, D., S. Uppala, A. Simmons, P. Berrisford, P. Poli, S. Kobayashi, U. Andrae, M. Balmaseda, G. Balsamo, P. Bauer, P. Bechtold, A. Beljaars, L. van de Berg, J. Bidlot, N. Bormann, C. Delsol, R. Dragani, M. Fuentes, A. Geer, L. Haimberger, S. Healy, H. Hersbach, E. Holm, L. Isaksen, P. Kalberg, M. Kohler, M. Matricardi, A. McNally, B. Monge-Sanz, J.-J. Morcrette, B.-K. Park, C. Peubey, P. de Rosnay, C. Tavolato, J.-N. Thepaut, and F. Vitart (2011), The era-interim reanalysis: configuration and performance of the data assimilation system, *Q.J.R. Meteorol. Soc.*, *137*, 553–597, doi:10.1002/qj.828.

Ezraty, R., F. Girard-Ardhuin, J. Piolle, L. Kaleschke, and G. Heygster (2007), Arctic and antarctic sea ice concentration and arctic sea ice drift estimated from special sensor microwave data, *User's Manuel Version 2.1, CERSAT*.

Fer, I., R. Skogseth, and F. Geyer (2010), Internal waves and mixing in the marginal ice zone near the yermak plateau, *Journal of Physical Oceanography*, *40*(7), 1613–1630, doi: http://dx.doi.org/10.1175/2010JPO4371.1.

Fer, I., M. Müller, and A. Peterson (2015), Tidal forcing, energetics, and mixing near the yermak plateau, *Ocean Science Discussions*, *11*(5), doi:10.5194/os-11-287-2015.

Gascard, J.-C., C. Richez, and C. Rouault (1995), New insights on large-scale oceanography in fram strait: The west spitsbergen current, *Arctic Oceanography: Marginal Ice Zones and Continental Shelves*, pp. 131–182, doi:10.1029/CE049p0131.

Gascard, J.-C., M. Beauverger, J. Lanoisellé, H. Le Goff, Z. Koenig, and C. Provost (2017), Adcp mooring data in 2007-2008 north of svalbard over the yermak plateau in the yermak pass, *SEANOE database*, doi:http://doi.org/10.17882/51023.

Hattermann, T., P. E. Isachsen, W.-J. Von Appen, J. Albretsen, and A. Sundfjord (2016), Eddy-driven recirculation of atlantic water in fram strait, *Geophysical Research Letters*, *43*(7), 3406–3414, doi:10.1002/2016GL068323.

Hunkins, K. (1986), Anomalous diurnal tidal currents on the yermak plateau, *Journal of Marine Research*, *44*(1), 51–69, doi:https://doi.org/10.1357/002224086788460139.

Ivanov, V., I. Polyakov, I. Dmitrenko, E. Hansen, I. Repina, S. Kirillov, C. Mauritzen, H. Simmons, and L. Timokov (2009), Seasonal variability in the atlantic water off spitsbergen, *Depp Sea Research, Part I*, *56*, 1–14, doi:10.1016/j.dsr.2008.07.013.

Kawasaki, H., T. ad Hasumi (2016), The inflow of atlantic water at the fram strait and its interannual variability, *J. Geophys. Res. Oceans.*, *121*, 502–519, doi:10.1002/2015JC011375.

Koenig, Z., C. Provost, N. Villacieros-Robineau, N. Sennéchael, and A. Meyer (2016), Winter ocean-ice interactions under thin sea ice observed by iaoos platforms during n-ice2015: Salty surface mixed layer and active basal melt, *Journal of Geophysical Research: Oceans*, *121*(10), 7898–7916, doi:10.1002/2016JC012195.

Koenig, Z., C. Provost, N. Villacieros-Robineau, N. Sennéchael, A. Meyer, J.-M. Lellouche, and G. Garric (2017), Atlantic waters inflow north of svalbard: Insights from iaoos observations and mercator ocean global operational system during n-ice2015, *Journal of Geophysical Research: Oceans*, *122*(2), 1254–1273, doi:10.1002/2016JC012424.

Kowalik, Z., and J. Luick (), *The oceanography of tides*.

Lellouche, J.-M., O. Le Galloudec, M. Drevillon, C. Régnier, E. Greiner, G. Garric, N. Ferry, C. Desportes, C.-E. Testut, C. Bricaud, et al. (2013), Evaluation of real time and future global monitoring and forecasting systems at mercator océan., *Ocean Science Discussions*, *9*(2).

Luneva, M., Y. Aksenov, J. Harle, and J. Holt (2015), The effect of tides on the water mass mixing and sea ice in the arctic ocean, *J. Geophys. Res. Oceans*, *120*, 6669–6699, doi: 10.1002/2014JC010310.

Madec, G., and N. Team (2008), Nemo ocean engine, *Note du Pole de modelisation, Inst. Pierre-Simon Laplace (IPSL), France*, *27*, doi:1288-1619.

Manley, T. (1995), Branching of atlantic water within the greenland-spitsbergen passage: An estimate of recirculation, *J. Geophys. Res.*, *100*(C10), 20,627–20,634.

Manley, T., R. Bourke, and K. Hunkins (1992), Near-surface circulation over the yermak plateau in northern fram strait., *Journal of Marine Systems*, *3*(1), 107–125.

Meyer, A., A. Sundfjord, I. Fer, C. Provost, N. Villacieros Robineau, Z. Koenig, I. H. Onarheim, L. H. Smedsrud, P. Duarte, P. A. Dodd, et al. (2017a), Winter to summer oceanographic observations in the arctic ocean north of svalbard, *Journal of Geophysical Research: Oceans*, doi:10.1002/2016JC012391.

Meyer, A., I. Fer, A. Sundfjord, and A. K. Peterson (2017b), Mixing rates and vertical heat fluxes north of svalbard from arctic winter to spring, *Journal of Geophysical Research: Oceans*, doi: 10.1002/2016JC012441.

Muench, R. D., M. McPhee, C. Paulson, and J. Morison (1992), Winter oceanographic conditions in the fram strait and yermak plateau region, *Journal of Geophysical Research: Oceans*, *97*(C3), 3469–3483, doi:91JC03107.

Nurser, A. J., and S. Bacon (2013), Eddy length scales and the rossby radius in the arctic ocean, *Ocean Sci. Discuss.*, *10*(5), 1807–1831.

Padman, L., and T. Dillon (1991), Turbulent mixing near the yermak plateau during the coordinated eastern arctic experiment, *J. Geophys. Res.*, doi:10.1029/90JC02260.

Padman, L., and S. Erofeeva (2004), A barotropic inverse tidal model for the arctic ocean, *Geophys. Res. Lett.*, *31*(2), doi:10.1029/2003GL019003.

Padman, L., A. Plueddemann, R. Muench, and R. Pinkel (1992), Diurnal tides near the yermak plateau, *J. Geophys. Res.*, doi:10.1029/92JC01097.

Peterson, A. K., I. Fer, M. G. McPhee, and A. Randelhoff (2017), Turbulent heat and momentum fluxes in the upper ocean under arctic sea ice, *Journal of Geophysical Research: Oceans*, *122*(2), 1439–1456, doi:10.1002/2016JC012283.

Pham, D., J. Verron, and M. Roubaud (1998), A singular evaluative extended kalman filter for data assimilation in oceanography, *J. Mar. Syst.*, *16*, 323–340.

Plueddemann, A. (1992), Internal wave observations from the arctic environmental drifting buoy, *Journal of Geophysical Research*, *97*(C8), 12,619–12,638, doi:10.1029/92JC01098.

Polton, J. (2015), Tidally induced mean flow over bathymetric features: A contemporary challenge for high-resolution wide-area models, *Geophys. Astrophys. Fluid Dyn.*, *109*, 207–215, doi:10.1080/03091929.2014.952726.

Provost, C., N. Sennéchael, J. Miguet, P. Itkin, A. Rösel, Z. Koenig, N. Villacieros-Robineau, and M. A. Granskog (2017), Observations of flooding and snow-ice formation in a thinner arctic sea ice regime during the n-ice2015 campaign: Influence of basal ice melt and storms, *Journal of Geophysical Research: Oceans*, doi:10.1002/2016JC012011.

Rainville, L., and R. A. Woodgate (2009), Observations of internal wave generation in the seasonally ice-free arctic, *Geophysical Research Letters*, *36*(L23604), doi:10.1029/2009GL041291.

Richez, C. (1998), The west spitsbergen current as seen by sofar floats during the arctemiz 88 experiment: Statistics, differential kinematic properties, and potential vorticity balance, *J. Geophys. Res.*, *103*(C8), 15,539–15,565, doi:10.1029/97JC02421.

Rudels, B. (2012), Arctic ocean circulation and variability-advection and external forcing encounter constraints and local processes, *Ocean Science*, *8*(2), 261, doi:10.5194/os-8-261-2012.

Sirevaag, A., and I. Fer (2009), Early spring oceanic heat fluxes and mixing observed from drift stations north of svalbard, *Journal of Physical Oceanography*, *39*(12), 3049–3069, doi: http://dx.doi.org/10.1175/2009JPO4172.1.

Sirevaag, A., S. Rosa, I. Fer, M. Nicolaus, M. Tjemström, and M. McPhee (2011), Mixing, heat fluxes and heat content evolution of the arctic ocean mixed layer., *Ocean Science*, *7*(3), 335–349, doi:10.5194/os-7-335-2011.

Teigen, S., F. Nilsen, and B. Gjevik (2010a), Barotropic instability in the west spitsbergen current, *J. Geophys. Res.*, *115*, doi:10.1029/2009JC005996.

Teigen, S., F. Nilsen, B. Gjevik, and A. Beszczynska-Möller (2010b), Baroclinic instability in the west spitsbergen current,, *J. Geophys. Res.*, *116*, doi:10.1029/2011JC006974.

Våge, K., R. S. Pickart, V. Pavlov, P. Lin, D. J. Torres, R. Ingvaldsen, A. Sundfjord, and A. Proshutinsky (2016), The atlantic water boundary current in the nansen basin: Transport and mechanisms of lateral exchange, *Journal of Geophysical Research: Oceans*, *121*(9), 6946–6960, doi:10.1002/2016JC011715.

Von Appen, W.-J., U. Schauer, T. Hattermann, and A. Beszczynska-Möller (2016), Seasonal cycle of mesoscale instability of the west spitsbergen current, *Journal of Physical Oceanography*, *46*(4), 1231–1254, doi:http://dx.doi.org/10.1175/JPO-D-15-0184.1.

Wijesekera, H., T. Dillon, and L. Padman (1993), Some statistical and dynamical properties of turbulence in the oceanic pycnocline, *Journal of Geophysical Research: Oceans*, *98*(C12), 22,665–22,679, doi:10.1029/93JC02352.

Zhao, M., M.-L. Timmermans, S. Cole, R. Krishfield, A. Proshutinsky, and J. Toole (2014), Characterizing the eddy field in the arctic ocean halocline, *Journal of Geophysical Research: Oceans*, *119*(12), 8800–8817, doi:10.1002/2014JC010488.

4.3 Perspective

The current observations analyzed in this chapter are from 2007-2008 and the Arctic Ocean in this area has been changing the last few years (*Polyakov et al.*, 2017). Moreover, no hydrographic data (temperature, salinity) were recovered by the mooring and we could not estimate any heat fluxes through the Pass in winter nor in summer. A new ADCP mooring was deployed at the same location in september 2017 (Figure 4.1). This new dataset will document the Yermak Pass 10 years after the first mooring. The ADCP measurements will be complemented by microcats at several depths to collect information about the temperature and salinity seasonal variations over the Yermak Pass. With this new mooring, we could look at the diapycnal mixing and internal waves. It is important to precisely quantify theses processes over the Yermak Plateau as it is the region of inflow of the Atlantic Water in the Arctic; the heat content of the Atlantic Water in the rest of the Arctic is dependant on the heat losses/exchanges happening over the Yermak Plateau. Moreover, the comparison between the two moorings (2007-2008 and 2017-2018) will allow us to examine the changes that the Yermak Pass Branch has undergone over the past 10 years.

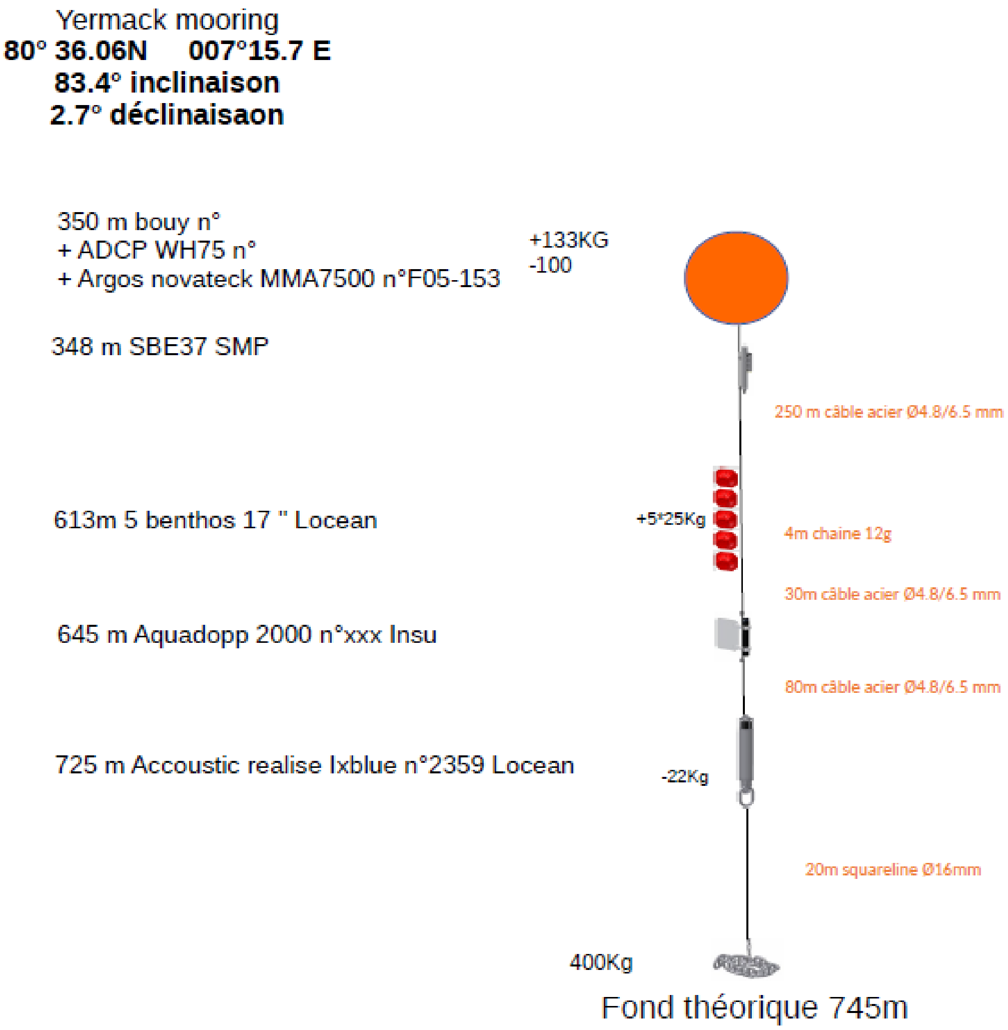

Figure 4.1: *Schematic of the mooring that will be deployed this summer in the Yermak Pass*

Chapter 5

Conclusions and Perspectives

Contents

5.1 Conclusions

We have examined the inflow of Atlantic Water (AW) from Fram Strait in the area North of Svalbard using observations from IAOOS platforms collected during N-ICE215 expedition. The expedition documented this region in winter for one of the first time (*Koenig et al.*, 2016). We found that:

- The surface mixed layer in winter was saltier than the climatology (about $0.1g/kg$). This result can be due to: either the mixed layer is saltier in winter than in summer (summer melt water, AW shallower in winter or more mixing with the storms?) as the climatology is biases with summer observations, or the mixed layer has been saltier in the recent years. With the latter hypothesis, the evolution of the Canadian and Eurasian basin differ significantly, as the Canadian surface ocean is freshening (*Rabe et al.*, 2011).
- Ocean-to-sea-ice heat fluxes larger than $400W.m^{-2}$ were documented on the Svalbard continental slope, inducing basal sea ice melt (reaching $10cm.d^{-1}$) in the middle of winter when air temperature was about $-30°C$.
- Near-inertial waves brought heat from the Atlantic Water layer over the continental slope up to the surface. Several possible causes are suggested: shallow Atlantic Water layer, rough topography, large tides, or large storms, several of them being observed at the same time hence it is very difficult to identify the precise origin of the near-inertial waves.

The *in situ* observations being limited in time and space, we complemented their analysis examining model outputs from the 1/12° Mercator operational model with data assimilation from January 2014 to April 2016. Since model outputs compared satisfactorily with IAOOS platform observations (*Koenig et al.*, 2017a), we inferred from the model outputs that:

- North of Svalbard, the Atlantic Water flows through the Yermak Branch and the Svalbard Branch in summer. In winter when the inflow of Atlantic Water is twice as large as in summer in the West Spitsbergen Current, a third branch is found: the Yermak Pass Branch that flows along isobaths $600 - 700m$ over the Yermak Plateau. This branch carries the largest volume transport of all branches in winter.
- Sea ice edge in winter 2015 and 2016 differs. Sea ice edge in winter 2015 is close to the Svalbard Archipelago while in winter 2016 sea ice edge is quite north following the deepest part of the Svalbard continental slope far east up to $30°E$. In autumn 2016, the wind induces Ekman pumping along the continental slope, bringing heat up to the surface. In winter 2016, winter convective mixing occurs over the continental slope north of Svalbard and brings heat from the Atlantic Water layer up to the surface and melts the sea ice.

In order to examine in more detail the Yermak Pass Branch that seems to be an important pathway for the Atlantic Water across the Yermak Plateau in the 1/12° Mercator Ocean operational model, we analyzed data from an upward looking Acoustic Doppler Current Profiler (ADCP) deployed for fourteen months (July 2007 - September 2008) in the Yermak Pass (*Koenig et al.*, 2017b). We complemented the analysis examining 10 years of 1/12° Mercator-Ocean operational model outputs to apprehend seasonal and year-to-year variations. We found that:

- The current through the Yermak Pass is dominated by tides, with a predominance of semi-diurnal and diurnal tides. Tides induce a significant rectified mean flow of $\pm 5cm/s$ to the northeast opposed to the background flow of Atlantic Water in the Yermak Pass.
- In winter baroclinic eddies at periods between 5 and 15 days are observed in the Atlantic Water layer.
- ADCP data confirm that the current through the Yermak Pass flows eastward in monthly/bi-monthly pulses only in winter.
- Model outputs suggest that the Yermak Pass Branch has been a robust winter pattern over the last 10 years, carrying on average 31% of the volume transport of the West Spitsbergen Current (36% in winter). This result has to be considered with caution as the model does not represent tides that have been shown to generate significant residual currents to the Northeast opposed to the Yermak Pass flow.

A flow of AW through the Yermak Pass Branch in winter can explain the warm Atlantic Water offshore the continental slope of Svalbard in the IAOOS data from the N-ICE2015 expedition (*Koenig et al.*, 2016). This has implications for the sea ice - ocean dynamics and for the ecosystems in the region as Atlantic Water is the main source of nutrients in the Arctic.

5.2 Perspectives

With climate change, dynamics of the entire Arctic Ocean are altered. Exchanges with the atmosphere and turbulence are expected to increase. With sea ice melting, the hydrography of the current will change, with a freshening of the surface of the ocean. The inflow of AW in the Arctic is getting warmer (*Walczowski et al.*, 2012) which could lead to more sea ice melt, affect the ecosystems and change the surface water properties (saltier in the eurasian Basin?). In this context, the Year of Polar Prediction (http://www.polarprediction.net/yopp/) will take place from mid 2017 to mid 2019 and aims at : "Enabling a significant improvement in environmental prediction capabilities for the polar regions and beyond, by coordinating a period of intensive observing, modelling, verification, user-engagement and education activities".

Data are still sparse in the Arctic Ocean, and even if several campaigns are planned in the future, the use of model outputs and especially realistic ones (operational) is a real asset to study the Arctic Ocean dynamic. This thesis illustrates that models can perform satisfactorily in the Arctic and that they are a very useful tool to put the sparse observations in a broader spatial and temporal context.

Concerning the observations, several projects aim at monitoring the Atlantic Water inflow north of Svalbard and the Atlantic Water Boundary Current in the Arctic Ocean and their respective dynamics in this new Arctic regime in the next few years. For instance, the mooring array at $30°E$ along the continental slope north of Svalbard was redeployed in September 2017 for at least another year by the Norwegian Polar Institute (A-TWAIN project). Several autonomous drifting platforms such as the american ice-tethered profilers (ITP) and the IAOOS platforms will be deployed in the next few years, trying to cover well the entire Arctic. As the Arctic Ocean is becoming more and more seasonally ice free, new autonomous instruments such as gliders could be deployed in the Arctic and represent a new way of observing the Arctic. Several glider measurements have been performed this summer around the Svalbard Archipelago, in the West Spitsbergen Current and along the continental slope North of Svalbard in collaboration between the UPMC and the NPI. Finally, the MOSAiC (Multidisciplinary drifting Observatory for the Study of Arctic Climate) project (mosaicobservatory.org) will consist of a transarctic drift of the *R/V Polarstern* from autumn 2019 to autumn 2020. The ice camp will provide the opportunity to document the Atlantic Water layer and its dynamic in winter in the central Arctic.

Concerning modelisation, models performances evolve all the time, and several improvements such as higher spatial and vertical resolution or representation of tides should be implemented in the future and will help the analysis of the observations.

Within the context of the Atlantification of the Eurasian Basin, the area North of Svalbard can be seen as a precursor of the state of the slope in the next few years. It is also the area of the inflow of the Atlantic Water in the Arctic; the Atlantic Water is still close to the surface and large exchanges of heat with the surface/the sea ice are observed. Hence in this region properties of the Atlantic Water are strongly altered and the Atlantic Water properties that will be encountered in the rest of the Arctic Ocean rely on the ocean processes occurring over the Yermak Plateau. The eddy field, a vector of heat transport from the continental slopes to the interior of the basin is still poorly known. Finally, how the Atlantic Water layer and the thermocline/halocline evolve in the entire Arctic Basin once in the Arctic Ocean, after the Yermak Plateau and the Santa Anna Trough? The following subsections will detail the above scientific problematics (oeaan dynamic over the Yermak Plateau, eddy fiel and thermocline/halocline evolution in the Arctic Ocean) and present some tools (observations and numerical simulations) that can be used to study them.

5.2.1 The ocean dynamic over the Yermak Plateau

As seen in Chapter 4, ocean dynamic over the Yermak Plateau is complex: mesoscale activity (eddies), tides... As the Yermak Pass Branch over the Yermak Plateau seems to be an important pathway of the Atlantic Water in the Arctic, it is necessary to better understand the ocean dynamic over the Yermak Plateau and be able to quantified heat fluxes that affect the Atlantic Water layer in this area. In this context, the mooring in the Yermak Pass has been redeployed this year, complemented with microcat to estimate year round heat fluxes over the Yermak Plateau (Figure 5.1).

In order to better understand the small scale dynamic over and around the Yermak Plateau (in the area of the Atlantic Water inflow in the Arctic), I deployed a Sea Explorer glider in July 2017 in collaboration with the Norwegian Polar Institute. The deployment was done from *R/V Lance* and lasted 13 days, during which the glider repeated 2 sections 3 times each, across the West Spitsbergen Curren (Figure 5.1). The glider was redeployed in September 2017 from the *R/V Lance* and crossed the West Spitsbergen Current, the Yermak Branch, the Yermak Plateau and the Svalbard Branch (Figure 5.1). This technology recorded temperature, salinity, dissolved oxygen and fluorescence data at a high vertical (less than a meter) and horizontal (more than 400 profiles up and down, which corresponds to more than 30 profiles per day) resolution. The analysis of these data will provide new insights on the small scales (eddies) of the inflow of Atlantic Water in the Arctic through its main branches.

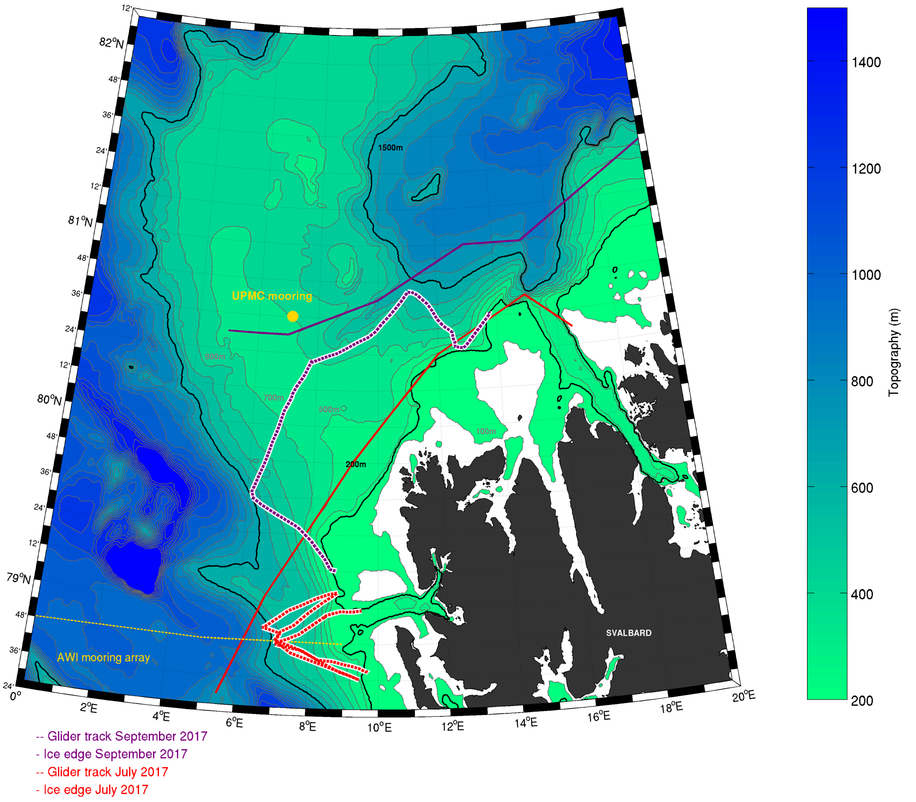

Figure 5.1: *Trajectory of the Sea Explorer glider deployed north of Svalbard in July 2017(red-white dotted line) and in September 2017 (purple-white dotted line). The red (purple) line is the roughly the sea nice edge in July (September). Background is the bathymetry. UPMC mooring corresponds to the location of the mooring deployed in 2007 and in September 2017 in the Yermak Pass.*

High resolution models with tides will help to understand the dynamic over the Yermak Plateau. However, a 1/12° resolution model as used in the thesis is only eddy-permitting and not eddy-resolving in the Arctic and do not represent tides, two processes of main importance over the Yermak Plateau. At Mercator Ocean, a pan-arctic configuration at 1/36° spatial resolution, with tides, will be tested by 2018 for a complete seasonal cycle. The ocean circulation in this simulation over the Yermak Plateau is expected to be improved, as tidal rectification current (due to semi diurnal and diurnal tides) can be important over the Yermak Plateau for instance (*Koenig et al.*, 2017b; *Padman et al.*, 1992).

5.2.2 The eddy field

Exchanges of momentum between the atmosphere and the ocean will become more intense with a smaller sea ice extent, and we expect the turbulence of the Arctic Ocean to increase (*Dosser and Rainville*, 2016). Particularly, the eddy field is of scientific interest as it may be a key vector of heat from the Atlantic Water Boundary Current to the interior of the basins (*Våge et al.*, 2016). Eddies have been observed and examined in the Beaufort Gyre (*Carpenter and Timmermans*, 2012) and a few have been documented on the continental slope north of Svalbard (*Våge et al.*, 2016) but studies are still sparse especially on the Eurasian side of the Arctic Ocean.

Concerning the deep Eurasian Basin, the use of ITPs and of IAOOS platforms deployed in the central Arctic in summer 2015 from the *Polarstern* will help to analyze the eddy field in the deep basins.

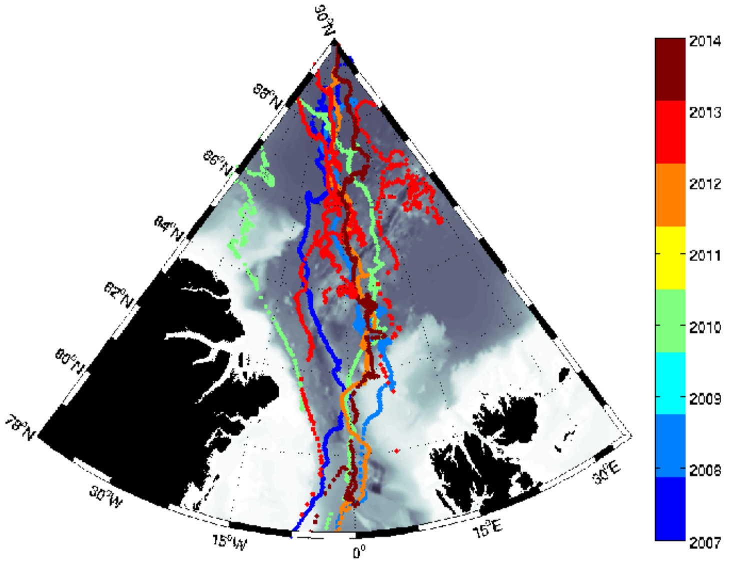

Figure 5.2: *Drift trajectories of the ITPs between North Pole and Fram Strait from 2007 to 2014. Colors correspond to the year of the drift for each ITP.*

We started to analyze the eddy field from 2007 to 2014 from North Pole to Fram Strait (Figure 5.2). We used data from ITPs that monitored the upper ocean during spring-summer 2007-2014 (Figure 5.2). We detected the eddies using a density anomaly detection scheme (*Zhao et al.*, 2014). The total number of anticyclonic eddies is 25 and the total number of cyclonic eddies is 7. We observed a predominance of anticyclonic eddies with a cold core located between 50 and 80m (Table 5.1). Eddy radii are of the same order as the Rossby deformation radius in the Eurasian Basin (5 to 10km). Some eddies are found in the Atlantic Water layer (core deeper

Table 5.1: *Statictics of the eddies : core depth, category, and mean extension.*

Core depth X	Type	Number	Mean vertical extension
X<80m	Anticyclone	16	140m
	Cyclone	5	90m
80m<X<200m	Anticyclone	6	210m
	Cyclone	0	nr
X>200m	Anticyclone	3	350m
	Cyclone	2	300m

than $200m$, table 5.1) and in the center of the basins, which is quite far from the continental slopes of the Arctic where the Atlantic Water flows and where the eddies are probably generated by baroclinic instability (*Zhao et al.*, 2014). These preliminary findings support the hypothesis that the eddies are a way of transporting heat and salt in the interior of the basins. With the decline of the sea ice cover, the eddy activity could increase and the heat diffuse more inside the basins.

Glider measurements from summer 2017 in the area around Svalbard will also provide information on the eddy field in this region where the Atlantic Water is very warm and salty and hence where the heat transport in the interior of the Nansen Basin could be of major importance.

To complete this process study, it would be useful to examine model outputs to put the observations in a broader spatial and temporal context. The 1/36° Pan-Arctic simulation of Mercator Ocean (eddy-resolving) could be used. This configuration will enable a proper study of the eddy field in Arctic and better complement the observations.

5.2.3 Evolution of the thermocline/halocline over the entire Arctic Ocean

In this thesis, we focused on the inflow of the Atlantic Water North of Svalbard where the Atlantic Water layer properties are altered by several processes over the Yermak Plateau. The Atlantic Water layer properties and its associated thermocline/halocline are also modified in the entire Arctic Basin. How are the properties of the Atlantic Water altered in the rest of the Arctic? Has the thermocline/halocline been eroded for the last 10 years as observed in the Eurasian Basin with its Atlantification? This problematic is basin wide and has probably evolve with time. The long-term changes of the Atlantic Water inflow can be apprehended examining the record of more than 10 years of the Fram Strait mooring array. To examine variations in the deep Arctic, ice-tethered profilers could be used. They have now been deployed for more than 10 years and long-term analysis with observations of the deep Arctic Basins are now possible. We present shortly in the following some very preliminary results of comparaisons between 2 IAOOS platforms deployed in summer 2015 and ITPs deployed in summer 2007 in the Canadian Basin and in the Chukchi Sea.

The thermocline structure from IAOOS platforms deployed in 2015 in the Chukchi Sea from the *R/V Araon* has been compared with the one from ITPs with similar trajectories 10 years earlier (ITP23 and ITP29, *Timmermans et al.* (2010)). ITP29 trajectory crosses IAOOS15 drift in the Chukchi Sea around $180 - 190^{\circ}E$, in the same period of the year (in autumn/winter). ITP23 and IAOOS15 have similar trajectories in a large part of the Canadian Basin (from $150^{\circ}W$ to $115^{\circ}W$), but do not drift at the same season: autumn/winter for ITP23 and spring/summer for IAOOS15 (Figure 5.3).

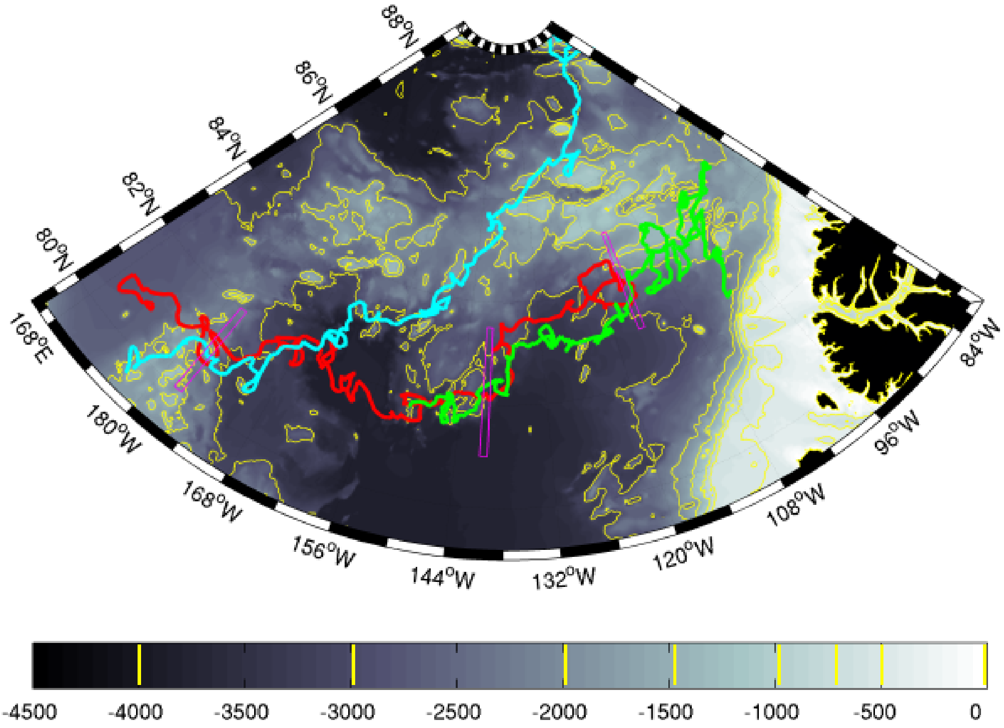

Figure 5.3: *Trajectories of IAOOS15 (in red), ITP29 (in cyan) and ITP23 (in green). The magenta boxes are the area where comparisons are made between the ITPs and the IAOOS platform hydrography data:* 182, 219 *and* $244^{\circ}E$*.*

.

Comparisons between IAOOS platform data and ITP23 and 29 data are presented in Figure 5.4. We plotted the profiles contained in 1° longitude on the same figure. We chose locations were the profiles from ITPs and IAOOS platforms were the closest.

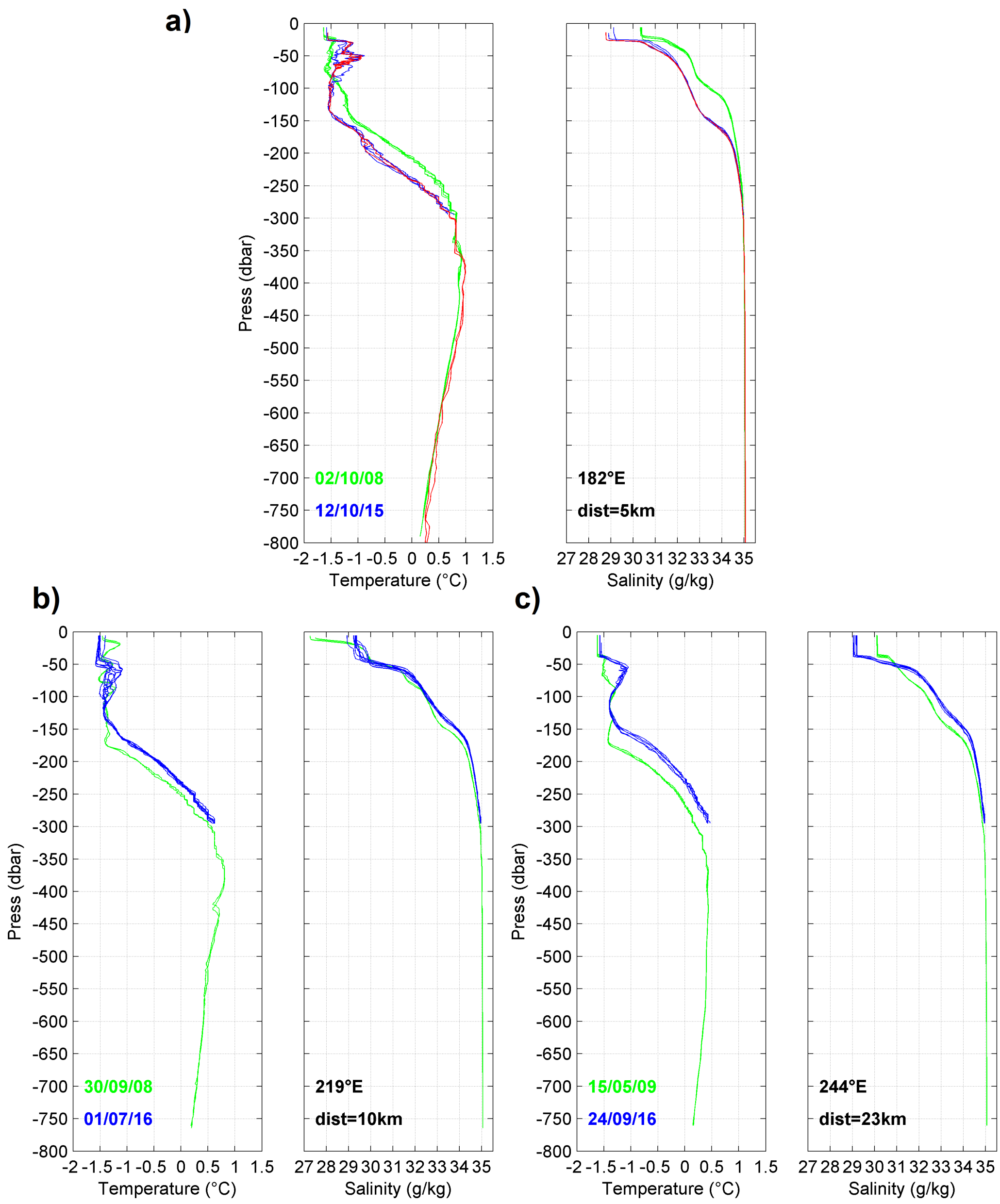

Figure 5.4: *Comparison of profiles of conservative temperature (°C) and absolute salinity (g/kg) at a) 182°E from the IAOOS platforms (in red IAOOS14, in blue IAOOS15) with ITP29 (in green).b) 219°E and c) 244°E longitude from the IAOOS platform (IAOOS15 in blue) with ITP23 (in green). The green date are the average depth of the ITP profiles, the blue one of the IAOOS profiles.*

.

At $182°E$ (magenta box on the left on Figure 5.3 and Figure 5.4 a), IAOOS14, IAOOS15 and ITP29 profiles are in the same area (mean of 5 km apart) during the same season (one week apart in October) but 7 years apart (2015 and 2008). Hence differences can only be due either to Arctic long-term trend or to the interannual variability of the Arctic. Interlayering at the base of the thermocline is slightly deeper ($10m$) in 2015 than in 2008 and the core of the Atlantic Water is warmer ($1°C$ instead of $0.7°C$) and slightly saltier in 2015 ($35.01g/kg$ instead of $35g/kg$). It features a change in the Atlantic Water inflow along the Arctic continental slope.

At $219°E$ ($141°W$ in the center of the Canadian Basin, magenta box in the middle on Figure 5.3), IAOOS15 and ITP23 are less than 10 km apart and drifted at different months: July 2016 and September 2008 (Figure 5.4 b). Compared to the Chukchi Sea, here in the middle of the Canadian Basin, the thermocline is shallower in 2016 than in 2008 (by about $30m$).This is in contrast to the observation of a deeper thermocline and larger freshwater content in the Chukchi Sea (Figure 5.4 b). At $244°E$ ($116°W$, east of the Canadian Basin, magenta box on the right on Figure 5.3), the thermocline in 2007 is deeper than in 2015, and the difference in the depth of the thermocline is larger at $244°E$ compared to $219°E$ (Figure 5.4 c).

These three comparisons suggest that over the last 10 years, changes occurred in the thermocline: the top of the Atlantic Water is shallower and could possibly melt sea ice more easily. Several questions remain, for instance: What are the impact of these changes on the sea ice? Is this shoaling of the thermocline observed in the entire Arctic Ocean?

One way of answering the spatial and temporal coverage of the observations will be to analyze model outputs in the Arctic Basin. Long-term time series (more than 10 years) would be needed. A simulation over the 25 years of altimetry (from 1993 to present) with assimilation and 1/12° spatial resolution is for instance planned at Mercator Ocean and will enable us to apprehend the low frequency variability of the Arctic Ocean and its evolution with the climate change.

Appendix A

Winter to summer oceanographic observations in the Arctic Ocean north of Svalbard

AGU PUBLICATIONS

Journal of Geophysical Research: Oceans

RESEARCH ARTICLE

10.1002/2016JC012391

Special Section:
Atmosphere-ice-ocean-ecosystem Processes in a Thinner Arctic Sea Ice Regime: the Norwegian Young Sea ICE Cruise 2015 (N-ICE2015)

Key Points:
- N-ICE2015 Arctic winter oceanographic observations are a key contribution in a region with extremely sparse winter data coverage
- Yermak Branch of Atlantic Water inflow is observed retroflecting around the northern tip of the Yermak Plateau
- Late spring shallow mixed layer over the Yermak Plateau associated with large sea ice melt

Correspondence to:
A. Meyer,
Amelie.Meyer@npolar.no

Citation:
Meyer, A., et al. (2017), Winter to summer oceanographic observations in the Arctic Ocean north of Svalbard, *J. Geophys. Res. Oceans*, *122*, doi:10.1002/2016JC012391.

Received 28 SEP 2016
Accepted 23 JAN 2017
Accepted article online 31 JAN 2017

Winter to summer oceanographic observations in the Arctic Ocean north of Svalbard

Amelie Meyer[1], Arild Sundfjord[1], Ilker Fer[3], Christine Provost[2], Nicolas Villacieros Robineau[2], Zoe Koenig[2], Ingrid H. Onarheim[3], Lars H. Smedsrud[3], Pedro Duarte[1], Paul A. Dodd[1], Robert M. Graham[1,4], Sunke Schmidtko[5], and Hanna M. Kauko[1]

[1]Norwegian Polar Institute, Fram Centre, Tromsø, Norway, [2]LOCEAN, Université Pierre et Marie Curie, Paris Cedex, France, [3]Geophysical Institute, University of Bergen and Bjerknes Centre for Climate Research, Bergen, Norway, [4]Alfred Wegener Institute, Helmholtz Centre for Polar and Marine Research, Bremerhaven, Germany, [5]GEOMAR, Helmholtz Centre for Ocean Research, Kiel, Germany

Abstract Oceanographic observations from the Eurasian Basin north of Svalbard collected between January and June 2015 from the N-ICE2015 drifting expedition are presented. The unique winter observations are a key contribution to existing climatologies of the Arctic Ocean, and show a ~100 m deep winter mixed layer likely due to high sea ice growth rates in local leads. Current observations for the upper ~200 m show mostly a barotropic flow, enhanced over the shallow Yermak Plateau. The two branches of inflowing Atlantic Water are partly captured, confirming that the outer Yermak Branch follows the perimeter of the plateau, and the inner Svalbard Branch the coast. Atlantic Water observed to be warmer and shallower than in the climatology, is found directly below the mixed layer down to 800 m depth, and is warmest along the slope, while its properties inside the basin are quite homogeneous. From late May onwards, the drift was continually close to the ice edge and a thinner surface mixed layer and shallower Atlantic Water coincided with significant sea ice melt being observed.

1. Introduction

The Arctic Ocean is connected to the Atlantic Ocean via the deep Fram Strait and the shallow Barents Sea. The exchange in the Fram Strait is dominated by northward flowing warm and saline Atlantic Water (AW) and southward cold Arctic water near the surface [*Rudels et al.*, 2000; *Spall*, 2013; *Rudels et al.*, 2015]. The warm AW is the primary source of heat for the Arctic Ocean [*Aagaard and Greisman*, 1975; *Carmack et al.*, 2015].

In Fram Strait, the inflow of warm AW advected by the West Spitsbergen Current splits as it reaches the Yermak Plateau [*Aagaard et al.*, 1987]. The Svalbard Branch follows the topography inshore of the Yermak Plateau between the 400 and 500 m isobaths [*Sirevaag and Fer*, 2009]. The Yermak Branch circulates anticyclonically around the Yermak Plateau's western slope and follows the 1500 m isobath [*Perkin and Lewis*, 1984; *Muench et al.*, 1992; *Gascard et al.*, 1995]. A substantial fraction of the Yermak Branch has been observed to cross the Plateau eastward at 80.4°N through the Yermak Pass at 700 m depth [*Gascard et al.*, 1995], but this has not been confirmed by other studies, possibly due to the scarcity of observations in that area (Figure 1). Another part of the Yermak Branch detaches from the continental slope and recirculates across Fram Strait [*Bourke et al.*, 1988]. It is thought that the remaining part of the Yermak Branch rejoins the inshore branch northeast of Svalbard but pathways past the northern tip of the Plateau are unclear. East of Svalbard, AW flows eastward along the slope of the Eurasian continent [*Treshnikov*, 1977], cooling and freshening, before it is eventually transported back to the Atlantic Ocean through the western Fram Strait [*Lique et al.*, 2010; *Polyakov et al.*, 2012] (Figure 1).

The Yermak Plateau is a local hotspot for vertical mixing and cooling of AW [*Fer et al.*, 2015]. Strong tidal currents around the slopes of the Plateau lead to increased internal wave activity and therefore enhanced mixing rates [*Padman and Dillon*, 1991; *Wijesekera et al.*, 1993; *Fer et al.*, 2010]. Mixing causes water mass modification affecting regional ice cover [*Fer et al.*, 2015]. North of Svalbard, inflowing AW

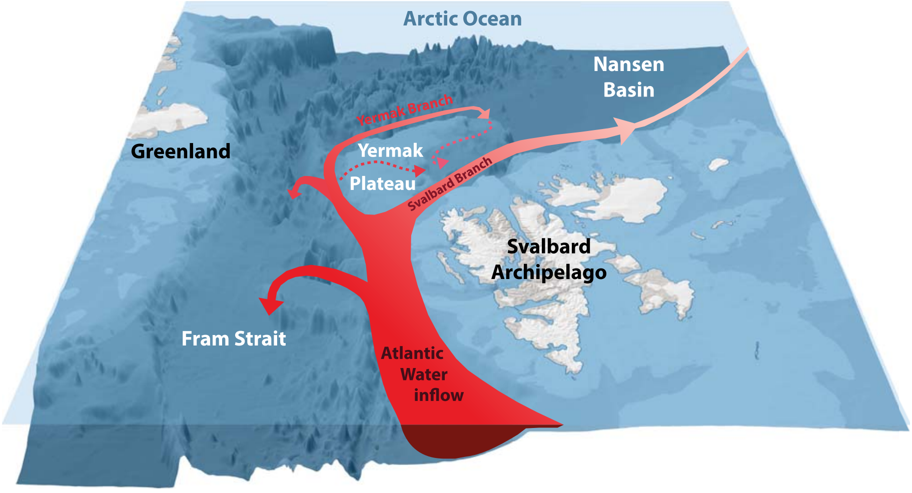

Figure 1. Regional circulation schematic of Atlantic Water inflow in Fram Strait and Nansen Basin, west and north of the Svalbard Archipelago following *Sirevaag and Fer* [2009] and *Polyakov et al.* [2012]. Dashed arrows represent uncertain Atlantic Water pathways around the Yermak Plateau and across the Plateau through the Yermak Pass. Bathymetry is from the ETOPO1 data set [*Amante and Eakins*, 2009].

interacts with the Arctic sea ice, and a fresher upper layer of Polar Water, is created [*Onarheim et al.*, 2014; *Rudels et al.*, 2015]. This region is therefore key for understanding the formation of the cold halocline that insulates sea ice from warm AW [*Rudels et al.*, 2004]. As noted by *Steele and Boyd* [1998], processes that create the Arctic Ocean stratification are best identified using winter observations when these processes are taking place.

The AW inflow to the Arctic has been warming since the late 1970s with the strongest warming signal over the Svalbard slope [*Grotefendt et al.*, 1998; *Schauer et al.*, 2004; *Ivanov et al.*, 2009; *Polyakov et al.*, 2012; *Beszczynska-Möller et al.*, 2012]. The warming of the AW layer could lead to substantial melt of the Arctic sea ice in particular near the AW source along the Svalbard continental slope [*Polyakov et al.*, 2013; *Onarheim et al.*, 2014; *Carmack et al.*, 2015].

The Arctic Ocean is undersampled compared to much of the world ocean [*Abrahamsen*, 2014]. Estimating trends and understanding mechanisms in an extreme seasonal environment is a challenge with few comprehensive observational campaigns outside the spring and summer periods [*Grotefendt et al.*, 1998].

The Norwegian young sea ICE expedition (N-ICE2015) took place north of Svalbard in 2015 to investigate the new thinner Arctic sea ice regime [*Renner et al.*, 2013] and associated interactions between the ice, ocean, and atmosphere, and the feedbacks between physical and biogeochemical processes [*Granskog et al.*, 2016]. We present hydrographic and ocean current observations collected from January to June 2015 during N-ICE2015 in the Nansen Basin and over the Yermak Plateau. These 6 months of observations, spanning the winter and spring is a unique data set and provides the oceanographic context for topical studies presented in N-ICE2015 companion papers. We investigate the hydrography and circulation, focusing on the AW pathways, characteristics, and impacts on sea ice. The data collection and quality control are described in section 2. In section 3, we give an overview of the water mass distribution, seasonal mixed layer, seasonal and regional variability, and currents. We discuss the implications in section 4 and conclude in section 5.

2. Data and Methods

2.1. N-ICE2015 Expedition

Between January and June 2015, during the N-ICE2015 expedition the R.V. Lance completed four drifts in the Arctic Ocean north of Svalbard, moored each time to a different sea ice floe (Figure 2 and Table 1). On each floe, hereinafter referred to as Floes 1–4, an ice camp was set up and oceanographic data as well as atmospheric, sea ice, snow, and biogeochemical data were collected [*Granskog et al.*, 2016].

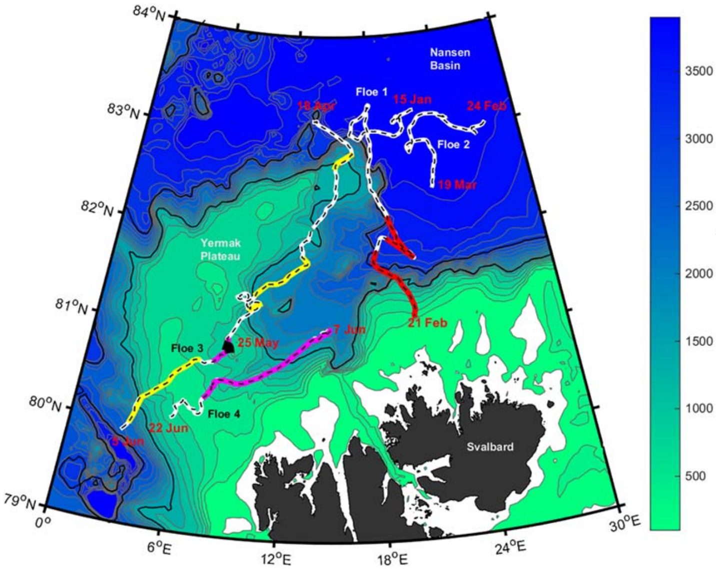

Figure 2. Trajectories of the four N-ICE2015 drift floes between 15 January and 22 June 2015 with underlying topographic contours ranging from 100 to 5000 m at 200 m intervals. Presence of Atlantic Water in the water column is indicated and labelled from either the Yermak Branch (yellow drift track), from undetermined origin (magenta drift track), or from the Svalbard Branch (red drift track). The 3000 and 1500 m isobaths represent the limits between the deep Nansen Basin, the slope areas and the shallower Yermak Plateau (thick black lines). Key dates are indicated in red.

The first drift took place in January and February 2015 lasting 38 days, partly in the Nansen Basin, partly at the northern edge of the Yermak Plateau, finishing on the Svalbard continental slope (Table 1). Drift 2 lasted 24 days over the Nansen Basin during February and March 2015. Drift 3, the longest, lasted 49 days from April until June 2015 from the northern slope of the Yermak Plateau, to the southern edge of the Plateau. Finally drift 4 took 16 days and covered a similar track to the last part of drift 3 on the Yermak Plateau. Drift 1 and 2 took place during winter, with drift 1 in full darkness and the first sunrise on 1 March 2015 during drift 2. Drift 3 and 4 took place during spring with the last sunset on 5 April 2015 during drift 3.

2.2. Collected Data

In this study, temperature and salinity profiles from several instruments are used: profiles from a vessel-mounted CTD processed to 1 m vertical average, profiles from Ice-Atmosphere-Arctic Ocean Observing System (IAOOS) profilers processed to 1 m vertical average, and profiles from microstructure profilers processed to 0.2 m vertical average). Also used in this study are dissolved oxygen concentrations from discrete

Table 1. N-ICE2015 Expedition Overview and Data Sets Used in This Study, Publicly Available at the Norwegian Polar Data Centre [*Dodd et al.*, 2016; *Meyer et al.*, 2016b, 2016; *Provost et al.*, 2016; *Dodd et al.*, 2016]

Ice Drift	Floe 1	Floe 2	Floe 3	Floe 4
Season	Winter	Winter	Spring	Spring
Start date	15 Jan 2015	24 Feb 2015	18 Apr 2015	7 Jun 2015
Start position	83.2°N 21.6°E	83°N 27.4°E	83.2°N 13.5°E	81.1°N 14.4°E
End date	21 Feb 2015	19 Mar 2015	5 Jun 2015	22 Jun 2015
End position	81.2°N 20.3°E	82.5°N 22.6°E	79.9°N 3.1°E	80.1°N 5.7°E
Duration (days)	38	24	49	16
Number of ship CTD casts	11	5	29	6
Number of on-ice CTD casts	21	19	39	13
Number of microstructure profiles (sets)	71 (21)	55 (25)	329 (94)	128 (29)
Number of IAOOS buoy profiles	112	16		
Vessel-mounted ADCP	15 Jan to 21 Feb 2015 38 days	24 Feb to 3 Mar 2015 8 days	18 Apr to 5 Jun 2015 49 days	7 Jun to 22 Jun 2015 16 days
Long Ranger ADCP			3 May to 4 Jun 2015 33 days	11 Jun to 19 Jun 2015 9 days

water samples, current velocity profiles from a medium range vessel-mounted ADCP (hourly temporal and 8 m vertical average), and current velocity profiles from a long ranger ADCP suspended beneath the ice floe (hourly temporal and 8 m vertical average). Each instrument and the associated data set are described in the following sections and summarized in Table 1. The data were analyzed using the Thermodynamic Equation of SeaWater 2010 (TEOS-10) and conservative temperature (CT) and Absolute Salinity (SA) is used throughout the text [*McDougall et al.*, 2012].

2.2.1. Ship-Board CTD Data

The ship-board CTD was a Sea-Bird Electronics SBE911 plus with two sets of sensors attached to a multibottle Sea-Bird carousel water sampler holding 11 Niskin bottles of 8 L each. Separate water samples for salinity analyses were drawn from the Niskin bottles immediately after the CTD package was secured in a heated area. These salinity samples were analyzed at sea using a Guildline Portasal salinometer with accuracy ca. ±0.003.

Prior to and after the N-ICE2015 expedition, the CTD sensors were calibrated at Sea-Bird. The temperature sensors drifts were negligible. The conductivity sensors had drifted and conductivity slope corrections were calculated using bottle salinity measurements. The data accuracy for conductivity estimates was ±0.0003 S m^{-1} and for temperature of ± 0.001°C.

A total of 51 ship CTD casts were carried out of which 25 stopped just above the seafloor. The remainder were shallow casts (less than 200 m) to collect biological water samples. The ship CTD sampling was usually weekly, except when interrupted between the 16 February and the 20 March 2015. During this period, sea ice under and by the side of the ship stacked up to 8 m thick, making the CTD hole maintenance impossible.

2.2.2. IAOOS Profilers Data

Two IAOOS buoys (http://iaoos.ipev.fr/index.php?lang=en) [*Provost et al.*, 2015; *Koenig et al.*, 2016] that carried ice-tethered profilers manufactured by NKE (PROVOR SPI) were deployed during Floe 1. The profilers were equipped with a Seabird 41CP CTD and an Aanderaa 4330 optode for dissolved oxygen. The profilers were set to collect two profiles per day down to 500 m depth, and gathered a total of 112 profiles. In addition, during Floes 1 and 2, tests were carried out involving a profiler on a 800 m long instrumented line in a tent-covered testing-hole. A total of 42 profiles used in this study were obtained with this set up (26 during Floes 1 and 16 during Floe 2). The vertical resolution of the processed CTD data is 1 dbar in the upper 400 dbars, 5 dbars from 400 to 550 dbars and 10 dbars from 550 to 850 dbars. The vertical resolution in dissolved oxygen is 2 dbars over all depths.

The profiler salinity data were calibrated using the ship CTD salinity [*Koenig et al.*, 2016]. Following quality control, all the temperature profiles were retained and 1% of the salinity and dissolved oxygen profiles were removed. Resulting data accuracy was ±0.002°C for temperature, ±0.02 for salinity, and ±3 μmol kg^{-1} for dissolved oxygen.

2.2.3. Microstructure Profiler Data

A total of 588 microstructure profiles were collected in 173 sets with two loosely tethered free-fall MSS-90 microstructure profilers [*Prandke and Stips*, 1998] developed by ISW Wassermesstechnik. A set, which corresponds here to consecutively sampled profiles, was usually composed of three profiles during the N-ICE2015 expedition. The profilers had precision conductivity, temperature, and depth sensors as well as turbulence sensors including two airfoil shear probes, a fast response thermistor, and a microconductivity sensor. Here we use the CTD profiles while details of the microstructure data processing and a description of the vertical mixing and turbulence characteristics can be found in *Meyer et al.* [2017].

The microstructure profilers were deployed through a hole in the sea ice from a heated tent a few hundred meters away from the ship. The profiles (only the downcasts are used) started immediately below the ice and reached on average 150 m during Floe 1 and 300 m during Floes 2, 3, and 4. Data processing followed *Fer* [2006]. High-resolution profiles, sampled at 1024 Hz, were vertically averaged to 20 cm. The CTD data from the microstructure profilers were compared with the ship CTD data for validation, and salinity drift corrections of 0.021 g kg^{-1} for one and 0.065 g kg^{-1} for the second profiler were applied.

2.2.4. Dissolved Oxygen Data (Water Samples)

A total of 175 samples of dissolved oxygen were collected directly from Niskin bottles on either the ship CTD rosette (68 samples) or from bottles on a Hydro-Bios water sampler deployed from the sea ice (107 samples). This small water sampler (SlimLine 6) with integrated CT-set, hereinafter “on-ice CTD,” was operated from the same tent and hole as the microstructure profiler, several hundred meters away from R.V. Lance. Individual sampling bottles with a nominal capacity of 115 mL were used. The analysis and calculations followed the modified Winkler procedure described in *Carpenter* [1965]: sulfuric acid had 50% volume concentration and the concentration of thiosulfate stock solution was 0.18 M. Titrations were carried out in two 50 mL aliquots taken from the dissolved oxygen bottles to check the reproducibility of the results. Consecutive titrations led to nonsignificantly different results. A digital Solarus burette from Hirschmann was used. Standards and blank were determined every time measurements were made. Dissolved oxygen concentrations were calculated in mL L^{-1} and converted to μmol kg^{-1} using potential temperature and surface pressure [*Weiss*, 1970].

2.2.5. Current Data: Vessel-Mounted ADCP Data

Current velocity in the upper 150 m was measured by a vessel-mounted broadband 150 kHz acoustic Doppler current profiler (ADCP) (Teledyne RD Instrument (RDI)). Vessel-mounted ADCP data were collected near continuously between 15 January and 22 June 2015, with a gap in data between 3 March and 19 March 2015 (Table 1) due to large ridging events blocking the ADCP transducers with sea ice. Profiles were averaged hourly in 8 m vertical bins with the first bin centered at 23 m.

2.2.6. Current Data: Long Ranger ADCP Data

During part of the N-ICE2015 expedition, time series of velocity were collected using a downward-looking RDI 75 kHz Long Ranger ADCP (Table 1). This ADCP was deployed just under the sea ice suspended with a chain and secured to the ice floe several hundreds of meters away from the ship. During drift 3, the instrument averaged 40 velocity profiles (pings) at 10 min intervals in 8 m thick cells, with the first cell centered at 21 m, while during drift 4, 55 velocity profiles were averaged at 20 min intervals, with the first cell centered at 19 m. Ensembles with excessive tilt (pitch and roll more than ±20°), and bins with weak average echo intensity (less than 40 counts) or less than 50% good three-beam and four-beam solutions were discarded. Absolute current velocity was obtained by adding the ice velocity as measured by the ship's Global Positioning System (GPS) to the relative velocity profile. The final vertical range of the Long Ranger ADCP data was 480 m which is typical for Arctic waters where acoustic scatterer concentrations are low.

2.3. Tides

In order to estimate the relative contribution of tides and background flows in the observed velocities, two approaches were used. First, tidal predictions from a model were derived along the drift tracks. Second, we attempted to isolate the tidal signal from the velocity observations. Both estimates are compared and discussed in the section 3.

2.3.1. Tidal Model: AOTIM-5 Tidal Current Predictions

We use the Arctic Ocean Tidal Inverse Model (AOTIM-5) [*Padman and Erofeeva*, 2004] to estimate the tidal current velocities associated with the four most energetic tidal components (M_2, S_2, O_1, and K_1) along the N-ICE2015 drift trajectories. The model provides 5 km horizontal grid resolution barotropic tidal velocities based on the *Egbert et al*. [1994] data assimilation scheme using all available tide gauge data in the Arctic Ocean.

2.3.2. Tidal Current Observations: Complex Demodulation

Our current observations were collected from a drifting platform. The time series are therefore affected by both temporal and spatial variability, and standard tidal harmonic analysis cannot be used. Using complex demodulation, we attempted to isolate the tidal signals in the ADCP current data time series. The algorithm is described in *Emery and Thomson* [2001, chap. 5, pp. 402–403]. Rotary component amplitude and phase of the diurnal and semidiurnal tides were estimated at, respectively, 24 and 12 h frequencies using 48 h long segments. Tidal estimates are not sensitive to the exact chosen time segment; the latest is determined by a compromise between too little data (short-time segment) and decreasing precision (large time segment). We cannot distinguish between the different constituents in the diurnal band or in the semidiurnal band. Furthermore, the inertial frequency is close to the semidiurnal band at these latitudes and will contaminate the tidal estimates (for the clockwise rotary component).

2.4. Climatologies and Reanalysis Products

2.4.1. Ocean Climatology: MIMOC

The global monthly isopycnal mixed-layer ocean climatology (MIMOC) covers the 0–1950 dbar range with 0.5° × 0.5° spatial resolution, uses objective mapping routines and emphasizes data from the last decade

[*Schmidtko et al.*, 2013]. For each location of observations along the N-ICE2015 drift tracks, we linearly interpolate MIMOC in space and time to derive the best guess climatological values from MIMOC for comparison with our observations. Thus, each interpolated MIMOC profile is based on the eight MIMOC profiles closest in space and time.

2.4.2. Reanalysis Product: ERA-Interim

The ERA-Interim reanalysis data set is a global atmospheric product that is updated in near real time. It is based on the ECMWF integrated Forecast System [*Dee et al.*, 2011]. It uses a fixed version of a numerical weather prediction system to produce reanalysed data. The spatial resolution is approximately 80 km with 60 vertical levels, while the temporal resolution is 6 hourly.

3. Results

3.1. Environmental Conditions

The drifts started inside the pack ice, and distance to open water decreased over time. The maximum distance to open water was at the start of Floe 2 with 474 km, and the minimum occurred at the end of Floe 4 with only 11 km. The overall mean distance to open water was 142 km. Distance to open water was estimated as the shortest distance from the R.V. Lance to the inner edge of the ice class "open water" ($<$10%) based on navigational sea ice charts produced by the Norwegian Meteorological Institute from satellite data [*Itkin et al.*, 2017]. Floes 1 and 2 during winter started out well inside the Nansen Basin with bottom depths ~4000 m. As the different drifts approached open water and Fram Strait, bottom depth generally decreased to ~500–800 m above the Yermak Plateau.

Air temperatures below −40°C occurred in January and February, while the lowest during March was approximately −20°C. Air temperatures were usually −10°C in May and approached 0°C in June [*Cohen et al.*, 2017; *Hudson et al.*, 2015]. Throughout the four drifts, a total of 18 atmospheric storms were recorded with roughly equal numbers in winter and spring [*Cohen et al.*, 2017, Table 2]. Storms herein cover periods when 10 min averaged wind speed was continuously greater than 8 m s^{-1} for at least 1 h. Major storms are those that are associated with a pressure decrease that exceeds 5 hPa in 6 h. The mean environmental conditions for each drift are given in Table 2. For a general description of the atmospheric conditions during the N-ICE2015 expedition [see *Cohen et al.*, 2017].

ERA-Interim reanalysis data [*Dee et al.*, 2011] show that the N-ICE2015 winter atmospheric conditions were cold compared to recent years, with mean January and February air temperatures −19°C, −9°C, −14°C, and −10°C for, respectively, 2015, 2014, 2013, and 2012 in the Floes 1 and 2 region (Figure 3b). The last particularly cold winter in the area was winter 2011 with mean January and February air temperature of −22°C. The 2015 cold winter conditions in the N-ICE2015 area led to large sea ice concentrations in the region as seen in ERA-Interim data (Figure 3a). The sea ice concentrations were respectively 82%, 56%, 47%, 64%, and 97% in 2015, 2014, 2013, 2012, and 2011. *Graham et al.* [2016] give a detailed comparison of the N-ICE2015 atmospheric observations with the 2015 ERA-Interim data.

Table 2. N-ICE2015 Expedition Environmental Conditions Presented as Time-Averaged Values Over Each Floe Drift[a]

	Floe 1	Floe 2	Floe 3	Floe 4
Drift speed (m s^{-1})	0.16	0.21	0.14	0.21
Mean distance to open water (km)	137	239	120	43
Mean depth (m)	3485	3990	1482	1176
Mean absolute current speed below 50 m (m s^{-1})	0.06	0.02	0.07	0.11
Mean predicted tidal currents (AOTIM-5) (m s^{-1})	0.02	0.01	0.05	0.07
Observed tidal current amplitude (m s^{-1})	0.06	0.02	0.08	0.10
Mean mixed-layer depth (m)	57.0	83.7	47.8	4.6
Mean mixed-layer temperature (°C)	−1.84	−1.85	−1.81	−1.35
Mean mixed-layer salinity (g kg^{-1})	34.43	34.50	34.34	33.52
Mean wind speed (m s^{-1})	7	6	6	7
Mean air temperature (°C)	−27	−14	−10	−0.4
Number of storms	5	3	8	2

[a] Air temperature, wind speed, and storms definitions come from *Cohen et al.* [2017]; definition of distance to open water in *Itkin et al.* [2017].

3.2. Hydrography and Water Masses

3.2.1. Hydrographic Overview

For large parts of the drifts, the hydrography showed classic Arctic Ocean properties, with a cold, relatively fresh, and deep mixed layer in winter between 50 and 100 m thick (Figures 4a and 4b). Warmer and more salty AW was found between 200 and 800 m depth. At the end of Floes 1, 3, and 4, warmer AW was found concurring with shallower

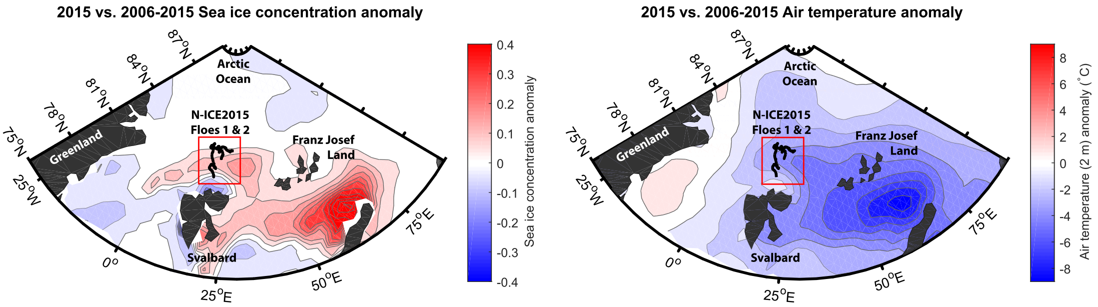

Figure 3. 2015 winter Sea ice concentration (a) and air temperature (b) anomalies relative to the 2006-2015 average ERA Interim reanalysis data. The red box represents the N-ICE2015 winter area.

topography (Figure 4f). Hydrographic conditions changed significantly after 25 May 2015, when water observed between 100 and 500 m depth was warmer and saltier, while the mixed layer became thinner, fresher, and warmer (Figures 4a and 4b).

3.2.2. Water Masses

During the drifts, six different water masses were identified using *Rudels et al*. [2000] classification (Figure 5). The water mass analysis was based on data from the ship CTD, the microstructure profilers and the IAOOS buoys profilers (Table 1).

At the surface, we found a layer of Polar Surface Water (PSW, $\sigma_0 < 27.70$ and $\theta < 0$°C) throughout the N-ICE2015 expedition, on average 93 m thick in winter and 78 m thick in spring (Figures 5 and 6). Its temperature was near freezing in winter (mean -1.76°C) and higher in the spring (mean -1.62°C).

Patches of warm Polar Surface Water (PSWw, $\sigma_0 < 27.70$ and $\theta < 0$°C), a signature of ice melt water, were observed in the upper 50 m during spring on the Yermak Plateau, at the end of Floes 3 and 4 (Figure 6). PSWw average temperature was 0.9°C and its maximum measured temperature was 4.3°C.

Atlantic Water (AW, $27.70 < \sigma_0 < 27.97$ and $\theta > 2$°C) was observed both on the continental slope of Svalbard (Svalbard Branch) and on the Yermak Plateau (Figure 2). On the Yermak Plateau, AW was found between 100 and 500 m depth (Figure 6). AW mean temperature was 2.7°C and mean salinity 35.15 g kg^{-1}, with a maximum temperature of 4.4°C. AW observed on or at the edge of the Yermak Plateau was defined as either of Yermak Branch origin, or undetermined branch (Figure 6). This classification is discussed in details in section 4.3. Dissolved oxygen concentrations in AW are typically the lowest observed during the expedition with values between 280 and 300 μmol kg^{-1} (Figure 5b). The exception is relatively high values of dissolved oxygen ($>$320 μmol kg^{-1}) found in the undetermined branch of AW in the southeast region of the Yermak Plateau (Figures 5b and 2, magenta drift track).

Modified Atlantic Water (MAW, $27.70 < \sigma_0 < 27.97$ and $\theta > 2$°C) is the result of AW cooling and mixing with polar waters as it circulates through the Arctic (Figure 5a). MAW was found from approximately 100 m depth to 500 m unless AW was present (Figures 5 and 6).

Intermediate Water (IW, $27.97 < \sigma_0, \sigma_{0.5} < 30.444$ and $\theta < 0$°C) and Nordic Deep Water (NDW, $\sigma_{0.5} > 30.444$) were found from 900 m and below in all ship CTD casts apart from over shallower parts of the Yermak Plateau (Figure 6).

3.3. Mixed-Layer Characteristics

The microstructure profiler data, averaged in 1 m bins, was used to derive the mixed-layer depth (Figures 7a, 4a, and 4b). In winter, the mixed-layer depth was defined as the depth in each profile where the potential density first exceeded the density at 20 m depth by 0.01 kg/m^3. In spring, we found the depth in each profile where the potential density first exceeded the surface (second good data point usually at 2 m depth) density by 0.003 kg/m^3. The lower density criteria used for spring was used to avoid overestimating the mixed-layer depth since the density gradient at the base of the mixed layer was smaller in spring than in winter. Overall, the mixed-layer depth estimates are not sensitive to the choice of density criteria, which are adjusted for the spatial and temporal coverage of data. Criteria definitions are typical for the Arctic region [*Peralta-Ferriz and Woodgate*, 2015].

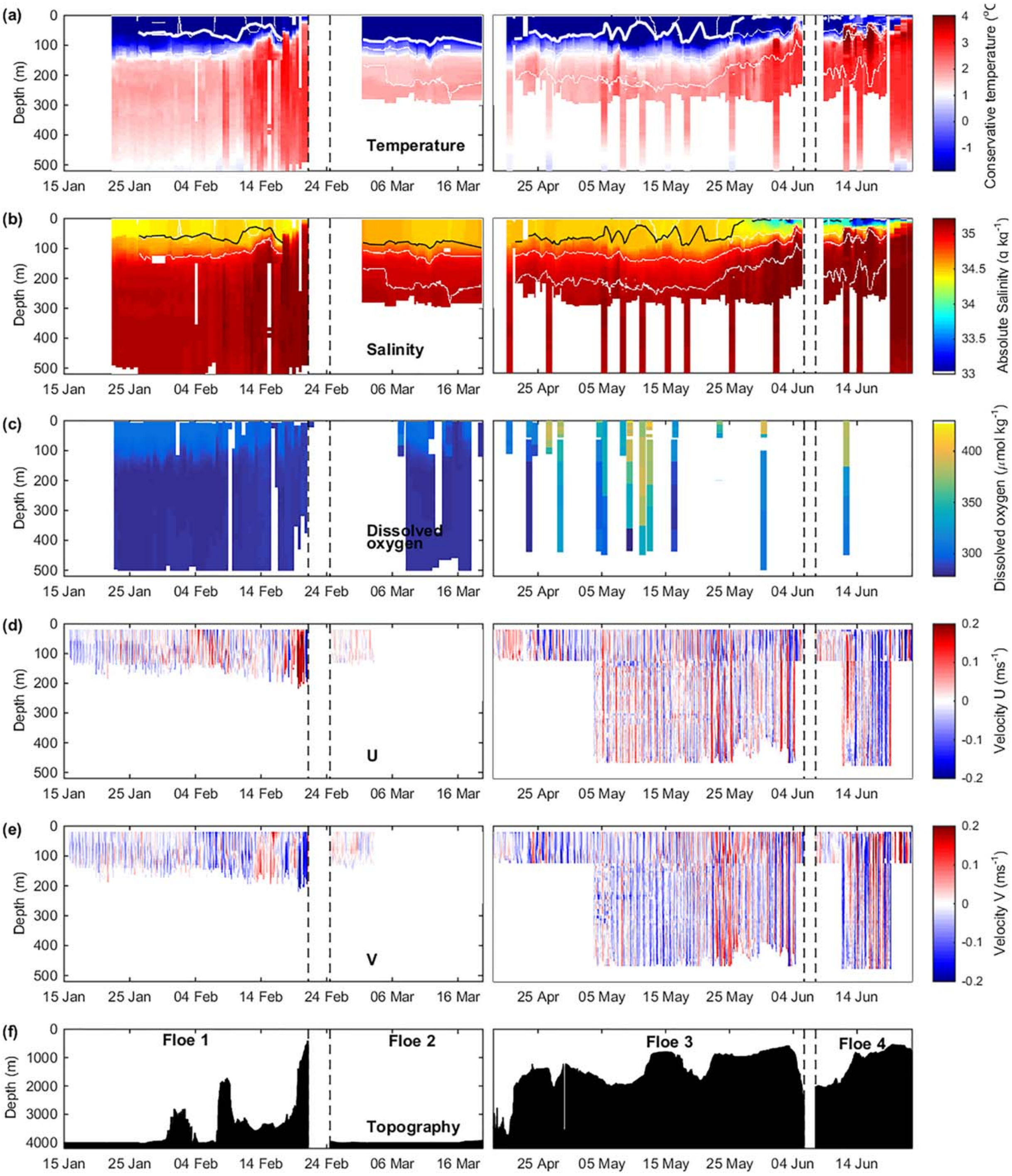

Figure 4. Vertical distribution of (a) conservative temperature and mixed-layer depth (thick white line), (b) Absolute Salinity and mixed-layer depth (thin black line), (c) dissolved oxygen, (d) zonal (U) and (e) meridional (V) component of the absolute current velocity, and (f) seafloor depth along the N-ICE2015 drifts trajectories. In (a) and (b), data above 300 m is from microstrcuture profilers and data below is from ship CTD, apart from Floe 1 where upper 200 m are microstructure profilers and below 200 m is IAOOS profilers. In (c), data is from IAOOS profilers for Floe 1 and from either ship CTD (profiles deeper 1000 m), or from the on-ice CTD (profiles shallower than 1000 m) for Floe 2, 3, and 4. In (d) and (e), data above 130 m is from the vessel-mounted ADCP while data below 130 m is from the Long-Ranger ADCP. White isolines correspond to selected potential density contours: 27.6, 27.8, and 27.9 kg m^{-3}. Vertical dashed lines separate drifts.

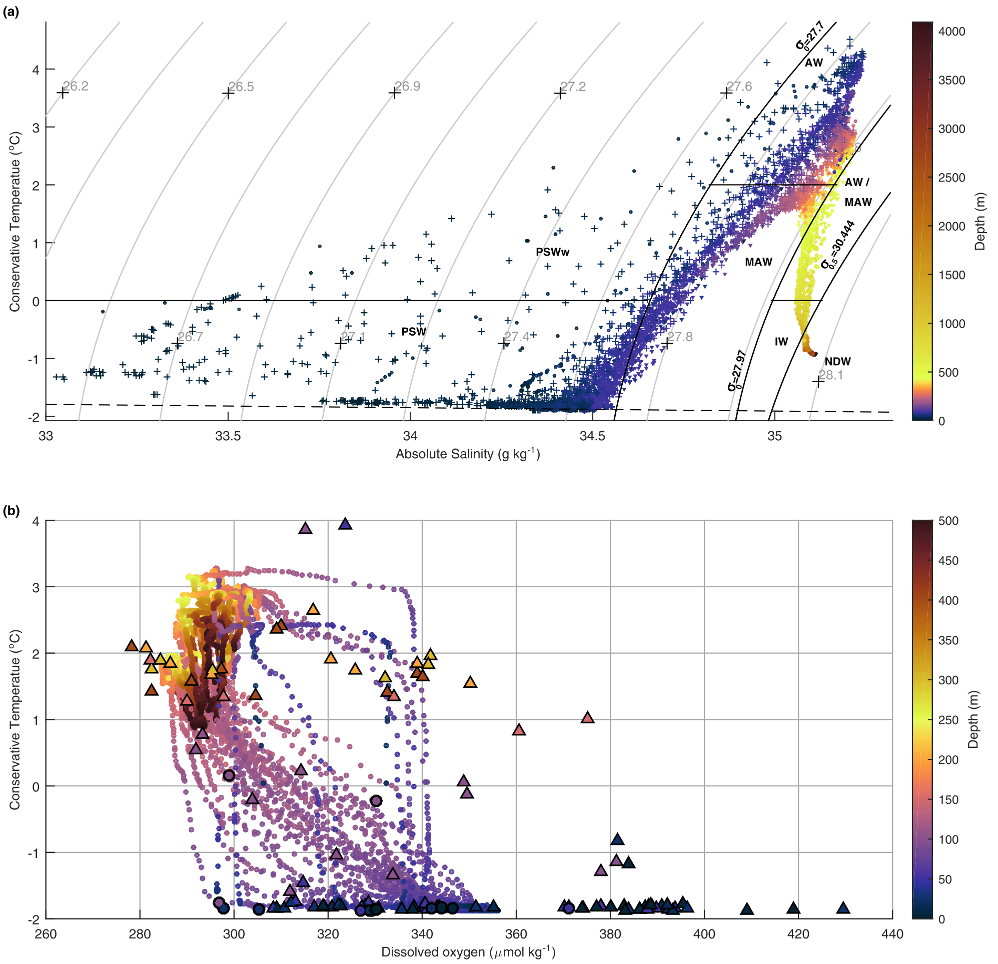

Figure 5. (a) Conservative temperature versus Absolute Salinity from ship CTD data (dots) and from microstructure profiler data (crosses) color-coded for observation depth. Definitions of water masses following *Rudels et al.* [2000] are indicated: Atlantic Water (AW), Modified Atlantic Water (MAW), Polar Surface Water (PSW), Warm Polar Surface Water (PSWw), Intermediate Water (IW), and Nordic Deep Water (NDW). The dashed line corresponds to the freezing point of seawater. (b) Conservative temperature versus dissolved oxygen from bottle CTD data (large dots and triangles) and from IAOOS profiler data (small dots). Color indicates the depth of each sample, all dots are winter samples, and triangles are spring samples.

The mean conservative temperature and Absolute Salinity within the mixed layer were derived and the local freezing temperature was calculated at 2 m depth. A measure of the vertical temperature gradient at the base of the mixed layer was derived applying a linear least square fit of conservative temperature values in the 5 m section directly below the base of the mixed layer (Figure 7b) [*Toole et al.*, 2010]. We also defined the departure from freezing temperature (δT) as the difference between the mean temperature in the mixed layer and the local freezing temperature $\delta T = T - T_f(S, p)$ (Figure 7c).

The mean mixed-layer depth for the expedition was 44 m with values ranging from 1 to 100 m (Table 2 and Figure 7a). The deepest mixed layers were observed in March and the shallowest in June. In winter, the mixed layer was close to freezing with $\delta T = 0.03$°C. During Floe 3, δT doubled to 0.06°C and it reached very large values in June with a mean of 0.47°C during Floe 4. The temperature gradient at the base of the mixed layer was occasionally negative in the late spring (end of Floes 3 and 4) as a result of strong vertical interleaving in the upper 80 m of the water column.

A dramatic change was seen in mixed-layer characteristics after 25 May, while the camp was drifting over the Yermak Plateau. Prior to the 25 May, the mixed layer was deep (average of 64 m) and close to the freezing point. After the 25 May, a different mixed layer was encountered. It was very shallow (average of 6 m)

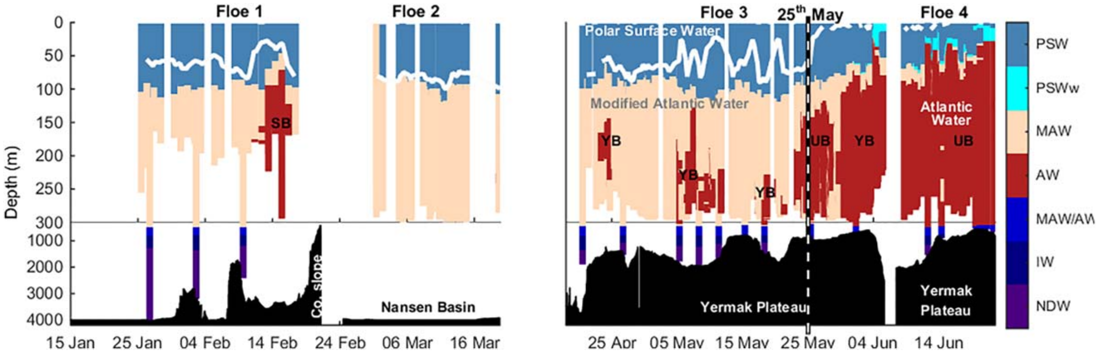

Figure 6. Vertical distribution of water masses along the N-ICE2015 drift trajectory. Water-masses are labeled by color: Atlantic Water (AW), Modified Atlantic Water (MAW), Polar Surface Water (PSW), Warm Polar Surface Water (PSWw), Intermediate Water (IW), and Nordic Deep Water (NDW) following *Rudels et al.*'s [2000] definitions. Patches of Atlantic Water are indicated coming from either the Svalbard Branch (SB), the Yermak Branch (YB), or undetermined (UB). The vertical scale is zoomed in the upper 300 m. The date of 25 May 2015 is indicated by a thick vertical black and white dashed line. Overlying the water masses color scale is a contour of the mixed-layer depth (white line). The corresponding depth (m) of the seafloor along the N-ICE2015 drift trajectory shows topographic features (black).

and had temperatures significantly above freezing. A remnant winter mixed layer was still present below the newly formed mixed layer for some time. The vertical temperature gradient at the base of the mixed layer also showed a shift on the 25 May with a mean value prior to this date of 0.25°C m^{-1} that dropped to 0.01°C m^{-1} afterward. Large basal sea ice melt events took place after 25 May driven by large ocean heat flux from Atlantic Water [*Peterson et al.*, 2017; *Meyer et al.*, 2017], leading to a freshening of the upper surface waters, an increase in buoyancy, and was likely responsible for the new shallow mixed layer.

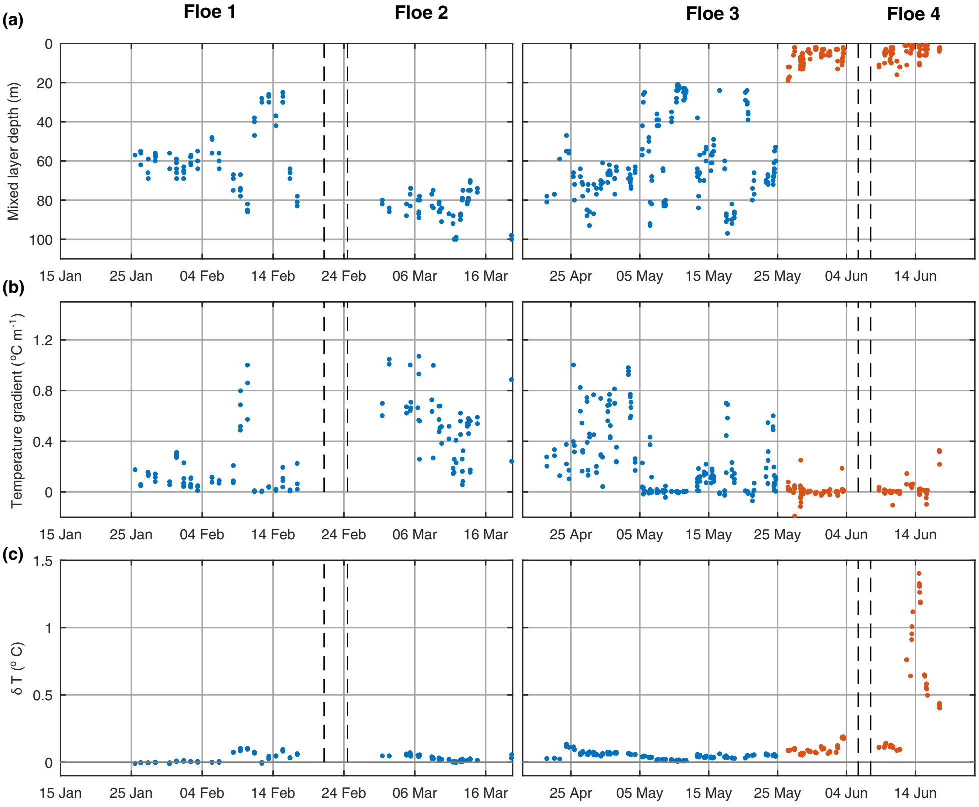

Figure 7. Time evolution during the N-ICE2015 expedition of (a) the mixed-layer depth, (b) the vertical conservative temperature gradient in the 5 m below the mixed-layer base, and (c) the mean mixed-layer temperature departure from freezing point ($\delta T = T - T_f(S, p)$) before 25 May 2015 (blue) and after 25 May 2015 (brown), from individual microstructure profiles.

3.4. Seasonal and Regional Variability

3.4.1. In the Observations

Winter drifts (Floes 1 and 2) were in waters on average deeper than 3000 m, with a deeper mixed layer and cooler waters throughout the water column (Table 2). Winter waters were depleted in dissolved oxygen compared to concentrations in the spring (Figure 4c).

The spring drifts (Floes 3 and 4) were in shallower waters, with a shallower mixed layer, warmer waters and higher air temperatures (Table 2). Dissolved oxygen profiles in the spring showed enhanced values in the upper 100–400 m (Figure 4c).

We further split the spring data in two periods: early spring (until 25 May 2015) and late spring (after 26 May 2015) based on changes observed in temperature and salinity at that time (Figure 6, thick black and white dashed line). The winter and early spring mean vertical profiles of temperature, salinity, and density were near identical (Figures 8a–8c). The mean winter dissolved oxygen profile showed a strong gradient from surface values of 340 to 290 μmol kg^{-1} at 200 m depth and below (Figure 8d). The late spring profiles, however, were very different from the winter profiles with warmer waters from surface down to 500 m, much fresher and lighter waters in the upper 50 m and saltier waters between 50 and 600 m depth. This corresponded to the presence of AW at depth. We do not have sufficient data on dissolved oxygen during spring to discuss changes during that period.

During the expedition, two areas were sampled twice: The northern tip of the Yermak Plateau was first sampled during Floe 1 (31 January to 3 February) and then revisited about three months later during Floe 3 (20–22 April). The south-west edge of the Plateau was sampled at the end of Floe 3 (28 May to 4 June) and again 17 days later at the end of Floe 4 (13–20 June) (Figure 2). We compared temperature and salinity data for both regions over time and found that changes from winter to spring on the northern tip of the Plateau were very small (Figure 8i, green and yellow colors). Only in the upper 40 m, we observed slightly fresher waters in winter ($-$0.06 g kg$^{-1)}$. Changes from late May to mid-June in the southwest part of the Plateau later were also small (Figure 8i, pink and purple colors). In June, AW was warmer and PSW was fresher than in May. This coincided with the June drift being closer to open water than the May drift.

Three bathymetric areas are defined for the N-ICE2015 data set: deep topography, deeper than 3000 m, corresponding to the Nansen Basin, slope area between 3000 m and 1500 m depth, and shallow topography, shallower than 1500 m, which corresponds mainly to the Yermak Plateau and partly to the upper continental slope at the end of Floe 1 (Figure 2). From deep to shallow topography, we saw a transition from PSW and MAW to PSWw and AW: waters became warmer from the surface down to 500 m depth, fresher and lighter at the surface, and saltier at depth (Figures 8e–8g). There was a strong deficit in dissolved oxygen concentrations in the upper layer (0–100 m) of the shallow profiles with a maximum difference in surface values of 310 μmol kg^{-1} compared to 340 μmol kg^{-1} in deeper profiles (Figure 8h).

Dissolved oxygen values were lower in winter and in shallow waters. Low-dissolved oxygen values in winter under the sea ice are expected since such regions have been isolated from the atmosphere for several months and minimal primary production takes place in that period. In shallow waters, low surface levels of dissolved oxygen could be due to significant remineralization over the continental shelf and exchanges between the mixed layer and AW due to enhanced mixing on the slope. Higher upper ocean dissolved oxygen values observed in the spring are likely the result of oxygen exchanges with the atmosphere through leads in the sea ice (ventilation) and biological production of oxygen in the water (photosynthetic activity) due to increased under ice light levels [*Timmermans et al*., 2010]. Such photosynthetic activity was observed with an under-ice phytoplankton bloom taking place in May and June 2015 during the expedition [*Assmy et al*., 2017].

3.4.2. Comparison With Ocean Climatology

The observations and derived MIMOC interpolated profiles of climatology (section 2.4.1) are binned in three time periods: winter for data between January and March; early spring for data between April and May and late spring for data in June. The number of profiles the climatology is based on in January is small (less than ten) for the N-ICE2015 January region (Figure 9a). This number increases to approximately 40 profiles in March, and to over 70 profiles in May (Figures 9b and 9c).

The key feature we found comparing the N-ICE2015 observations with the MIMOC ocean climatology was that the upper Atlantic Water layer is warmer, more saline and shallower in the new observations compared to the climatology, throughout the N-ICE2015 expedition (Figures 9d–9i). The signal of higher

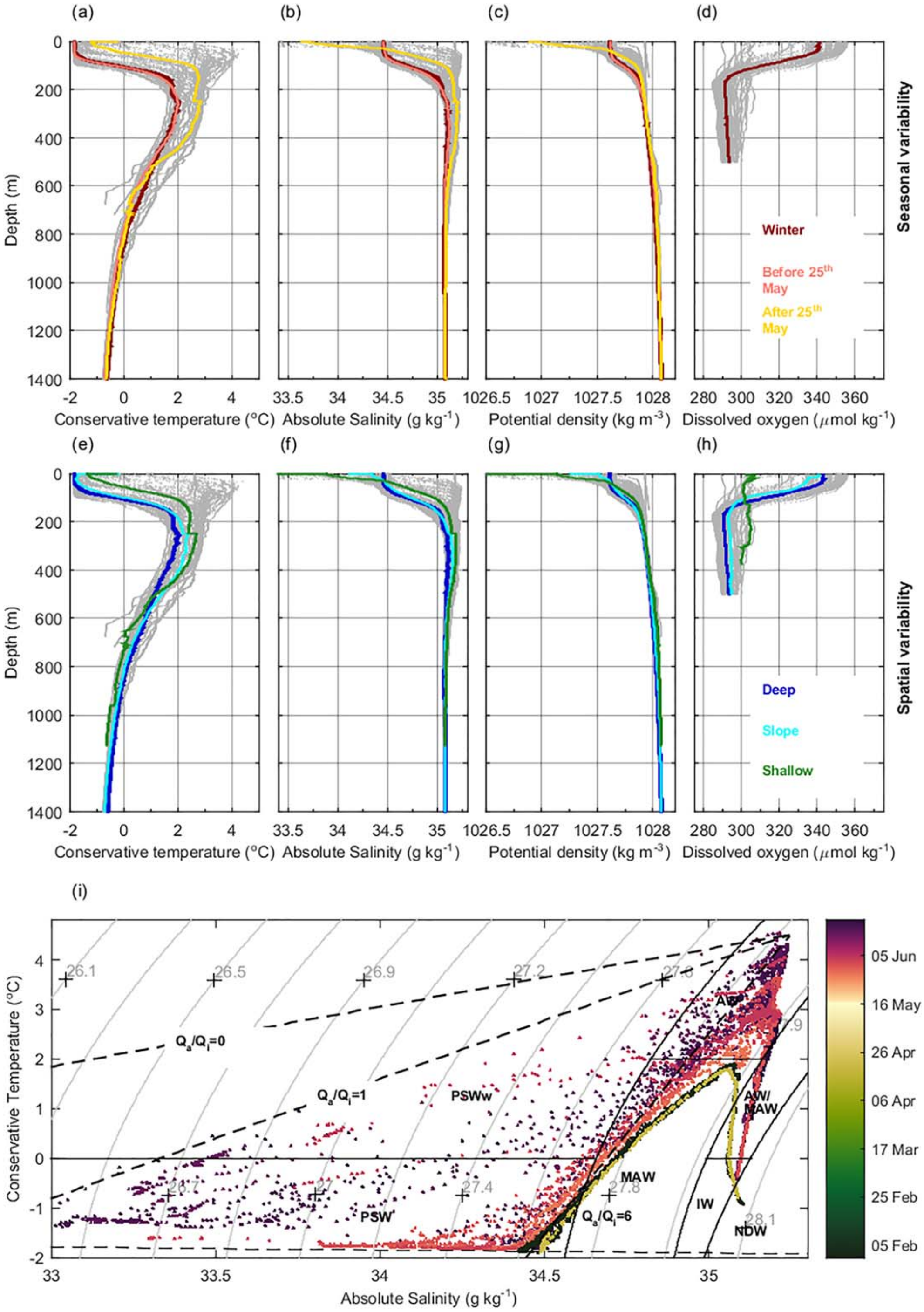

Figure 8. Mean vertical profiles of (a and e) conservative temperature, (b and f) Absolute Salinity, (c and g) potential density, and (d and h) dissolved oxygen. In Figures 8a–8d, data are averaged by seasons where winter is from 15 January to 19 March (red line), early spring is from 18 April to 25 May (pink line) and late spring is from 26 May to 22 June (yellow line). In Figure 8e–8h, data are averaged by location where deep is deeper than 3000 m (dark blue line), slope is between 3000 m (cyan line) and 1500 m depth and shallow is shallower than 1500 m (green line). (i) Conservative temperature versus Absolute Salinity from ship CTD data and from microstructure profiler data. Colors indicate the dates at which data were sampled: Dark green and yellow points are from the northern tip of the Yermak Plateau in January and April respectively; pink and purple points are from the south-west edge of the Plateau in May and June respectively. Black dashed lines show various values of the atmospheric cooling (Q_a) to ice melt (Q_i) ratio. In Figures 8a–8c, 8e, 8f, and 8g, data above 300 m is from microstructure profilers while data below 300 m is from the ship CTD. In Figures 8d and 8h, data are from the IAOOS profilers (Floe 1 only).

temperature and salinity is seen between 100 and 220 m depth in the Nansen Basin and on the northern section of the Yermak Plateau, while it reaches as deep as 500 m depth on the southern section of the Yermak Plateau.

Another clear difference is the higher salinity of surface waters in winter and early spring (Figures 9e and 9g, upper 40 m). Such high salinities could be due to stronger local sea ice formation during winter 2015 than in previous years, leading to brine release in the upper water column. In the late spring, the warm shallow AW led to sea ice melt [*Meyer et al.*, 2017] and a pronounced drop in subsurface salinities in the observations. Here the climatology does not capture this surface melt water signal and observed salinity in the upper 30 m is much lower than in the climatology.

3.4.3. Cold Halocline and Sea Ice

The upper mixed layer in the observations is more saline than the climatology, a sign of more sea ice formation in the region, consistent with measurements of divergent sea ice motion during winter storms of the N-ICE2015 expedition [*Itkin et al.*, 2017]. Indeed, large sea ice divergence events suggest that leads opened in the ice. This would have led to high sea ice growth rates under the anomalous low atmospheric temperatures. The deep mixed layer observed could be the result of deep convection following strong freezing and resulting brine release.

The shape of temperature versus salinity profiles is associated with surface heat loss due to atmospheric cooling and to ice melting [*Boyd and D'Asaro*, 1994; *Cokelet et al.*, 2008]. The temperature and salinity slopes of constant atmospheric cooling (Q_a) to ice melt (Q_i) were derived using

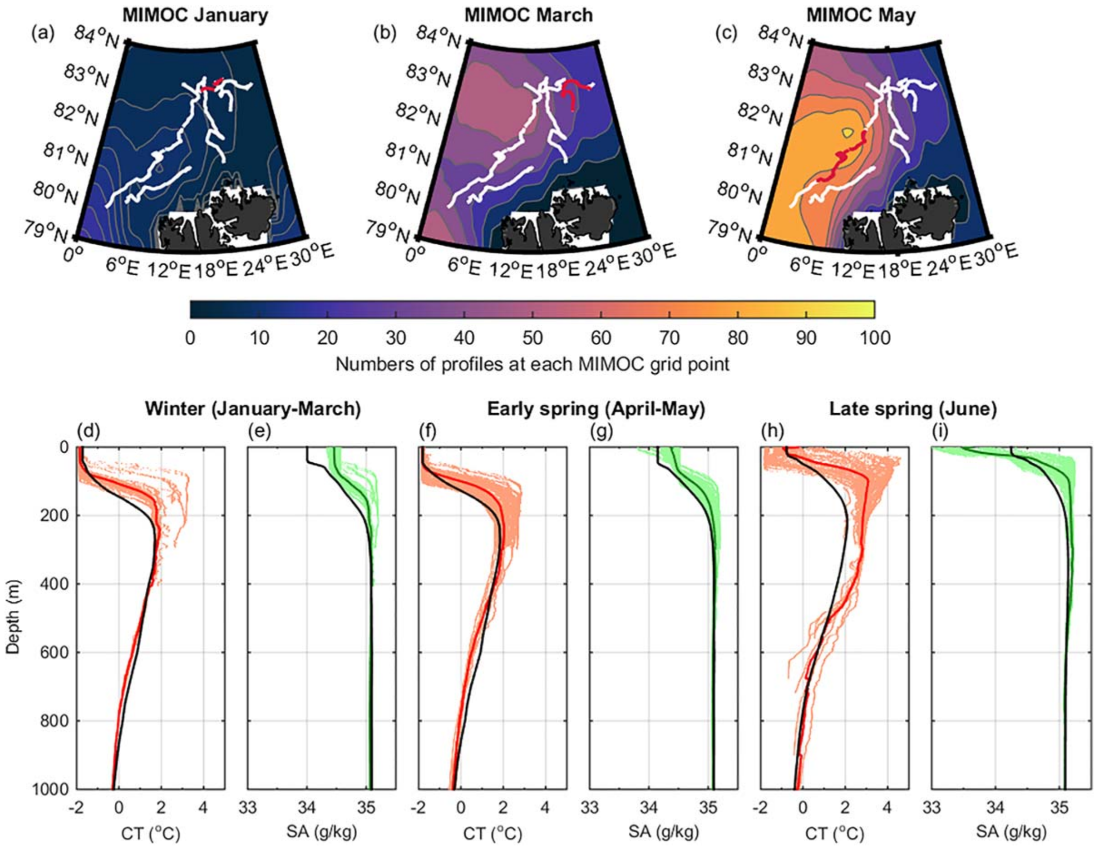

Figure 9. (a) Maps with the number of profiles at each grid point of the MIMOC climatology for the month of January with contour intervals every two profile, (b) March with contour intervals every 10 profile, and (c) May with contour intervals every 10 profile. Overlay in white are the drift tracks of the N-ICE2015 expedition and in red the respective drift sections for the shown month. Mean vertical profiles of conservative temperature (CT) and Absolute Salinity (SA) from the N-ICE2015 expedition observations (color) and from MIMOC climatology (black), (d and e) for winter, (f and g) early spring, and (h and i) late spring. Data above 300 m include microstructure profilers and ship-board CTD. Data below 300 m is from the ship-board CTD only.

$$T = T_0 + 79.2\left(1+\frac{Q_a}{Q_i}\right)\ln\left(\frac{S-S_i}{S_0-S_i}\right), \tag{1}$$

where $T_0 = 4.5°\mathrm{C}$ and $S_0 = 35.25$ g kg^{-1} represent the virtual AW maximum, and $S_i = 5$ is an assumed sea ice salinity [*Cokelet et al*., 2008]. These slopes are appropriate for surface waters where atmospheric cooling and sea ice melt take place. The $Q_a/Q_i=0$ slope theoretically corresponds to no atmospheric sensible heat transfer and large sea ice melt (Figure 8i). The N-ICE2015 late spring temperature and salinity data had Q_a/Q_i ratios as low as 1 (Figure 8i), consistent with both ice melting and heat loss to the atmosphere taking place. In winter and early spring however, the Q_a/Q_i ratio was approximately 6, indicative of Polar Surface Water formation with very little ice melt taking place.

3.5. Surface Currents and Drift

Drift speed of the ice camps throughout the expedition averaged 0.17 m s^{-1} with peaks above 0.50 m s^{-1} (Figure 10a). The overall drift direction was south-west towards Fram Strait. The sea ice drift is determined by a combination of wind forcing, sea ice stresses and ocean forcing (tides and currents). During the N-ICE2015 expedition, the wind component was largest when the ice camps were closest to the ice edge (Floes 3 and 4) [*Peterson et al.*, 2017]. When drifting deeper inside the pack ice (Floes 1 and 2), internal sea ice stress and oceanic forcing dominated.

Stronger mean ocean currents were generally recorded at the end of each drift when the ice camp approached the sea ice edge, shallower bathymetry, and the AW inflow. Figure 10 shows this increase in current speed when the distance to open water decreases, and when AW is present at depth (Figure 10c).

Most of the observed peaks in drift speed (Figure 10a) were clearly associated with the passage of atmospheric low pressure events, recorded as storms [*Cohen et al*., 2017]. The storms also appear to have influenced the observed mean absolute current speeds in the upper 23–55 m (Figure 10b). When drift speed exceeded 0.4 m s^{-1}, mean current speed in the upper 55 m rose from an average 0.06–0.12 ms^{-1}. Large upper ocean mean current speeds nearly always matched storm events, apart from a period after 17 June at the end of the N-ICE2015 expedition. After that date, large drifting speeds were associated with large upper ocean current speeds but with no corresponding storm. That period corresponded to the largest predicted and observed tidal signal suggesting that the large current and drift speeds were tide driven.

3.6. Deeper Circulation

Observed absolute mean current speeds below 50 m depth varied from a minimum of 0.02 m s^{-1} with direction rotating with tides in the Nansen Basin during Floe 2, to quite high values above 0.20 m s^{-1} flowing north-east on the Svalbard continental shelf during Floe 1. In the south-western part of the Yermak Plateau current speed was moderate with westwards and north-west direction; 0.11 m s^{-1} during Floe 3 and 0.17 m s^{-1} during Floe 4 (Figures 4d and 4e). Data from the two ADCPs showed barotropic flow with little vertical variability in the velocity profiles (Figures 4d and 4e). Some exceptions were observed following atmospheric storm events and on the Svalbard continental slope (not shown).

Overall, the ocean flow below 50 m depth was westwards and north-west in the south-west area of the Yermak Plateau close to the slope. At the northern tip of the Yermak Plateau, the mean current curled around the tip of the plateau (Figure 11d). Along the eastern slope of the Plateau, the consistent weak south, south-west current had a mean speed of 0.06 m s^{-1}. Finally, a strong north-east flowing current signal was observed on the upper Svalbard continental slope (Figures 11a–11c). With corresponding AW characteristics (Figure 11b), this strong current was the Svalbard Branch of the AW inflow with a narrow core found below 50 m depth and reaching at least down to 200 m depth (Figure 11b). This core had an average current speed of 0.25 m s^{-1} located above the 600 and 900 m isobaths.

3.7. Tides and Oscillations

Tidal current predictions were estimated along the four drifts using the AOTIM-5 model (Figures 12a and 12b, red curves). Current signals at tidal frequencies (24 and 12 h) were estimated using the vessel-mounted ADCP data (Figures 12a and 12b, blue curves). Tidal signals were weak in the Nansen Basin with both observed and predicted average current values of 0.02 m s^{-1} (Table 2). Tides on the Yermak Plateau and on its slopes were relatively strong and dominated the current signal (Figure 11a, red areas), with observed current signals at tidal frequencies reaching 0.42 m s^{-1}.

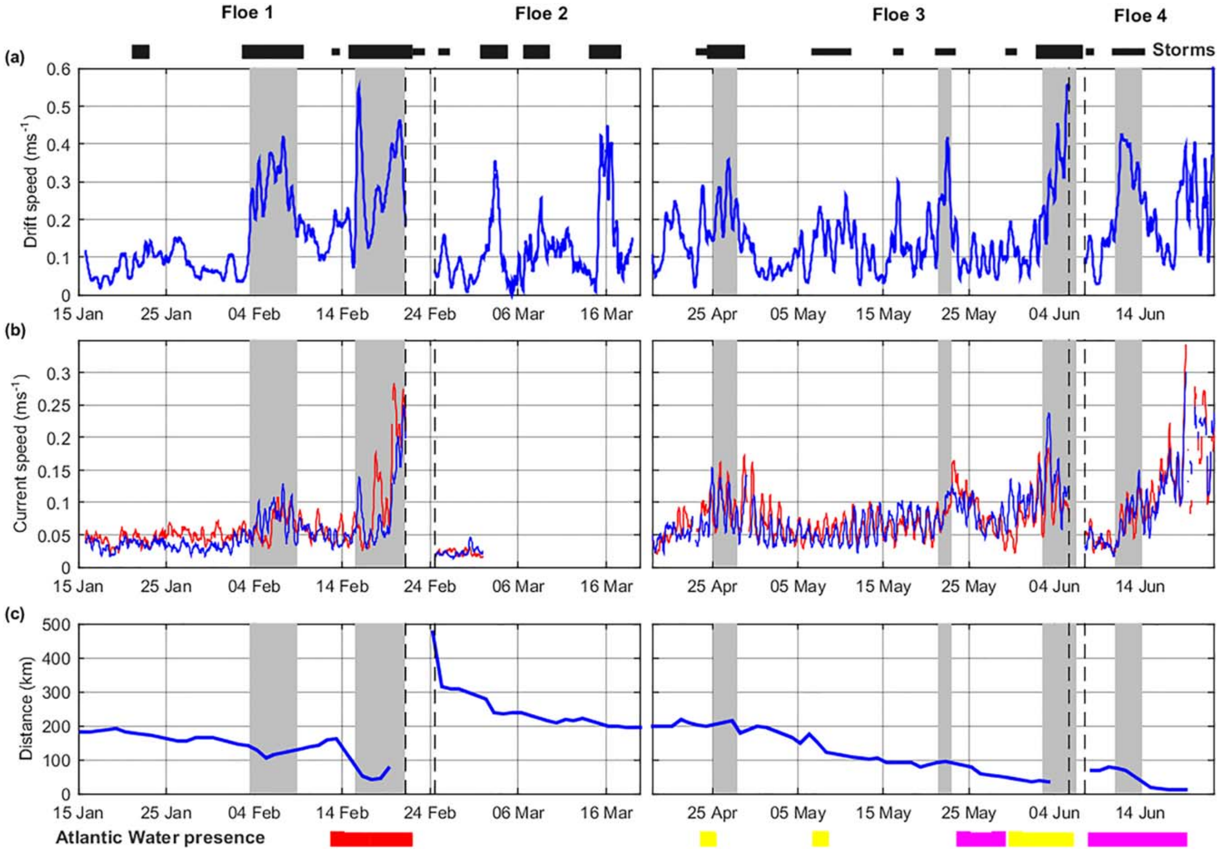

Figure 10. Time evolution during the N-ICE2015 expedition of (a) the drift speed of the ice, (b) mean absolute current speed (vessel-mounted ADCP data) in the upper 23–55 m (blue) and mean absolute current speed in the 100–150 m depth range (red), and (c) distance from the drifting ice floe to open water [*Itkin et al.*, 2017]. Black blocks indicate major storms (thicker boxes) and minor storms (thinner boxes) [*Cohen et al*., 2017]. Presence of Atlantic Water in the water column is indicated and labeled from either the Yermak Branch (yellow blocks), from undetermined origin (magenta blocks), or from the Svalbard Branch (red blocks). Storm events associated with large drift speeds and increased observed current speeds are highlighted in gray across the plots. Note that the vessel-mounted ADCP was non-operational after the 3 March 2015 during drift 2 when the ship bow was lifted out of the water by sea ice compression events.

The phase of the predicted tides matched observed signals well, and the amplitudes of observed and predicted tidal signal were comparable during Floe 2, for the end of Floe 3 and for Floe 4. The amplitude of the observed signals was however larger than predicted tides during Floe 1 and during the first part of Floe 3 (Table 2). The difference might be due to predicted tidal signal being underestimated by the AOTIM-5 model. For example, its bathymetry may be inaccurate as it does not incorporate recently collected data and its resolution is coarse (5 km). This particularly affects tidal estimates near slopes and in coastal regions.

4. Discussion

The new observations from the N-ICE2015 expedition have long lasting potential to improve our understanding of the processes governing the Arctic Ocean during winter. N-ICE2015 was able to collect more than 250 winter CTD casts from ship CTD, microstructure profiles, and buoys, in a region with extremely sparse winter data coverage (Figure 9a). N-ICE2015 creates an unprecedented basis for studies on Arctic ocean winter processes and thus is crucial to reduce bias for modelling future Arctic conditions. This region is in a transition period, with basin wide sea ice thickness reduced from 3.60 to 1.25 m between 1975 and 2012 [*Lindsay and Schweiger*, 2015]. The general trend of thinning sea ice in the Fram Strait area is similar to that in the wider Arctic Ocean [*Renner et al*., 2014], and given that sea ice in the Yermak Plateau area generally drifts from the interior basin towards Fram Strait, a similar trend is also expected there. However, larger variability is observed north of Svalbard [*Renner et al*., 2013], likely associated with a larger fraction of first-year ice in this region.

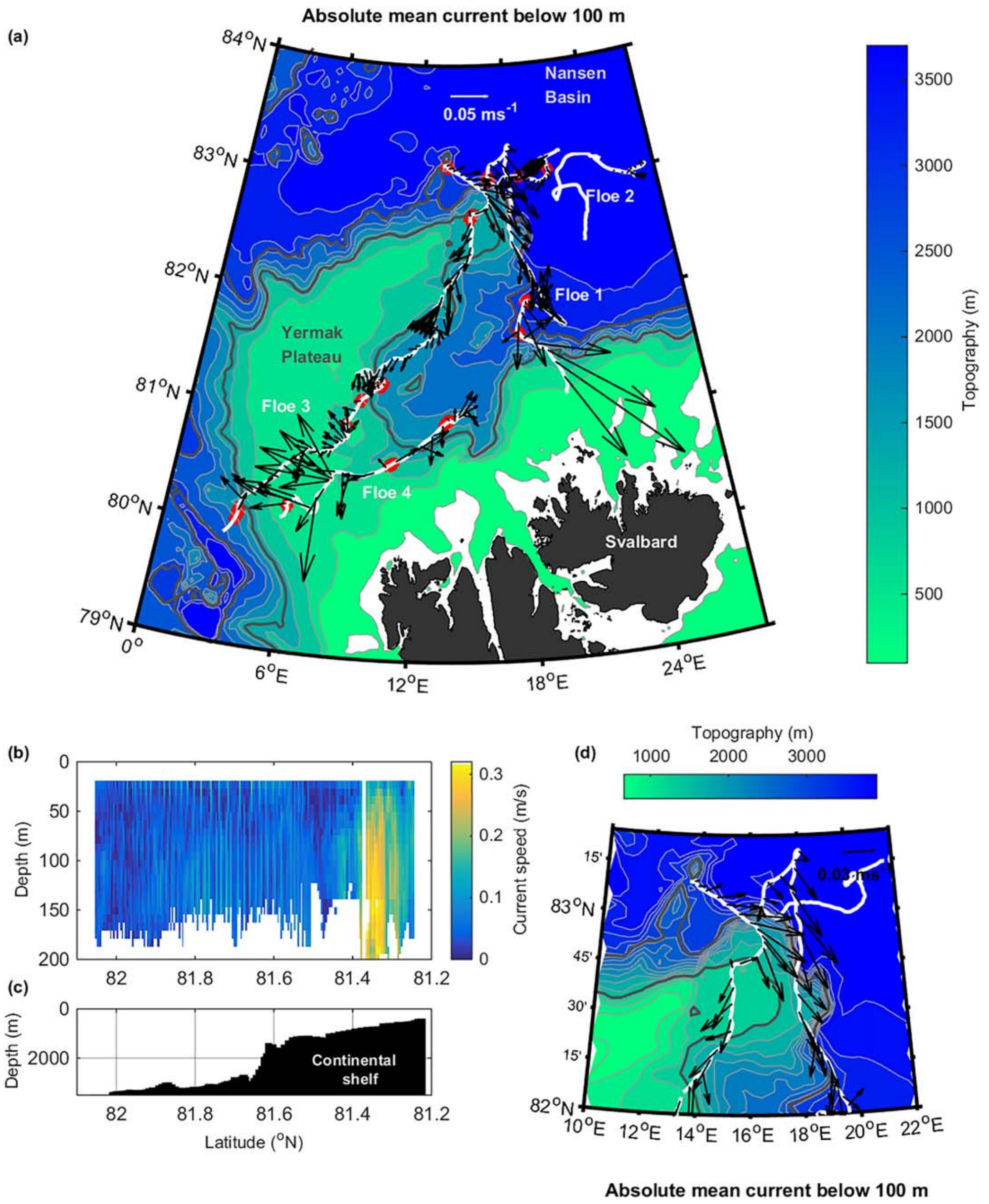

Figure 11. (a) Mean absolute ocean currents below 100 m depth from available Vessel-Mounted ADCP data overlaying topographic contours ranging from 100 to 4000 m at 400 m intervals (color). Red sections along drift tracks correspond to areas where estimated tidal speed dominates observed absolute current speed. (b) Section plot of residual current speed while drifting onto the continental shelf at the end of Floe 1 (Vessel-Mounted ADCP data). (c) Corresponding underlying topography. (d) Mean absolute currents at the northern tip of the Yermak Plateau below 100 m depth from available Vessel-Mounted ADCP data overlaying topographic contours at 200 m intervals (color). In both (a) and (d), the 3000 and 1500 m isobaths are shown as thick gray lines while the trajectories of Floe 1 and 3 are indicated with white lines.

4.1. Upper Layer Characteristics and Formation of the Cold Halocline

Our observations are consistent with the general description of dominating processes in the area. Nowadays, the region north of Svalbard likely receives a thinner sea ice cover by predominantly wind driven sea ice transport [*Hansen et al*., 2013; *Renner et al*., 2013, 2014; *Lindsay and Schweiger*, 2015]. Snow-free and thinner sea ice would allow for further growth in particular during cold winters, despite the relatively large ocean heat flux in the region [*Peterson et al*., 2016, 2017; *Meyer et al*., 2017]. Snow cover was however thick during N-ICE2015 [*Merkouriadi et al*., 2017; *Rösel et al*., 2016] insulating the ice from the atmosphere and

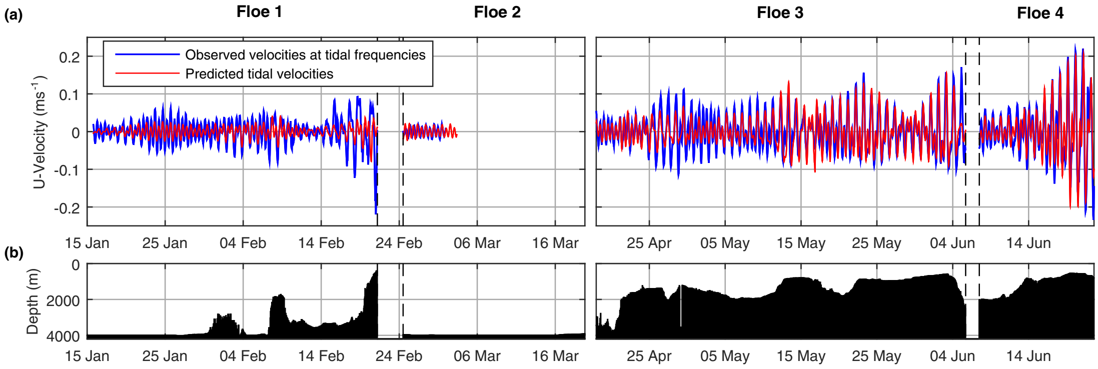

Figure 12. Time evolution during the N-ICE2015 expedition of (a) Observed U-velocities of waves with 12 and 24 h frequencies between 100 and 250 m depth from vessel-mounted ADCP data (blue) and predicted tidal velocities from AOTIM-5 (red). V-velocities (not shown) are similar. (b) Corresponding depth (m) of the seafloor along the N-ICE2015 drift trajectory.

preventing sea ice growth (A. Rösel, personal communication, September 2016). It is instead in the many observed leads that strong thin ice growth was observed. A negative feedback loop might then come into effect where sea ice growth drives vertical convection, bringing up more of the Atlantic Water heat to the sea ice, preventing its growth [*Ivanov et al*., 2016].

4.2. Atlantic Water Characteristics and Circulation

On the western side of the Yermak Plateau, AW observed from 30 m depth with 2.8°C mean temperature is identified as part of the Yermak Branch of inflowing AW (Figure 2, yellow drift track). At the northern end of the Yermak Plateau, currents were consistently observed curling around the tip of the Plateau, when the ice camps drifted across both in winter and in spring (Figure 11d). Concurrently, AW was observed from 130 m depth, with 2.1°C mean temperature above the 1500 m isobaths (Figure 2), similar characteristics to those observed by *Rudels et al*. [2005]. We identify this section as the Yermak Branch retroflecting around the northern tip of Yermak Plateau. Further downstream, along the eastern side of the Yermak Plateau, AW was observed again at, respectively, 128 and 230 m depth, with mean temperatures of 2.3 and 2.0°C C over the 1900 and 1600 m isobaths (Figure 2). With absolute current speeds that were consistently south along that section (Figure 11a), we identify this section as the Yermak Branch that has cooled down and eroded after circulating around the Yermak Plateau. This is similar to previous findings in the area [*Rudels et al*., 2000; *Marnela et al*., 2013]. What happens to the Yermak Branch south of 81° latitude on the eastern side of the Plateau is unclear. AW is observed again on the Plateau and on its eastern slope but this AW is much shallower (120 and 30 m depth), much warmer (2.8 and 3°C) and over shallower topography (900 and 1200 m isobaths) (Figure 2, magenta drift track). Current speeds in the area are low and tidal dominated (Figure 11a). This AW, referred to as the undetermined branch (Figure 6), could be coming from the Yermak Branch through the Yermak Plateau Pass taking a short-cut across the Plateau [*Gascard et al*., 1995]. Alternatively, this AW could have "leaked" from the Svalbard Branch, with eddies [*Våge et al*., 2016; *Koenig et al*., 2017] and slowly accumulated in that area.

The Svalbard branch of inflowing AW was clearly observed in the ocean current observations between the 600 and 1000 m isobaths at 81.5°N (Figures 11b and 2, red track). The observed distribution and T-S characteristics of AW over this part of the continental slope was very similar to that found by *Cokelet et al*. [2008]. They calculated geostrophic currents in the AW core of order 5 cm^{-1}, significantly lower than the 25 cm^{-1} measured during N-ICE2015. Apart from differences between geostrophic estimates and direct measurement, this difference could be due to short-term variability as well as seasonality of the inflow; based on mooring records, *Randelhoff et al*. [2015] show that the Svalbard Branch is stronger in winter (N-ICE2015 observations) and spring than in summer and autumn [*Cokelet et al*., 2008, observations]. Similar seasonal variability of the Svalbard Branch is presented in *Koenig et al*. [2017].

Even though AW has been shown to have a hydrographic seasonal cycle [*Schauer et al*., 2002; *Ivanov et al*., 2009], this data set does not allow for such analysis. The changes in temperature and salinity observed during the N-ICE2015 expedition seem to be dominated by the presence of AW on the slopes and over the

Yermak Plateau. Changes from winter to spring near the northern part of the Plateau were near to none and restricted to the upper 40 m, while changes on the south-west edge of the Plateau seemed driven by the location of AW and distance to the ice edge (Figure 8i).

Overall, AW was observed close to the surface under the sea ice when within 100 km from open ocean. This is consistent with the idea that warm AW in this area defines the ice boundary by providing heat to and therefore melting the sea ice from below [*Untersteiner*, 1988]. A comparison with climatology data shows a warmer, shallower, and more saline AW during N-ICE2015. This could point either to a higher than usual inflow of AW in early 2015, or to a continuation of the signal of the previously reported warming trend of AW inflow in the Svalbard region [*Grotefendt et al*., 1998; *Schauer et al*., 2004; *Ivanov et al*., 2009; *Polyakov et al*., 2012; *Beszczynska-Möller et al*., 2012].

5. Conclusions

The N-ICE2015 expedition data set spanning January to June 2015 provides an updated picture of the hydrography and circulation in the Arctic Ocean north of Svalbard. In addition, these rare winter data are valuable to the community with the potential to reduce bias when modelling the new Arctic. The new observations show a surprisingly deep mixed layer for the first five months of the N-ICE2015 expedition likely due to high sea ice growth rates in numerous leads, a characteristic of the area [*Willmes and Heinemann*, 2016]. Because few earlier observations are available, it is not possible to conclude whether this is unusual and a result from the “new Arctic” with a thinner sea ice cover, or if this has been the typical state for this region in past decades. Late spring conditions, closer to the ice edge are dominated by a strong pycnocline and shallow mixed layer, the result of large sea ice melt events.

We find that the Atlantic Water inflow north of Svalbard was warmer, more saline and shallower in 2015 than in available climatology data. The inflow is steered by topography, partly flowing along the Svalbard coast (Svalbard Branch), and partly flowing around the Yermak Plateau (Yermak Branch), shown for the first time to retroflect around its northern tip. The Atlantic Water present on the Yermak Plateau is associated with a shallow mixed layer and low sea ice concentrations. In the deep basin, Atlantic Water is found further down in the water column.

In the late spring, it is likely that the combination of strong tides, warm Atlantic Water and a shallow mixed layer during the N-ICE2015 expedition led to local enhanced heat fluxes from the ocean to the sea ice with significant implications for the sea ice energy budget.

Acknowledgments
This work has been supported by the Norwegian Polar Institutes Centre for Ice, Climate and Ecosystems (ICE) through the N-ICE project. Additional support was obtained from the Centre for Climate Dynamics at the Bjerknes Centre through grant BASIC: Boundary Layers in the Arctic Atmosphere, Seas and Ice Dynamics. CP, NVR and ZK acknowledge support from the ANR 469 EQUIPEX IAOOS project, through ANR-10-EQPX-32-01 grant, and the ICE-ARC programme from the European Union 7th Framework Programme, grant 603887. HK was funded through Research Council of Norway project Boom or Bust number 244646. We thank N-ICE2015 participants, the captains, crews and N-ICE2015 scientists for their help in making this study possible. We thank two anonymous reviewers for valuable comments that greatly improved the submitted manuscript. The following data sets were used in this study and are publicly available at the Norwegian Polar Data Centre: vessel-mounted CTD [*Dodd et al*., 2016], microstructure sonde [*Meyer et al*., 2016], vessel-mounted ADCP [*Meyer et al*., 2016], long ranger ADCP [*Provost et al*., 2016], and dissolved oxygen concentrations [*Dodd et al*., 2016] (https://data.npolar.no/dataset/?filter-sets=N-ICE2015). The IAOOS platform data are available at LOCEAN (Christine Provost, cp@locean-ipsl.upmc.fr).

References

Aagaard, K., and P. Greisman (1975), Toward new mass and heat budgets for the Arctic Ocean *of major estimate of Coilin, J. Geophys. Res.*, *80*(27), 3821–3827, doi:10.1029/JC080i027p03821.

Aagaard, K., A. Foldvik, and S. R. Hillman (1987), The West Spitsbergen Current: Disposition and water mass transformation, *J. Geophys. Res.*, *92*(C4), 3778–3784.

Abrahamsen, E. P. (2014), Sustaining observations in the polar oceans, *Philos. Trans. R. Soc. London A*, *372*(2025), 20130337, doi:10.1098/rsta.2013.0337.

Amante, C., and B. Eakins (2009), ETOPO1 1 arc-minute global relief model: Procedures, data sources and analysis, *NOAA Tech. Mem. NESDIS NGDC-24* (March), 19 pp., Natl. Oceanic and Atmos. Admin., Boluder, Colo., doi:10.1594/PANGAEA.769615.

Assmy, P., et al. (2017), Leads in the Arctic pack ice enable early phytoplankton blooms below snow-covered sea ice, *Scientific Reports*, doi:10.1038/srep40850, in press.

Beszczynska-Möller, A., E. Fahrbach, U. Schauer, and E. Hansen (2012), Variability in Atlantic water temperature and transport at the entrance to the Arctic Ocean, 1997–2010, *ICES J. Mar. Sci.*, *69*, 852–863, doi:10.1093/icesjms/fss056.

Bourke, R. H., A. M. Weigel, and R. G. Paquette (1988), The westward turning branch of the West Spitsbergen Current, *J. Geophys. Res.*, *93*(C11), 14,065–14,077, doi:10.1029/JC093iC11p14065.

Boyd, T. J., and E. A. D'Asaro (1994), Cooling of the West Spitsbergen Current: Wintertime observations west of Svalbard, *J. Geophys. Res.*, *99*(C11), 22,597–22,618.

Carmack, E. C., et al. (2015), Towards quantifying the increasing role of oceanic heat in sea ice loss in the New Arctic, *Bull. Am. Meteorol. Soc.*, *96*(12), 2079–2105, doi:10.1175/BAMS-D-13-00177.1.

Carpenter, J. H. (1965), The Chesapeake Bay Institute technique for the Winkler dissolved oxygen method, *Limnol. Oceanogr.*, *10*(1), 141–143, doi:10.4319/lo.1965.10.1.0141.

Cohen, L., S. R. Hudson, V. P. Walden, R. M. Graham, and M. A. Granskog, (2017), Meteorological conditions in a thinner Arctic sea ice regime from winter through summer during the Norwegian young sea ICE expedition (N-ICE2015), *J. Geophys. Res. Atmos.*, doi:10.1002/2016JD026034, in press.

Cokelet, E. D., N. Tervalon, and J. G. Bellingham (2008), Hydrography of the West Spitsbergen Current, Svalbard Branch: Autumn 2001, *J. Geophys. Res*, *113*, C01006, doi:10.1029/2007JC004150.

Dee, D. P., et al. (2011), The ERA-Interim reanalysis: Configuration and performance of the data assimilation system, *Q. J. R. Meteorol. Soc.*, *137*(656), 553–597.

Dodd, P., et al. (2016), N-ICE2015 bottle data from ship water sampler., data set, Norwegian Polar Institute, doi:10.21334/npolar.2016.516bc529.

Dodd, P., et al. (2016), N-ICE2015 ship-based conductivity-temperature-depth (CTD) data, Data set, Norwegian Polar Institute, doi:10.21334/npolar.2017.92262a9c.

Egbert, G. D., A. F. Bennett, and M. G. G. Foreman (1994), TOPEX/POSEIDON tides estimated using a global inverse model, *J. Geophys. Res.*, *99*(C12), 24,821–24,852, doi:10.1029/94JC01894.

Emery, W. J., and R. E. Thomson (2001), *Data Analysis Methods in Physical Oceanography*, 2nd ed., chap. 5, 638 pp., Elsevier, Amsterdam.

Fer, I. (2006), Scaling turbulent dissipation in an Arctic fjord, *Deep Sea Res., Part II*, *53*, 77–95.

Fer, I., R. Skogseth, and F. Geyer (2010), Internal waves and mixing in the marginal ice zone near the Yermak Plateau, *J. Phys. Oceanogr.*, *40*(7), 1613–1630, doi:10.1175/2010JPO4371.1.

Fer, I., M. Müller, and A. K. Peterson (2015), Tidal forcing, energetics, and mixing near the Yermak Plateau, *Ocean Sci.*, *11*, 287–304, doi:10.5194/os-11-287-2015.

Gascard, J. C., C. Richez, and C. Rouault (1995), New insights on large-scale oceanography in Fram Strait: The West Spitsbergen Current, in *Oceanography of the Arctic: Marginal Ice Zones and Continental Shelves*, edited by W. Smith and J. Grebmeier, pp. 131–182, AGU, Washington, D. C.

Granskog, M. A., P. Assmy, S. Gerland, G. Spreen, H. Steen, and L. H. Smedsrud (2016), Arctic research on thin ice: Understanding the consequences of ongoing Arctic sea ice loss (N-ICE2015), *Eos, Trans. AGU*, *97*, 22–26, doi:10.1029/2016EO044097.

Graham, R. M., A. Rinke, L. Cohen, S. R. Hudson, V. P. Walden, M. A. Granskog, W. Dorn, M. Kayser, and M. Maturilli (2016), A comparison of the two Arctic atmospheric winter states observed during N-ICE2015 and SHEBA, *J. Geophys. Res. Atmos.*, *121*, doi:10.1002/2016JD025475.

Grotefendt, K., K. Logemann, D. Quadfasel, and S. Ronski (1998), Is the Arctic Ocean warming?, *J. Geophys. Res.*, *103*(C12), 27,627–679,687.

Hansen, E., S. Gerland, M. A. Granskog, O. Pavlova, A. H. H. Renner, J. Haapala, T. B. Løyning, and M. Tschudi (2013), Thinning of Arctic sea ice observed in Fram Strait: 1990–2011, *J. Geophys. Res. Oceans*, *118*, 5202–5221, doi:10.1002/jgrc.20393.

Hudson, S. R., L. Cohen, and V. Walden (2015), N-ICE2015 surface meteorology, Data set, Norwegian Polar Institute, doi:10.21334/npolar.2015.056a61d1.

Ivanov, V. V., I. V. Polyakov, I. A. Dmitrenko, E. Hansen, I. A. Repina, S. S. Kirillov, C. Mauritzen, H. L. Simmons, and L. A. Timokhov (2009), Seasonal variability in Atlantic Water off Spitsbergen, *Deep Sea Res., Part I*, *56*, 1–14.

Ivanov, V. V., I. Alexeev, Vladimir Koldunov, Nikolay V. Repina, and A. Sandø, Anne Britt Smedsrud, Lars Henrik Smirnov (2016), Arctic Ocean Heat Impact on Regional Ice Decay: A Suggested Positive Feedback, *J. Phys. Oceanogr.*, *46*(5), 1437–1456.

Itkin, P., G. Spreen, B. Cheng, M. Doble, F. Girard-Ardhuin, J. Haapala, N. Hughes, L. Kaleschke, M. Nicolaus, and J. Wilkinson (2017), Thin ice and storms: Sea ice deformation from buoy arrays deployed during N-ICE2015, *J. Geophys. Res. Oceans*, doi:10.1002/2016JC012403, in press.

Koenig, Z., C. Provost, N. Villacieros-Robineau, N. Sennéchael, and A. Meyer (2016), Winter ocean-ice interactions under thin sea ice observed by IAOOS platforms during N-ICE2015: Salty surface mixed layer and active basal melt, *J. Geophys. Res. Oceans*, *121*, 7898–7916, doi:10.1002/2016JC012195.

Koenig, Z., C. Provost, N. Villacieros-Robineau, N. Sennéchael, A. Meyer, J.-M. Lellouche, and G. Garric (2017), Atlantic waters inflow north of Svalbard: Insights from IAOOS observations and Mercator Ocean global operational system during N-ICE2015, *J. Geophys. Res. Oceans*, *122*, 1254–1273, doi:10.1002/2016JC012424.

Lindsay, R., and A. Schweiger (2015), Arctic sea ice thickness loss determined using subsurface, aircraft, and satellite observations, *Cryosphere*, *9*(1), 269–283.

Lique, C., A. M. Treguier, B. Blanke, and N. Grima (2010), On the origins of water masses exported along both sides of Greenland: A Lagrangian model analysis, *J. Geophys. Res.*, *115*, C05019, doi:10.1029/2009JC005316.

Marnela, M., B. Rudels, M. N. Houssais, A. Beszczynska-Möller, and P. B. Eriksson (2013), Recirculation in the Fram Strait and transports of water in and north of the Fram Strait derived from CTD data, *Ocean Sci.*, *9*(3), 499–519, doi:10.5194/os-9-499-2013.

McDougall, T. J., D. R. Jackett, F. J. Millero, R. Pawlowicz, and P. M. Barker (2012), A global algorithm for estimating Absolute Salinity, *Ocean Sci.*, *8*(6), 1123–1134.

Merkouriadi, I., J.-C. Gallet, G. E. Liston, C. Polashenski, R. M. Graham, A. Rösel, and S. Gerland (2017), Winter snow conditions on Arctic sea ice north of Svalbard during the Norwegian young sea ICE (N-ICE2015) expedition, *J. Geophys. Res. Atmos.*, *122*, doi:10.1002/2017JD026753.

Meyer, A., et al. (2016), N-ICE2015 ocean microstructure profiles (MSS90L), Data set, Norwegian Polar Institute, doi:10.21334/npolar.2016.774bf6ab.

Meyer, A., I. Fer, M. Muilwijk, L.-H. Smedsrud, J. Miguet, N. Kusse-Tiuz, and P. A. Dodd (2016), N-ICE2015 Ocean currents: Vessel Mounted acoustic Doppler current profiler, Data set, Norwegian Polar Institute, doi:10.21334/npolar.2017.e400ef79.

Meyer, A., I. Fer, A. Sundfjord, and A. K. Peterson (2017), Mixing rates and vertical heat fluxes north of Svalbard from Arctic winter to spring, *J. Geophys. Res. Oceans*, doi:10.1002/2016JC012441, in press.

Muench, R. D., M. G. McPhee, C. A. Paulson, and J. H. Morison (1992), Winter oceanographic conditions in the Fram Strait-Yermak Plateau region, *J. Geophys. Res.*, *97*(C3), 3469–3483.

Onarheim, I. H., L. H. Smedsrud, R. B. Ingvaldsen, and F. Nilsen (2014), Loss of sea ice during winter north of Svalbard, *Tellus, Ser. A*, *66*(1), 23933.

Padman, L., and T. M. Dillon (1991), Turbulent mixing near the Yermak Plateau during the Coordinated Eastern Arctic Experiment, *J. Geophys. Res.*, *96*(C3), 4769–4782, doi:10.1029/90JC02260.

Padman, L., and S. Y. Erofeeva (2004), A barotropic inverse tidal model for the Arctic Ocean, *Geophys. Res. Lett.*, *31*, L02303, doi:10.1029/2003GL019003.

Peralta-Ferriz, C., and R. A. Woodgate (2015), Seasonal and interannual variability of pan-Arctic surface mixed layer properties from 1979 to 2012 from hydrographic data, and the dominance of stratification for multiyear mixed layer depth shoaling, *Prog. Oceanogr.*, *134*, 19–53, doi:10.1016/j.pocean.2014.12.005.

Perkin, R. G., and E. L. Lewis (1984), Mixing in the West Spitsbergen Current, *J. Phys. Oceanogr.*, *14*, 1315–1325.

Peterson, A. K., A. Randelhoff, I. Fer, A. Meyer, L. Håvik, L. H. Smedsrud, I. Onarheim, M. Muijlwick, A. Sundfjord, and M. G. McPhee (2016), N-ICE2015 ocean turbulent fluxes from under-ice turbulent cluster (TIC), Data set, Norwegian Polar Institute, doi:10.21334/npolar.2016.ab29f1e2.

Peterson, A. K., I. Fer, M. G. McPhee, and A. Randelhoff (2017), Turbulent heat and momentum fluxes in the upper ocean under Arctic sea ice, *J. Geophys. Res. Oceans*, *122*, 1439–1456, doi:10.1002/2016JC012283.

Polyakov, I. V., A. V. Pnyushkov, R. Rember, V. V. Ivanov, Y.-D. Lenn, L. Padman, and E. C. Carmack (2012), Mooring-based observations of double-diffusive staircases over the Laptev Sea Slope, *J. Phys. Oceanogr.*, *42*, 95–109, doi:10.1175/2011JPO4606.1.

Polyakov, I. V., A. V. Pnyushkov, R. Rember, L. Padman, E. C. Carmack, and J. M. Jackson (2013), Winter convection transports atlantic water heat to the surface layer in the Eastern Arctic Ocean, *J. Phys. Oceanogr.*, *43*(1981), 2142–2155, doi:10.1175/JPO-D-12-0169.1.

Prandke, H., and A. Stips (1998), Test measurements with an operational microstructure-turbulence profiler: Detection limit of dissipation rates, *Aquat. Sci.*, *60*(3), 191–209, doi:10.1007/s000270050036.

Provost, C., et al. (2015), IAOOS (Ice-Atmosphere-Arctic Ocean Observing System, 2011–2019), *Mercator Ocean Quart. Newslett.*, *51*, 13–15.

Provost, C., I. Onarheim, A. Randelhoff, A. Meyer, L.-H. Smedsrud, V. Rerolle, N. Villacieros Robineau, I. Fer, and A. Petersson (2016), N-ICE2015 Ocean currents: RDI Long Ranger acoustic Doppler current profiler, Data set, Norwegian Polar Institute, doi:10.21334/npolar.2017.accb9dd5.

Randelhoff, A., A. Sundfjord, and M. Reigstad (2015), Seasonal variability and fluxes of nitrate in the surface waters over the Arctic shelf slope, *J. Geophys. Res.*, *49*, 3442–3449, doi:10.1002/2015GL063655.

Renner, A. H. H., S. Hendricks, S. Gerland, J. Beckers, C. Haas, and T. Krumpen (2013), Large-scale ice thickness distribution of first-year sea ice in spring and summer north of Svalbard, *Ann. Glaciol.*, *54*(62), 13–18.

Renner, A. H. H., S. Gerland, C. Haas, G. Spreen, J. F. Beckers, E. Hansen, M. Nicolaus, and H. Goodwin (2014), Evidence of Arctic sea ice thinning from direct observations, *Geophys. Res. Lett.*, *41*, 5029–5036, doi:10.1002/2014GL060369.

Rösel, A., et al. (2016), N-ICE2015 snow depth data with Magna Probe, Data set, Norwegian Polar Institute, doi:10.21334/npolar.2016.3d72756d.

Rudels, B., R. Meyer, E. Fahrbach, V. V. Ivanov, S. Østerhus, D. Quadfasel, U. Schauer, V. Tverberg, and R. A. Woodgate (2000), Water mass distribution in Fram Strait and over the Yermak Plateau in summer 1997, *Ann. Geophys.*, *18*(6), 687–705, doi:10.1007/s005850000216.

Rudels, B., E. P. Jones, U. Schauer, and P. Eriksson (2004), Atlantic sources of the Arctic Ocean surface and halocline waters, *Polar Res.*, *23*(2), 181–208.

Rudels, B., G. Björk, J. Nilsson, P. Winsor, I. Lake, and C. Nohr (2005), The interaction between waters from the Arctic Ocean and the Nordic Seas north of Fram Strait and along the East Greenland Current: Results from the Arctic Ocean-02 Oden expedition, *J. Mar. Syst.*, *55*(1–2), 1–30.

Rudels, B., M. Korhonen, U. Schauer, S. Pisarev, B. Rabe, and A. Wisotzki (2015), Circulation and transformation of Atlantic water in the Eurasian Basin and the contribution of the Fram Strait inflow branch to the Arctic Ocean heat budget, *Prog. Oceanogr.*, *132*, 128–152, doi:10.1016/j.pocean.2014.04.003.

Schauer, U., H. Loeng, B. Rudels, V. K. Ozhigin, and W. Dieck (2002), Atlantic Water flow through the Barents and Kara Seas, *Deep Sea Res., Part I*, *49*(12), 2281–2298.

Schauer, U., E. Fahrbach, S. Osterhus, and G. Rohorardt (2004), Arctic warming through the Fram Strait: Oceanic heat transport from 3 years of measurements, *J. Geophys. Res.*, *109*, C06026, doi:10.1029/2003JC001823.

Schmidtko, S., G. C. Johnson, and J. M. Lyman (2013), MIMOC: A global monthly isopycnal upper-ocean climatology with mixed layers, *J. Geophys. Res. Oceans*, *118*, 1658–1672, doi:10.1002/jgrc.20122.

Sirevaag, A., and I. Fer (2009), Early Spring oceanic heat fluxes and mixing observed from drift stations North of Svalbard, *J. Phys. Oceanogr.*, *39*(12), 3049–3069, doi:10.1175/2009JPO4172.1.

Spall, M. A. (2013), On the circulation of Atlantic Water in the Arctic Ocean, *J. Phys. Oceanogr.*, *43*, 2352–2371.

Steele, M., and T. J. Boyd (1998), Retreat of the cold halocline layer in the Arctic Ocean, *J. Geophys. Res.*, *103*(C5), 10,419–10,435.

Timmermans, M. L., R. A. Krishfield, S. Laney, and J. M. Toole (2010), Ice-Tethered profiler measurements of dissolved oxygen under permanent ice cover in the Arctic Ocean, *J. Atmos. Oceanic Technol.*, *27*(11), 1936–1949.

Toole, J. M., M.-L. Timmermans, D. K. Perovich, R. A. Krishfield, A. Proshutinsky, and J. A. Richter-Menge (2010), Influences of the ocean surface mixed layer and thermohaline stratification on Arctic Sea ice in the central Canada Basin, *J. Geophys. Res.*, *115*, C10,018, doi:10.1029/2009JC005660.

Treshnikov, A. F. (1977), Polar oceans, in *Polar Oceans*, edited by M. Dunbar, pp. 17–31, Arctic Inst. North Am., Calgary, Alberta, Canada.

Untersteiner, N. (1988), On the ice and heat balance in Fram Strait, *J. Geophys. Res.*, *93*(7), 527–531.

Våge, K., R. S. Pickart, V. Pavlov, P. Lin, D. J. Torres, R. B. Ingvaldsen, A. Sundfjord, and A. Proshutinsky (2016), The Atlantic Water boundary current in the Nansen Basin: Transport and mechanisms of lateral exchange, *J. Geophys. Res. Oceans*, *121*, 6946–6960, doi:10.1002/2016JC011715.

Weiss, R. F. (1970), The solubility of nitrogen, oxygen and argon in water and seawater, *Deep Sea Res. Oceanogr. Abstr.*, *17*(4), 721–735.

Wijesekera, H. W., L. Padman, T. M. Dillon, M. Levine, C. Paulson, and R. Pinkel (1993), The application of internal-wave dissipation models to a to a region of strong mixing, *J. Phys. Oceanogr.*, *23*(2), 269–286.

Willmes, S., and G. Heinemann (2016), Sea-ice wintertime lead frequencies and regional characteristics in the Arctic, 2003–2015, *Remote Sens.*, *8*(1).

Appendix B

Observations of flooding and snow-ice formation in a thinner Arctic sea ice regime during N-ICE2015 campaign: influence of basal ice melt and storms.

AGU PUBLICATIONS

JGR

Journal of Geophysical Research: Oceans

RESEARCH ARTICLE

10.1002/2016JC012011

Special Section:

Atmosphere-ice-ocean-ecosystem Processes in a Thinner Arctic Sea Ice Regime: The Norwegian Young Sea ICE Cruise 2015 (N-ICE2015)

Key Points:

- We report the first direct observations of in situ snow-ice formation in the high Arctic
- Snow-ice formation occurred after storms and/or basal ice melt
- The midwinter observations document intense sea-ice basal melt over warm Atlantic waters

Correspondence to:

C. Provost,
cp@locean-ipsl.upmc.fr

Citation:

Provost, C., N. Sennéchael, J. Miguet, P. Itkin, A. Rösel, Z. Koenig, N. Villacieros-Robineau, and M. A. Granskog (2017), Observations of flooding and snow-ice formation in a thinner Arctic sea-ice regime during the N-ICE2015 campaign: Influence of basal ice melt and storms, *J. Geophys. Res. Oceans*, *122*, doi:10.1002/2016JC012011.

Received 3 JUN 2016
Accepted 8 FEB 2017
Accepted article online 14 FEB 2017

Observations of flooding and snow-ice formation in a thinner Arctic sea-ice regime during the N-ICE2015 campaign: Influence of basal ice melt and storms

Christine Provost[1], Nathalie Sennéchael[1], Jonas Miguet[1], Polona Itkin[2], Anja Rösel[2], Zoé Koenig[1], Nicolas Villacieros-Robineau[1], and Mats A. Granskog[2]

[1]Laboratoire LOCEAN-IPSL, Sorbonne Universités (UPMC, Univ. Paris 6)-CNRS-IRD-MNHN, Paris, France, [2]Norwegian Polar Institute, Fram Centre, Tromsø, Norway

Abstract Seven ice mass balance instruments deployed near 83°N on different first-year and second-year ice floes, representing variable snow and ice conditions, documented the evolution of snow and ice conditions in the Arctic Ocean north of Svalbard in January–March 2015. Frequent profiles of temperature and thermal diffusivity proxy were recorded to distinguish changes in snow depth and ice thickness with 2 cm vertical resolution. Four instruments documented flooding and snow-ice formation. Flooding was clearly detectable in the simultaneous changes in thermal diffusivity proxy, increased temperature, and heat propagation through the underlying ice. Slush then progressively transformed into snow-ice. Flooding resulted from two different processes: (i) after storm-induced breakup of snow-loaded floes and (ii) after loss of buoyancy due to basal ice melt. In the case of breakup, when the ice was cold and not permeable, rapid flooding, probably due to lateral intrusion of seawater, led to slush and snow-ice layers at the ocean freezing temperature (-1.88°C). After the storm, the instruments documented basal sea-ice melt over warm Atlantic waters and ocean-to-ice heat flux peaked at up to 400 W m^{-2}. The warm ice was then permeable and flooding was more gradual probably involving vertical intrusion of brines and led to colder slush and snow-ice (-3°C). The N-ICE2015 campaign provided the first documentation of significant flooding and snow-ice formation in the Arctic ice pack as the slush partially refroze. Snow-ice formation may become a more frequently observed process in a thinner ice Arctic.

1. Introduction

Changes to the Arctic climate system are symptomatic of ongoing global climate change. These changes are magnified compared to lower latitudes and result in a smaller, thinner, and faster moving ice cover than just a decade ago [*Lindsay and Schweiger*, 2015; *Spreen et al.*, 2011]. Progressive degradation of multiyear ice in the 1990s and 2000s has led to the prevalence of seasonal ice after 2007 [*Maslanik et al.*, 2007]. The changes in sea-ice extent and physical structure are causing dramatic shifts in the interactions between sea-ice and both the atmosphere and the underlying ocean [e.g., *Perovich and Richter-Menge*, 2009; *Boisvert and Stroeve*, 2015]. Despite advances in numerical modeling, the reliability of present-day climate and numerical prediction models is limited in the Arctic with considerable uncertainties in the projected rates of sea-ice decline [*Overland and Wang*, 2013]. Small-scale physical processes that play an important role in the Arctic atmosphere-snow-sea-ice-ocean system, in particular at the interfaces, are not well represented in models [*Vihma et al.*, 2014].

The shift of the Arctic ice pack to a predominantly thinner and seasonal one, may introduce conditions that more closely resemble the Antarctic ice pack, where the formation of snow-ice is a common process [e.g., *Eicken et al.*, 1994], fostered by a relatively thin ice cover [*Worby et al.*, 2008] and abundant snow fall [*Bromwich et al.*, 2004]. Indeed, snow-ice formation results from the freezing of a mixture of snow and seawater produced by the flooding of ice floes. Flooding can result from negative freeboard conditions due to a heavy snow load relative to ice thickness (crack in the ice, edge of floes, permeable ice) or from capillary wicking of brines even in positive freeboard conditions [*Massom et al.*, 2001; *Lewis et al.*, 2011]. The slush resulting from flooding solidifies into snow-ice if a sufficient heat sink is available (cold atmosphere or/and cold underlying sea-ice). Snow-ice contributes to about a quarter of the total sea-ice formation in the Antarctic zone as suggested by isotope analyses [*Jeffries et al.*, 1997, 2001] and satellite estimates [*Maksym and Markus*, 2008]. In the high Arctic, the ratio of snow thickness to ice thickness has usually been small and snow-ice formation has not received much attention [*Vihma et al.*, 2014]. Only a few observations show snow-ice formation in the central Arctic. *Tucker et al.* [1991] present observations that point toward formation of snow-ice in the winter marginal ice zone in Fram Strait. Work on landfast ice has reported variable contributions of snow-ice. *Kawamura et al.* [2001], in one of the few studies in the high Arctic, found no evidence of snow-ice in landfast ice cores taken from the North Water Polynya region in Northern Baffin Bay, while in coastal areas and marginal seas with thinner ice cover, snow contribution can be significant [e.g., *Weeks and Lee*, 1958; *Ukita et al.*, 2000; *Granskog et al.*, 2003; *Kirillov et al.*, 2015]. Climate models project an increase in annual precipitation over the Arctic [*Overland et al.*, 2012; *Bintanja and Selten*, 2014]. Larger snow fall rates after sea-ice freezeup would promote snow-ice formation. However, whether the increased precipitation will fall as snow or rain on sea-ice is still uncertain [e.g., *Hezel et al.*, 2012: *Bintanja and Selten*, 2014]. Observations suggest regional differences in snow loading over the Arctic sea-ice: snow depth on first-year sea-ice has decreased in the western Arctic [*Webster et al.*, 2014], while north of Svalbard there is very little snow depth data to conclude whether this is a pan-Arctic phenomena, although recent observations point to thick snow covers in this region [*Haapala et al.*, 2013; *Rösel et al.*, 2016]. An increase in snow precipitation together with the thinning of the sea-ice cover could result in more extensive occurrence of snow-ice, with larger contributions to total ice mass [*Granskog et al.*, 2017].

The Norwegian young sea ICE (N-ICE2015) expedition [*Granskog et al.*, 2016] with the research vessel Lance frozen in the Arctic ice pack provided a research platform for studying the atmosphere, snow, sea-ice, ocean and marine ecosystem throughout the Arctic winter and spring. During winter 2015, the Arctic vortex was strong with large amount of northward meridional transport over the Greenland Sea. Six synoptic events occurred bringing warm and moist air from the south, strong winds and precipitation [*Graham et al.*, 2017; *Cohen et al.*, 2017]. Precipitation rates based on ERA-Interim reanalysis [*Dee et al.*, 2011] show that winter 2015 was exceptional in terms of snowfall. The snowfall in February 2015 was the largest in the ERA-Interim reanalysis record (1979–2015) for the N-ICE2015 region.

Here we present observations from seven ice mass balance instruments that drifted with pack ice from 83.5°N to 81°N around 16°E–18°E from mid-January to mid-March 2015. The instruments, which remained close to each other, were deployed in a wide variety of initial snow and ice thicknesses. Basal sea-ice melt in the middle of winter is observed by all the instruments and, for the first time in the high Arctic, snow-ice formation is observed in situ. The paper is organized as follows: observations and methods to derive interfaces and fluxes from the data are presented in section 2. In section 3, the evolution of the floes along the drift as documented by the seven instruments is described. Finally, section 4 summarizes the results and provides a future outlook.

2. Material and Methods

2.1. Ice Mass Balance Instruments and Deployments

The ice mass balance instruments deployed during N-ICE2015 (Table 1) were developed by the Scottish Association for Marine Science (SAMS) [*Jackson et al.*, 2013]. Hereafter, we call them SIMBAs standing for SAMS ice mass balance for the Arctic. SIMBAs are equipped with a 5 m long chain cable hanging through air, snow, sea-ice and ocean comprising solid-state sensors that measure temperature profiles with 2 cm vertical resolution at approximately 0.1°C accuracy. They also feature a heating mode that provides a proxy for thermal diffusivity, which can be used to discriminate between different media, especially between snow and ice [*Jackson et al.*, 2013]. Temperature was measured every 3 or 6 h, while heating with a duration of 120 s was performed once or twice per day (Table 1). During the heating mode that immediately follows one of the temperature profiles (T_0), temperature is measured after 30 and 120 s (T_1 and T_2) and the ratio of the observed temperature changes $(T_2 - T_0)/(T_1 - T_0)$ is the proxy for thermal diffusivity.

Seven SIMBAs were deployed between 15 January and 29 January (Table 1), during the first phase of the N-ICE2015 campaign using the research vessel Lance as a base for an ice station [*Granskog et al.*, 2016]. The SIMBAs were typically deployed on level parts of floes, remote from immediate active sea-ice deformation processes (leads and ridges), thus they likely recorded conditions that are representative of level ice. The

Table 1. Temporal Coverage, Initial Conditions (Measured at Time of Deployment), and Sampling Frequency of the Seven SIMBAs Deployed in January During N-ICE2015[a]

	SIMBA_2015h	SIMBA_2015a	SIMBA_2015i	SIMBA_2015f	SIMBA_2015b	SIMBA_2015g	SIMBA_2015e
Drift Time							
Start	24 Jan	15 Jan	27 Jan	25 Jan	16 Jan	29 Jan	27 Jan
End	16 Mar	16 Mar	21 Feb	19 Feb	16 Feb	28 Feb	26 Feb
Record length (days)	53	61	26	27	33	30	32
Ice type	SYI	N/A	SYI	FYI	FYI[b]	FYI[b]	FYI[b]
Initial Thickness (cm)							
Snow (point)	55	47	53	43	30	36	0
Snow (area)	49 (10)	59 (9)	49 (10)	33 (14)	44 (8)	41 (3)	21 (6)
Transect length	1.7 km	30 m	1.7 km	1.2 km	30 m	15 m	15 m
Ice	155	133	119	90	134	108	152
Freeboard	2	1	−4	−1	2	2	9
Frequency (h)							
GPS	2	1	2	1	1	1	6
Temperature	3	6	3	6	6	6	6
Heating cycle	24	24	12	24	24	24	24

[a] The initial thickness of snow (point) is the value observed at the SIMBAs at deployment. The initial thickness of snow (area) is the average value and standard deviation in parentheses from nearby snow depth transect lines at deployment date. Length of transect lines varied and are indicated. Initial ice and freeboard were measured at the SIMBAs.

[b] Ice type suggested from the relatively low averaged snow depth in the vicinity of the deployment site (although snow thickness is not a reliable metrics for distinguishing sea-ice age).

typical floe size was 100–500 m in diameter. The SIMBA chain cable was mounted on a tripod or on a horizontal pole extended from an uplifted platform and a 5 cm hole was drilled through the ice through which the chain was deployed. After the deployment we attempted to reconstruct the original sea-ice thickness by adding cold fresh water into the ice hole and by carefully filling in the snow to the original level. This last step was not done in the case of SIMBA_2015e (Table 1), where we intentionally left the ice bare to observe how fast the snow cover restored itself (snow depth on that floe was 21 cm at deployment). Data (including GPS coordinates, see Figure 1a) from SIMBAs were sent by satellite at regular intervals (Table 1). The shortest distance between any pair of instruments was only about 500 m (initially on the same floe) and the largest distance never exceeded 50 km at any time (Figure 1b). All SIMBAs experienced similar drifts with hourly drift velocities that exceeded 0.2 m s^{-1} during the six major storms (M1–M6) [*Cohen et al*., 2017] (Figure 1c). Table 1 summarizes the temporal extension, initial snow and ice conditions, and measurement setup of the SIMBAs. Most SIMBAs either stopped working or were recovered when the floe around Lance broke up on 21 February during storm M3. Two of them, however, kept functioning until 16 March. One of the latter, SIMBA_2015h, was deployed close enough to Lance to allow for periodical checks of the surface components until 21 February.

2.2. Identification of the Material Interfaces

We define the interfaces between the air/snow, snow/ice, and ice/ocean based on the temperature profiles and the thermal diffusivity proxy. SIMBA_2015h features highest temporal resolution (Table 1) and is used as an example in the subsections below. The calculated interfaces are marked in Figure 2 and they agree well with a visual interpretation of the profiles.

2.2.1. Air/Snow Interface

Diffusivity proxy alone can unfortunately not be used to reliably estimate the snow surface level due to icing (hoar frost) on the chain (Figure 2d). Instead we examined the vertical gradient of temperature and simultaneously the standard deviation over 24, 48, and 72 h period. Starting from the top of the chain we looked for a sharp increase in the vertical temperature gradient and a decrease in the standard deviation. This simple semiautomatic procedure provides a satisfying interface consistent with the time derivative of temperature and the diffusivity proxy with a rather constant snow thickness of 52 cm increasing to 88 cm on 16 February during storm M3 (Figure 2). The error range is small, about 2 cm on average, and does not exceed 6 cm at any time.

2.2.2. Snow/Ice Interface

The snow/ice interface is simple to derive from the sharp contrast in the diffusivity proxy values between both media. The snow/ice interface does not change except for slush formation associated with flooding on

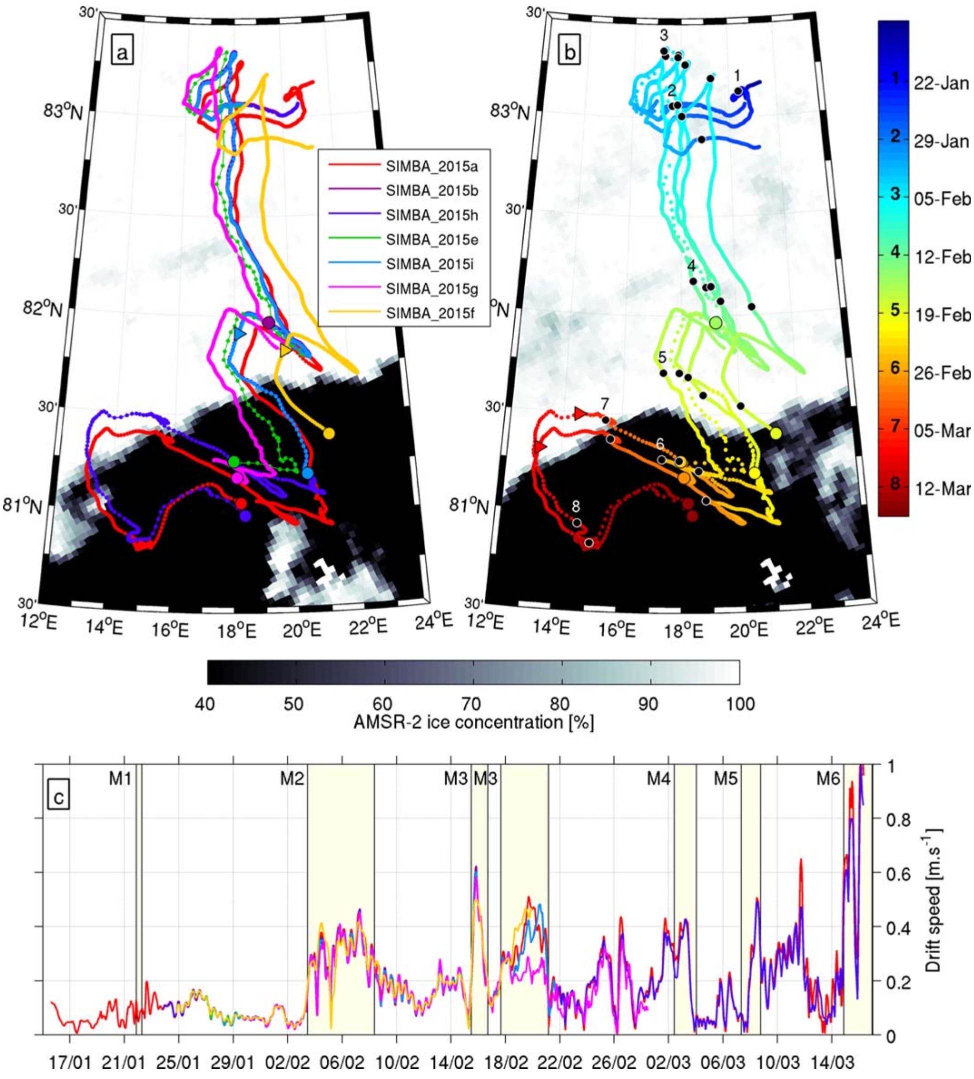

Figure 1. (a) Trajectories of the seven SIMBAs deployed in January–February of the N-ICE2015 campaign. Triangles indicate onset of the first snow-ice formation (SIF) event. Circles indicate the location of end of SIMBA record. Background is AMSR-2 ice concentration (%) on 17 February, the date of the first SIF event. (AMSR-2, advanced microwave scanning radiometer daily product on a 0.25° × 0.25° grid.) (b) Time along trajectories. Digits are used as points of reference (see colorbar). Background is AMSR-2 ice concentration (%) on 9 March, the date of the second SIF event. Triangles indicate onset of the second SIF event and circles are as in Figure 1a. (c) SIMBA drift velocities (m s^{-1}). Major storms are labeled M1, M2, . . ., M6 as described in *Cohen et al*. [2017].

8 March (see section 3). It is worth noting that the diffusivity proxy is not accurate enough to distinguish between slush and snow-ice. This will be further discussed in section 3.5.

2.2.3. Ice/Ocean Interface

Since the winter sea-ice remains colder than the ocean, the sea-ice/ocean interface can be estimated from temperature profiles alone. The ocean just below the ice is at or just above the freezing temperature (estimated from a near surface conductivity-temperature-depth (CTD) sensor see *Koenig et al.* [2016]). The first sensor of the SIMBA chain in the ocean was determined as the first sensor, downward of the snow/ice interface, with a temperature above the ocean freezing temperature. The location of the last sensor in the ice was determined as the sensor with a temperature that was below the mean ocean temperature by at least twice the ocean temperature standard deviation in that profile. Finally, the ice/ocean interface is defined as half way between the last sensor in the ice and the first sensor in the ocean. It can typically be estimated with 2 cm accuracy. This interface estimate is consistent with

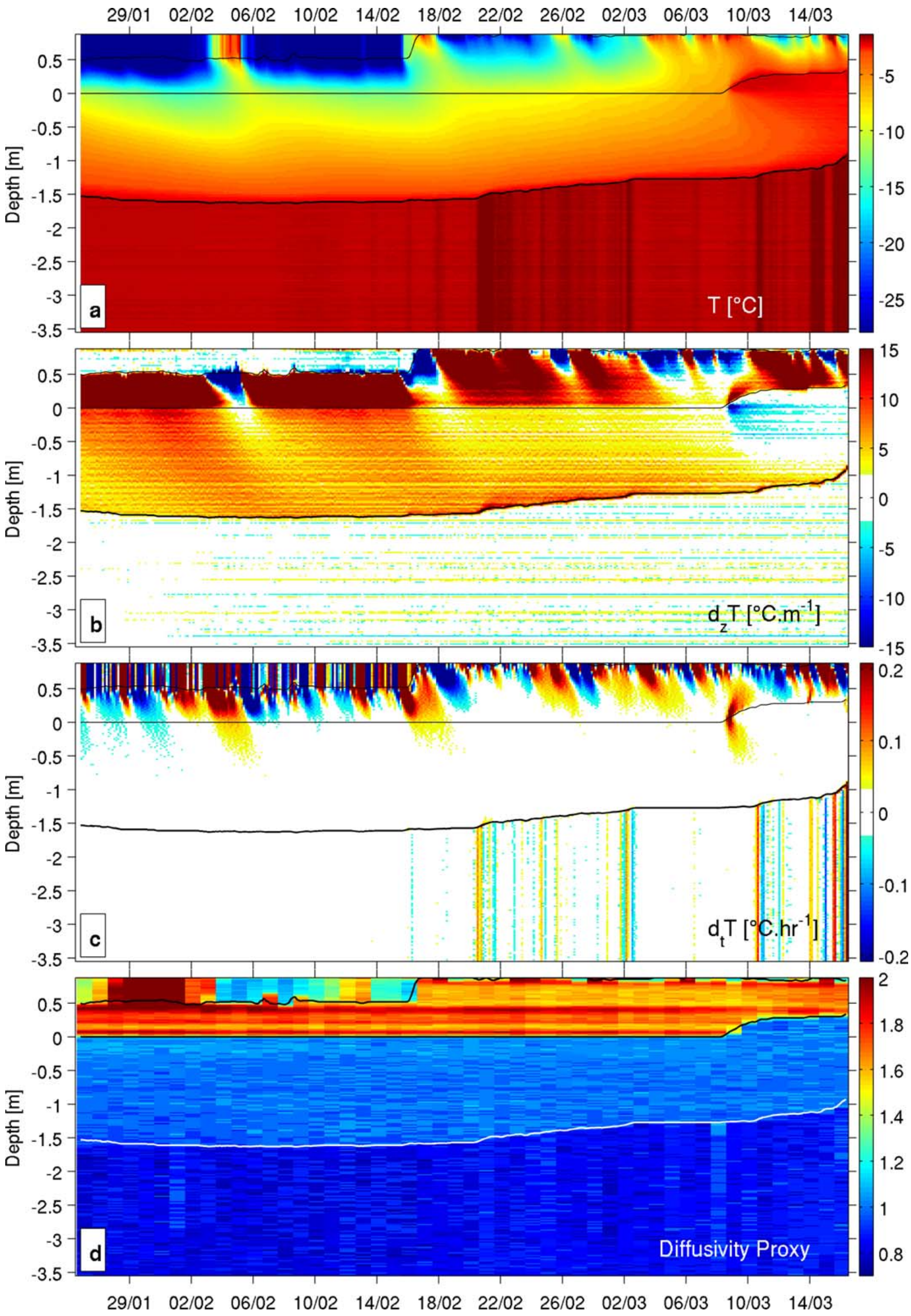

Figure 2. Data from SIMBA_2015h from top to bottom, (a) temperature (°C), (b) derivative of temperature with respect to the vertical (°C m^{-1}), (c) derivative of temperature with respect to time (°C h^{-1}), and (d) diffusivity proxy (no units) obtained from the heating mode. *y* axis is vertical distance (m) referenced to the initial ice-snow interface. Vertical resolution is 2 cm on all plots. Time resolution is 3 h on the 3 top figures and 24 h for diffusivity proxy. Isolines (24 h running mean) correspond to the air/snow, snow/ice, and ice/ocean interfaces derived as explained in section 2. Color scale in panel a is nonlinear in order to show temperature changes in the ocean.

the thermal diffusivity proxy (Figure 2d) and the vertical and temporal derivatives of temperature (Figures 2b and 2c) and features basal melt events after 20 February corresponding to temperature changes in the ocean (Figure 2c).

2.3. One-Dimensional Ocean to Sea-Ice Flux Densities

In this section we present the calculations of the heat fluxes. We assume a horizontally homogeneous environment. The *z* axis is positive in the direction toward the sky and the heat from the ocean toward the ice is likewise positive. The examples are again from SIMBA_2015h. In the parameterization, when needed, the ice salinity is assumed to be 5 PSU and temperature in the ice is provided by the SIMBA.

2.3.1. Latent Heat Flux

We define the latent flux density as

$$F_l=\rho_{si}\frac{dh}{dt}$$

where ρ_{si} is the sea-ice density (900 kg m^{-3}), L is the latent heat of fusion of sea-ice (J kg^{-1}), and h is the sea-ice-ocean interface depth (m). Following *Bitz and Lipscomb* [1999], we estimate $L = 0.89\ L_0$ where L_0 is the latent heat of fusion of pure ice. The latent flux is directly proportional to the change in time of the interface depth (Figure 3b). The uncertainty on the latent heat flux estimate assuming a 2 cm accuracy on h is 56 W m^{-2} for data with a 3 h resolution (101 W m^{-2} for data with 6 h resolution). The resulting latent heat flux values for SIMBA_2015h range from -100 to 400 W m^{-2}, while the basal melt events associated with ocean temperature increase stand out (Figures 3a and 3b).

2.3.2. Conductive Heat Flux

The classical formula for conductive heat flux F_c in the one-dimensional case reads

$$F_c=-k_{si}\frac{dT}{dz}$$

where k_{si}, the sea-ice thermal conductivity, is derived from equation $k = 2.03 + 0.117\ S/T$ [*Maykut and Untersteiner*, 1971] for S = 5 psu and T is the observed temperature from the SIMBA. The sea-ice thermal conductivity k varied between 1.8 and 1.9 W m^{-1} K^{-1} for SIMBA2015-h. These values are consistent with those measured and estimated in *Pringle et al.* [2006] for second-year ice (SYI). We estimated conductive fluxes every 2 cm and chose to show depths that were indicative of atmospheric influence 20 cm below ice-snow interface, ocean influence 6 cm above ice-ocean interface and two intermediate depths between those two levels (Figure 3c). Those precise values are not critical, the purpose is just to illustrate how atmospheric and ocean influence are felt through the ice. The vertical gradients at the three upper levels were estimated by linear interpolation around the position and the gradient at the lower level by second order polynomial regression over 12 sensors above the interface as profiles are less linear near the ice bottom when ocean temperature changes. Resulting conductive fluxes for SIMBA_2015h range between -7 and $+ 22$ W m^{-2}. As expected, the conductive flux near the snow/ice interface (Figure 3c) has the largest amplitude variations and reflects atmospheric temperature changes with about 8 day lag at the beginning of the time series, between 25 January and 16 February, when snow is 42 cm thick. After 16 February, the 88 cm-thick snow cover insulates the ice from atmospheric fluctuations and the conductive flux remains below 10 W m^{-2} until 8 March when snow-ice formation occurs (section 3) and the conductive flux becomes negative. The conductive flux at 30 cm above the ice/ocean interface (Figure 3c) remains around 10 W m^{-2} except after the formation of snow-ice. The near bottom flux (Figure 3c) is positive during basal melt events following the ocean temperature peaks (Figure 3a) except after 8 March during snow-ice formation (section 3).

2.3.3. Sensible Heat Flux

The sensible heat flux in the ice between two levels distant by p sensors (2p cm) is given by

$$F_s(i)=\sum_{j=i}^{i+p}\rho_{si}C_{si}\frac{dT}{dt}_j\ Dz$$

where C_{si} is the effective specific heat of sea-ice as defined by *Ono* [1967] and Dz is the distance between 2 sensors (2 cm). The sum is computed between sensor i at level z1 and sensor i + p at level z1 + 2p. The sensible heat flux between 6 and 30 cm above the ice-ocean interface varies between -4 and $+10$ W m^{-2} (Figure 3d).

In principle the residual flux, computed as the sum of the conductive heat fluxes at 6 and 30 cm and the sensible heat flux between those two levels, ($F_{Re} = F_{C6cm} + F_{C30cm} + F_{S6\text{-}30}$), should be zero under the assumption of a horizontally homogeneous environment. The residual flux never exceeds 2.9 W m^{-2} (Figure 3e). The residual flux can be seen as the sum of the errors in the three fluxes. The accuracy on the sensible heat flux is estimated to be 2.3 W m^{-2} considering the accuracy of temperature measurements (0.1°C) as

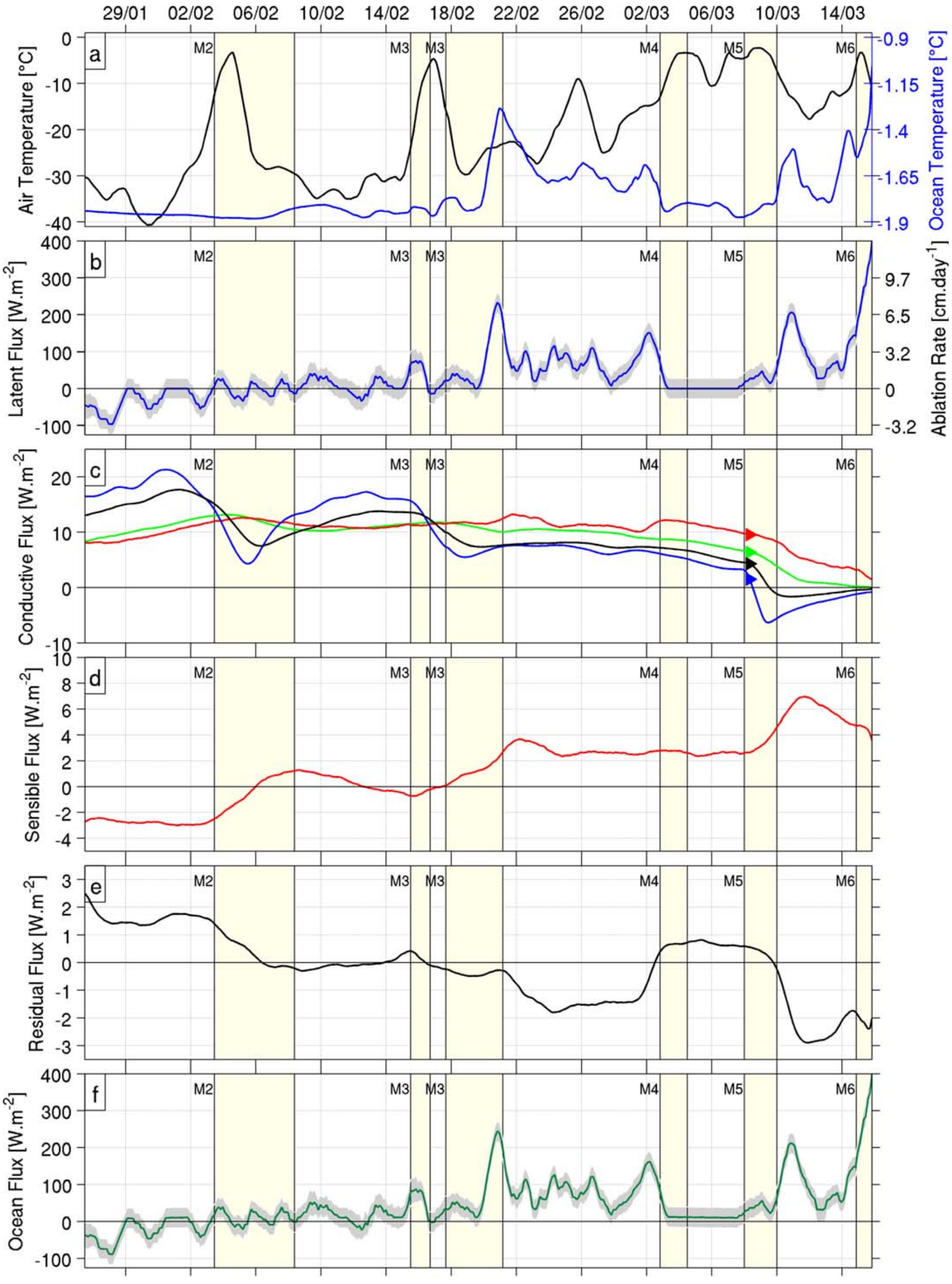

Figure 3. (a) Time series of air temperature from the weather station on the IAOOS (Ice Atmosphere Ocean Observing System) ice-tethered platform [*Koenig et al.*, 2016] hosting SIMBA_2015h (black line, left axis) and ocean temperature from SIMBA_2015h (mean of ocean temperatures, blue line, right axis); time series of heat flux densities (W m^{-2}) estimated from SIMBA_2015h. (b) Latent heat flux (left axis) and basal ablation rate (cm d^{-1}) (right axis), (c) conductive heat flux (blue: 20 cm below the snow-ice interface; black: 50 cm below the snow-ice interface; green: 30 cm above the ice-ocean interface; and red: 6 cm above the ice-ocean interface), (d) sensible heat flux between 30 and 6 cm above the ocean interface, (e) residual heat flux: sum of the conductive heat fluxes at 30 and 6 cm above the ice-ocean interface and the sensible heat flux between those two levels, and (f) ocean heat flux (latent heat flux plus conductive heat flux 6 cm above ice-ocean interface). All time series are smoothed with a 24 h running mean.

the sole source of uncertainty and taking a mean value for C_{si}. The accuracy for conductive fluxes can therefore be estimated to be less than 1 W m^{-2} and allows for confident use of the conductive flux calculated 6 cm above the interface in the following.

2.3.4. Ocean Heat Flux

The flux from the ocean to the ice can be derived as

$$F_{ocean} = F_l + F_c$$

F_l is the latent flux and F_c the conductive flux in the lower portion of the ice, here estimated 6 cm above the ice/ocean interface. As the latent heat flux is an order of magnitude larger than the conductive heat flux, the ocean heat flux is approximately equal to the latent heat flux (Figure 3f).

3. Evolution of the Snow and Ice Mass Balance

The methods described above were applied to the seven SIMBA records (Table 2, Figures 4 and 5) to retrieve the interfaces and compute heat fluxes. We first describe data and interfaces, then freeboard, and basal sea-ice melt, flooding and snow-ice formation. Basal ice melt is clear in all records after 15 February and flooding with snow-ice formation occurred at the end of the records of four SIMBAs (SIMBA_2015a, SIMBA_2015h, SIMBA_2015f, and SIMBA_2015i) (Figures 4 and 5). The seven SIMBAs were, at all times, located within a distance less than 50 km of each other (Figure 1).

3.1. Initial Conditions

In spite of their spatial proximity, the seven SIMBAs feature significantly different initial snow and ice thicknesses (Table 1). Initial snow thickness varied from 21 (SIMBA_2015e) to 55 cm (SIMBA_2015h) and initial ice thickness from 90 (SIMBA_2015f) to 158 cm (SIMBA_2015e). The average snow thickness in the region of the deployment site agrees well with the initial values of the SIMBAs (Table 1). During the winter months of the N-ICE 2015 camp, observed snow thicknesses, on average 33 ± 14 cm over first-year ice (FYI) and 52 ± 12 cm over second-year ice (SYI) [*Rösel et al.*, 2016], were larger than expected based on climatology (from 28 to 35 cm without distinction of ice type) [*Warren et al.*, 1999]. Note that snow was intentionally removed at SIMBA_2015e.

All freeboards were small (less than +4 cm) and even negative at two sites (–4 and −1 cm at SIMBA_2015i and SIMBA_2015f). Differences in initial conditions depend upon the local floe history prior to deployment (young, old, level or deformed ice, surface topography for snow deposition) and the location of the SIMBA on the floe. The age of the sea-ice on which the instruments were deployed varied from SYI to FYI (Table 1). Sea-ice cores were taken only for a number of the ice floes in the close vicinity of the research vessel and we can only establish with certainty that SIMBA_2015h and SIMBA_2015i were deployed on older sea-ice with a desalinated top part, while the ice at SIMBA_2015f had a typical salinity profile of FYI. The lower average amount of snow cover in the vicinity of the deployment site for SIMBA_2015b, SIMBA_2015e, and SIMBA_2015g might suggest that the floes would be FYI, although snow thickness is not a reliable metrics for distinguishing sea-ice age.

Table 2. Snow and Ice Thicknesses and Ice Freeboard: Initial Values, Values at the Onset, and After Snow-Ice Formation (SIF)[a]

	SIMBA_2015h	SIMBA_2015a	SIMBA_2015i	SIMBA_2015f	SIMBA_2015b	SIMBA_2015g	SIMBA_2015e
Snow-Ice Formation (SIF)							
SIF onset (DD/MM HH UTC)	8/03 8 A.M.	9/03 3 P.M.	17/02 7 P.M.	17/02 4 P.M.	No snow-ice observed		
SIF record length (h)	192	162	90	48			
Total Snow Thickness (cm)							
Initial	55	46	53	43	30	36	21/0
At SIF onset	90	50	85	55			
After SIF	55	35	43	37	No snow-ice observed		
Ice Thickness Budget (cm)							
Bottom ablation	71	71	15	2	9	20	8
Snow-ice	32	18	40	18			
Total change	−39	−53	25	16	No snow-ice observed		
Fraction of snow-ice (%)	27.6	22.8	27.8	17.0			
Estimated Freeboard (cm)							
Initial	2	2	−4	−1	4	2	2
At SIF onset	−12	−1	−12	−4			
After SIF	+0	+1	+3	+3	No snow-ice observed		

[a] Fraction of snow-ice thickness (%) to total ice thickness at the end of the records is also given.

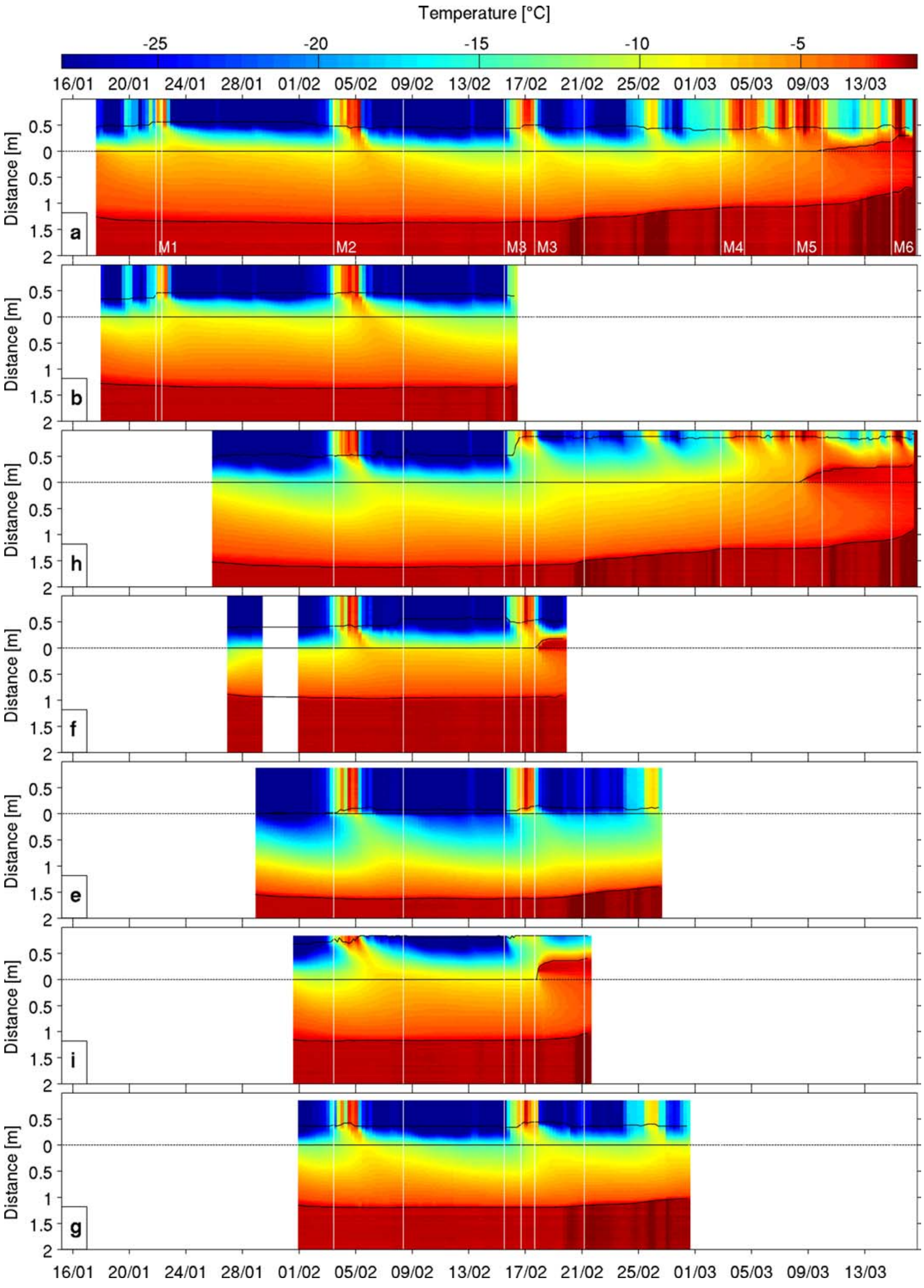

Figure 4. Temperature profiles (°C) and interfaces as a function of time for the seven SIMBAs. Color scale is nonlinear in order to show temperature changes in the ocean. Temporal resolution varies as indicated in Table 1 (3 h for SIMBA_2015i and SIMBA_2015h and 6 h for the others). *y* axis is vertical distance (m) referenced to the initial ice-snow interface. Vertical resolution is 2 cm. Black isolines (24 h running mean) correspond to the air/snow, snow/ice, and ice/ocean interfaces derived as explained in section 2.

3.2. Evolution of Temperature Profiles, Thermal Diffusivity Profiles, and Interfaces

All SIMBAs experienced similar atmospheric conditions as they were close to each other. In fact, the parts of the chain deployed through the air all show sudden temperature peaks associated with the storms and a gradual warming trend [*Hudson et al.*, 2016] through the observation period (Figure 4). Air temperatures

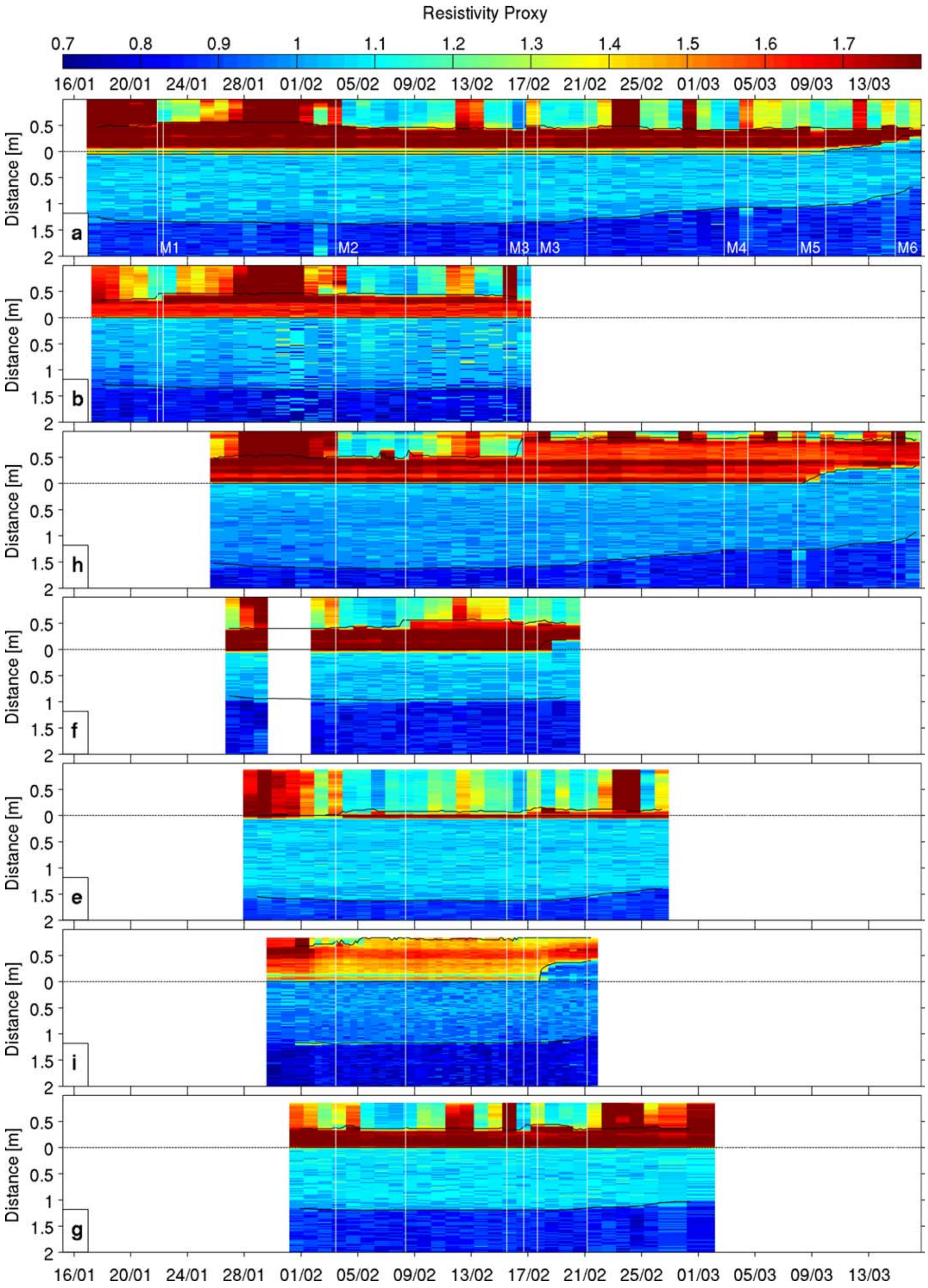

Figure 5. Thermal diffusivity proxy profiles and interfaces as a function of time for the seven SIMBAs. Time resolution varies as indicated in Table 1 (12 h for SIMBA_2015i and 24 h for the others). *y* axis is vertical distance (m) referenced to the initial ice-snow interface. Vertical resolution is 2 cm. Isolines (24 h running mean) correspond to the air/snow, snow/ice, and ice/ocean interfaces.

varied from −42 to 0°C. Note that the top of SIMBA_2015h chain was entirely covered by snow from 17 February onward (Figures 4 and 5) and the snow thickness was estimated to be 90 cm (Table 2).

Snow thickness, with initial values ranging from 21 cm (SIMBA2015-e intentionally artificially turned to 0 cm) to 55 cm (SIMBA2015-h), evolved only during storms and during flooding events leading to snow-ice formation (Figure 6a). The change in snow thickness observed during the storms varied greatly from one SIMBA to

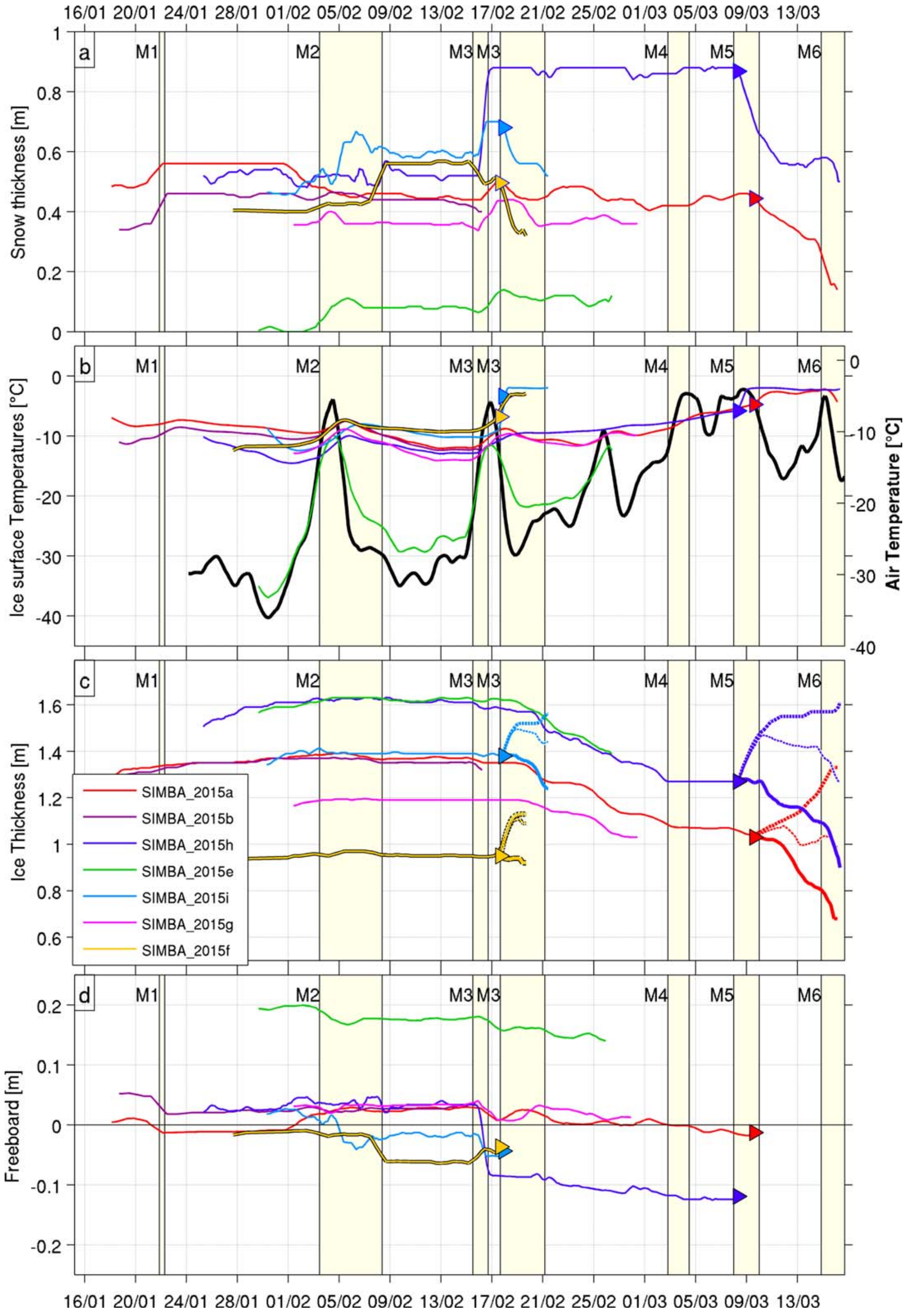

Figure 6. Times series of (a) snow thickness (m), (b) temperature (°C) at the snow-ice interface (color) and air temperature (black line), and (c) ice thickness (m). Note that when slush/snow-ice formation occurs, the ice thickness line separates into three branches: the bottom one (thick) indicates the ice thickness without taking the slush/snow-ice into account, the top one (thick) the ice thickness without taking into account basal melt, and the one in the middle (thin line) the ice thickness including slush/snow-ice, and (d) freeboard estimates (m). All time series are smoothed with a 24 h running mean. Color associated to each SIMBA is indicated in insert. Triangles indicate onset of snow-ice formation. Storm periods are indicated as in Figure 1c.

another, suggesting important differences in snow redistribution, accumulation or ablation, likely due to interaction of winds and snow transport with the surface topography of the floe, and possibly also local snow accumulation/erosion due to the SIMBA support structures. During M1, the only two active SIMBAs, SIMBA_2015a and SIMBA_2015b, recorded a 10 cm increase in snow depth. During M2, only three SIMBAs out of seven (SIMBA_2015e, i, and f) showed significant snow accumulation (10, 25, and 15 cm, respectively) which did not occur on the same day. Three others (SIMBA_2015b, h, and g) did not show any change while SIMBA_2015a showed a decrease of 15 cm. During M3, SIMBA_2015h experienced 45 cm of snow accumulation whereas SIMBA_2015f and SIMBA_2015i experienced significant drops of 20 and 30 cm in snow thickness, respectively, because of flooding (Figure 6a). Thereafter, snow thicknesses did not change much until flooding after M5 (40 cm decrease for SIMBA_2015h and 30 cm for SIMBA_2015a). Note that SIMBA_2015e (green line in Figure 6), which was intentionally left with bare ice, retrieved 17 cm of snow.

The insulating effect of the snow layer can be readily appreciated when comparing temperatures at the ice-snow interface to air temperatures (Figure 6b). The air temperature range exceeds 40°C, whereas temperature at the snow-ice interface remain around $-10°C$ ($\pm 5°C$) except in the case of SIMBA_2015e where temperature at the top of the ice followed air temperature as the snow cover was nonexistent or very thin (Figure 6b). The snow cover provides thermal insulation from air temperature, regulates temperature fluxes, and affects the thermal evolution of sea-ice [*Massom et al.*, 2001].

During M3, when Floe 1 of the N-ICE2015 campaign broke up, two SIMBAs (SIMBA_2015b and SIMBA-2015f) stopped working. All the other SIMBAs documented significant ice ablation at the bottom (Figure 6c). Basal ice melt started around 18 February, when the distance to the open water was 45 km and went on until the end of the time series, with a pause between M4 and M5. By 15 March, when the distance to the open water was just 2 km, total ice ablation was about 68 cm at the two remaining SIMBAs (SIMBA_2015a and SIMBA_2015h) (Table 2). This is discussed further in section 3.4.

Four SIMBAs displayed a typical signal for a flooding above the initial ice/snow interface (SIMBA_2015f and SIMBA_2015i around 17 February, SIMBA_2015a and SIMBA_2015h around 8 March, Figures 4 and 5). The flooding heats the base of the snow, which in turn heats the surrounding snow and ice. The thermal diffusivity proxy (Figure 5) readily turns from snow values to values typical of ice. Slush is formed. The flooding events leading to slush and subsequent transformation of slush into snow-ice are further examined in section 3.5.

3.3. Freeboards

The sea-ice thickness and snow depth time series were used to estimate the freeboard development for each SIMBA using Archimedes buoyancy principle, that is a vertical buoyancy balance where a mass per unit volume of sea water supports sea-ice and snow. The freeboard h_f is given by

$$h_f = h_i - \frac{\rho_i h_i + \rho_s h_s}{\rho_w}$$

where h_i is the ice thickness, h_s the snow thickness, ρ_w the density of seawater, ρ_s the density of snow, and ρ_i the density of sea-ice. Typical density values (1028 kg m^{-3} for ρ_w, 330 kg m^{-3} for ρ_s, and 900 kg m^{-3} for ρ_i) provided reasonable estimates of the freeboard (Figure 6d). The initial estimated freeboard values are of the same sign and magnitude (within 2 cm) as the observed initial conditions, except in the case of SIMBA_2015e. At this buoy, the original snow cover depth was not restored after the deployment and while the initial estimated freeboard is about $+18$ cm (in green in Figure 6d), the observed initial freeboard is only $+2$cm (Table 1). If we replace the snow depth measured by the SIMBA chain by the average snow depth measured in the vicinity of the buoy (Table 1), the calculated freeboard agrees with the observed initial freeboard. The estimated freeboards tend to decrease with time as snow accumulates (Figures 6a and 6d). The decrease in estimated freeboard varies with snow accumulation and is largest for SIMBA_2015h (Figure 6d). The four SIMBAs with a positive estimated freeboard right before the floe broke up (SIMBA_2015a, b, e, and g) did not observe flooding (slush formation, Table 2), while SIMBA_2015f and SIMBA_2015i with negative estimated freeboards of -10 cm at the time of M3, showed flooding. Slush formation reduced the snow thickness (–20 cm at SIMBA_2015f and -40 cm at SIMBA_2015i, Figure 6a), increased the ice thickness (by 20 and 40 cm, respectively, including thickness of the slush layer, Figure 6c). SIMBA_2015h has a similar estimated negative freeboard (–10 cm) but did not show slush formation at the end of storm M3. This suggests that SIMBA_2015h was on a floe that did not break up or that the snow accumulated very locally around the SIMBA chain. Note that until storm M3 ice thickness changes are small, and that freeboard changes are due to snow accumulation. Basal melt starts after storm M3. After storm M3, the ice thickness diminished (Figure 6c) while snow thickness was unchanged and freeboard decreased further for SIMBA_2015a and SIMBA_2015h (Figures 6a, 6c, and 6d). During storm M5, flooding occurred with a slush layer of 30 cm at SIMBA_2015h and 25 cm at SIMBA_2015a (see Table 2).

The flooding events on 19 February (two SIMBAs during storm M2) and on 8 March onward (two SIMBAs after and during intense basal ice melt) and subsequent refreezing of slush into snow-ice are examined in more detail in section 3.5.

3.4. Heat Fluxes and Basal Melt

Conductive heat flux densities in the ice estimated at the interface with snow range from 90 to -50 W m^{-2} (Figure 7a). They vary with atmospheric temperatures (Figure 6b): they are in phase for SIMBA_2015e (not shown), the location with no or little snow cover, and with some delay for the others. Negative values are observed at SIMBA_2015e during storms when the air temperatures peak (not shown) and at the four SIMBAs that experienced flooding at the interface with the warm slush. These conductive fluxes away from the slush are used to estimate how much slush solidifies into snow-ice in section 3.5.

All conductive heat flux densities estimated 6 cm above the ice/ocean interface are in the range 5–32 W m^{-2} (Figure 7b). Until 15 February, while the ocean is at the freezing temperature (Figure 7e), they vary with atmospheric temperatures with some delay (Figure 6b). After this date, they reflect ocean temperature changes and temperature changes due to flooding and snow-ice formation.

Latent heat flux densities, which are proportional to ablation rates, (Figure 7c) feature values larger than 100 W m^{-2} several times after 15 February. The bottom melt common to all SIMBAs occurs in rather short, sporadic events associated with warm ocean temperature pulses (Figure 7e). High melting rates ($>$6 cm d^{-1}), such as reported in *Sirevaag* [2009] in the same area, are observed. Values of latent heat flux densities as large as 400 W m^{-2} are found at the end of the time series. The negative values at the beginning of all latent flux density time-series (during 2–3 days) result from the refreezing of the drilled hole (2 in. diameter) through which the SIMBA string was deployed. They are not only driven by vertical fluxes but also horizontal conduction in the ice.

Ocean heat fluxes estimated as the sum of the conductive flux 6 cm above the sea-ice-ocean interface and the latent heat flux associated with ice melting mimic the latent heat fluxes which are an order of magnitude larger than the conductive fluxes (Figure 7d). These large ocean fluxes, with peak values of 400 W m^{-2}, are associated with warmer ocean temperatures when the ice floes drifted on top of shallow Atlantic waters north of Svalbard [*Koenig et al*., 2016]. The mean ocean-to-ice heat flux over the Svalbard continental slope was 150 W m^{-2} leading to a basal ice melt of 60 cm in less than 15 days. *Koenig et al*. [2016] showed that the sea-ice melt events were associated with near 12 h fluctuations in the upper ocean temperature and salinity corresponding to the periodicity of tides and near-inertial waves potentially generated by winter storms. These values are comparable to ice-ocean heat fluxes estimated in the same region in April 2003 (values peaking at 600 W m^{-2}) [*Sirevaag*, 2009] or estimated over the Yermak Plateau in February 2003 (values peaked at 100 W m^{-2}) [*McPhee et al*., 2003].

3.5. Flooding and Snow-Ice Formation

Flooding and slush formation were readily seen on the diffusivity proxy (Figures 4 and 5) and on the temperature itself (Figures 4 and 5). Indeed, the flooding has a strong temperature signature with initial warming at the ice-snow interface and subsequent heat propagation throughout the snow and ice system (Figures 4 and 5). At flooding, the diffusivity proxy values drop to ice-like values (Figure 5). Snow flooded by salty water, through either vertical infiltration through brine channels or lateral infiltration from seawater, forms a warm layer of slush (Figures 8a and 8b). Then the slush progressively solidifies into snow-ice as latent heat flux of snow-ice formation is converted into conductive heat fluxes in the snow above and ice below [*Eicken et al*., 1994]. The diffusivity proxy values do not allow distinguishing between slush and snow-ice (Figure 8b).

The temperature changes associated with the flooding are best observed in the time derivatives of temperature which peaks at 2.4°C/h (Figure 8c). Then, there is progressive freezing into snow-ice as latent heat

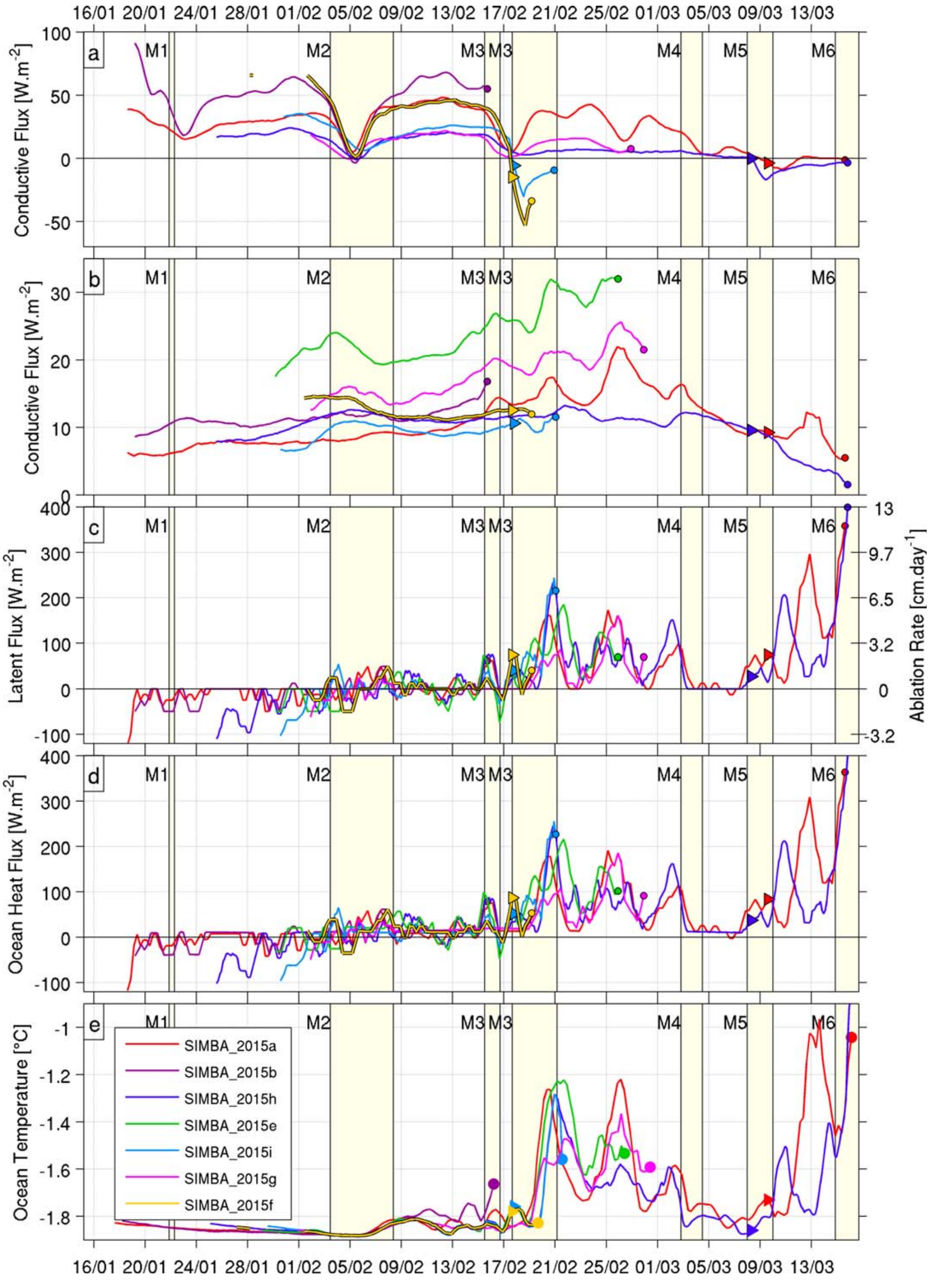

Figure 7. SIMBA time series of (a) conductive heat flux densities in the ice at the snow-ice interface (W m^{-2}) (SIMBA-2015e provides larger values), (b) conductive heat flux densities 6 cm above the ice-ocean interface (W m^{-2}), (c) latent heat flux densities at the ice-ocean interface (W m^{-2} left axis) and equivalent ablation rate (right axis in cm d^{-1}), (d) ocean heat flux densities (W m^{-2}), and (e) ocean temperature (°C) (mean of observations in the ocean). All time series are smoothed with a 24 h running mean. Color code corresponds to the different IMBs as indicated. Triangles indicate onset of snow-ice formation. Storm periods are indicated as in Figure 1c.

from solidifying ice is expelled from the flooded snow layer through conductive fluxes in the snow above and ice below (Figure 8d). Assuming that the mass fractions of snow and water in snow-ice are 2/3 and 1/3, respectively [*Eicken et al.*, 1995; *Kirillov et al.*, 2015], the thickness of slush that turns into snow-ice at each time t can be estimated as

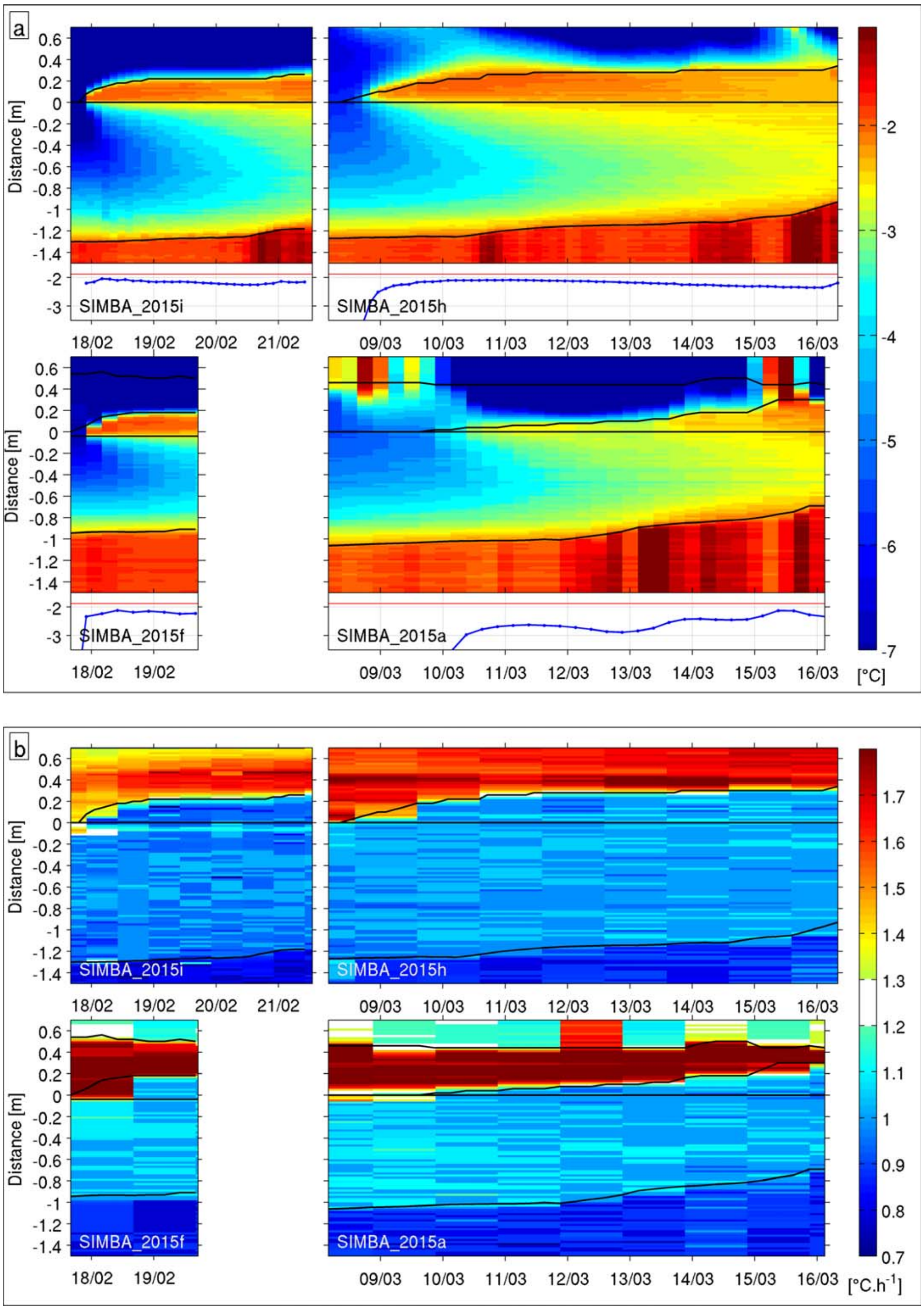

Figure 8. (a) Close-up of temperature profiles (°C) during periods of flooding and snow-ice formation (SIMBA_2015i, SIMBA_2015h, SIMBA_2015f, SIMBA_2015a). Temperature scale is nonlinear. The blue curve below corresponds to the average temperature values between real time and initial snow/ice interface. Red line is ocean freezing temperature. (b) Close-up of diffusivity proxy profiles (°C) during periods of slush/snow-ice formation (SIMBA_2015i, SIMBA_2015h, SIMBA_2015f, SIMBA_2015a). (c) Close-up of the profiles of the time derivative of temperature (°C h^{-1}) in the course of slush/snow-ice formation (SIMBA_2015i, SIMBA_2015h, SIMBA_2015f, SIMBA_2015a). (d) Close-up of the profiles of the vertical derivative of temperature (°C m^{-1}) in the course of slush/snow-ice formation (SIMBA_2015i, SIMBA_2015h, SIMBA_2015f, SIMBA_2015a). The black curve below corresponds to the flooded snow thickness, the blue (red) curve to the part that solidified into snow-ice due to conductive fluxes through the ice (ice and snow). *y* axis is vertical distance (m) referenced to the initial ice-snow interface. Vertical resolution is 2 cm. Black isolines from top to bottom represent air/snow interface, initial snow/ice interface, and ice/ocean interface. Green isolines represent snow/ice interface evolution.

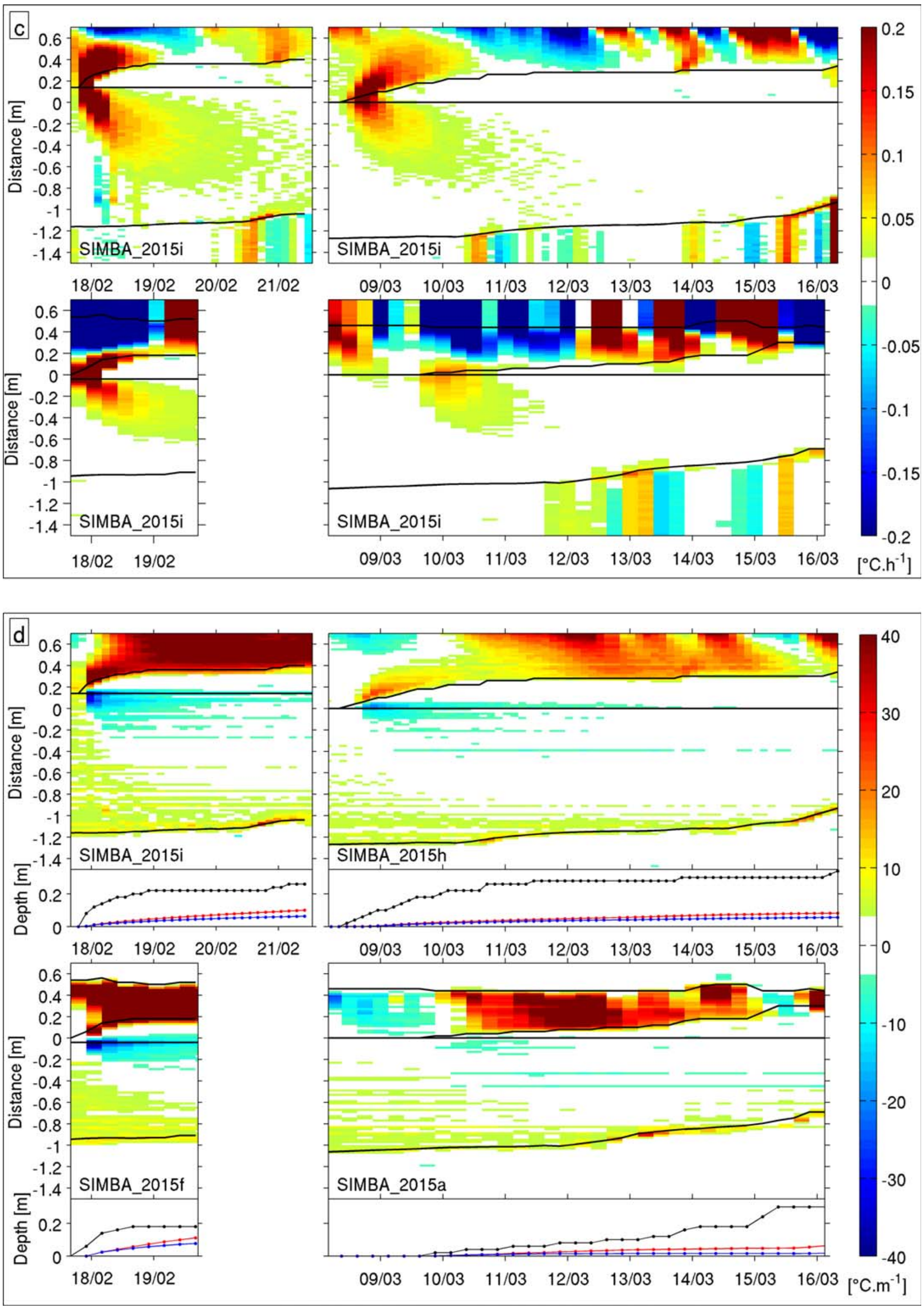

Figure 8. (continued).

$$h(t)=\frac{3(F_S(t)+F_i(t))}{\rho L}$$

where $F_S(t)$ and $F_i(t)$ are the conductive heat flux densities in the snow and in the ice at the flooded layer interface at time t, ρ is the ice density (taken as 900), and L the latent heat of fusion. These conductive flux densities (F = –k dT/dz) are calculated with k ≅ 0.3 W m^{-1} K^{-1} at the base of the snow [*Yen*, 1981] and k in the ice as in section 2.3.2. The snow-ice layer thickness H(t) is then estimated as

$$\int_{t_0}^{t} h(s)\ ds$$

with the time integration running from the time of the flooding t_0 until time t (Figure 8d). This rough calculation, which neglects any lateral flux, gives an order of magnitude of about 10 cm of snow-ice at the end of the four records (Figure 8d).

During the first flooding event (17 February, SIMBA_2015i and SIMBA_2015f), the temperature of the new slush layer right after flooding was close to the ocean freezing point (Figure 8a). In 3 h, 25 and 10 cm of slush was formed at SIMBA_2015i and SIMBA-2015f, respectively. The initial temperature at the snow/ice interface before flooding was about −8.5°C and the 3 h resolution record at SIMBA_2015i indicates that the ocean freezing temperature of about −2°C was reached in less than 3 h (blue line in Figure 8a). The heat release associated with the flooding on 18 February propagated through the ice and increased the ice temperature by about 3°C down to 70 cm depth (Figures 8a and 8b). The 4 day long record at SIMBA_2015i shows that the flooded layer temperature decreases slightly (blue line in Figure 8a) and then increases again to ocean freezing temperature as further flooding takes place on 21 February (5 cm) as corroborated by another subsurface peak in the time derivative of temperature (Figure 8a). The amplitude of the peak in time derivative is smaller as the ice was warmer and closer to ocean freezing temperature (Figure 8c). This second period of flooding follows 5 cm of basal melt (Figure 8a), suggesting freeboard adjustment to changed ice thickness. Estimates of the conductive fluxes suggest a latent heat change within the flooded layer sufficient to freeze the equivalent of 10 cm of snow-ice in 3 days, or the equivalent of half the total slush layer thickness. The short 2 day record of flooding and subsequent snow-ice formation for SIMBA_2015f provides information that are consistent with SIMBA_2015i: a rapid flooding with a strong heat release, underlying ice warming by 3°C over 50 cm depth (Figures 8a and 8b), progressive snow-ice formation of about 11 cm in 2 days estimated from the heat release by conductive fluxes (Figure 8d). Conductive fluxes through the snow at the flooded layer interface at SIMBA-2015f were larger than at SIMBA_2015i as the remaining snow layer above the flooded layer was thinner (35 versus 55 cm). In both cases, although air temperatures fell below −20°C after the storm M3, the remaining snow layer damped heat exchanges with the slush layer and conductive fluxes through the ice, although the ice had been heated up by the flooding, had a larger contribution to the solidification of the slush than conductive fluxes through the snow (Figure 8d).

The second major flooding event occur later in March and further south at a time when ice temperature at the surface was −4°C (SIMBA_2015h on 9 March and SIMBA_2015a on 10 March and onward) (Figure 8a).

Flooding at SIMBA_2015h, documented with a 3 h time resolution, is gradual as a 20 cm-thick slush layer is formed in 2 days. Slush temperature right after flooding is also near ocean freezing temperature (blue line in Figure 8a). The temperature of the flooded layer then decreases slowly as it is cooled from above and below. A second flooding event at SIMBA-2015h is detected on 13 March, with 5 cm more of flooding and a small heat release (Figures 8a and 8c). Conductive flux densities at the flooded layer interface are smaller than during the February flooding event as ice and snow temperatures are larger than in February and about 8 cm of slush solidified into snow-ice in 7.5 days (Figure 8d).

The flooding event on 10 March at SIMBA_2015a is rather different than the one just described. The amount of slush formation at SIMBA_2015a on 10 March is small and increases gradually, with a few cm on 13 March and 5 cm on 15 March. The temperature of the slush is colder (–3°C) at formation until 14 March and it increases to ocean freezing temperature on 15 March (Figure 8a). Slush formation occurs at a time when the sea-ice, only 1 m thick, has been warmed up from below and above: the ice temperature on 9 March, right before slush formation, ranges between −2 and −4.7°C from bottom to top. The ice is probably more permeable [*Golden et al.*, 1998] and the cold temperature of the slush formed (–3°C), well below ocean freezing temperature, could be a sign of a process including vertical infiltration of brines rather than just lateral infiltration of seawater. However, the temperature pulse at flooding is at the base of the snow suggesting that flooding was from seawater intrusion (or brine that percolated up nearby and spread horizontally at the ice surface). Alternatively, the colder temperature of the slush could be due to the slow rate of intrusion, and the water was cooled as it flooded. Temperature pulses on 13 and 15 March at the base of the snow layer (Figure 8c) correspond to ocean temperature (–1.88°C) (Figure 8a) and further lateral flooding (5 cm on 13 March and 10 cm on 15 March) due to further freeboard adjustment as basal melt is active (25 cm of sea-ice melted between 12 and 16 March) (Figure 8). About 6 cm of slush solidified into snow-ice.

In all cases, the records after flooding are short (from 2 to 7 days) and stop before the whole slush layer solidified. The estimates of solidified snow-ice were produced assuming that the slush was made of 2/3 snow and 1/3 of water. If the initial snow was less dense and slush made of half water and half snow, the thickness of solidified snow-ice would be reduced by one third. The ratio of the slush thickness to the total ice thickness ranged between 17 and 28%.

4. Summary and Discussion

Seven SIMBAs, within a distance of 50 km from each other, continuously recorded snow and ice conditions in the Arctic Ocean north of Svalbard in the midwinter (January–March) 2015. The SIMBAs repeatedly observed temperature and thermal diffusivity proxy profiles with a 2 cm vertical resolution in air, snow, ice, and ocean below, allowing precise determination of interfaces and estimates of heat fluxes. They recorded temperature and snow depth changes associated with the six distinct synoptic events. Snow depths ranged from 30 to 90 cm and ice thicknesses from 0.9 to 1.6 m. The SIMBAs registered intense basal sea-ice melt when drifting over warm Atlantic waters north of Svalbard and ocean-to-ice fluxes peaked at 400 W m^{-2}. Four SIMBAs documented flooding and snow-ice formation. These are the first direct observations of snow-ice formation in the high Arctic. Flooding is evident from the simultaneous change in thermal diffusivity proxy (from high snow values to lower slush values), temperature increase and heat propagation throughout the snow and ice. Subsequent freezing of slush into snow-ice was estimated from the conductive fluxes into the snow above and ice below. The freezing was progressive and the records ended before the whole slush layer froze into snow-ice.

Two major flooding events were observed, one occurring after storm-induced floe break up, the other after intense basal sea-ice melt. The first flooding event (17 February) occurred at about 45 km from the open water (Figure 1a), preceded the basal melt onset and was associated to a major storm (M3) that lasted from 15 to 21 February [*Cohen et al.*, 2017]. In the vicinity of R/V Lance, cracks appeared on 16 February gradually breaking the floe into pieces less than 100 × 100 m large. On 17 February in the morning, we revisited SIMBA_2015f, while the base of snow cover was not flooded. SIMBA_2015f and SIMBA_2015i both detected flooding in the evening, while numerous cracks were visible from R/V Lance. From this moment on, revisits were no longer possible. Most probably, cracks allowed the ocean water to flood the floe surfaces. The ice before snow-ice formation was cold (profile temperature between −2 and −15°C) and impermeable. Most likely the snow-ice interface was forced down below sea level by the thick snow layer. Indeed, the consolidated ridges at the floe edges prevented lateral infiltration of seawater until the break up after which the snow was flooded and converted to slush at about the ocean freezing temperature. A layer of 25 cm of slush was formed in less than 3 h (time resolution of the instrument). The heat associated with the flooding increased the underlying ice temperatures by about 3°C. Then further heat was released into the snow above and the ice below as the slush layer progressively solidified. During the storm, the air temperatures rose above the freezing point (Figure 6b) and prevented the cracks and ridges to consolidate, but they dropped abruptly below −20°C by 18 February and facilitated the heat loss to the atmosphere (Figure 8d). However, the remaining snow after the flooding insulated the slush layer from the cold atmosphere and the contribution of the conductive fluxes through the snow to the freezing of the slush was smaller than that of the conductive fluxes through the ice. About 10 cm of slush solidified into snow-ice in 2–4 days (Figure 8d).

The second flooding event occurred during periods of intense basal melt, near the ice edge (about 15 km from the open ocean, Figure 1b), due to warm ocean temperatures (9–15 March). Flooding was gradual (a few days) and followed basal ice ablation. The ice before flooding showed temperatures above −4.5°C and it was likely permeable [*Golden et al.*, 1998]. The heat released by the flooding contributed to warm the ice from above (+3°C). Further lateral flooding at the ocean temperature (–1.88°C) was observed simultaneously on the two SIMBAs (5 cm on 13 March and 10 cm on 15 March) due to further freeboard adjustment due to intense basal melt (25 cm of sea-ice melted between 12 and 16 March) (Figure 8). Conductive fluxes from the slush layer to the snow and ice layers were smaller than in February as the snow and ice were warmer and the slush layer colder. The estimated thickness of snow-ice formed (about 6–8 cm) was smaller than in February, although the records were longer (7 days versus 2 or 4).

In the Antarctic, flooding of the snow base is widespread because sea-ice thickness is small and snow fall abundant. Because of this, snow/ice interface is often pushed below sea level, hydraulically forcing the infiltration of brines (vertically) or seawater (laterally) into snow forming snow-ice [*Eicken et al*., 1994]. The contribution of snow-ice to the total ice mass in the Arctic has not received much attention so far. This is due to the fact that snow-ice has not been expected to form in the Arctic since the ratio of snow thickness to ice thickness being usually low [*Vihma et al*., 2014].

Here the snow-ice records are quite short, 7 days for the longest one (SIMBA_2015h), as the SIMBAs stopped recording soon after flooding either because they were recovered (SIMBA_2015h and SIMBA_2015i) or damaged. This could imply that the ice floes with snow-ice rapidly deteriorated over warm water and were a transient feature, and that the flooding accelerated the decline of the ice cover by warming the ice, thus accelerating the basal melt, and also mechanically weakening the ice cover. However, the particular event of flooding and subsequent snow-ice formation caused by floe break up and lateral flooding (opposed to the snow-ice formation caused by basal melt) may imply that in the future Arctic Ocean with possibly more abundant snow precipitation [*Overland et al*., 2012; *Bintanja and Selten*, 2014], generally thinner [*Maslanik et al*., 2007; *Lindsay and Schweiger*, 2015] and weaker sea-ice, more storms penetrating to high latitudes [*Graham et al*., 2017] and consequently higher deformation rates [*Itkin, et al*., 2017], we might expect more snow-ice formation that is not associated only with the marginal ice zone. Indeed, the observations of significant amounts of snow-ice and superimposed ice in ice cores collected during N-ICE2015 [*Granskog et al*., 2017], supports that assumption. We need more measurements and model studies to establish the importance of snow-ice formation in the future Arctic. Indeed the marginal ice zone is expected to encompass the entire Arctic in a seasonally-ice-free Arctic.

Acknowledgments

We deeply thank the crew and scientists on board R/V Lance. Special thanks to Bengt Rotmo and Michel Calzas for assistance with deployment of the buoys. The Finnish Meteorological Institute contributed with three ice mass balance instruments. This work has been supported by the Norwegian Polar Institute's Centre for Ice, Climate and Ecosystems (ICE) through the N-ICE project. N-ICE acknowledges the in-kind contributions provided by other national and international projects and participating institutions, through personnel, equipment, and other support. In particular we acknowledge support from the ANR EQUIPEX IAOOS project, through ANR-10-EQPX-32-01 grant, and the ICE-ARC programme from the European Union 7th Framework Programme, grant 603887. The SIMBA data are available in *Itkin et al.* [2015] and C. Provost (cp@locean-ipsl.upmc.fr).

References

Bintanja, R., and F. M. Selten (2014), Future increases in Arctic precipitation linked to local evaporation and sea-ice-retreat, *Nature*, *509*, 479–484, doi:10.1038/nature13259.

Bitz, C. M., and W. H. Lipscomb (1999), An energy conserving thermodynamic model of sea ice, *J. Geophys. Res.*, *104*, 15,669–15,677.

Boisvert, L. N., and J. C. Stroeve (2015), The Arctic is becoming warmer and wetter as revealed by the Atmospheric Infrared Sounder, *Geophys. Res. Lett.*, *42*, 4439–4446, doi:10.1002/2015GL063775.

Bromwich, D. H., Z. Guo, L. Bai, and Q.-S. Chen (2004), Modeled Antarctic precipitation. Part I: Spatial and temporal variability, *J. Clim.*, *17*, 427–447.

Cohen, L., S. R. Hudson, V. P. Walden, R. M. Graham, and M. A. Granskog (2017), Meteorological conditions in a thinner Arctic sea ice regime from winter to during the Norwegian young sea ICE expedition (N-ICE2015), *J. Geophys. Res. Atmos.*, *122*, doi:10.1002/2016JD026034, in press.

Dee, D. P., et al. (2011), The ERA-Interim reanalysis: Configuration and performance of the data assimilation system, *Q. J. R. Meteorol. Soc.*, *137*(656), 553–597, doi:10.1002/qj.828.

Eicken, H., M. A. Lange, H. W. Hubberten, and P. Wadhams (1994), Characteristics and distribution patterns of snow and meteoric ice in the Weddell Sea and their contribution to the mass balance of sea ice, *Ann. Geophys.*, *12*, 80–93.

Eicken, H., H. Fischer, and P. Lemke (1995), Effects of snow cover on Antarctic sea ice and potential modulation of its response to climate change, *Ann. Glaciol.*, *21*, 369–376.

Golden, K. M., S. F. Ackley, and V. I. Lytle (1998), The percolation phase transition in sea ice, *Science*, *282*, 2238–2241, doi:10.1126/science.282.5397.2238.

Graham, R. M., A. Rinke, L. Cohen, S. R. Hudson, V. P. Walden, M. A. Granskog, W. Dorn, M. Kayser, and M. Maturilli (2017), A comparison of the two Arctic atmospheric winter states observed during N-ICE2015 and SHEBA, *J. Geophys. Res. Atmos.*, *122*, 5716–5737, doi:10.1002/2016JD025475.

Granskog, M., P. Assmy, S. Gerland, G. Spreen, H. Steen, and L. H. Smedsrud (2016), Arctic research on thin ice—Consequences of Arctic sea ice loss, *Eos Trans. AGU*, *97*(5), 22–26, doi:10.1029/2016EO044097.

Granskog, M. A., T. A. Martma, and R. A. Vaikmäe (2003), Development, structure and composition of land-fast sea ice in the northern Baltic Sea, *J. Glaciol.*, *49*(164), 139–148.

Granskog, M. A., A. Rösel, P. A. Dodd, D. V. Divine, S. Gerland, T. Martma, and M. J. Leng (2017), Snow contribution to first-year and second-year Arctic sea ice mass balance north of Svalbard, *J. Geophys. Res. Oceans*, *122*, 2539–2549, doi:10.1002/2016JC012398.

Haapala, J., M. Lensu, M. Dumont, A. H. H. Renner, M. A. Granskog, and S. Gerland (2013), Small-scale horizontal variability of snow, sea-ice thickness and freeboard in the first-year ice region north of Svalbard, *Ann. Glaciol.*, *54*(62), 261–266, doi:10.3189/2013AoG62A157.

Hezel, P. J., X. Zhang, C. M. Bitz, B. P. Kelly, and F. Massonnet (2012), Projected decline in spring snow depth on Arctic sea ice caused by progressively later autumn open ocean freeze-up this century, *Geophys. Res. Lett.*, *39*, L17505, doi:10.1029/2012GL052794.

Hudson, S., L. Cohen, and V. Walden (2016), *N-ICE2015 Surface Meteorology*, Norw. Polar Inst., Tromsø, Norway, doi:10.21334/npolar.2015.056a61d1.

Itkin, P., G. Spreen, S. R. Hudson, M. A. Granskog, S. Gerland, B. Cheng, and H. Steen (2015), *N-ICE2015 Buoy Data [Data Set]*, Norw. Polar Inst., doi:10.21334/npolar.2015.6ed9a8ca.

Itkin, P., G. Spreen, B. Cheng, M. Doble, F. Girard-Ardhuin, J. Haapala, N. Hughes, L. Kaleschke, M. Nicolaus, and J. Wilkinson (2017), Thin ice and storms: Sea ice deformation from buoy arrays deployed during N-ICE2015, *J. Geophys. Res. Oceans*, *122*, 4661–4674, doi:10.1002/2016JC012403, in press.

Jackson, K., J. Wilkinson, T. Maksym, D. Meldrum, J. Beckers, C. Haas, and D. McKenzie (2013), A novel and low-cost sea-ice mass balance buoy, *J. Atmos. Oceanic. Technol.*, *30*, 2676–2688, doi:10.1175/JTECH-D-13-00058.

Jeffries, M. O., A. Worby, K. Morris, and W. F. Weeks (1997), Seasonal variations in the properties and structural composition of sea ice and snow cover in the Bellingshausen and Amundsen Seas, Antarctica, *J. Glaciol.*, *43*, 138–151.

Jeffries, M. O., R. H. Krouse, B. Hurst-Cushing, and T. Maksym (2001), Snow-ice accretion and snow-cover depletion on Antarctic first-year sea-ice floes, *Ann. Glaciol.*, *33*, 51–60.

Kawamura, T., K. Shirasawa, and K. Kobinata (2001), Physical properties and isotopic characteristics of landfast sea ice around the North Water (NOW) Polynya region, *Atmos. Ocean*, *39*(3), 173–182, doi:10.1080/07055900.2001.9649674.

Kirillov, S., I. Dmitrenko, D. Babb, S. Rysgaard, and D. Barber (2015), The effect of ocean heat flux on seasonal ice growth in Young Sound (Northeast Greenland), *J. Geophys. Res. Ocean*, *120*, 4803–4824, doi:10.1002/2015JC010720.

Koenig, Z., C. Provost, N. Villacieros-Robineau, N. Sennéchael, and A. Meyer (2016), Winter ocean-ice interactions under thin sea ice observed by IAOOS platforms during N-ICE 2015: Salty surface mixed layer and active basal melt, *J. Geophys. Res. Oceans*, *121*, 7898–7916, doi:10.1002/2016JC012195.

Lewis, M. J., J. L. Tison, B. Weissling, B. Delille, S. F. Ackley, F. Brabant, and H. Xie (2011), Sea ice and snow cover characteristics during the winter-spring transition in the Bellingshausen Sea: An overview of SIMBA 2007, *Deep Sea Res., Part II*, *58*(9), 1019–1038, doi:10.1016/j.dsr2.2010.10.027.

Lindsay, R., and A. Schweiger (2015), Arctic sea ice thickness loss determined using subsurface, aircraft, and satellite observations, *Cryosphere*, *9*, 269–283, doi:10.5194/tc-9-269-2015.

Maksym, T., and T. Markus (2008), Antarctic sea-ice thickness and snow to ice conversion from atmospheric reanalysis and passive microwave snow depth, *J. Geophys. Res.*, *113*, C02S12, doi:10.1029/2006JC004085.

Maslanik, J. A., C. Fowler, J. Stroeve, S. Drobot, J. Zwally, D. Yi, and W. Emery (2007), A younger, thinner Arctic ice cover. Increased potential for rapid extensive sea-ice loss, *Geophys. Res. Lett.*, *34*, L24501, doi:10.1029/2007GL032043.

Massom, R. A., et al. (2001), Snow on Antarctic sea ice, *Rev. Geophys.*, *39*, 413–445.

Maykut, G. A., and N. Untersteiner (1971), Some results from a time-dependent thermodynamical model of sea-ice, *J. Geophys. Res.*, *76*, 1550–1575.

McPhee, M. G., T. Kikuchi, J. H. Morison, and T. P. Stanton (2003), Ocean-to-ice heat flux at the North Pole environmental observatory, *Geophys. Res. Lett.*, *30*(24), 2274, doi:10.1029/2003GL018580.

Ono, N. (1967), Physics of snow and ice, in *Specific Heat and Heat of Fusion of Sea Ice*, pp. 599–610, Inst. of Low Temp. Sci., Hokkaido, Japan.

Overland, J. E., and M. Wang (2013), When will the summer Arctic be nearly sea ice free?, *Geophys. Res. Lett.*, *40*, 2097–2101, doi:10.1002/grl.50316.

Overland, J. E., M. Wang, J. E. Walsh, J. H. Christensen, V. M. Kattsov, and W. L. Chapman (2012), Climate model projections for the Arctic, in *Snow, Water, Ice and Permafrost in the Arctic*, chap. 3, pp. 3.1–3.18, Arctic Monitoring and Assessment Programme, Oslo.

Perovich, D. K., and J. A. Richter-Menge (2009), Loss of sea ice in the Arctic, *Ann. Rev. Mar. Sci.*, *1*, 417–441, doi:10.1146/annurev.marine.010908.163805.

Pringle, D. J., H. J. Trodahl, and T. G. Haskell (2006), Direct measurements of sea ice thermal conductivity: No surface reduction, *J. Geophys. Res.*, *111*, C05020, doi:10.1029/2005JC0002990.

Rösel, A., et al. (2016), *N-ICE2015 Snow Depth Data With Magna Probe [Data Set]*, Norw. Polar Inst., doi:10.21334/npolar.2016.3d72756d.

Sirevaag, A. (2009), Turbulent exchange coefficients for the ice/ocean interface in case of rapid melting, *Geophys. Res. Lett.*, *36*, L04606, doi:10.1029/2008GL036587.

Spreen, G., R. Kwok, and D. Menemenlis (2011), Trends in Arctic sea ice drift and role of wind forcing: 1992–2009, *Geophys. Res. Lett.*, *38*, L19501, doi:10.1020/2011GL048970.

Tucker, W. B., T. C. Grenfell, R. G. Onstott, D. K. Perovich, A. J. Gow, R. A. Shuchman, and L. L. Sutherland (1991), Microwave and physical properties of sea ice in the winter marginal ice zone, *J. Geophys. Res.*, *96*, 4573–4587, doi:10.1029/90JC02269.

Ukita, J., T. Kawamura, N. Tanaka, T. Toyota, and M. Wakatsuchi (2000), Physical and stable isotopic properties and growth processes of sea ice collected in the southern Sea of Okhotsk, *J. Geophys. Res.*, *105*, 22,083–22,093.

Vihma, T., et al. (2014), Advances in understanding and parameterization of small-scale physical processes in the marine Arctic climate system: A review, *Atmos. Chem. Phys.*, *14*, 9403–9450, doi:10.5194/acp-14-9403-2014.

Webster, M. A., I. G. Rigor, S. V. Nghiem, N. T. Kurtz, S. L. Farrell, D. K. Perovich, and M. Sturm (2014), Interdecadal changes in snow depth on Arctic sea ice, *J. Geophys. Res. Oceans*, *119*, 5395–5406, doi:10.1002/2014JC009985.

Warren, S. G. et al. (1999), Snow depth on Arctic sea ice, *J. Clim.*, *12*, 1814–1829.

Weeks, W. F., and O. S. Lee (1958), Observations on the physical properties of sea-ice at Hopedale, Labrador, *Arctic*, *11*(3), 135–155.

Worby, A. P., C. A. Geiger, M. J. Pager, M. L. Van Woert, S. F. Ackley, and T. L. DeLiberty (2008), The thickness distribution of Antarctic sea ice, *J. Geophys. Res.*, *113*, C05592, doi:10.1029/2007JC004254.

Yen, Y. C. (1981), Review of thermal properties of snow, ice and sea ice, *Rep. 81-10*, 27 pp., U.S. Army Cold Reg. Res. and Eng. Lab., Hanover, N. H.

Appendix C

Leads in Arctic pack ice enable early phytoplankton blooms below snow-covered sea ice.

www.nature.com/scientificreports

SCIENTIFIC REPORTS

OPEN

Leads in Arctic pack ice enable early phytoplankton blooms below snow-covered sea ice

Received: 23 September 2016
Accepted: 09 December 2016
Published: 19 January 2017

Philipp Assmy[1], Mar Fernández-Méndez[1], Pedro Duarte[1], Amelie Meyer[1], Achim Randelhoff[1,2], Christopher J. Mundy[3], Lasse M. Olsen[1], Hanna M. Kauko[1], Allison Bailey[1], Melissa Chierici[4], Lana Cohen[1], Anthony P. Doulgeris[5], Jens K. Ehn[3], Agneta Fransson[1], Sebastian Gerland[1], Haakon Hop[1,2], Stephen R. Hudson[1], Nick Hughes[6], Polona Itkin[1], Geir Johnsen[7,8], Jennifer A. King[1], Boris P. Koch[9], Zoe Koenig[10], Slawomir Kwasniewski[11], Samuel R. Laney[12], Marcel Nicolaus[9], Alexey K. Pavlov[1], Christopher M. Polashenski[13], Christine Provost[10], Anja Rösel[1], Marthe Sandbu[7], Gunnar Spreen[1,14], Lars H. Smedsrud[15,16], Arild Sundfjord[1], Torbjørn Taskjelle[17], Agnieszka Tatarek[11], Jozef Wiktor[11], Penelope M. Wagner[6], Anette Wold[1], Harald Steen[1] & Mats A. Granskog[1]

The Arctic icescape is rapidly transforming from a thicker multiyear ice cover to a thinner and largely seasonal first-year ice cover with significant consequences for Arctic primary production. One critical challenge is to understand how productivity will change within the next decades. Recent studies have reported extensive phytoplankton blooms beneath ponded sea ice during summer, indicating that satellite-based Arctic annual primary production estimates may be significantly underestimated. Here we present a unique time-series of a phytoplankton spring bloom observed beneath snow-covered Arctic pack ice. The bloom, dominated by the haptophyte algae *Phaeocystis pouchetii*, caused near depletion of the surface nitrate inventory and a decline in dissolved inorganic carbon by $16 \pm 6\,\mathrm{g\,C\,m^{-2}}$. Ocean circulation characteristics in the area indicated that the bloom developed *in situ* despite the snow-covered sea ice. Leads in the dynamic ice cover provided added sunlight necessary to initiate and sustain the bloom. Phytoplankton blooms beneath snow-covered ice might become more common and widespread in the future Arctic Ocean with frequent lead formation due to thinner and more dynamic sea ice despite projected increases in high-Arctic snowfall. This could alter productivity, marine food webs and carbon sequestration in the Arctic Ocean.

Annual phytoplankton net primary production in the Arctic Ocean has increased by 30% since the late 1990's mainly due to the declining sea ice extent and an increasing phytoplankton growth season[1]. However, there is considerable uncertainty about the future change in Arctic Ocean primary productivity largely attributed to the

[1]Norwegian Polar Institute, Fram Centre, 9296 Tromsø, Norway. [2]Department of Arctic and Marine Biology, Faculty of Biosciences, Fisheries and Economics, UiT The Arctic University of Norway, 9037 Tromsø, Norway. [3]Centre for Earth Observation Science, University of Manitoba, Winnipeg, MB R3T 2N2, Canada. [4]Institute of Marine Research, 9019 Tromsø, Norway. [5]Department of Physics and Technology, Faculty of Science and Technology, UiT The Arctic University of Norway, 9037 Tromsø, Norway. [6]Norwegian Meteorological Institute, 9239 Tromsø, Norway. [7]Centre for Autonomous Marine Operations and Systems, Department of Biology, Norwegian University of Science and Technology, 7491 Trondheim, Norway. [8]University Centre in Svalbard, Post box 156, 9171 Longyearbyen, Norway. [9]Alfred Wegener Institute, Helmholtz Center for Polar and Marine Research, 27570 Bremerhaven, Germany. [10]LOCEAN, UMR 7159, CNRS/UPMC/MNHN/IRD, Pierre and Marie Curie University, Paris cedex, France. [11]Institute of Oceanology, Polish Academy of Sciences, 81-712 Sopot, Poland. [12]Biology Department, Woods Hole Oceanographic Institution, Woods Hole, MA 02543, USA. [13]U.S. Army, Cold Regions Research and Engineering Laboratory, Hanover, NH 03755, USA. [14]Institute of Environmental Physics, University of Bremen, 28334 Bremen, Germany. [15]Bjerknes Centre for Climate Research, 5007 Bergen, Norway. [16]Geophysical Institute, University of Bergen, 5007 Bergen, Norway. [17]Department of Physics and Technology, University of Bergen, 5007 Bergen, Norway. Correspondence and requests for materials should be addressed to P.A. (email: Philipp.Assmy@npolar.no)

different representation of the intricate balance between nutrient and light availability in coupled physical and biological ocean models[2,3]. The sea ice zone was identified as the area with largest model uncertainty[2]. Thus, a better understanding of the processes that control primary productivity in ice-covered waters will help to reduce this uncertainty.

Phytoplankton production beneath the ice-covered Arctic Ocean is assumed negligible because of the strong light attenuation properties of snow and sea ice, despite sporadic reports of phytoplankton growth beneath Arctic sea ice over the past decades[4–8]. This paradigm has recently been challenged by observations of under-ice phytoplankton blooms during the summer melt season[9–12]. In these studies, snowmelt onset and subsequent melt-pond formation permitted sufficient light transmission through the consolidated ice cover to trigger diatom-dominated phytoplankton blooms fuelled by underlying nutrient-rich waters[9–12]. In areas where extensive diatom blooms under thinning Arctic ice cover occur, current satellite-based estimates of annual primary production could be underestimated by an order of magnitude and change our perception of Arctic marine ecosystems[10]. In this study, we show for the first time that an under-ice phytoplankton bloom dominated by *Phaeocystis pouchetii* was actively growing beneath snow-covered pack ice at higher latitudes and earlier in the season than previously observed.

We studied the ice-associated ecosystem and the environmental factors shaping it in the Arctic Ocean north of Svalbard from 11 January to 24 June 2015 during the Norwegian young sea ICE (N-ICE2015) expedition[13]. Four ice camps were established during N-ICE2015[13], but herein we focus on drifts of ice floes 3 and 4 covering early spring to early summer (Fig. 1a). Chlorophyll (Chl *a*) concentrations in the water column were low ($<0.5\,\mu g\,L^{-1}$) until 25 May when we first drifted into an under-ice phytoplankton bloom over the Yermak Plateau (YP) 80 km north of the ice edge (Fig. 1a) and remained within it until the end of the expedition on 22 June (Fig. 1b). The onset of the bloom coincided with shallowing of the pycnocline (Fig. 1b) and reduction in turbulent mixing (Table S1). This resulted in an increased residence time in the surface layer and thus light exposure of phytoplankton. Maximum Chl *a* concentrations of $7.5\,\mu g\,L^{-1}$ were observed on 2 June and 50 m depth-integrated Chl *a* and particulate organic carbon (POC) standing stocks ranged between 109–233 mg Chl *a* m^{-2} and 9–22 g C m^{-2}. The under-ice bloom (10–80 km from open waters) nearly depleted the surface nitrate inventory (Fig. 1c) and reduced dissolved inorganic carbon (DIC) at depths down to 50 m (Fig. S1). The depth of nutrient depletion clearly indicates drawdown by phytoplankton rather than ice algal growth. Indeed, the ice algal community, dominated by pennate diatoms, was distinct from the under-ice bloom. The under-ice bloom was dominated by *P. pouchetii* (Fig. 2a), which accounted for 55–92% of phytoplankton abundance and 12–93% of phytoplankton biomass and occurred both in its flagellate stage (Fig. 2b) and as large colonies (Fig. 2c). Furthermore, ice algal standing stocks were low (<3 mg Chl *a* m^{-2}) throughout the drift indicating that contributions from the ice to water column stocks were negligible. A detailed list of protist plankton taxa observed during the bloom period can be found in the Supplementary Information (Table S2).

Regional ice thickness surveys with radius up to 50 km from the ice camp showed a total (ice plus snow) modal thickness of 1.8 m, with a secondary mode at 0.2 m, representing thin, lead ice (Fig. S2). Local surveys on floes 3 and 4 agreed, showing a modal ice thickness of 1.46 ± 0.66 m for the thick ice, covered by 0.39 ± 0.21 m of snow (Fig. S2), while snow thickness on the thin ice ranged from 0.01–0.06 m. Thus, for modelling of the under-ice light field and primary production, we treat all ice as being one of these two modal types either 'thick ice' with thick snow cover or 'thin ice' representative of recently refrozen leads with thin snow cover. The dominant snow-covered thick ice transmitted, on average, only $<1\%$ of the incident photosynthetic active radiation (E_{PAR}) to the underlying water column. On the other hand, E_{PAR} transmittance for thin ice examined near camp in a refrozen lead was 20% on average, ranging from 6.3–42.2%. Leads in the ice pack (Fig. S3) were frequently created by ice divergence events (Fig. S5) prior to and during the bloom period. This high lead fraction is characteristic of the pack ice north of Svalbard[14]. Satellite-based ice type classification (Fig. S4 and Table S3) indicated that open water and thin, newly formed ice covered 1–33% of the area during the bloom period (Fig. 3a). Melt ponds were not a major factor in light availability during this study. Snowmelt did not start until early June and melt ponds formed only towards the end of the study period, covering $<10\%$ of the ice surface. We combined the estimated aerial fractions of open water, thin ice and thick, snow-covered ice with E_{PAR} transmittance through these surfaces to estimate the aggregate light field (Fig. 3a and Figs S6 and S7) experienced by phytoplankton.

The growth potential of *P. pouchetii* was modelled based on ^{14}C photosynthesis-irradiance (PE) relationships obtained from a *P. pouchetii* bloom in the Greenland Sea[15], taking into account the underwater light field based on measured[16] and modelled irradiance through three different surface types (open water, thin ice with thin snow cover and thicker ice with thick snow cover) encountered during the study. The primary production (PP) model supports the observation that the bloom was actively growing beneath the ice despite the low irradiance (Fig. 3b). This is in accordance with previous studies showing that *Phaeocystis* is particularly well adapted to low light environments[17,18]. *In vivo* photosynthetic parameters, obtained with the Pulse Amplitude Modulation (PAM) method to assess the photo-acclimation status of the bloom, corroborate this finding (Table S5). High maximum quantum yields of charge separation in photosystem II (Chl *a* fluorescence of dark-acclimated cells) of 0.48–0.66 showed that the bloom-forming species were in good condition and actively growing. The maximum light utilization coefficient (α) of 0.188–0.295, obtained from Rapid Light Curves, also illustrates that the bloom exhibited high photosynthetic rates at low irradiances. Furthermore, the low POC/Chl *a* ratio of 31.4 in the upper 25 m of the under-ice water column suggests a relatively high investment in photosynthetic pigments, indicative of shade-acclimation. On the other hand, light saturation (E_k) values of 137–584 μmol photons $m^{-2}\,s^{-1}$ suggests that the phytoplankton community was at the same time acclimated to relatively high irradiances. This apparent inconsistency can be explained by the plasticity in photosynthetic performance of *P. pouchetii* that seems to be a characteristic feature of this species[15] promoting its dominance under the highly variable light regime encountered during this study. The relatively minor contribution of diatoms to the under-ice bloom (Fig. 2a), with the exception of 8 June, is supported by the PP model results (Table S4). Diatoms are usually a major component of the phytoplankton spring bloom in the marginal ice zone north of Svalbard[19] and have been reported to dominate

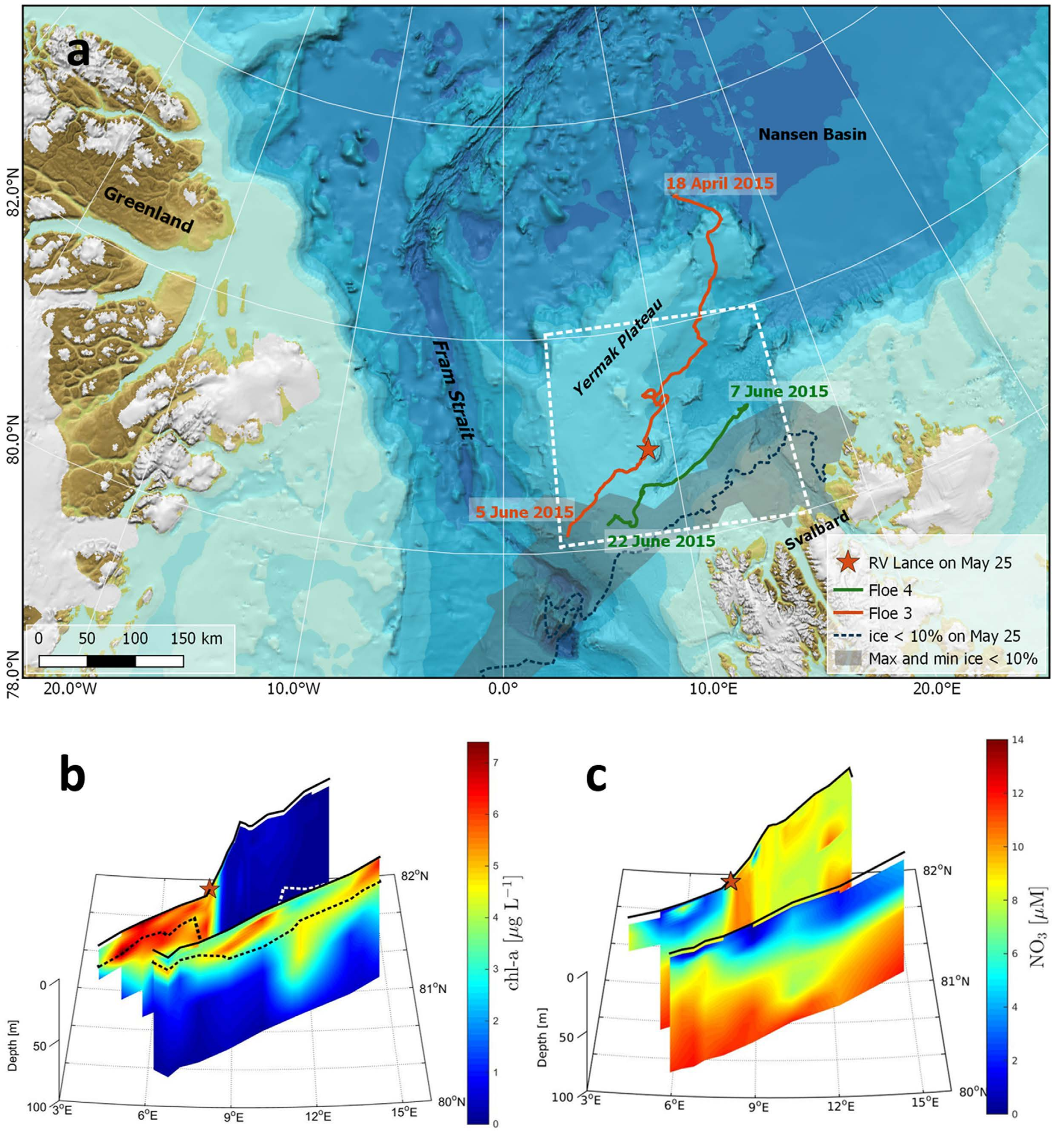

Figure 1. Study location and vertical and spatial extent of the under-ice bloom. (**a**) European Arctic with bathymetry. Orange and green lines are the drift trajectories of floes 3 and 4, respectively, with start and end dates. The location when we first drifted into the under-ice bloom on 25 May is indicated with an orange star. The area demarcating the ice-edge positions between April and June 2015 is shaded in grey. The ice-edge position on 25 May is indicated by the broken blue line and is representative for the bloom period. We define the ice edge as the outer perimeter of a polygon where ice concentration is >10%. The white outline demarcates the area shown in panels b and c. Map created by the Norwegian Polar Institute, Max König with permission from IBCAO[47]. Drift trajectories of floes 3 and 4 showing (**b**) Chlorophyll *a*, and (**c**), nitrate concentrations for the upper 100 m of the water column. The dashed line in (**b**) indicates depth of the pycnocline.

under-ice blooms below ponded ice in summer[9–12]. The dynamic light conditions beneath the snow-covered drifting pack ice interspersed with transparent leads were apparently not sufficient to sustain growth rates for diatom bloom build-up[20]. Silicic acid concentrations in the upper 50 m during the bloom period remained close to winter values at $4.0 \pm 0.4\,\mu\text{mol L}^{-1}$ (Fig. S8), suggesting that no substantial diatom growth had taken place in these waters.

Measurements made with a vessel-mounted profiling current meter during the drifts over the YP indicated that transport velocities in Polar Surface Water (PSW) were weak. Time-mean current velocity components in PSW at 20–30 m depth for the bloom period were $2.2\,\text{cm s}^{-1}$ heading nearly due west (Table S6). While these observations do not explicitly cover areas upstream of the drift itself, they indicate that advection over this part of YP was very weak during the expedition. An operational ocean model (PSY4, Mercator-Ocean, Table S6) shows similar, but smaller, net currents due west (Fig. 3c) at the same depth. These simulations do not contain tidal forcing and thus no tidal residual currents.

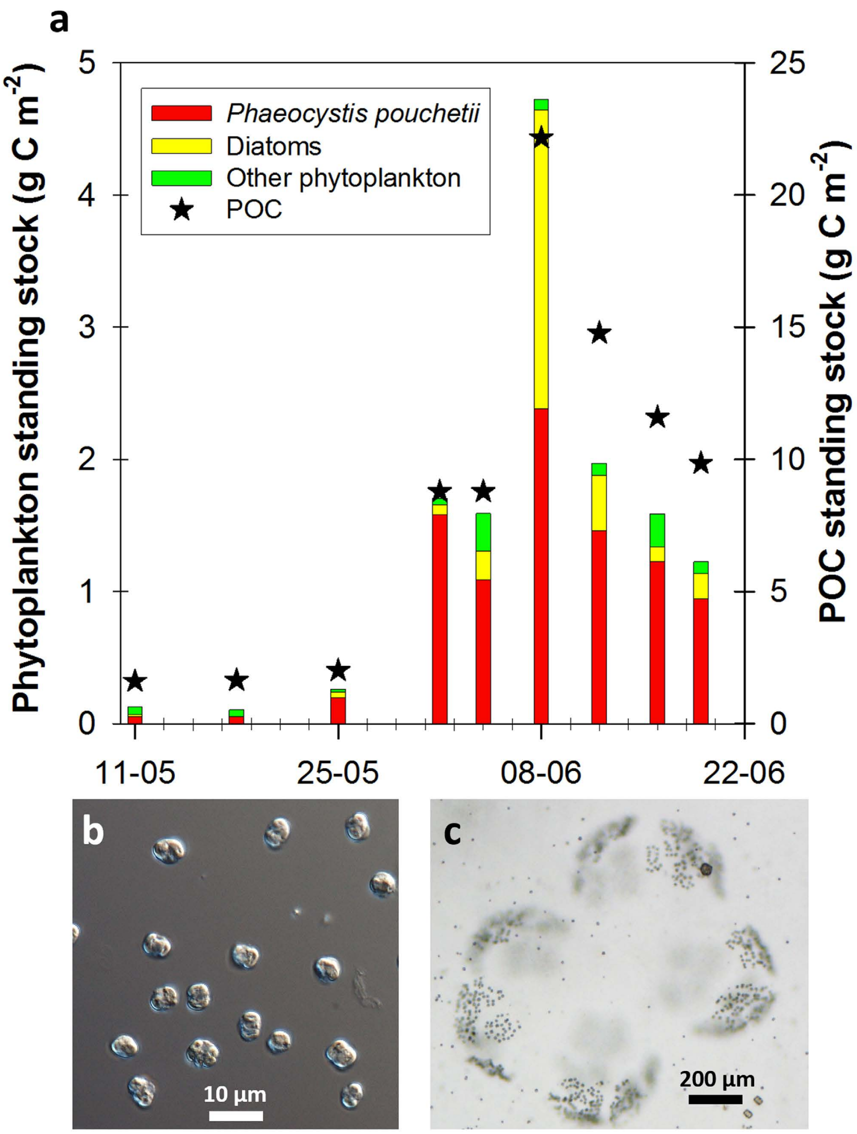

Figure 2. Composition of the under-ice phytoplankton bloom and particulate organic carbon standing stocks. (**a**) Integrated stocks of phytoplankton carbon (coloured bars) with contributions of *Phaeocystis pouchetii*, diatoms and other phytoplankton and particulate organic carbon (black stars) for the upper 50 m surface layer. Micrographs of (**b**), solitary cells (600x magnification) and (**c**), a colony of *P. pouchetii* (100x magnification).

Model and observations both suggest that surface waters over the interior YP were not advected from open water regions. During the bloom, model and observations show the presence of Atlantic Water (AW) masses at greater depths (Fig. 3d). The overall circulation regime was not favourable for rapid advection of AW from the main branches of the West Spitsbergen Current into the interior part of the YP. Mean currents on the YP itself were weak and not capable of advecting substantial volumes of surface waters from the ice edge to the northern-most part of the observed bloom on time scales less than six weeks. Six weeks prior to the observed under-ice bloom (12 and 13 April), we measured Chl *a* concentrations of $<0.1\,\mu g\,L^{-1}$ in open waters across the shelf slope north of Svalbard on transit to floe 3. Thus, the weak re-circulation pattern over YP implies that the bloom grew *in situ* beneath the ice pack. The area that floes 3 and 4 drifted over towards the end of their respective drifts in June was open water in mid-April when the ice edge was at its northern-most position during the period April to June 2015 (Fig. 1a and Supplementary Video). Considering the low Chl *a* concentration measured in April, our observations also discount the alternative explanation that the bloom developed in open waters and was subsequently covered by drifting sea ice. However, enhanced vertical mixing over the YP[21] supports the theory that *P. pouchetii* cells were likely mixed upwards from the sub-surface AW into the bloom in the PSW, thus contributing to the seeding of the bloom. This is consistent with observations that *P. pouchetii* is affiliated with AW[22]. Furthermore, in winter AW can be found close to the surface over the southern parts of YP providing another potential seeding mechanism.

The mean integrated drawdown of $16 \pm 6\,g\,C\,m^{-2}$ in the DIC inventory and a nitrate uptake equivalent to $15 \pm 5\,g\,C\,m^{-2}$ for the bloom period agreed well with the build-up in POC standing stocks. The biogeochemical footprint

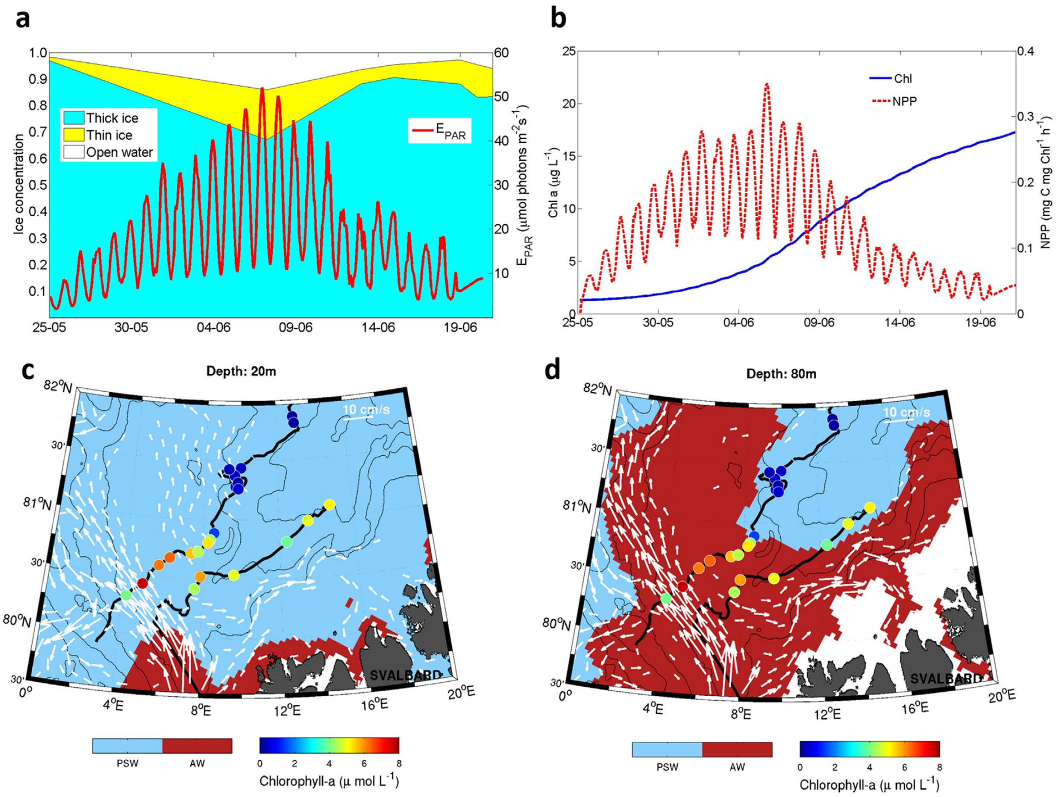

Figure 3. Primary production model and water mass circulation over the Yermak Plateau. (**a**) Open water, thin and thick ice concentration and weight-averaged E_{PAR} right below the sea surface based on the aerial fractions of the three different surface types. The white and coloured areas represent the area fraction of open water and sea ice, respectively, derived from satellite data (Supplementary Fig. S4). E_{PAR} values are modelled from surface E_{PAR} measurements and taking into account the diurnal cycle, different fractions of ice and open water and their respective optical properties. (**b**) Temporal evolution of Chl *a* concentration and net primary production (NPP) during the bloom period predicted by the model. Map of (**c**), surface (20 m) and (**d**), subsurface (80 m) simulated currents from model outputs with currents $>2\,\mathrm{cm\,s^{-1}}$. Current velocity is indicated by the size of the vectors (scale on figure). Black lines show drift trajectories. Colour dots show surface Chl *a* concentrations as measured along track indicating the bloom locations. Background colours show surface and subsurface water masses where blue is Polar Surface Water (PSW) and red is Atlantic Water (AW). Areas shallower than 20 m (**c**) and 80 m (**d**) are white. Topography of the Yermak Plateau is shown as thin black lines (500, 1000, 2000 and 3000 m). The maps in (**c**) and (**d**) were generated with the m-map package of Matlab 8.4 (https://www.eoas.ubc.ca/~rich/map.html).

of the bloom was comparable to a diatom bloom beneath ponded, more transparent sea ice at a lower latitude[12]. Carbon export rates at 100 m increased from 74 to 244 mg C m^{-2} d^{-1} during the bloom period. Inspection of 100 m depth sediment-trap material revealed that the bulk of vertical carbon export was mediated via *P. pouchetii* aggregates, while zooplankton faecal pellets accounted for <2%. Out of the 63 zooplankton taxa identified in 200 µm MultiNet samples taken during the bloom period, the three dominant *Calanus* species (*C. finmarchicus*, *C. glacialis* and *C. hyperboreus*) accounted for 89 ± 8% of the total zooplankton biomass. The apparently low grazing impact on the *P. pouchetii* bloom by the dominant *Calanus* copepods is supported by the finding that *P. pouchetii* does not significantly contribute to *Calanus* diet[23]. Daily export rates were low, corresponding to 0.9–2% of POC standing stocks in the upper 100 m. This is consistent with previous measurements from the Barents Sea[24] and supports the finding that *P. pouchetii* does not contribute much to deep carbon sequestration, which is generally mediated by diatoms[25,26]. This is corroborated by the dominance of fatty acid trophic markers from diatoms, rather than *Phaeocystis*, in benthic macrofauna[27]. Significant export of *P. pouchetii* biomass below 100 m has been reported previously[28,29], but has been attributed to downwelling[29], deep vertical mixing[26] or could potentially be attributed to other mechanisms facilitating deep export such as mineral ballasting.

Our observations extend the spatial and temporal domains of known under-ice blooms. High lead fraction provided sufficient light to initiate and sustain an under-ice spring bloom dominated by *P. pouchetii,* despite the thick snow cover and limited light transmission. High lead fractions in Fram Strait, the Barents Sea, and in other parts of the Arctic Ocean[14] suggest that early phytoplankton blooms under snow-covered sea ice might be widespread and become more prevalent in the future Arctic Ocean under an increasingly thinner and dynamic ice cover[30] and a projected increase in high-Arctic snowfall[31]. This trend could be reinforced by the recent increase in advective transport of AW into the European Arctic[32] seeding PSW with shade-adapted *P. pouchetii*, a conjecture that is corroborated by a shift in dominance from diatoms towards *P. pouchetii* in Fram Strait since 2006[33–35]. Nutrient depletion by early *P. pouchetii* blooms under snow-covered sea ice would constrain diatom blooms during the melt season, with far-reaching repercussions on bloom timing and composition, strength of the biological carbon pump and energy flow through Arctic marine food webs.

Methods

Standard analytical procedures. Chl *a* samples were collected on 25-mm GF/F filters (Whatman), extracted in 100% methanol for 12 h at 5 °C on board the ship and measured fluorometrically with an AU10 Turner Fluorometer (Turner Design, Inc.). Phaeopigments were measured by fluorescence after acidification with 5% HCl. Calibration of the Turner Fluorometer was carried out following the JGOFS protocol[36]. Chl *a* measurement uncertainty (5.5% of measured values) was estimated from triplicate water samples taken from depths ranging between 5 and 100 m. Particulate organic carbon (POC) and particulate organic nitrogen (PON) samples were collected onto pre-combusted 25-mm GF/F filters (Whatman), dried at 60 °C and stored at room temperature in PALL filter slides until analysis with continuous-flow mass spectrometry (CF-IMRS) carried out with a Roboprep/tracermass mass spectrometer (Europa Scientific, UK). All POC/N values were corrected for instrument drift and blanks. Water samples for inorganic nutrients were collected in 20 mL scintillation vials, fixed with 0.2 mL chloroform and stored refrigerated until sample analysis approximately 6 months later. Nitrite, nitrate, phosphate and silicic acid were measured spectrophotometrically at 540, 540, 810 and 810 nm, respectively, on a modified Scalar autoanalyser. The measurement uncertainty for nitrite is 0.06 μmol L^{-1} and 10% or less for nitrate, phosphate and silicic acid. Seawater for DIC analyses was sampled in 250 mL borosilicate bottles, preserved with 60 μL saturated mercuric chloride solution and stored dark and cool. DIC was determined using gas extraction followed by colourometric detection[37]. Certified Reference Material (CRM from A. Dickson at Scripps Institution of Oceanography, USA) was used for calibration and to check the accuracy of the analysis. The integrated nutrient drawdown in the upper 50 m for the bloom period was estimated from salinity-normalized (34.33) nDIC and nNO_3^- (nitrate) for all stations and converted to carbon using the measured POC/PON ratio of 5.7 ± 1.3. The complete N-ICE2015 water column biogeochemical dataset has been published in the Norwegian Polar Data Centre[38].

Sediment traps. Ice-tethered sediment traps (KC Denmark) were deployed four times at 5, 25, 50 and 100 m depth during the bloom period. Deployment time varied between 36 and 72 h, but was usually close to 48 h. Before deployment, each trap cylinder was filled with a saturated NaCl solution to reduce microbial activity and thus increase the retention of organic matter. The traps were carefully deployed and retrieved to avoid loss of trap material. Swimmers (copepods and other zooplankton) were removed before sub-sampling for Chl *a*, POC, plankton taxonomy, and faecal pellets.

Phyto-PAM measurements. The maximum quantum yield of charge separation in photosystem II Chl *a* fluorescence (ΦPSII-max), the light saturation parameter (E_k), the maximum light utilization coefficient (α) and the maximum relative electron transfer rate ($rETR_{max}$) were obtained using the Pulse Amplitude Modulated (PAM) fluorometry method with a Phyto-PAM (Walz, Germany) following established protocols[39].

Phyto- and zooplankton analysis. Phytoplankton samples were settled in 50 mL Utermöhl sedimentation chambers (HYDRO-BIOS©, Kiel, Germany) for 48 h. Phytoplankton was identified and enumerated at 100–600× magnification using an inverted Nikon Ti-S light and epifluorescence microscope. The organisms were identified to the lowest taxonomic level possible under inverted light microscopy, ideally to species level, otherwise to genus level or grouped into size-classes. Microscopic counts of the dominant organisms at each depth were always well above the recommended number of 50 per sample. Further, the water column stocks presented in Fig. 2 are integrations of 4 discrete samples from the upper 50 m of the water column, so the total number of specimens counted per predominating species per water column was >100 in most cases, reducing the error to <20%. Randomly chosen individuals of each phytoplankton species/group were measured and the average cell size was used to calculate the biovolume from equivalent geometrical shapes[40]. The biovolume was converted to cellular carbon content using published carbon conversion factors[41].

Mesozooplankton was sampled with a MultiNet (HYDRO-BIOS©, Kiel, Germany) consisting of five nets with a 0.25 m^2 opening and 200 μm mesh size at the following depth strata: 0–20, 20–50, 50–200 and 200 m-bottom. Zooplankton were preserved using 4% formaldehyde solution in seawater buffered with hexamethylentetramine and identified to species and stage[42].

Irradiance measurements. Solar spectral planar irradiance (E_λ) was measured simultaneously with two upward-looking Ramses spectral radiometers with cosine collectors (Ramses ACC-VIS, Trios GmbH, Germany). One measured the incident and the second the transmitted irradiance at the bottom of the ice. These measurements were integrated over the wavelength band of photosynthetically active radiation (PAR, 400–700 nm) and then used to estimate the transmittance (fraction of transmitted to incident radiation) of E_{PAR}, photosynthetically active radiation (PAR, 400–700 nm) through the ice and snow. The measurements were conducted continuously during floes 3 and 4 at a site representative of the thick snow-covered ice[43]. The same type of sensors were used to determine the transmittance of E_{PAR} for thin ice (<0.25 m) in a refrozen lead. In addition, incident irradiance and irradiance under thick and thin ice was measured with Satlantic HyperOCR hyperspectral radiometers with cosine collectors, at the surface and mounted to a remotely operated vehicle (ROV) respectively. From these measurements, transmittance of E_{PAR} was calculated as with the Ramses data.

Primary production model. A simple primary production model was applied using photosynthesis versus irradiance data obtained during an Arctic *Phaeocystis*-dominated phytoplankton bloom[15] combined with measured[16] and modelled irradiance through thick ice with thick snow cover, thin ice with thin snow cover and open water taking into account the areal fractions of the three different surface types. A detailed description of the primary production model can be found in the Supplementary Information.

Ice and snow thickness measurements. Total ice and snow thickness was measured with a portable electromagnetic instrument (EM31, Geonics Ltd., Mississauga, Ontario, Canada) mounted on a sledge[44]. In addition, large-scale surveys of total ice and snow thickness were conducted with a helicopter-borne EM instrument (HEM, Ferra Dynamics Inc, Mississauga, Ontario, Canada)[45]. The EM31 and HEM measurements use the same principle. The height above the bottom of the ice is derived from the strength of electromagnetic induction in the conductive sea water under the ice. For the HEM measurements, the height of the instrument above the surface of the ice or snow is determined with a laser altimeter included in the HEM instrument. The EM31 conductivity values were calibrated with drill-hole measurements and post processed to derive total thickness of ice and snow. Snow thickness was measured with a GPS snow probe (Magnaprobe, Snow-Hydro, Fairbanks, AK, USA)[46]. When used together, these two instruments give the spatial distribution of both the total thickness of the ice and snow (from EM31) and the snow depth (from Magnaprobe). For direct comparison of the values, and to subtract' the snow from the EM31 data, we re-sampled the EM31 data on the Magnaprobe track and applied a Gaussian filter to the EM31 data. The EM31 and Magnaprobe datasets were median-sampled on a 5 m regular grid. Snow depth was subtracted from the EM31 values to derive sea-ice thickness.

References

1. Arrigo, K. R. & van Dijken, G. L. Continued increases in Arctic Ocean primary production. *Progr. Oceanogr*. **136,** 60–70 (2015).
2. Vancoppenolle, M. *et al.* Future Arctic Ocean primary productivity from CMIP5 simulations: Uncertain outcome, but consistent mechanisms. *Global Biogeochem. Cy.* **27,** 605–619 (2013).
3. Popova, E. E. *et al.* What controls primary production in the Arctic Ocean? Results from an intercomparison of five general circulation models with biogeochemistry. *J. Geophys. Res.* **117,** C00D12 (2012).
4. Michel, C., Legendre, L., Therriault, J. C., Demers, S. & Vandevelde, T. Springtime coupling between ice algal and phytoplankton assemblages in southeastern Hudson Bay, Canadian Arctic. *Polar Biol.* **13,** 441—449 (1993).
5. Strass, V. H. & Nöthig, E. M. Seasonal shifts in ice edge phytoplankton blooms in the Barents Sea related to the water column stability. *Polar Biol.* **16,** 409—422 (1996).
6. Pomeroy, L. R. Primary production in the Arctic Ocean estimated from dissolved oxygen. *J. Mar. Syst.* **10,** 1–8 (1997).
7. Gosselin, M. *et al.* New measurements of phytoplankton and ice algal production in the Arctic Ocean. *Deep Sea Res. PT II* **44,** 1623–1644 (1997).
8. Fortier, M., Fortier, L., Michel, C. & Legendre, L. Climatic and biological forcing of the vertical flux of biogenic particles under seasonal Arctic sea ice. *Mar. Ecol. Prog. Ser.* **225,** 1—16 (2002).
9. Arrigo, K. R. *et al.* Massive phytoplankton blooms under Arctic sea ice. *Science* **336,** 1408–1408 (2012).
10. Arrigo, K. R. *et al.* Phytoplankton blooms beneath the sea ice in the Chukchi Sea. *Deep-Sea Res. PT II* **105,** 1–16 (2014).
11. Mundy, C. J. *et al.* Contribution of under-ice primary production to an ice-edge upwelling phytoplankton bloom in the Canadian Beaufort Sea. *Geophys. Res. Lett.* **36,** L17601 (2009).
12. Mundy, C. J. *et al.* Role of environmental factors on phytoplankton bloom initiation under landfast sea ice in Resolute Passage, Canada. *Mar. Ecol. Prog. Ser.* **497,** 39–49 (2014).
13. Granskog, M. A. *et al.* Arctic research on thin ice: Consequences of Arctic sea ice loss. *EOS Trans. AGU* **97,** 22–26 (2016).
14. Willmes, S. & Heinemann, G. Sea-ice wintertime lead frequencies and regional characteristics in the Arctic, 2003–2015. *Remote Sens*. **8,** doi: 10.3390/rs8010004 (2016).
15. Cota, G. F., Smith, W. O. Jr. & Mitchell, B. G. Photosynthesis of *Phaeocystis* in the Greenland Sea. *Limnol. Oceanogr.* **39,** 948–953 (1994).
16. Taskjelle, T., Granskog, M. A., Pavlov, A. K., Hudson, S. R. & Hamre, B. Effects of an Arctic under-ice bloom on solar radiant heating of the water column. *J. Geophys. Res. Oceans*, doi: 10.1002/2016JC012187 (2016).
17. Palmisano, A. C. *et al.* Photoadaptation in *Phaeocystis pouchetii* advected beneath annual sea ice in McMurdo Sound, Antarctica. *J. Plankton Res.* **8,** 891–906 (1986).
18. Sakshaug, E. & Skjoldal, H. R. Life at the ice edge. *Ambio* **18,** 60–67 (1989).
19. Degerlund, M. & Eilertsen, H. C. Main species characteristics of phytoplankton spring blooms in NE Atlantic and Arctic Waters (68–80 degrees N). *Estuaries and Coasts* **33,** 242–269 (2010).
20. Hoppe, C. J. M., Holtz, L.-M., Trimborn, S. & Rost, B. Ocean acidification decreases the light-use efficiency in an Antarctic diatom under dynamic but not constant light. *New Phytol* **207,** 159–171 (2015).
21. Rippeth, T. P. *et al.* Tide-mediated warming of Arctic halocline by Atlantic heat fluxes over rough topography. *Nature Geosci*. **8,** 191–194 (2015).
22. Metfies, K., von Appen, W.-J., Kilias, E., Nicolaus, A. & Nöthig, E.-M. Biogeography and photosynthetic biomass of Arctic marine pico-eukaryotes during summer of the record sea ice minimum 2012. *PLoS ONE* **11,** e0148512, doi: 10.1371/journal.pone.0148512 (2016).
23. Ray, J. L. *et al.* Molecular gut content analysis demonstrates that *Calanus* grazing on *Phaeocystis pouchetii* and *Skeletonema marinoi* is sensitive to bloom phase but not prey density. *Mar. Ecol. Prog. Ser.* **542,** 63—77 (2016).
24. Reigstad, M., Wexels Riser, C., Wassmann, P. & Ratkova, T. Vertical export of particulate organic carbon: Attenuation, composition and loss rates in the northern Barents Sea. *Deep Sea Res. PT II* **55,** 2308–2319 (2008).
25. Wassmann, P., Vernet, M., Mitchell, B. G. & Rey, F. Mass sedimentation of *Phaeocystis pouchetii* in the Barents Sea. *Mar. Ecol. Prog. Ser.* **66,** 183–195 (1990).
26. Reigstad, M. & Wassmann, P. Does *Phaeocystis* spp. contribute significantly to vertical export of organic carbon? *Biogeochem*. **83,** 217–234 (2007).
27. Søreide, J. E. *et al.* Sympagic-pelagic-benthic coupling in Arctic and Atlantic waters around Svalbard revealed by stable isotopic and fatty acid tracers. *Mar. Biol. Res.* **9,** 831–850 (2013).
28. Le Moigne, F. A. C. *et al.* Carbon export efficiency and phytoplankton community composition in the Atlantic sector of the Arctic Ocean. *J. Geophys. Res.* **120,** 3896–3912 (2015).
29. Lalande, C., Bauerfeind, E. & Nothig, E.-M. Downward particulate organic carbon export at high temporal resolution in the eastern Fram Strait: influence of Atlantic Water on flux composition. *Mar. Ecol. Prog. Ser.* **440,** 127–136 (2011).
30. Kwok, R., Spreen, G. & Pang, S. Arctic sea ice circulation and drift speed: Decadal trends and ocean currents. *J. Geophys. Res.* **118,** 2408–2425 (2013).

31. Bintanja, R. & Selten, F. M. Future increases in Arctic precipitation linked to local evaporation and sea-ice retreat. *Nature* **509,** 479–484 (2014).
32. Carmack, E. *et al.* Towards quantifying the increasing role of oceanic heat in sea ice loss in the new Arctic. *B. Am. Meteorol. Soc.* **97,** 2079–2105 (2015).
33. Lasternas, S. & Agusti, S. Phytoplankton community structure during the record Arctic ice-melting of summer 2007. *Polar Biol.* **33,** 1709–1717 (2010).
34. Lalande, C., Bauerfeind, E., Nöthig, E.-M. & Beszczynska-Moller, A. Impact of a warm anomaly on export fluxes of biogenic matter in the eastern Fram Strait. *Progr. Oceanogr.* **109,** 70–7 (2013).
35. Nöthig, E.-M. *et al.* Summertime plankton in Fram Strait – a compilation of long- and short-term observations. *Polar Res.* **34,** 23349 (2015).
36. Knap, A., Michaels, A., Close, A., Ducklow, H. & Dickson, A. Measurement of Chlorophyll *a* and Phaeopigments by fluorometric analysis. *JGOFS Rep.* **19,** 118–122 (1996).
37. Dickson, A. G., Sabine, C. L. & Christian, J. R. Guide to best practices for ocean CO_2 measurements. *PICES Spec. Publ.* **3,** 191 pp (2007).
38. Assmy, P. *et al.* N-ICE2015 water column biogeochemistry (v1.0) [Data set]. Norwegian Polar Institute. doi: 10.21334/npolar.2016.3ebb7f64 (2009).
39. Nymark, M. *et al.* An integrated analysis of molecular acclimation to high light in the marine diatom *Phaeodactylum tricornutum*. *PloS ONE* **11,** e7743 (2009).
40. Hillebrand, H., Duerselen, C. D., Kirschtel, D., Pollingher, U. & Zohary, T. Biovolume calculation for pelagic and benthic microalgae. *J Phycol* **35,** 403–424 (1999).
41. Menden-Deuer, S. & Lessard, E. J. Carbon to volume relationships for dinoflagellates, diatoms and other protist plankton. *Limnol. Oceanogr.* **45,** 569–579 (2000).
42. Kwasniewski, S., Hop, H., Falk-Petersen, S. & Pedersen, G. Distribution of *Calanus* species in Kongsfjorden, a glacial fjord in Svalbard. *J. Plankton. Res.* **25,** 1–20 (2003).
43. Taskjelle, T., Hudson, S. R., Pavlov, A. & Granskog, M. A. N-ICE2015 surface and under-ice spectral shortwave radiation data (v1.4) [*Data set*]. *Norwegian Polar Institute*, doi: 10.21334/npolar.2016.9089792e (2016).
44. Rösel, A. *et al.* N-ICE2015 total (snow and ice) thickness data from EM31 (v1.0) [Data set]. Norwegian Polar Institute. doi: 10.21334/npolar.2016.70352512 (2016).
45. King, J., Gerland, S., Spreen, G. & Bratrein, M. N-ICE2015 sea-ice thickness measurements from helicopter-borne electromagnetic induction sounding [Data set]. Norwegian Polar Institute. doi: 10.21334/npolar.2016.aa3a5232 (2016).
46. Rösel, A. *et al.* N-ICE2015 snow depth data with Magna Probe [Data set]. Norwegian Polar Institute. doi: 10.21334/npolar.2016.3d72756d (2016).
47. Jakobsson, M. *et al.* The International Bathymetric Chart of the Arctic Ocean (IBCAO) Version 3.0. *Geophys. Res. Lett.* **39,** L12609 (2012).

Acknowledgements

We are indebted to the captains and crew of RV *Lance*. This study was supported by the Centre for Ice, Climate and Ecosystems (ICE) at the Norwegian Polar Institute, the Ministry of Climate and Environment, Norway, the Research Council of Norway (projects Boom or Bust no. 244646, STASIS no. 221961, CORESAT no. 222681, CIRFA no. 237906 and AMOS CeO no. 223254), and the Ministry of Foreign Affairs, Norway (project ID Arctic), the ICE-ARC program of the European Union 7th Framework Program (grant number 603887), the Polish-Norwegian Research Program operated by the National Centre for Research and Development under the Norwegian Financial Mechanism 2009–2014 in the frame of Project Contract Pol-Nor/197511/40/2013, CDOM-HEAT, and the Ocean Acidification Flagship program within the FRAM- High North Research Centre for Climate and the Environment, Norway. The ALOS-2 Palsar-2 scene was provided by JAXA under the 4th Research Announcement program. Radarsat-2 data were provided by NSC/KSAT under the Norwegian-Canadian Radarsat agreement 2015. Thanks also to Max König, Thomas Kræmer and Malin Johansson for coordination of satellite acquisitions during N-ICE2015. We thank the Norwegian Meteorological Institute for ice chart data and the crew from Airlift that undertook the helicopter operations. We kindly acknowledge three anonymous reviewers and the editors of *Scientific Reports* for their valuable comments on the manuscript.

Author Contributions

H.S., M.A.G., S.R.H., S.G., G.S., L.H.S., N.H., A.S., P.A. and P.D. designed the field campaign. M.F.M., H.M.K., L.M.O., C.J.M., H.H., A.W., A.B., M.S., P.D., M.C., A.F., M.A.G., S.R.L., B.P.K. and P.A. collected and analysed the biogeochemical data. M.S., P.D., H.M.K. and G.J. performed the Phyto-PAM measurements and analysed the data. L.C., M.A.G. and S.R.H. conducted the atmospheric measurements. A.T. and J.W. performed the phytoplankton analysis and S.K. the zooplankton analysis. A.M., A.Ra., L.H.S. and Z.K. performed the oceanographic measurements. Z.K. and C.P. contributed with the operational model PSY4 from Mercator-Ocean. A.R., J.A.K., P.I., G.S., M.N., C.M.P. and S.G. contributed sea ice, snow and ice dynamics data. T.T., C.J.M., A.K.P., S.R.H., H.M.K., J.K.E. and M.A.G. conducted the irradiance measurements and analysed the data. P.M.W., N.H. and A.P.D. contributed remote sensing data and the sea ice classification. P.A. drafted the first manuscript; and all authors contributed to the final version.

Additional Information

Supplementary information accompanies this paper at http://www.nature.com/srep

Competing financial interests: The authors declare no competing financial interests.

How to cite this article: Assmy, P. *et al.* Leads in Arctic pack ice enable early phytoplankton blooms below snow-covered sea ice. *Sci. Rep.* **7**, 40850; doi: 10.1038/srep40850 (2017).

Bibliography

Aagaard, K., and E. C. Carmack (1989), The role of sea ice and other fresh water in the arctic circulation, *Journal of Geophysical Research: Oceans*, *94*(C10), 14,485–14,498, doi:10.1029/JC094iC10p14485.

Aksenov, Y., S. Bacon, A. C. Coward, and A. G. Nurser (2010a), The north atlantic inflow to the arctic ocean: High-resolution model study, *Journal of Marine Systems*, *79*(1), 1–22, doi:10.1016/j.jmarsys.2009.05.003.

Aksenov, Y., S. Bacon, A. C. Coward, and N. P. Holliday (2010b), Polar outflow from the arctic ocean: A high resolution model study, *Journal of Marine Systems*, *83*(1), 14–37.

Aksenov, Y., V. Ivanov, A. Nurser, S. Bacon, I. Polyakov, A. Coward, A. Naveira-Garabato, and A. Beszczynska-Möller (2011), The arctic circumpolar boundary current, *Journal of Geophysical Reserach: Oceans*, *116*(C9), doi:10.1029/2010JC006637.

Assmy, P., M. Fernández-Méndez, P. Duarte, A. Meyer, A. Randelhoff, C. J. Mundy, L. M. Olsen, H. M. Kauko, et al. (2017), Leads in arctic pack ice enable early phytoplankton blooms below snow-covered sea ice, *Scientific reports*, *7*, 40,850, doi:doi:10.1038/srep40850.

Bebieva, Y., and M.-L. Timmermans (2017), The relationship between double-diffusive intrusions and staircases in the arctic ocean, *Journal of Physical Oceanography*, *47*(4), 867–878, doi:http://dx.doi.org/10.1175/JPO-D-16-0265.1.

Beszczynska-Möller, A., E. Fahrbach, U. Schauer, and E. Hansen (2012), Variability in atlantic water temperature and transport at the entrance to the arctic ocean, 1997–2010, *ICES Journal of Marine Science: Journal du Conseil*, p. fss056, doi:https://doi.org/10.1093/icesjms/fss056.

Bintanja, R., and O. Andry (2017), Towards a rain-dominated arctic, *Nature Climate Change*, *7*(4), 263–267, doi:10.1038/NCLIMATE3240.

Bintanja, R., and F. Selten (2014), Future increase in arctic precipitation linked to local evaporation and sea-ice retreat, *Nature*, *509*(7501), 479–482, doi:10.1038/nature13259.

Boisvert, L., and J. Stroeve (2015), The arctic is becoming warmer and wetter as revealed by the atmospheric infrared sounder, *Geophysical Research Letters*, *42*(11), 4439–4446, doi:10.1002/2015GL063775.

Bourgain, P. (2012), The upper arctic ocean variability at a time of rapid arctic climate change, Ph.D. thesis, Paris 6.

Bourgain, P., and J.-C. Gascard (2012), The atlantic and summer pacific waters variability in the arctic ocean from 1997 to 2008, *Geophysical Research Letters*, *39*(5), doi:10.1029/2012GL051045.

Carmack, E., I. Polyakov, L. Padman, I. Fer, E. Hunke, J. Hutchings, J. Jackson, D. Kelley, R. Kwok, C. Layton, et al. (2015), Toward quantifying the increasing role of oceanic heat in sea ice loss in the new arctic, *Bulletin of the American Meteorological Society*, *96*(12), 2079–2105.

Carpenter, J., and M.-L. Timmermans (2012), Deep mesoscale eddies in the canada basin, arctic ocean, *Geophysical Research Letters*, *39*(20), doi:10.1029/2012GL053025.

Cohen, L., S. R. Hudson, V. P. Walden, R. M. Graham, and M. A. Granskog (2017), Meteorological conditions in a thinner arctic sea ice regime from winter through summer during the norwegian young sea ice expedition (n-ice2015), *Journal of Geophysical Research: Atmospheres*, doi:10.1002/2016JD026034.

Dosser, H. V., and L. Rainville (2016), Dynamics of the changing near-inertial internal wave field in the arctic ocean, *Journal of Physical Oceanography*, *46*(2), 395–415, doi:http://dx.doi.org/10.1175/JPO-D-15-0056.1.

Dosser, H. V., L. Rainville, and J. M. Toole (2014), Near-inertial internal wave field in the canada basin from ice-tethered profilers, *Journal of Physical Oceanography*, *44*(2), 413–426, doi:http://dx.doi.org/10.1175/JPO-D-13-0117.1.

Dupont, F., S. Higginson, R. Bourdallé-Badie, Y. Lu, F. Roy, G. Smith, J.-F. Lemieux, G. Garric, and F. Davidson (2015), A high-resolution ocean and sea-ice modelling system for the arctic and north atlantic oceans, *Geoscientific Model Development*, *8*(5), 1577–1594, doi:10.5194/gmd-8-1577-2015.

Falk-Petersen, S., V. Pavlov, J. Berge, F. Cottier, K. Kovacs, and C. Lydersen (2014), At the rainbow's end: high productivity fueled by winer upwelling along an arctic shelf, *POlar Biol.*, *38:5*(11), 5–11, doi:10.1007/s00300-014-1482-1.

Fer, I., R. Skogseth, and F. Geyer (2010), Internal waves and mixing in the marginal ice zone near the yermak plateau, *Journal of Physical Oceanography*, *40*(7), 1613–1630, doi:http://dx.doi.org/10.1175/2010JPO4371.1.

Gascard, J.-C., C. Richez, and C. Rouault (1995), New insights on large-scale oceanography in fram strait: The west spitsbergen current, *Arctic Oceanography: Marginal Ice Zones and Continental Shelves*, pp. 131–182, doi:10.1029/CE049p0131.

Gervais, M., E. Atallah, J. R. Gyakum, and L. B. Tremblay (2016), Arctic air masses in a warming world, *Journal of Climate*, *29*(7), 2359–2373, doi:http://dx.doi.org/10.1175/JCLI-D-15-0499.1.

Hattermann, T., P. E. Isachsen, W.-J. Von Appen, J. Albretsen, and A. Sundfjord (2016), Eddy-driven recirculation of atlantic water in fram strait, *Geophysical Research Letters*, *43*(7), 3406–3414, doi:10.1002/2016GL068323.

Ilıcak, M., H. Drange, Q. Wang, R. Gerdes, Y. Aksenov, D. Bailey, M. Bentsen, A. Biastoch, A. Bozec, C. Böning, et al. (2016), An assessment of the arctic ocean in a suite of interannual core-ii simulations. part iii: Hydrography and fluxes, *Ocean Modelling*, *100*, 141–161, doi:https://doi.org/10.1016/j.ocemod.2016.02.004.

Ivanov, V., V. Alexeev, N. V. Koldunov, I. Repina, A. B. Sandø, L. H. Smedsrud, and A. Smirnov (2016), Arctic ocean heat impact on regional ice decay: A suggested positive feedback, *Journal of Physical Oceanography*, *46*(5), 1437–1456, doi:http://dx.doi.org/10.1175/JPO-D-15-0144.1.

Janout, M. A., J. Hölemann, and T. Krumpen (2013), Cross-shelf transport of warm and saline water in response to sea ice drift on the laptev sea shelf, *Journal of Geophysical Research: Oceans*, *118*(2), 563–576, doi:10.1029/2011JC007731.

Kikuchi, T., K. Hatakeyama, and J. H. Morison (2004), Distribution of convective lower halocline water in the eastern arctic ocean, *Journal of Geophysical Research: Oceans*, *109*(C12), doi:10.1029/2003JC002223.

Koenig, Z., C. Provost, N. Villacieros-Robineau, N. Sennéchael, and A. Meyer (2016), Winter ocean-ice interactions under thin sea ice observed by iaoos platforms during n-ice2015: Salty surface mixed layer and active basal melt, *Journal of Geophysical Research: Oceans*, *121*(10), 7898–7916, doi:10.1002/2016JC012195.

Koenig, Z., C. Provost, N. Villacieros-Robineau, N. Sennéchael, A. Meyer, J.-M. Lellouche, and G. Garric (2017a), Atlantic waters inflow north of svalbard: Insights from iaoos observations and mercator ocean global operational system during n-ice2015, *Journal of Geophysical Research: Oceans*, *122*(2), 1254–1273, doi:10.1002/2016JC012424.

Koenig, Z., C. Provost, N. Sennéchael, G. Garric, and J.-C. Gascard (2017b), The yermak pass branch, a major pathway for the atlantic water north of svalbard?, *Journal of Geophysical Research: Oceans*, doi:10.1002/2017JC013271.

Kwok, R., and G. Cunningham (2015), Variability of arctic sea ice thickness and volume from cryosat-2, *Phil. Trans. R. Soc. A*, *373*(2045), doi:10.1098/rsta.2014.0157.

Kwok, R., and D. Rothrock (2009), Decline in arctic sea ice thickness from submarine and icesat records: 1958–2008, *Geophysical Research Letters*, *36*(15), doi:10.1029/2009GL039035.

Lellouche, J.-M., O. Le Galloudec, M. Drevillon, C. Régnier, E. Greiner, G. Garric, N. Ferry, C. Desportes, C.-E. Testut, C. Bricaud, et al. (2012), Evaluation of real time and future global monitoring and forecasting systems at mercator océan., *Ocean Science Discussions*, *9*(2).

Lique, C., and M. Steele (2012), Where can we find a seasonal cycle of the atlantic water temperature within the arctic basin?, *Journal of Geophysical Research: Oceans*, *117*(C3), doi:10.1029/2011JC007612.

Luneva, M. V., Y. Aksenov, J. D. Harle, and J. T. Holt (2015), The effects of tides on the water mass mixing and sea ice in the arctic ocean, *Journal of Geophysical Research: Oceans*, *120*(10), 6669–6699, doi:10.1002/2014JC010310.

Manucharyan, G., and M.-L. Timmermans (2013), Generation and separation of mesoscale eddies from surface ocean fronts, *Journal of Physical Oceanography*, *43*, 2545–2562, doi:10.1175/JPO-D-13-094.1.

Mariage, V., J. Pelon, F. Blouzon, S. Victori, N. Geyskens, N. Amarouche, C. Drezen, A. Guillot, M. Calzas, M. Garracio, et al. (2017), Iaoos microlidar-on-buoy development and first atmospheric observations obtained during 2014 and 2015 arctic drifts, *Optics Express*, *25*(4), A73–A84, doi:10.1002/2015JC011186.

Martin, T., M. Tsamados, D. Schroeder, and D. L. Feltham (2016), The impact of variable sea ice roughness on changes in arctic ocean surface stress: A model study, *Journal of Geophysical Research: Oceans*, *121*(3), 1931–1952, doi:10.1002/2015JC011186.

Meyer, A., A. Sundfjord, I. Fer, C. Provost, N. Villacieros Robineau, Z. Koenig, I. H. Onarheim, L. H. Smedsrud, P. Duarte, P. A. Dodd, et al. (2017a), Winter to summer oceanographic observations in the arctic ocean north of svalbard, *Journal of Geophysical Research: Oceans*, doi:10.1002/2016JC012391.

Meyer, A., I. Fer, A. Sundfjord, and A. K. Peterson (2017b), Mixing rates and vertical heat fluxes north of svalbard from arctic winter to spring, *Journal of Geophysical Research: Oceans*, doi:10.1002/2016JC012441.

Morison, J., M. McPhee, T. Curtin, and C. Paulson (1992), The oceanography in winter leads, *Journal of Geophysical Research: Oceans*, *97*(C7), 11,199–11,218, doi:10.1029/92JC00684.

Onarheim, I., L. Smedsrud, I. R.B., and F. Nilsen (2014), Loss of sea ice during winter north of svalbard, *Tellus A: Dynamic Meteorology and Oceanography*, *66*(1), 23,933, doi:10.3402/tellusa.v66.23933.

Padman, L., and T. M. Dillon (1987), Vertical heat fluxes through the beaufort sea thermohaline staircase, *Journal of Geophysical Research: Oceans*, *92*(C10), 10,799–10,806, doi:10.1029/JC092iC10p10799.

Padman, L., and T. M. Dillon (1991), Turbulent mixing near the yermak plateau during the coordinated eastern arctic experiment, *Journal of Geophysical Research: Oceans*, *96*(C3), 4769–4782, doi:10.1029/90JC02260.

Padman, L., R. Plueddemann, R. Munech, and R. Pinke (1992), Diurnal tides near the yermak plateau, *Journal of Geophysical Research: Oceans*, doi:10.1029/92JC01097.

Park, D.-S. R., S. Lee, and S. B. Feldstein (2015), Attribution of the recent winter sea ice decline over the atlantic sector of the arctic ocean, *Journal of climate*, *28*(10), 4027–4033, doi:http://dx.doi.org/10.1175/JCLI-D-15-0042.1.

Perez-Hernandez, M., R. Pickart, A. Sundfjord, R. Ingvaldsen, and A. Renner (2017), Characteriscs of the svalbard branch of the atlantic water boundary current, *ASOF meeting*.

Perovich, D., and J. Richter-Menge (2000), Ice growth and solar heating in springtime leads, *Journal of Geophysical Research: Oceans*, *105*(C3), 6541–6548, doi:10.1029/1999JC900321.

Perovich, D., K. Jones, B. Light, H. Eicken, T. Markus, J. Stroeve, and R. Lindsay (2011), Solar partitioning in a changing arctic sea-ice cover, *Annals of Glaciology*, *52*(57), 192–196.

Perovich, D., W. Meier, M. Tschudi, S. Farrell, S. Gerland, and S. Hendricks (2015), Sea ice, *Arctic Report Card (NOAA)*.

Peterson, A. K., I. Fer, M. G. McPhee, and A. Randelhoff (2017), Turbulent heat and momentum fluxes in the upper ocean under arctic sea ice, *Journal of Geophysical Research: Oceans*, *122*(2), 1439–1456, doi:10.1002/2016JC012283.

Pinto, J., J. Curry, and K. McInnes (1995), Atmospheric convective plumes emanating from leads: 1. thermodynamic structure, *Journal of Geophysical Research: Oceans*, *100*(C3), 4621–4631, doi:10.1029/94JC02654.

Polyakov, I. V., A. V. Pnyushkov, M. B. Alkire, I. M. Ashik, T. M. Baumann, E. C. Carmack, I. Goszczko, J. Guthrie, V. V. Ivanov, T. Kanzow, et al. (2017), Greater role for atlantic inflows on sea-ice loss in the eurasian basin of the arctic ocean, *Science*, *356*(6335), 285–291, doi:10.1126/science.aai8204.

Provost, C., N. Sennéchael, N. Villacieros-Robineau, Z. Koenig, P. Itkin, A. Rösel, and M. Granskog (2016), Observatioons of snow-ice formation in a thinner arctic sea ice regime during the n-ice2015 campaign: influence of basal ice melt and storms, *FAMOS meeting*.

Provost, C., N. Sennéchael, J. Miguet, P. Itkin, A. Rösel, Z. Koenig, N. Villacieros-Robineau, and M. A. Granskog (2017), Observations of flooding and snow-ice formation in a thinner arctic sea ice regime during the n-ice2015 campaign: Influence of basal ice melt and storms, *Journal of Geophysical Research: Oceans*, doi:10.1002/2016JC012011.

Rabe, B., M. Karcher, U. Schauer, J. M. Toole, R. A. Krishfield, S. Pisarev, F. Kauker, R. Gerdes, and T. Kikuchi (2011), An assessment of arctic ocean freshwater content changes from the 1990s to the 2006–2008 period, *Deep Sea Research Part I: Oceanographic Research Papers*, *58*(2), 173–185, doi:https://doi.org/10.1016/j.dsr.2010.12.002.

Rainville, L., and P. Winsor (2008), Mixing across the arctic ocean: Microstructure observations during the beringia 2005 expedition, *Geophysical Research Letters*, *35*(8), doi:10.1029/2008GL033532.

Randelhoff, A., A. Sundfjord, and M. Reigstad (2015), Seasonal variability and fluxes of nitrate in the surface waters over the arctic shelf slope, *Geophysical Research Letters*, *42*(9), 3442–3449, doi:10.1002/2015GL063655.

Rippeth, T. P., B. J. Lincoln, Y.-D. Lenn, J. M. Green, A. Sundfjord, and S. Bacon (2015), Tide-mediated warming of arctic halocline by atlantic heat fluxes over rough topography, *Nature Geoscience*, *8*(3), 191–194, doi:10.1038/ngeo2350.

Rudels, B. (2012), Arctic ocean circulation and variability-advection and external forcing encounter constraints and local processes, *Ocean Science*, *8*(2), 261, doi:10.5194/os-8-261-2012.

Rudels, B., L. Anderson, and E. Jones (1996), Formation and evolution of the surface mixed layer and halocline of the arctic ocean, *Journal of Geophysical Research: Oceans*, *101*(C4), 8807–8821, doi:10.1029/96JC00143.

Rudels, B., R. Meyer, E. Fahrbach, V. Ivanov, S. Østerhus, D. Quadfasel, U. Schauer, V. Tverberg, and R. Woodgate (2000), Water mass distribution in fram strait and over the yermak plateau in summer 1997, in *Annales Geophysicae*, vol. 18, pp. 687–705, Springer, doi:10.1007/s00585-000-0687-5.

Rudels, B., E. P. Jones, U. Schauer, and P. Eriksson (2004), Atlantic sources of the arctic ocean surface and halocline waters, *Polar Research*, *23*(2), 181–208, doi:http://dx.doi.org/10.3402/polar.v23i2.6278.

Rudels, B., N. Kuzmina, U. Schauer, T. Stipa, and V. Zhurbas (2009), Double-diffusive convection and interleaving in the arctic ocean–distribution and importance, *Geophysica*, *45*(1-2), 199–213.

Rudels, B., M. Korhonen, U. Schauer, S. Pisarev, B. Rabe, and A. Wisotzki (2015), Circulation and transformation of atlantic water in the eurasian basin and the contribution of the fram strait inflow branch to the arctic ocean heat budget, *Progress in Oceanography*, *132*, 128–152, doi:https://doi.org/10.1016/j.pocean.2014.04.003.

Saloranta, T., and P. Haugan (2001), Interannual variability in the hydrography of atlantic water northwest of svalbard, *Journal of Geophysical Research: Oceans*, *106*(C7), 13,931–13,943, doi:10.1029/2000JC000478.

Schauer, U., and A. Beszczynska-Möller (2009), Problems with estimation and interpretation of oceanic heat transport–conceptual remarks for the case of fram strait in the arctic ocean, *Ocean Science*, *5*(4), 487–494, doi:www.ocean-sci.net/5/487/2009/.

Screen, J. A., and I. Simmonds (2010), The central role of diminishing sea ice in recent arctic temperature amplification, *Nature*, *464*(7293), 1334–1337, doi:10.1038/nature09051.

Sirevaag, A., and I. Fer (2009), Early spring oceanic heat fluxes and mixing observed from drift stations north of svalbard, *Journal of Physical Oceanography*, *39*(12), 3049–3069, doi:http://dx.doi.org/10.1175/2009JPO4172.1.

Stocker, T., D. Qin, G.-K. Plattner, M. Tignor, S. Allen, J. Boschung, A. Nauels, Y. Xia, V. Bex, and P. M. Midgley (2013), Climate change 2013: The physical science basis. contribution of working group i to the fifth assessment report of the intergovernmental panel on climate change, 1535pp.

Timmermans, M.-L., J. Toole, A. Proshutinsky, R. Krishfield, and A. Plueddemann (2008), Eddies in the canada basin, arctic ocean, observed from ice-tethered profilers, *Journal of Physical Oceanography*, *38*(1), 133–145, doi:http://dx.doi.org/10.1175/2007JPO3782.1.

Timmermans, M.-L., R. Krishfield, S. Laney, and J. Toole (2010), Ice-tethered profiler measurements of dissolved oxygen under permanent ice cover in the arctic ocean, *Journal of Atmospheric and Oceanic Technology*, *27*(11), 1936–1949, doi:http://dx.doi.org/10.1175/2010JTECHO772.1.

Tsubouchi, K., W.-J. Von Appen, and U. Schauer (2017), The arctic ocean volume, heat and freshwater transports during 2004-2010, *ASOF meeting*.

Tsubouchi, T., S. Bacon, A. Naveira Garabato, Y. Aksenov, S. Laxon, E. Fahrbach, A. Beszczynska-Möller, E. Hansen, C. M. Lee, and R. Ingvaldsen (2012), The arctic ocean in summer: A quasi-synoptic inverse estimate of boundary fluxes and water mass transformation, *Journal of Geophysical Research: Oceans*, *117*(C1), doi:10.1029/2011JC007174.

Våge, K., R. S. Pickart, V. Pavlov, P. Lin, D. J. Torres, R. Ingvaldsen, A. Sundfjord, and A. Proshutinsky (2016), The atlantic water boundary current in the nansen basin: Transport and mechanisms of lateral exchange, *Journal of Geophysical Research: Oceans*, *121*(9), 6946–6960, doi:10.1002/2016JC011715.

Vaughan, D. G., J. C. Comiso, I. Allison, J. Carrasco, G. Kaser, R. Kwok, P. Mote, T. Murray, F. Paul, J. Ren, et al. (2013), Observations: cryosphere, *Climate change*, *2103*, 317–382.

Vihma, T., R. Pirazzini, I. Fer, I. A. Renfrew, J. Sedlar, M. Tjernström, C. Lüpkes, T. Nygard, D. Notz, J. Weiss, et al. (2014), Advances in understanding and parameterization of small-scale physical processes in the marine arctic climate system: a review, *Atmospheric Chemistry and Physics (ACP)*, *14*(17), 9403–9450, doi:10.5194/acp-14-9403-2014.

Von Appen, W.-J., U. Schauer, T. Hattermann, and A. Beszczynska-Möller (2016), Seasonal cycle of mesoscale instability of the west spitsbergen current, *Journal of Physical Oceanography*, *46*(4), 1231–1254, doi:http://dx.doi.org/10.1175/JPO-D-15-0184.1.

Walczowski, W., J. Piechura, I. Goszczko, and P. Wieczorek (2012), Changes in atlantic water properties: an important factor in the european arctic marine climate, *ICES Journal of Marine Science*, *69*, 864–869, doi:10.1093/icesjms/fss068.

Wekerle, C., Q. Wang, S. Danilov, V. Schourup-Kristensen, W.-J. von Appen, and T. Jung (2017), Atlantic water in the nordic seas: Locally eddy-permitting ocean simulation in a global setup, *Journal of Geophysical Research: Oceans*, *122*(2), 914–940, doi:10.1002/2016JC012121.

Woodgate, R. A., K. Aagaard, and T. J. Weingartner (2005), Monthly temperature, salinity, and transport variability of the bering strait through flow, *Geophysical Research Letters*, *32*(4), doi:10.1029/2004GL021880.

Woodgate, R. A., A. Nguyen, P. Heimbach, J. Raymond-Yakoubian, and C. Peralta-Ferriz (2017), Understanding recent change in the bering strait, *ASOF meeting*.

Woods, C., and R. Caballero (2016), The role of moist intrusions in winter arctic warming and sea ice decline, *Journal of Climate*, *29*(12), 4473–4485, doi:http://dx.doi.org/10.1175/JCLI-D-15-0773.1.

Zhao, M., M.-L. Timmermans, S. Cole, R. Krishfield, A. Proshutinsky, and J. Toole (2014), Characterizing the eddy field in the arctic ocean halocline, *Journal of Geophysical Research: Oceans*, *119*(12), 8800–8817, doi:10.1002/2014JC010488.

Zuo, H., R. I. Mugford, K. Haines, and G. C. Smith (2011), Assimilation impacts on arctic ocean circulation, heat and freshwater budgets, *Ocean Modelling*, *40*(2), 147–163, doi:10.1016/j.ocemod.2011.08.008.